Title

Physics of Optoelectronic and Plasmonic Devices: Cavities, Waveguides, Modulators and Lasers

Permalink

https://escholarship.org/uc/item/8ft5s2cr

Author

Sorger, Volker J.

Publication Date

2011

Peer reviewed|Thesis/dissertation

Physics of Optoelectronic and Plasmonic Devices: Cavities, Waveguides, Modulators and Lasers

By

Volker Jendrik Sorger

A Dissertation Submitted In Partial Satisfaction of the

Requirements for the Degree of

Doctor of Philosophy

In

Engineering-Mechanical Engineering

And the Designated Emphasis

In

Nanoscale Science and Engineering

In the

Graduate Division

of the

University of California, Berkeley

Committee in Charge:

Professor Xiang Zhang

Professor Samuel Mao

Professor Connie Chang-Hasnain

Spring 2011

Abstract

"Physics of Optoelectronic and Plasmonic Devices: Cavities, Waveguides, Modulators and Lasers"

By

Volker Jendrik Sorger

Doctor of Philosophy in Engineering-Mechanical Engineering

And the Designated Emphasis In

Nanoscale Science and Engineering

University of California, Berkeley

Professor Xiang Zhang, Chair

This dissertation explores the fundamental interactions between light and matter towards devices applications in the field of Opto-electronics and metal-optics, or plasmonics. In its core, this dissertation attempts, and succeeds to demonstrate strong enhancements of such interactions. Here, surface plasmon polaritons, collective electronic oscillations at metal-dielectric interfaces, play a significant role, as they allow for nano-scale wavelengths with visible and near-infrared light. In particular the rate of spontaneous emission was shown to be significantly increased via increasing the local electromagnetic field density surrounding a photonic emitter. A nanoscale plasmonic cavity has been fabricated and shown to provide reasonable feedback while confining the optical mode beyond the diffraction limit of light. In addition microcavities cavities were coated with metal demonstrating the highest cavity quality-factor for a plasmonic system to date.

Furthermore, a low loss deep-subwavelength waveguide has been proposed and experimentally demonstrated. This novel waveguide uniquely combines ultra-small squeezed optical propagating fields with semiconductor technology, allowing for high waveguiding figure-of-merits; wave propagation versus mode confinement. Deploying near-field scanning optical microscopy, the tiny optical mode of such waveguides has been probed, revealing the first images of truly nanoscale optical waveguiding.

The challenge to demonstrate a sub-wavelength plasmon Nanolaser was successfully overcome by deploying the aforementioned hybrid plasmonic waveguide architecture. Such Nanolasers were found to operate close to the thresholdless, ideal regime for lasers. The high optical loss of

such plasmon Nanolasers was mitigated by utilizing the unique physical mechanism inside the plasmon Nanolaser cavity. In particular, this dissertation shows, that ultra-small optical modes are enhancing laser-mode selection leading to higher laser efficiencies and potentially reduced laser thresholds. Furthermore, this study of plasmon Nanolasers suggests a direct laser modulation bandwidth far exceeding that of any traditional laser and lastly discusses the integration of coherent nanoscale light source into ultra-compact integrated photonic on-chip solutions.

Enhanced light-matter-interactions have further been explored towards combining photonic and logic, or computation. Here, plasmonic-optically enhanced architectures were used to create optical non-linear effects with unprecedented efficiency and ultra-small device foot-prints. In particular, the electro-optical effect was deployed in a novel device interfacing silicon-on-insulator technology with hybrid plasmonics. First results show that one to two volt of electrical bias can switch an optical signal requiring only a few micrometer-long light-matter-interaction lengths. Furthermore, higher order non-linear effects, e.g. 3rd order, have been predicted to boost such interactions even further paving the way towards efficient nanoscale all-optical transistors and routers.

Light-emitting tunnel junctions on the basis of metal-insulator-semiconductors were realized showing the highest quantum efficiency for such devices to date. Such 100% CMOS compatible on-chip silicon-based light sources were simulated yielding direct modulation speeds far exceeding the tea-hertz range.

In conclusion Opto-electronic device physics has been explored on a fundamental level towards enhancing light matter interactions. On this basis, novel nanophotonics building blocks have been realized and found to potentially out-perform traditional pure electronic or photonic devices. These findings are of importance towards fueling the global exponentially growing demand for data-bandwidth and novel functionalities such as sensing and bio-medical applications as well as ultrafast on-chip photonics. Especially with the raising energy consumption of information technology, nanoscale integrated hybrid circuits not only hold promise to deliver higher performance but also energy concise solutions due to enhanced physical effects.

To Marietta

Table of Contents

Preface

Living in this information age, we all have noticed the trend of becoming connected. The internet is expanding and ever novel technology allows us to access more information within shorter time scales. For instance, soon we will be able to download a high-definition movie within a second, cars start to actively communicate with each other and 'cloud-computing' in data centers together with the Web 2.0 is forming soft boundaries between human-information and machines. In short, everyone and thing is becoming more and more connected. Witnessing, these trends, one should ask, how can we constantly deliver such a fast growing performance of data communication? What technology do we need to research now, such that in 3, 5 or 10 years we can benefit from such solutions? Among others these are central questions this dissertation attempts to address.

Before the revolution of the electrical integrated circuit (IC), devices were slow and bulky. ICs could address the size issue by scaling down individual devices; it was possible to integrate massive numbers of components onto the same platform, which lead to modern computers. While this integration allows for some increasing in the data speed, the current semiconductor and IT industry is challenged on many fronts. For instance the computers' clock-speed has essentially stagnated for the last 10 years due to increasing interconnect delays. However, while creating the data streams, called logic or computation, is still the stronghold of ICs, photonics or light has emerged within the last 20 year as the dominate means to send or route information across the globe, because the very nature of light packets, photons, allows for ultra high data bandwidths. Such optical networks, however, are similar to computers in the 1960, because each individual optical component is individually placed inside the large und failure prone optical network. The natural attempt to drive this optical network technology further is to integrate photonic components onto the same chip increasing functionality, cost and bandwidth performance of such optical networks. However, unlike electronics optics faces a fundamental challenge if such integrated optical chips are made smaller and smaller. This fundamental physical limit places a natural barrier to the smallest dimensions light can be confined. If, for example, a typical fiber-optical telecommunication wavelength is to be deployed as the operating wavelength of such photonic integrated circuits, then the smallest size a photonic device is about half a micrometer. Such sizes are comparable to electronic devices from the late 1980's.

A solution to this challenge has recently emerged in form of 'light-on-metal', so called surface plasmon polaritons. Due to its unique light characteristics such metal-optics allows for nanoscale wavelengths at visible and near infrared frequencies. While such metal optics can enable ultra-small optics with comparable sizes to current state-of-the-art electronics technology, this dissertation also reports that plasmonics will enable for ultra-fast and efficient processes at the

nanoscale. For instance, this dissertation demonstrates worlds' smallest semiconductor laser that, from a theoretical standpoint, is able to provide unprecedented direct modulation capabilities. This is possible due to the internal physical processes in such a laser. Here the plasmonic nature and ultra-small optical field of the laser mode create novel physical effects that effectively allow for such ultrafast and yet efficient lasing action.

Furthermore, this dissertation answers the long outstanding question regarding the optical losses of metal-optics. The results show that the emission dynamics of a small emitter can be significantly enhanced leading to brighter and more efficient use of the emitted photons. In addition such emission can be strongly coupled into a deep sub-wavelength mode-sized waveguide. Such work is a stepping stone to single-photon transistors and future quantum communication.

On a very fundamental level, this dissertation closes the gap between electronics and photonics in a most integrated way. Key to this success was to analyze, test and implement methods and solutions to enhance light-matter-interactions. A solution was found in a hybrid approach of electronics-photonics merging into plasmonics, or metal-optics. Here, a single photon effectively can do the job of hundreds. Thus, inherently weak non-linear optical effects are strongly enhanced and can now be integrated into smallest integrated Opto-electronic hybrid circuits. In this dissertation a plasmonic enhanced non-linear effect towards realizing an electro-optical-modulator was found to path the way to outperform current (pure) photonic technology.

Within currently emerging funding programs from governmental agencies, it seems to be understood that integrated opto-electronic hybrid circuits are the next stepping stone for this fast growing information age. In conclusion, this dissertation aided paving the way towards achieving this milestone.

Berkeley California, the 23th of April 2011

Acknowledgements

Colleagues

The author thanks the following individuals for valuable discussions:
Professor Dr. Xiang Zhang, Professor Dr. Samuel Mao, Professor Dr. Carsten Ronning, Dr. Rupert F. Oulton, Dr. Ren-Min Ma, Dr. Thomas Zentgraf, Dr. Daniel L. Kimura, Dr. Guy Bartal , Dr. Xiaobo Yin, Dr. David F. Pile, Dr. Murali Ambati, Dr. Dentcho Genov, Dr. Pavel Kolchin, Dr. Ertugrul Cubukcu, Dr. Yuan Wang, Dr. Jason Valentine, Dr. Jie Yao, Dr. Zhoawei Liu, Dr. Ming Liu, Majid Gharghi, Ziliang Ye, Ong Nitipat Pholchai, Chris Gladden and Peter Park.

Family

Finally I would like to thank my beloved wife, Marietta Gelfort, for her tremendous support throughout these years. Special thanks also go to my parents Dieter Boeckling-Sorger, Gertrude Anna Sorger and brothers Daniel, Caspar and Valentin Sorger.

Curriculum Vitae

Education

- Ph.D. Mechanical Engineering, University of California, Berkeley (GPA 3.8/4.0), 2011
- Management of Technology Certificate, Walter HAAS School of Business, UC Berkeley, 2011
- Designated Emphasis in Nanoscale Science and Engineering Program, UC Berkeley, 2010
- Masters, Physics, University of Texas, Austin TX, (GPA 4.0/4.0), 2005
- Pre-Diploma, Physics, University of Wuerzburg, Germany (GPA 3.8/4.0), 2003
- Abitur, Peter-Altmeier High-School, Montabaur (GPA 3.8/4.0), 2000

Relevant Experience

1999-2011

Technical Achievements: Publications & Presentations Summary
Total of 20 (2 invited) technical papers, 5+ in prestigious scientific journals (Nature Publishing Group & Science). Held 20+ talks & presentations (12 invited) at conferences & meetings with international exposure. Expertise covered: Semiconductor Processing, MOSFET, Memories, Laser & Modulators, Opto-Electronics, IC & Photonic Integration, Nanotechnology, Telecommunication, Fiber Optics, Material Science & Synthesis, Metamaterials.

since 2006

PhD Mechanical Engineering (Graduation May-2011)   **University of California, Berkeley**
Advisor: Professor Dr. Xiang Zhang
- Research Topics: Opto-Electronics Research, Demonstrated worlds smallest Lasers, Ultra-small Electro-Optical Modulators, Fiber & Non-linear Optics, Tele-Communications Engineering, Solid State Physics and Material Science, Metamaterials (e.g. Optical Cloaking)
- Advanced skills in Optical and Electronic Measurements (see list below for details)
- State-of-the-art performance in Micro- and Nano-Semiconductor Device Processing

2009-2011

Certificate in Management of Technology (MOT)   **Walter A. HAAS School of Business, UC Berkeley**
- Topics covered: Technology Innovation, Business of Nanotechnology, Opportunity Recognition in Silicon Valley, Strategy Planning, Patent/IP-101

2006

Internship - Intel Corp. Components Research   **Hillsboro, OR**
Developed enhanced Nanowire and Nano-Tube field-effect-transistors for future logic devices. Advanced MOSFET E-test, Material Metrology (AFM, Raman, SEM and TEM) and Nanowire CVD Development.

2004-05

Masters – Physics Department   **University of Texas, Austin**
Advisor: Professor Dr. Zhen Yao
- Researched on novel Carbon Nano-Tube Field-Effect-Transistor and Flash Memory Devices
- Conducted E-Test measurements, low Temperature & Opto-Electronic switching Tests

2003-04

Research Assistant   **Julius Maximilians University of Wuerbzurg, GER**
Advisor: Professor Dr. Laurens Molenkamp
- Planned, installed and measured Magneto-Optical-Kerr-Effect on nanofabricated Devices
- Optimized High-Magnetic-Field / Dilution Cryostat measurement setup Interface

Additional
- Finalist (top 0.3%) of European Space Agency (ESA) Astronaut selection process (2008-09)
- U.S. Patent on Plasmonic Nanolaser light sources, status - Pending
- Golfing - Handicap 20+
- German (Native), English (Business fluent), Chinese (Basic), Qualification in Latin ("Latium")

Publication "Short-List" (selected)

- **<u>V. J. Sorger</u>** and X. Zhang „Plasmon Nanolasers: tiny and fast" (invited) accepted *Science* April (2011)
- **<u>V. J. Sorger</u>**, Z. Ye, R. F. Oulton, G. Bartal, Y. Wang and X. Zhang "Observation optical waveguiding in deep-subwavelength plasmon waveguides" accepted *Nature Communication* April (2011)
- R.-M. Ma, R. F. Oulton, **<u>V. J. Sorger</u>**, G. Bartal and X. Zhang "Room-temperature sub-diffraction-limited plasmon laser by total internal reflection" *Nature Materials* **10**, 110-113 (2010)
- R. F. Oulton[*], **<u>V. J. Sorger</u>[*]**, T. Zentgraf[*], R.-M. Ma, C. Gladden, L. Dai, G. Bartal and X. Zhang "Plasmon lasers at deep subwavelength scale" *Nature* **461**, 629-631 (2009)
- **<u>V. J. Sorger</u>**, R. F. Oulton, J. Yao, G. Bartal and X. Zhang "Fabry-Perot Plasmonic Nanocavity" *Nano Letters* **9**, 3489-3493 (2009)
- B. Min, E. Ostby, **<u>V. J. Sorger</u>**, E. Ulin-Avila, L. Yang, X. Zhang, K. Valhalla "High-Q surface plasmon-polariton whispering-gallery

2007-2011	**Grant & Third-Party Funding**

Wrote and Negotiated for these Grants for my PI Prof. Xiang Zhang
- Air Force Office of Scientific Research (AFSOR) FY2011 #17, Multidisciplinary Research Program of the University Research Initiative (MURI), Title "Large Scale Integrated Hybrid Nanophotonics".
- Air Force Office of Scientific Research (AFSOR) Title: "Electrically Pumped Plasmonic Nano-Laser: Physics, Devices and Applications".
- Lawrence Berkeley National Laboratory – Molecular Foundry User Proposal, Title "Silicon on insulator Plasmonic Modulator".

2006-current	**Extra-Curricular & Community Leadership**	**UC Berkeley**

- **Vice President OSA/SPIE Berkeley Chapter:** Responsible for planning & organization of outreach programs & member events (e.g. field trips to greater bay-area Corporations and National Laboratories).
- **Chief Technology Officer Berkeley Nanotechnology Club:** Responsible for Technical Relations & organization of Nanoforum conference & field-trips to Silicon Valley companies.

2005-2010	**Leadership & Team-Work**	**UC Berkeley, Nano-Club, MOT Program**

- **Board Advisor:** for Nanotechnology Start-up: *"Anchor Science"* (2005-2007)
- **Class Team Projects:** e.g. analyzed vertical vs. horizontal integration strategies in Infinera Inc. case project
- **Organization Teams:** Lead-Organization of Nanoforum-Conference through CTO position in Nanoclub (2007) and of the German National Academic Foundation Annual North America meeting (2007).

2005-current	**Taking-on Responsibility**

- **Piloting Aircrafts:** executing the privileges of being the "pilot-in-command" on U.S. commercial pilot license. Final authority for my passengers & responsible for the safe operation (Total time 275 hrs).
- **Financial:** Responsibility for selecting & purchasing a tool (thin-film evaporator) (250,000$).
- **Social:** Mentored junior Master's student in Prof. Zhang's group (2008-2009).

Teaching Experience   **UC Berkeley, Uni. Wuerzburg**

- Supervised undergraduate physics student lab groups in various experiments
- Evaluated students performance in 1:1 interviews and lectured theory topics
- Mentored Masters Student (1:1) in UC Berkeley
- Personal Tutor (5+ yrs) subjects: Math, Physics, Chemistry, English

Professional Memberships

- Deutsche Physikalische Gesellschaft (DPG)
- Studienstiftung des Deutschen Volkes
- Institute of Electrical and Electronic Engineers(IEEE)
- International Society of Optical Engineers (SPIE)
- Optical Society of America (OSA)
- Material Research Society (MRS)
- Aircraft Owner and Pilot Association (AOPA)

Press Coverage (Featuring Achievements - Selected)

- Science News: 'Better living through plasmonic' By J. Lauren Lee, **176**, p.26 (2009)
- MIT Technology Review: '50th Anniversary of the Laser' (2010)
- Science Mag: 'Tiny Laser could light the way to new Microchip Technology' By D. Cho (2009)
- Nature Photonics: news & views (2009)
- UK Telegraph: 'World's smallest laser created by scientists' (2009)

Honors & Awards (top 4 - 0.1%)

- Newport Travel Grant (2011) – In recognition of the research excellence of students presenting their work at the Conference on Lasers and Electro-Optics (CLEO)
- Material Research Society Gold Award (2011) – In recognition of exceptional ability & promise for significant future achievement in materials research (top 4%).
- Best Annual Student Paper Award by the U.S. National Academy of Sciences (2010) (top 0.1%).
- 1st Price for best Poster Presentation at Berkeley Nanoforum Conference (2010).
- OSA Emil Wolf Student Competition Winner (2009) – Recognition of the innovation, research and presentation excellence of students presenting their work during "Frontiers-in-Optics" conference.
- BACUS scholarship (2009) - To reward the most qualified students in the fields of photomask and microlithography manufacturing for the semiconductor industry.
- SPIE Scholarship (2008 & 2007) – For the most qualified students who wish to work in the fields of photomask and microlithography manufacturing for the semiconductor industry.
- Intel PhD Graduate Fellowship (2007-2009) – For outstanding students in Engineering, Computer Science and other technical majors focusing on semiconductor technologies.
- Intel Corporation, CTG KUDOS Award (2006) – For outstanding scientific performance and collaboration skills.
- University of Texas College of Natural Science Fellowship (2005) – For best 2% of graduating class.
- Hoelderlin Stipend (SAP Fast-Track Scholar) (2005) – For outstanding future foresight and international relations.
- Studienstiftung des Deutschen Volkes Fellowship (2002-07) – Recommended by Gymnasium & passed assessment center based on: Performance, Initiative and Responsibility ("Leistung, Initiative und Verantwortung").
- German Physics Society Award (2000) – for excellent performance (top 2%) in Physics A-Level Graduation.
- Science Competition: "Jugend Forscht" State Winner (in GER) (1998).

Conference / Invited talks

- **Coming up in 2011: MRS oral & CLEO oral**
- **Stanford-University Photonics Retreat (SUPR)**   **Point Reyes, CA**
  Poster: "Plasmon Nanolasers – Light from the Nanoworld"
- **Berkeley Nano-Science and Engineering Seminar (invited)** (2011)   **UC Berkeley, CA**
  Talk: "Plasmonics and Photonic Integration for the 21st Century"
- **IEEE Photonics / OSA Winter Photonics (invited)** (2011)   **Keystone, CO**
  Talk: "Integrated Hybrid Nano-Photonics"
- **Naval Post Graduate School – Seminar (invited)** (2010)   **Monterey, CA**
  Talk: "Metamaterials, Plasmonics and Photonic Integration"
- **Lawrence Berkeley National Lab: Molecular Foundry (invited)** (2010)   **Berkeley, CA**
  Talk: "Hybrid Platform for Photonic Integrated Circuits"
- **SPIE Optics & Photonic (invited)** (2010)   **San Diego, CA**
  Talk: "Plasmonic light sources for integrated Photonics"
- **OSA Integrated Photonic Research –** (2010)   **Monterey, CA**
  Talk: "Sub-λ Plasmon Laser"
- **MRS Spring Meeting –** (2010)   **San Francisco, CA**
  Talk: "Sub-λ Plasmon Laser"
- **CIFAR – Nano-Electronics (invited)** (2009)   **Quebec, Canada**
  Talk: "Nanophotonics – A Sub-λ Plasmon Laser"
- **Lawrence Berkeley National Lab: Molecular Foundry (invited)** (2009)   **Berkeley, CA**
  Talk: "Light Unlimited: Plasmon laser at deep sub-wavelength scales"
- **FiO –** (2009)   **San Jose, CA**
  Talk: "Light Unlimited: Plasmon laser at deep sub-wavelength scales"
- **SPRC – Extreme Lasers (invited)** (2009)   **Stanford University, CA**
  Talk: "Deep Sub-wavelength plasmon laser"
- **CLEO** (2009)   **Baltimore, MD**
  Talk: "Plasmonic Nanocavity"
- **Photonic and Plasmonic Seminar (invited)** (2009)   **UC Berkeley, CA**
  Talk: "A novel Plasmonic Nanolaser"
- **Gordon research conference - Plasmonic** (2008)   **Tilton, NH**
  Poster: "Plasmonic Nanocavity"
- **CLEO** (2007)   **San Jose, CA**
  Talk: "Novel Hybrid Approach for on-chip Waveguiding"
- **SPIE** (2007)   **San Diego, CA**
  Talk: "Plasmonic Nanocavity"
- **Portland State University (invited)** (2006)   **Portland, OR**
  Carbon Nanotube Devices in Front-End
- **MRS Spring Meeting** (2006)   **San Francisco, CA**
  Talk: "Carbon Nanotube Flash Memory"
- **Nano Night** (2004)   **Microelectronic Research Center, Austin TX**
  Poster: "Electron Transport with Single walled Nanotubes"
- **Hands on Physics Conference (invited)** (1999)   **University of Duisburg, GER**
  Talk: Fabrication and experiments of a "Cloud-chamber"
  for nuclear particle detection based on the Peltier-Effect
- **European Technology Exchange Meeting (invited)** (1998)   **Toulouse, F**
  Represented Germany's Youth Science Teams with "Cloud-chamber Project"

Technical Skill List

Measurement Techniques
Opto-Electronic Device Test
Fiber Optics
Laser Device Test & Spectroscopy
Electro-Optical Modulator Device Test
Integrated Photonic Circuits
fs-Laser Spectroscopy
Single Photon-Counting Measurements
Electrical Device Characterization (2-4 Terminal)
Cryo-Temperature Opto-electronic Measurements

Miscellaneous
Multi-Physics Simulation (Comsol, Spice, Mathematica)
Extensive Safety Training
Clean Room Trained (various locations)

Materials Deployed
Semiconductors (Group IV, III-V, II-VI)
Oxides (SiO_2, Al_2O_3, HfO, MgF_2)
Metals (Au, Ag, Cr, Al, Ti, Pd, Pt)
Metamaterials

Metrology
Scanning Electron Microscopy
Atomic Force Microscopy
Raman Spectroscopy
Nanowire/Nanotube Synthesis
Ellipsometry
Magneto-Optical-Kerr-Measurements
Electron Diffraction Spectroscopy
Photoluminescence Spectroscopy

Semiconductor Device Fabrication
UV-Optical Lithography
Electron Beam Lithography
Chemical Vapor Deposition
Thin Film Deposition & RF Sputtering
Focused Ion Beam Lithography
Reactive Ion/Plasma Etching

1. Introduction

1.1 General Picture

If we take a 'snap-shot' of our world today (2011) like the camera in the upper left corner of Figure 1.1.1 suggests, we observe a trend that can be summarized in one word: Connectivity. People using more and more online sharing and social network cites to stay or become connected with friends, families and colleagues [1]. Likewise, the same trend of staying connected is visible in the transportation section, where cars or airplanes are not single entities in space, but through data-links become part of a large grid or network. In the case of aviation for instance, the high positioning accuracy of the global positioning system (GPS) [2] in conjunction with additional ground based radio stations, the wide area augmentation system (WAAS) recently introduced, [3] allows positioning accuracies down to single digit meters. Similarly there are tremendous research and development trusts from the automotive industries to allow individual cars to 'talk' to each other towards increased safety and early accident avoidance [4].

The trend of connectivity continues to energy management in particular of electricity of home owners. Advances in electricity grip technology like smart metering [5] allow for higher level of monitoring solutions of a home's power consumption via integrated sensors and 'smart' electronics. Such 'connected-homes' are in particular interesting within the trend of expanding solar (photo-voltaic) power generation and the emerging boom in electric and hybrid vehicles [6].

Furthermore the world wide growing media awareness and private usage of media content in form of internet, connected TV's [7] paired with falling costs for large panel displays and high-definition TV standards [8] drive an exponentially growing data bandwidth demand.

Connectivity continues over essentially all sectors of modern life as shown in Figure 1.1.1. The requirements however are stringent and call for high data bandwidth technologies, increasingly faster computing power with ever falling device footprints and power per bit functions. Such requirements drive the need for exploratory research towards finding solutions to these future IT requirements. This dissertation summarizes research based on finding such solutions on a device level via exploring synergies between photonics and electronics at nanoscale dimensions. In particular the emerging field of metal optics or plasmonics provides a promising path towards ultra fast yet small and efficient device architectures that, if developed further could lead to meeting such high data bandwidth demand by introducing large scale hybrid nanophotonic circuit technology.

Our World today – *Connectivity!*

Connected …

People

Cars

Homes

Media

Warfare

Cloud-Comput.

…

Requirements:
- High data Bandwidths
- Faster Computing
- Lower Energy/bit

Figure 1.1.1 | A 'Snap-Shot' of our world. Summarized in a one single phrase, we observe that almost every person or item is becoming increasingly connected with each other. This massive data-sharing trend, however, requires high data bandwidths, faster computation with ever decreasing energy per bit functions. In a nutshell this is the motivation for this dissertation, namely to explore novel physics on a device level targeting photonics and electronics components alike that are able to provide this level of performance and opens new opportunities for future research directions.

1.2 Fundamentals

Before we start exploring the rich physics of the devices and components studies in this dissertation, let us briefly discuss a selected number of physical basic concepts which are critically needed to comprehend the more detailed discussions in the following chapters.

Quantum Theory of Radiative Absorption and Emission

The quantum theory of electromagnetic radiation predicts the absorption and emission of radiation whenever an atom transitions between two possible quantum states. For simplicity consider a 2-level atom with a lower state 1 and upper state 2 (Figure 1.2.1). Generally speaking, when radiation gets absorbed, the atom switches from the lower to the upper state and emits the stored energy in the reverse process. The transition energy needed to absorb radiation equates the energy difference between the two levels such that, if the two levels have the energy E_1 and E_2, absorption or emission happens for $hv = E_2 - E_1$, where h is the Planck constant and v the frequency of the radiation. This simple relationship can be thought of as energy conservation during this process.

While for an atom in the excited state, statistical physics tells us that it can relax statistically after a time τ, leading to spontaneous emission processes (middle of Fig. 1.2.1), the atom cannot spontaneously jump from the lower to the upper level. Thus, absorption requires incoming radiation in order to make the upward transitions (left of Fig. 1.2.1). We therefore are allowed to call 'absorption' more precisely 'stimulated absorption'.

In the following we will quantify the rate of the three processes in more detail. Let A be the Einstein coefficient for spontaneous emission, it quantifies the probability per unit time that an electron (red dot in Fig. 1.2.1) drops from level 2 to level 1. The transition probability therefore is proportional to the number of electrons in the upper level, namely N_2. Thus the change of electrons in the upper level due to spontaneous relaxation processes can be written as

$$\frac{dN_2}{dt} = -A_{21}N_2 \qquad (1)$$

where the indices '21' denote the transition from level 2 to level 1. Solving Eqn (1) yields the solution for $N_2(t) = N_2(0)\,exp(-A_{21}t)$ with $\tau = 1/A_{21}$, where τ is the natural radiative lifetime of the excited state. Thus we see that the electron concentration in level 2 decays exponentially in time with the time constant τ. While the spontaneous emission processes is described by the A coefficient, (stimulated) absorption can be characterized by Einstein's B coefficient. Thus we model the absorption rate for electrons in the lower level via Eqn. (2)

$$\frac{dN_1}{dt} = -B_{12}N_1u(v) \qquad (2)$$

where $N_1(t)$ are the number of electrons in the lower level at time t, B_{12} the Einstein coefficient for the transition and $u(\nu)$ the energy density (in units Jm^{-3}) of the incoming electromagnetic wave with frequency ν. Note that the energy density's frequency has to match the energy conservation equation from above.

The last process for light-matter interactions is stimulated emissions (right of Fig. 1.2.1), where excited electron in the upper state can be triggered to transition to the lower state by an incoming electromagnetic wave. Since stimulated emission is a coherent effect the resulting emission is spectrally and temporally coherent to the incoming radiation. Thus, if an atom is paced inside a cavity, which builds up preferential wavelengths (cavity modes with a mode spacing equal to the free-spectral-range of the cavity), lasing operations can be reached. Stimulated emission is governed by the Eqn (3),

$$\frac{dN_2}{dt} = -B_{21}N_2 u(\nu) \qquad (3)$$

The three Einstein coefficients do have a distinct relation to each other. That is, the rate of upward transitions has to equal the rate of all downward transitions yielding equilibrium for a steady-state situation. The physical picture to understand this equilibrium is to imagine the atom being placed inside a black box with an ambient temperature, T, and exposed to radiation of frequency ν. After some time the atom will be in thermal equilibrium with the incoming radiation and the surrounding box because the radiation absorption will be exactly balanced by the two emission processes. This steady-state situation can be expressed as shown in Eqn (4)

$$B_{12}N_1 u(\nu) = A_{21}N_2 + B_{21}N_2 u(\nu) \quad (4)$$

This thermal equilibrium can be used to describe the energy levels of the atom in the steady state case. The ratio of N_2 to N_1 will therefore be governed by the thermal Boltzmann law:

$$\frac{N_2}{N_1} = \frac{g_2}{g_1} exp\left(-\frac{h\nu}{k_B T}\right) \qquad (5)$$

where g_1 and g_2 are the degeneracies of the two levels respectively and k_B the Boltzmann constant. With the electromagnetic radiation following the Planck formula
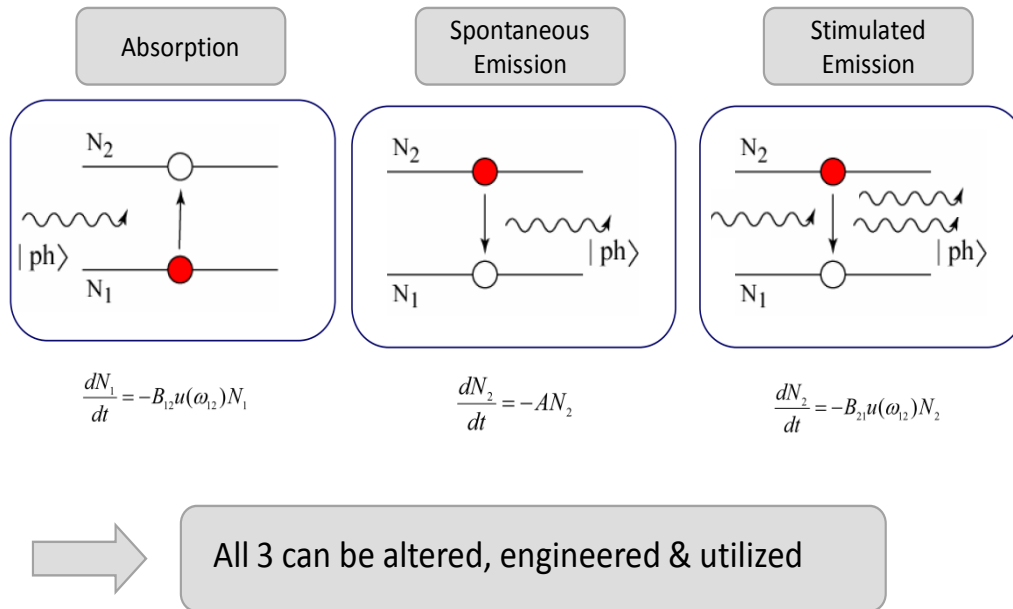
$$u(\nu) = \frac{8\pi h\nu^3}{(c/n)^3} \frac{1}{exp\left(\frac{h\nu}{k_B T}\right)-1} \qquad (6)$$

we can bring the equations (4) – (7) into constancy if we have:

$$g_1 B_{12} = g_2 B_{21} \qquad (7)$$

$$A_{21} = \frac{8\pi h\nu^3}{(c/n)^3} B_{21} \qquad (8)$$

where c is the speed of light in vacuum and n the refractive index of surrounding the atom. This interesting finding hints towards the fact that a high absorption probability will also have a high emission probability, i.e. both spontaneous and stimulated. This fact will play an important role in the gain material selection in chapter 4 where we will discuss novel plasmon Nanolasers light sources. In particular the enhancement of the spontaneous emission rate, also known as Purcell Effect [1], will be a key focus in this dissertation. The reader finds a brief discussion of the generic Purcell effect in this chapter below.
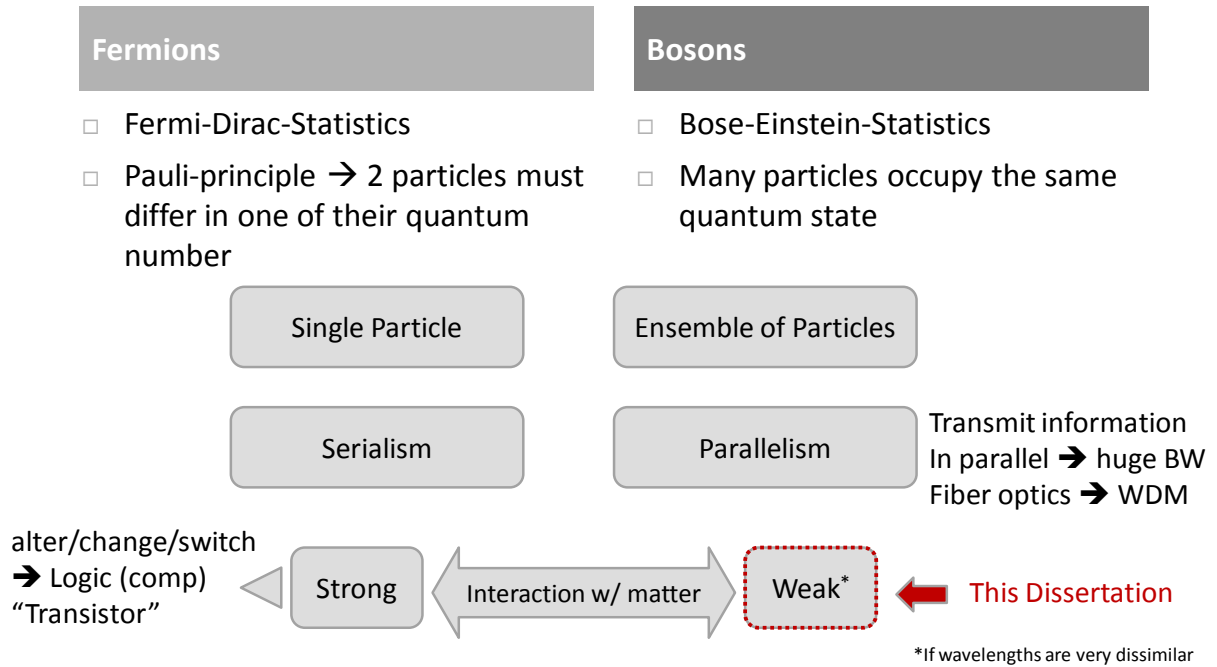

| Absorption | Spontaneous Emission | Stimulated Emission |

$$\frac{dN_1}{dt} = -B_{12}u(\omega_{12})N_1 \qquad \frac{dN_2}{dt} = -AN_2 \qquad \frac{dN_2}{dt} = -B_{21}u(\omega_{12})N_2$$

All 3 can be altered, engineered & utilized

Figure 1.2.1 | Fundamental Ways of Light-Matter-Interaction. The Einstein Coefficients B_{12} A, and B_{21} determine the rates of three fundamental processes light can interact with matter; that is via absorption of a photon (left), and the subsequent emission with spontaneous (middle) or stimulation (right) channels, respectively. In this dissertation we will focus on altering and thus engineering all three processes with a particular focus on enhancing spontaneous emission rates [1].

About the Roots of Information Technology

Fermions and Bosons are two of the mainly utilized particle families by humanity. While two fermions must differ by at least one quantum number when occupying the same quantum state i.e. the Pauli-Principle, bosons behave more like large families, where all 'members' can occupy the same state without interfering with each other (e.g. in a Bose-Einstein Condensate [2]). These two fundamental differences of the two particle families consequently lead to different

utilizations; while the serialism and strong matter interaction of for instance fermionic electrons lead to the discovery of the transistor enabling the computer revolution, it is the nature of the bosonic parallelism leading to fiber optics delivering huge data bandwidth in form of optical packets due to wavelength-division-multiplexing, a concept impossible for fermionic electrons (Fig. 1.2.2). The reason why photons are not used for logic or switching, thus far, lies in the weak interaction of light with matter. This is because the wavelength of optics and electronics are typically orders of magnitude different. This dissertation addresses this question in detail, namely, how we can strengthen the light-matter-interaction. The reward of such realization is great, since it would allow to build photonic components and systems that would not only benefit from the bosonic potential for high data bandwidths, but would also allow to shrink down optical components to the nanoscale, rivaling dimensions of electronics devices.

Fermions	Bosons
□ Fermi-Dirac-Statistics	□ Bose-Einstein-Statistics
□ Pauli-principle → 2 particles must differ in one of their quantum number	□ Many particles occupy the same quantum state

Single Particle — Ensemble of Particles

Serialism — Parallelism

Transmit information
In parallel → huge BW
Fiber optics → WDM

alter/change/switch → Logic (comp) "Transistor"

Strong ← Interaction w/ matter → Weak*

This Dissertation

*If wavelengths are very dissimilar

Figure 1.2.2 | The roots of Information Technology. While fermions yield to the Pauli-Principle and thus behave like single particles, bosons can form ensembles of particles all occupying the same quantum state. These two major distinctions have been realized and deployed in various technologies leading logic computations via the transistor device for fermions (electrons) and to huge data bandwidths that are send in parallel for bosons (electromagnetic waves, photons). This dissertation addresses the natural weak interaction of light with matter, by introducing optical confinement which effectively bridges the gap between electronic and photonic wavelengths. This in turn leads to strong light-matter interactions which can be utilized in various devices and effects (e.g. non-linear optics), as we will discuss in consecutive chapters.
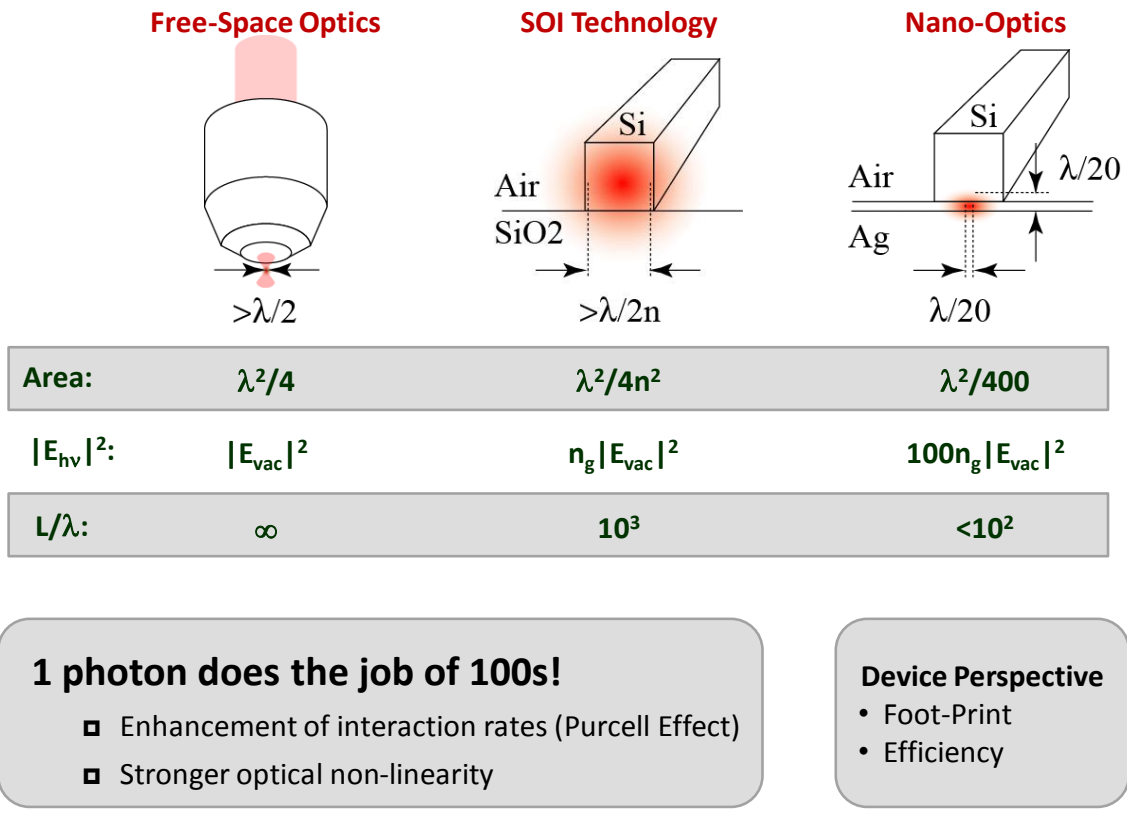
Enhancing light Matter interactions

The in the previous sub-chapter mentioned intrinsically weak interaction between light and matter is again illustrated in Figure 1.2.3. For instance the interaction of light with a wavelength in the visible or infrared spectrum having a wavelength of around 1000 nanometers is three orders of magnitude dissimilar to electronic wavefunctions which are on the order of a single nanometer. This prospective is of interest with the aim of utilizing ultra-small, nanoscale emitters like quantum dots or nitrogen-vacancy (NV) centers. Such nano-emitters are ideal candidates for novel and efficient devices due to their small size, high quantum yield and single photon emitting capabilities. The latter is of great interest for the field of quantum physics. Thus, closing the gap of such nanoscale electronic systems and optical electromagnetism has the potential to create novel physical effects on nanometer scales.
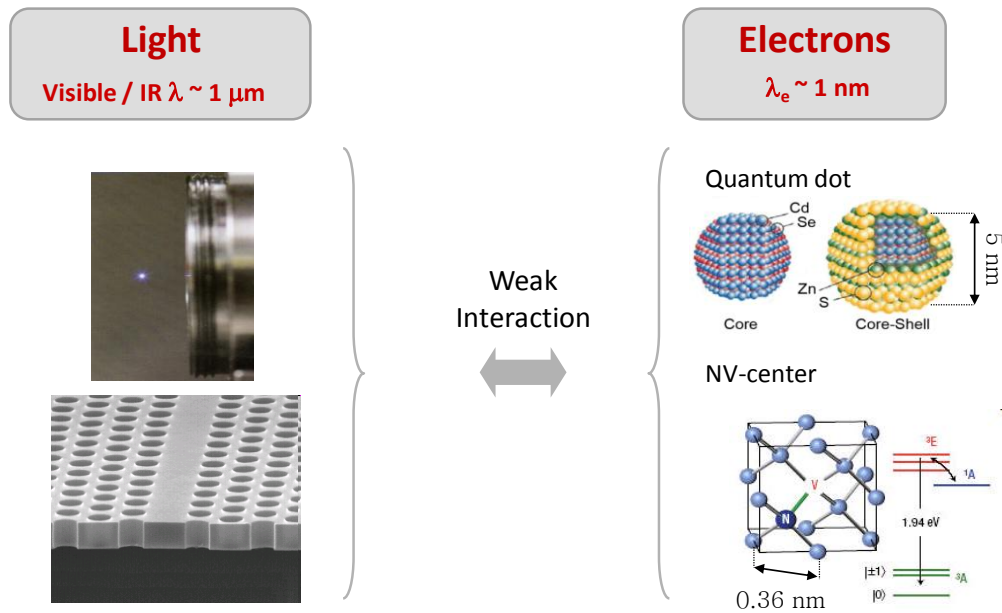
Figure 1.2.3 | Difference in Length Scales of visible and infrared light to electronic wavefunctions. The large discrepancy of several orders of magnitude of optical and electronic wavefunctions leads to the well known inherently weak interaction between these two regimes. The aim of this dissertation is to explore novel solutions on strengthening this interaction and to deploy such solutions in device demonstrations which would be impossible to achieve elsewise.

However, what concrete goals or advantages on a device level can bridging the gap between electronic and electromagnetic length scales enable? In order to answer this questions let us draw a comparison between three measures (Fig. 1.2.4); the optical mode area, the energy density of this mode and the associated propagation length. Here, we compare free-space optics with integrated photonics (like silicon-on-insulator (SOI) waveguides [3]) to nano photonic waveguides as studied in this dissertation. Free-space modes can be focused at best to the diffraction limit of light in air, namely in terms of mode area $(\lambda/2)^2$ (left Fig. 1.2.4). Such mode's energy density is equal to the vacuum energy of the field and essentially has an infinite propagation length if collimated properly.

	Free-Space Optics	**SOI Technology**	**Nano-Optics**
	$>\lambda/2$	$>\lambda/2n$	$\lambda/20$
Area:	$\lambda^2/4$	$\lambda^2/4n^2$	$\lambda^2/400$
$\|E_{h\nu}\|^2$:	$\|E_{vac}\|^2$	$n_g\|E_{vac}\|^2$	$100n_g\|E_{vac}\|^2$
L/λ:	∞	10^3	$<10^2$

1 photon does the job of 100s!
- ◻ Enhancement of interaction rates (Purcell Effect)
- ◻ Stronger optical non-linearity

Device Perspective
- Foot-Print
- Efficiency

Figure 1.2.4 | Why match Optical & Electronic Length Scales? The short answer is to increase efficiency and decrease device footprints. This can be achieved with Nano-Optics where the electromagnetic field density can be extremely high [4-6]. Thus a single photon can induce the same effect as 100 in free-space. This is a thus far unexplored direction opening potentials in non-linear optics with ultra-small footprints and high conversion efficiencies. In this dissertation we will discuss examples of devices base on such Nano-Photonic building blocks.

Integrated waveguides like those demonstrate in SOI [3] gain essentially a factor of n, where n is the effective mode index, which is largely determined by the materials refractive index at the operation wavelength (middle Fig. 1.2.4). Thus, for a SOI waveguide, where $n_{mode} \sim 3.x$ the optical mode can be as small as about $1/10^{th} (\lambda/2)^2$ with the energy density boosted by the group index. However, the propagation length also diminishes to about 10^3 times the operation wavelength. The situation strongly changes if nano photonic waveguides are deployed with a mode area of e.g. $(\lambda/20)^2$ (right Fig. 1.2.4) [4-6]. The strong field enhancement allows the energy density to reach one hundred times that of a diffraction limited focused spot in free space. This in turn means, that a single photon in a nano Photonic waveguide does the job of hundreds (Fig. 1.2.4).

Such large enhancement can be utilized for strongly enhanced non-linear photonics or enhancing the spontaneous emission rates [1,4,6]. In addition, the latter will become important towards designing plasmon Nanolasers, an increased emission rate into a nano-photonic mode also leads to a mode selection which is important to lower the threshold of high-loss laser sources like Nanolasers. We will discuss this physical effect and its demonstration in chapter 4 and on a more fundamental level in chapter 8. However, strong optical confinement comes with a trade-off, namely with reduced propagation length. For the nano-photonic waveguide (right Fig. 1.2.4) typical propagation distances are below 100 times its operation wavelength. While this seems like a strong limitation, it is actually not a large concern, since the 100 times enhanced energy density allows to create e.g. optical non-linearities that are more than 100 times stronger compared to free-space. In fact this effect can be 10000 times stronger if a third-order non-linear effect is being deployed as we will discuss in chapter 5. Such strong effect enhancements allow reducing the optical intensity or the optical interaction path-length to create the desired effect by 10^4. Thus, nano-Photonics has the potential to create non-linear devices like optical transistors or electro-optical modulators with device footprints that are on the order of a single wavelength.

Introduction to Surface Plasmon Polaritons

Surface plasmon polaritons (SPP) are a natural occurrence of the solution of Maxwell's equations of the mode problem of a metal-dielectric interface [7,8]. The surface plasmon mode can be understood as a collective electronic surface wave oscillating with the frequency of light (lower right Fig. 1.2.6). The field decays exponentially into both half-spaces but has an imaginary wave phase, thus propagates along the surface (lower left Fig. 1.2.6). Solving the permittivity of the metal yields an ohmic loss term which is characterized by the damping rate, γ. Thus, since the optical field resides partially inside the metal, a SPP wave experience optical losses as it propagates along the surface, leading to typical propagation lengths with 100 times its operating wavelength. The potential of SPPs comes into the picture when their dispersion relation is considered (upper right Fig. 1.2.6). This 'curving' dispersion relation shows the potential of SPPs to provide high k-vectors (ultra-small wavelengths) for a marginal increase in frequency. This means if the surface plasmon resonance is excited with e.g. visible light, the effective wavelength of the surface plasmon can be in the x-ray region. This in turn allows constructing nano-scale optical components like for instance cavities with volumes below the diffraction limit of light. Notice, these high k-vectors are unattainable with classical photonics

which are limited by the so called 'light cone' as they follow the dispersion relation $\omega = c\,k$, where ω is the photon frequency, c the speed of light in vacuum and $k = 2\pi/\lambda$ the propagation constant (upper right Fig. 1.2.6).
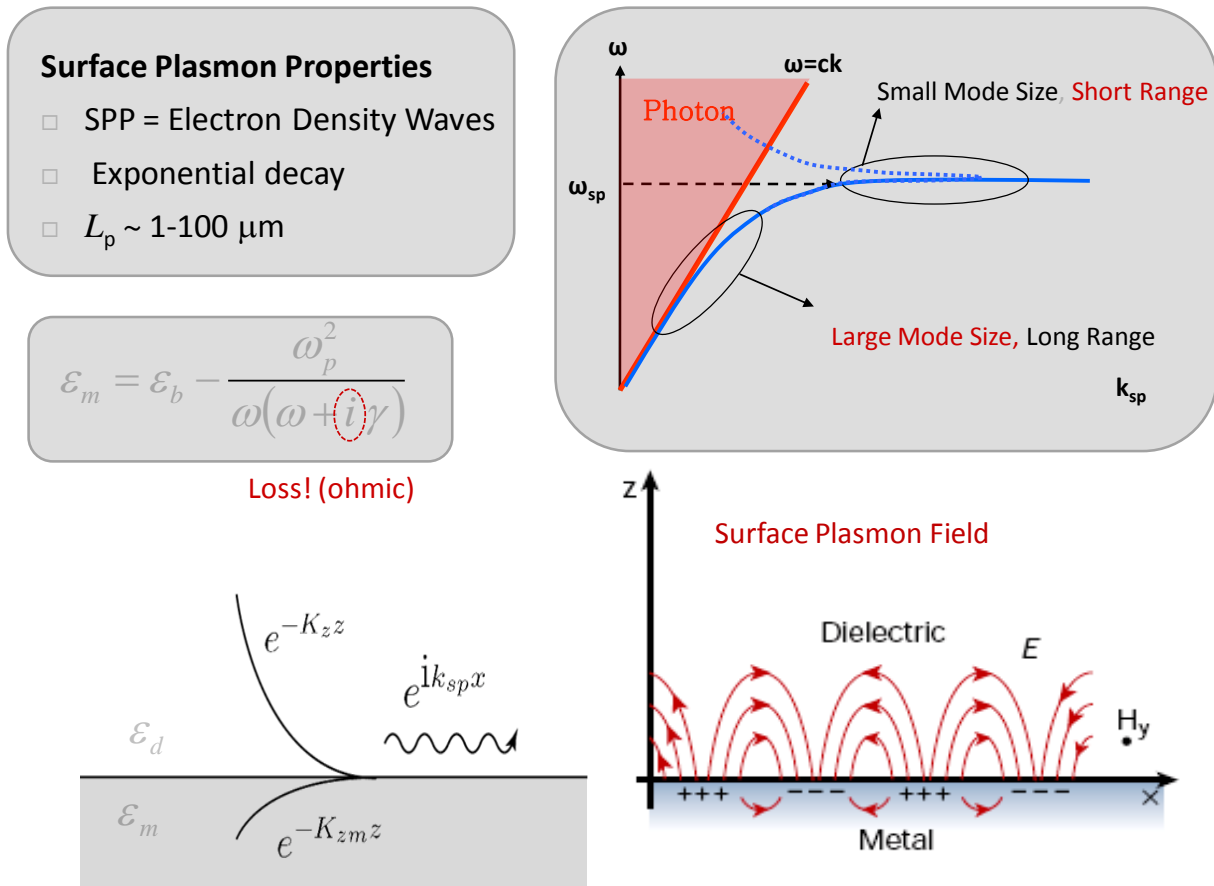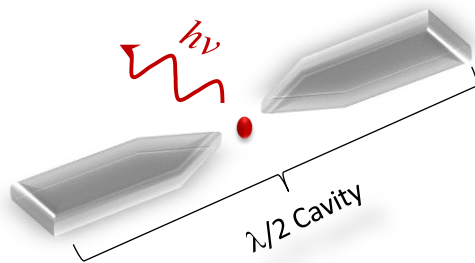

Figure 1.2.6 | Surface plasmon polaritons (SPPs) [7,8]. The solution of Maxwell's equations for a metal-dielectric interface yield a metal-bound surface wave that decays exponentially into both half-spaces, but propagates along the surface (lower left). Here electronic charges of the Fermi sea inside the metal oscillate with the frequency of the electromagnetic wave (lower right). Due to ohmic losses the propagation lengths are limited to about 100 μm. The potential of SPP-based photonics lies in its unique dispersion relation which allows for deep-subwavelength fields (upper right).

Understanding Purcell-Effect

From the three possibilities of how an electromagnetic wave can interact with matter (Fig. 1.2.1), spontaneous emission was thought for a long time as 'un-engineer-able' since, as the name suggests, the emission occurs statistically and unpredictably. While this is still true, Edward Purcell proposed in 1946 that spontaneous emission, however, can be modified namely the

spontaneous emission rate, τ, can be accelerated or decelerated [1,9]. His analysis predicted that if an intrinsic radiative spontaneous emission process has a rate of, γ_0, that an rate enhancement can be achieved that is given by the Purcell factor $F_p = \gamma_{\text{enhanced}}/\gamma_0$. The factor or rate enhancement can be analytically calculated by dividing the solution of the dipole's emission rate into e.g. a cavity by its free space emission rate (top Fig. 1.2.7).

$$F_p = \div \begin{cases} \boxed{\text{Em. Rate into cavity}} & \left(\dfrac{1}{\tau_{sp}}\right)_{cav} = \dfrac{4\pi^2}{\hbar}\dfrac{|qx|^2}{4\pi\varepsilon_0}\dfrac{Q}{V_{eff}} \\[2em] \boxed{\text{Em. Rate into free space}} & \left(\dfrac{1}{\tau_{sp}}\right)_0 = \dfrac{4}{3}\dfrac{|qx|^2 n\omega^3}{\hbar c^3} \end{cases} = \dfrac{3}{8\pi}\dfrac{\lambda^3}{V_{eff}}Q$$

$h\nu$

$\lambda/2$ Cavity

(1912-1997)

E. Purcell *Phys. Rev.* **69**, 681 (1946)

Engineer Spontaneous Emission
→ increase Emission Rate (Speed), Brightness, …

Figure 1.2.7 | Purcell Effect. Edward Purcell predicted in 1946 [1,4-6] that spontaneous emission, while being spontaneous in nature, can actually be enhanced or inhibited [9] if the electromagnetic environment of surrounding an emitter can be altered. Thus, if for instance a radiating dipole (red dot in center) is placed into a cavity (center) with enhanced electromagnetic field densities, then the spontaneous emission rate can be enhanced. In chapter 4 and 8 will discuss experimental examples of such so called Purcell enhancements.

The resulting term for F_p indicated two findings: (i) if the cavity Q-factor is large and/or (ii) the cavity or mode volume is small then the effect is emission rate is enhanced (top Fig. 1.2.7). The former realization led many micro cavity research teams to strive to optimize the cavity quality Q-factor [10]. However similar or even stronger enhancements can be achieved if the Q-factor is moderate or even small, but the cavities' volume is being shrunk into the deep sub-wavelength

scale. This is the regime where plasmonics unfolds its potential; the lossy character of plasmonics is rather unimportant compared to its potential to strongly enhance optical fields and compress them into nanoscale volumes [4,-6,11,12]. In chapters 2, 4 and 8 we will discuss devices and applications of experimental demonstrations utilizing such plasmonically induced Purcell enhancements toward strengthening light-matter interactions.

1.3 Dissertation Sub-title: "Integrated Hybrid Nanophotonics"

The general aim of this dissertation and its overall placement into the current research and technology landscape can be made transparent with the help of its sub-title (Fig. 1.3.1). Starting with the last word *'Photonics'*, the argumentation is to push photonics research forward since it has been realized as the superior means of transmitting and routing data as discussed ealier. While the in-and-output (I/O) of modern computing cores is experiencing a performance challenges due to the limited number of available pins to send the data to the outside, transmitting (Tx) and receiving (Rx) chips are key research areas since most of the energy of a modern computer is not used to do logic (switch a transistor), but used to send information. In terms of the chip-set of a computer this can already approach 80% of its total power consumption [1,2].

Nanotechnology not only enables to scale down devices and provide the appropriate process infrastructure and metrology, but also novel physical effects like the Purcell effect as discussed before. In addition in terms of modulation or switching speed 'small' also means low capacitance which allows for short RC constants. Here, we target the device level in particular.
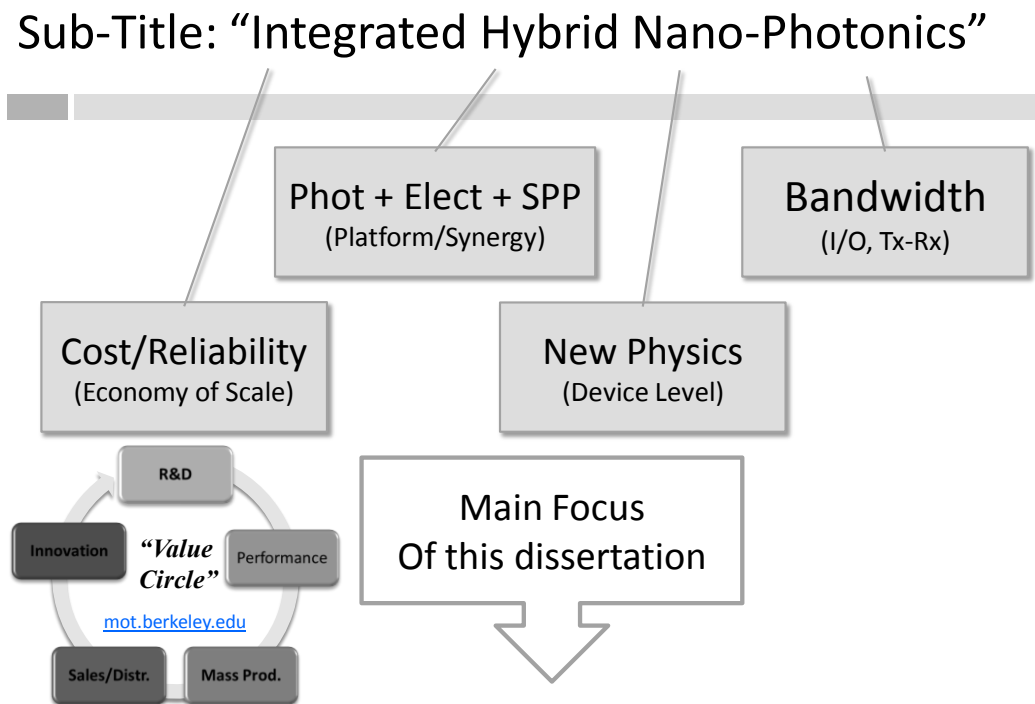
Figure 1.3.1 | Dissertation Sub-Title. The main focus of this dissertation is to study novel effects on a device level and incorporate the 'best-of-three-worlds' namely from and photonics, electronics and metal optics or plasmonics point of view. This work investigates synergies between these technologies towards a novel platform with unprecedented device performance, foot-prints and functionalities.

'Hybrid' means the effective combination and utilization of photonics, electronics and surface plasmons or metal optics at the same time. The idea here is to create synergies between all technologies. The second meaning addresses a platform approach where photonic components are integrated onto the same wafer or at least the same chip alongside with traditional semiconductor devices.

Lastly, the successful 'integration' of this novel platform into hybrid nano-Photonic circuitry is important to provide competitive cost functions and allow for sufficient reliability control. In business terms this means that a learning curve from economy-of-scale should be deployed if this technology is supposed to make an impact on the market and therefore society.
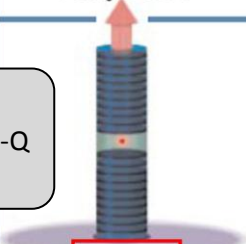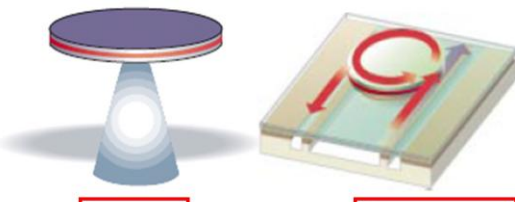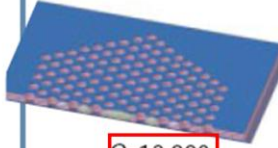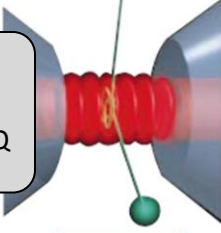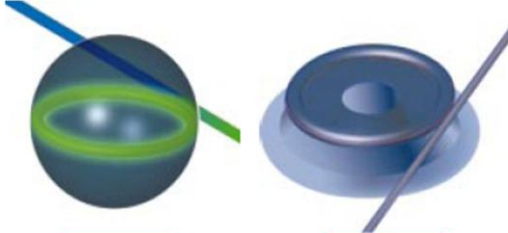
2. Plasmonic Nano-Cavities

2.1. Introduction

Optical Cavities

An optical cavity is essentially a resonator for electromagnetic fields. If at least one dimension of the cavity is longer than the diffraction limit of light, a standing wave can form inside the resonator. Thus, a cavity stores electromagnetic energy in space and time. The cavities quality Q-factor relates to the cavities feedback mechanism; the higher the cavity's mirror reflectivity, the higher is the Q-factor, and thus the sharper the resonance (spectrally). We can relate this to first-principles like the Heisenberg-uncertainty principle, where we know that the product of energy and time must yield a constant. Therefore if a photon is stored inside a cavity for a long time due to high reflecting mirrors (high Q-factor), the electromagnetic field energy built up yields a short or narrow energy response, namely a sharp resonance spectrum. While one goal of cavity research is to shrink the cavity from macro sizes into the micro regime, a second goal is to increase the cavity's feedback at the same time.

However in terms if scaling photonic cavities, the diffraction limit of light ($\lambda/2n_m$), where n_m is the effective mode index, places a natural lower volume limit. Thus, if the goal is to enhance the light matter interaction it was perceived to optimize the Q-factor rather than scale the cavity beyond the diffraction limit. Figure 2.1.1 highlights this trend by showing a cavity zoo exhibiting ultra-high feedback [1]. Empirically we also find that generally the higher the quality-factor, the larger the cavity volume is, and vice versa [2]. This comes to no surprise, since the in chapter 1 introduced Purcell-factor relates to the ratio of the quality factor and cavity volume, and is a trade-off parameter which has to be optimized. With the aim to enhance the light-matter-interaction with the use of a cavity, the high-Q approach was taken by many research groups.

However, an ultra high Q-factor also limits the utilizable bandwidth of the cavity; a cavity with a operating wavelength of 1 micrometer and a quality factor of 10^8, has a resonance response of 10^{-5} nanometer equivalent to a frequency of 30 terahertz. Thus a second approach to enhance the light-matter-interactions is to not use high Q -factors, but to scale the cavity volume stronger than the Q-factor can drop which lead to the exploration of plasmonic micro and nanocavities as we will discuss next.

Figure 2.1.1 | Optical Cavities [1]. While the cavities quality-factor, Q, can be designed to be extremely high, the cavity volume follows the trend of Q. A large Q-factor cavity also has a large volume and vice versa.

The Purcell Effect in a Plasmonic Nano-Cavity

Having demonstrated the feasibility of the cavity design, we envision plasmonic cavities as a tool for enhancing optical interaction processes with matter. For example, Purcell [3] predicted that the spontaneous emission rate of an emitter is not intrinsic to the emitter, but depends on the surrounding electromagnetic environment. A modification of this environment can enhance the emission rate of an atom, which is quantified by the Purcell enhancement Factor, F, which is expressed as

$$F = \frac{6}{\pi^2} \frac{(\lambda/2n)^3}{V} \frac{Q_e Q}{Q_e + Q} \tag{1}$$

Here, Q_e and Q are the quality factors of the atomic emission line and cavity mode respectively; V is the volume of the optical mode; and n is the refractive index of the medium surrounding the atom. In the literature typically $Q_e \gg Q$ is assumed, thus Q/V is often quoted for F. Estimation of the Purcell factor for an emitter within a nano-cavity, F_{nc}, can be calculated using Fermi's golden rule.
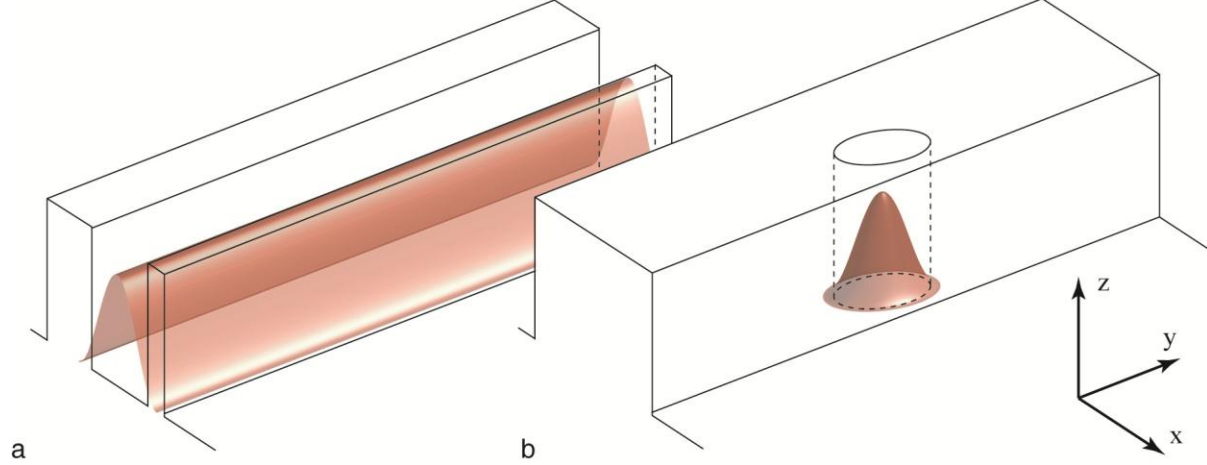
Figure 2.1.2 | Schematics of the 2D and 3D nano-cavities with an illustration of the in-plane variation of the cavity mode field distributions. a, 2D Fabry-Pérot nano-cavity with one degree of freedom in the y-direction as experimentally studied in the manuscript. b, a 3D version of the nano-cavity.

The nano-cavity discussed in the manuscript provides confinement in 2 dimensions as shown in Figure 2.1.2**a**. We have calculated the Purcell factor for this geometry to be

$$F_{nc} = \frac{3}{\pi} \frac{n_{sp} n_g}{n(r_e)^3} \frac{(\lambda/2)}{L_{sp}} \sqrt{Q} = 2 F_{sp} \sqrt{Q} \tag{10}$$

Where F_{sp} is the Purcell factor for SPPs without the cavity, n_{sp} is the SPP effective phase index, n_g is the SPP group index and $n(r_e)$ is the local refractive index near the atom's position.

A nano-cavity that includes lateral confinement, such as the one shown in Figure 2.1.2b, can confine light in all 3 dimensions. This leads to a Purcell factor of

$$F_{nc} = \frac{8}{j_{0,1}^2 J_1(j_{0,1})^2} \frac{n_{sp}}{n_g} F_{sp} Q \approx 5.13 \left(1 - \frac{\omega}{n_{sp}} \frac{dn_{sp}}{d\omega} \right) F_{sp} Q \tag{13}$$

where $j_{0,1} \approx 2.404$ is the first root of the zero-order Bessel function of the first kind.
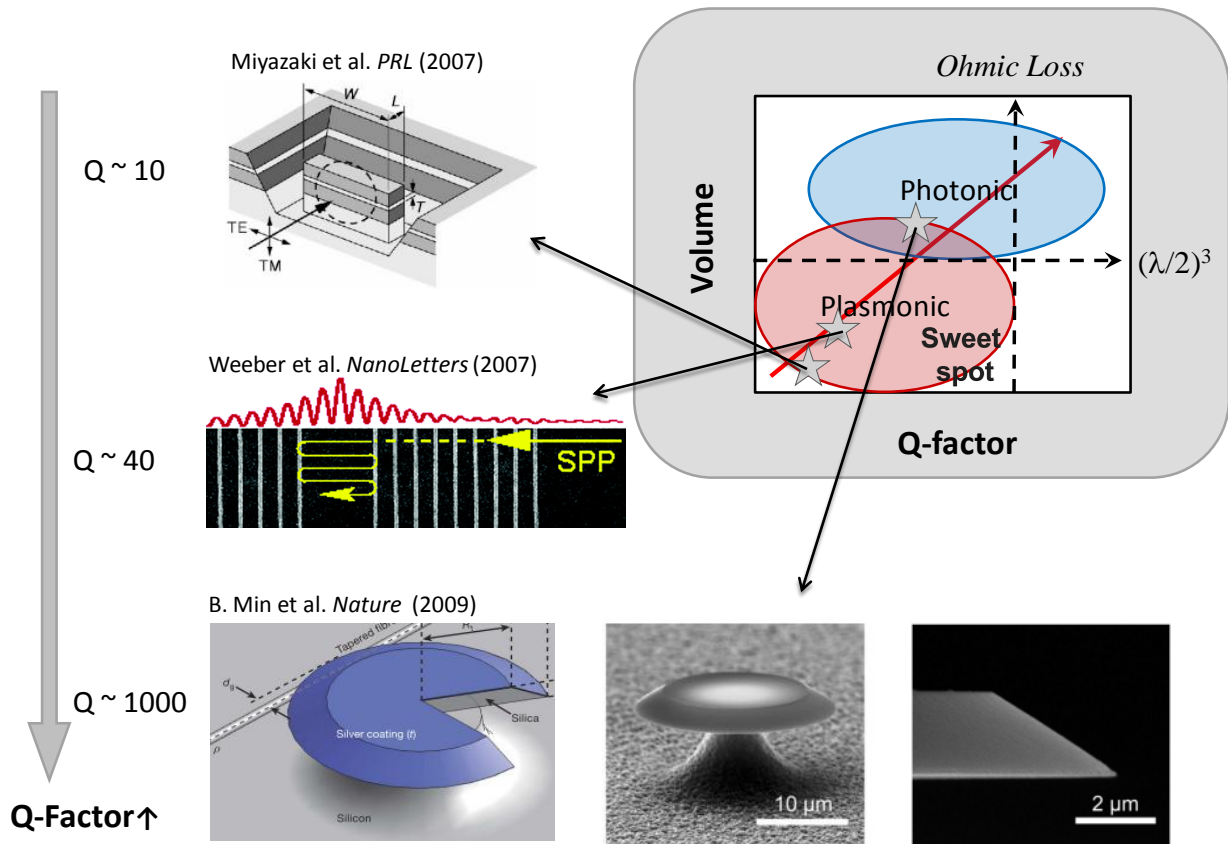
2.2 Plasmonic Cavities towards improving Q/V

Empirical one finds a proportional relation between a cavity's quality factor and its volume (upper right Fig. 2.2.1); increasing one requires increasing the other [1]. Aiming for strong light-matter-interactions and high Purcell effects a possible approach is to decrease the volume for low to medium quality factor ('sweet spot' Fig. 2.2.1). While Photonic cavities (blue circle Fig. 2.2.1) can provide high cavity qualities due to their low loss trapping the photon for long times inside the cavity such cavities are bound to the diffraction limit of light, $(\lambda/2)^3$ [2]

Within this context, a second approach is pursued towards achieving high Purcell factors [3]. Using plasmonics, the cavity volume can now be shrunk beyond such diffraction limit sizes (red circle Fig. 2.2.1). The cost for such small nanoscale cavities is the ohmic loss associated with surface plasmon polaritons, which limits the cavity's quality factor. Thus the ideal placement in this 2-parameter space is high-Q, but low volume, therefore on the lower right corner of Figure 2.2.1 on the upper-right panel, noted as 'sweet spot'. Various cavities towards this goal were explored. Miyazaki et al. for instance deployed an 'organ-pile' style plasmonic cavity with an ultra-small mode volume [4]. However, the cavities resonance is barely discernable from the spectra, leading to a Q-factor of about 10. A second approach was to deploy a distributed Bragg-mirror in conjunction with a plasmonic cavity [5]. While this approach yielded an increased quality, the far extending Bragg-mirrors resulted in a large cavity volume.

In a third approach an axisymmetric whispering-gallery high-Q SPP microcavity that can be implemented by coating the surface of high-Q silica microresonators with a thin layer of noble metal was demonstrated [6]. This structure enables room-temperature high-Q operation up to 1376 ± 65 in the near infrared for surface plasmonic whispering-gallery modes. This nearly ideal value, which is close to the theoretical metal-loss-limited Q-factor, is attributed to the suppression and minimization of radiation and scattering losses that are made possible by the geometrical structure and the fabrication method. The SPP eigenmodes, as well as the dielectric eigenmodes, are confined within the whispering gallery microcavity and accessed evanescently by using a single strand of low-loss tapered optical waveguide. This coupling scheme provides a convenient way for selectively exciting confined SPP eigenmodes, with up to half of the input power transfer, which is made possible by phase-matching control between the microcavity SPP and the tapered fiber eigenmodes [6].

However, a fundamental bottleneck for the realization of SPP nano-optical functional devices stems from large intrinsic metal loss at optical frequencies induced by resistive heating. Hence, any type of plasmonic resonator based on a plasmonic waveguiding principle is inevitably limited by the intrinsic metal loss in addition to other sources of losses, such as roughness-induced scattering, radiation into free space and the substrate, and bending-induced radiation. While other types of plasmonic cavities can be built, whispering-gallery resonances, which are observed in circular or elliptical resonant structures, are especially attractive due to their extremely large photon lifetime. The smaller optical mode volume can be engineered with the proposed structure when compared to the bare silica toroidal microcavity with a sacrifice in the Q-factor [6].

Fig. 2.2.1 | Nano-and Microscale Plasmonic Cavities. Empirical one finds a proportional relation between a cavity's quality factor and its volume (upper right); increasing one requires increasing the other. Aiming for strong light-matter-interactions, and high Purcell effects a possible approach is to decrease the volume for low to medium quality factor ('sweet spot' upper right). Three examples of increasing quality factor plasmon cavities are shown; however, the volume is subsequently increased as well. In chapter 2.3 we will be discussing a cavity that breaks out from this tradition, demonstrating a reasonable quality factor, yet a sub-diffraction limited cavity volume.

While these three plasmonic cavity demonstrations show the trend of increasing cavity qualities, *Q*, their mode volume, *V*, is also increasing along with the quality factor. Thus the ratio of *Q/V* is not significantly enhanced, if at all. In the following chapter we will be discussing a plasmonic cavity demonstration that exhibits a cavity volume below the diffraction limit of light, but still maintains a medium quality factor [7]. This is possible due to both the realization of strong surface plasmon reflectors and low-loss nano fabrication.

2.3 Plasmonic Fabry-Pérot Nano-Cavity

Abstract

The miniaturization of laser devices to nano-scale dimensions is a fundamental challenge imposed by the diffraction limit of light. Surface Plasmons Polaritons (SPPs) [1,2] show the potential to overcome this limitation opening new fields such as integrated nano-photonics [2-7] and enabling unprecedented enhancement of light-matter interactions [8-13]. While the mode sizes of conventional dielectric micro-cavities [8,14-16] are larger than the wavelength, plasmonic cavities can support truly nanoscale modes [5]. However, high ohmic and scattering losses, inherent in small metallic structures, are commonly perceived to prohibit high Finesses and quality factors in plasmonic cavities. Here we experimentally demonstrate a plasmonic Fabry-Pérot nano-cavity that confines light to a sub-wavelength scale while achieving a Finesse as high as conventional large-volume Fabry-Pérot étalons. Such high performance nano-cavities are capable of enhancing inherently weak optical processes such as spontaneous [9,10] and stimulated emission [8,11-13] opening the way to low-threshold nano-lasers.

Introduction

The emerging field of *Nano Plasmonics* exploits the ability of metal nanostructures to confine light to sub-wavelength length scales that surpass fundamental diffraction limitations [1,2]. Surface Plasmon Polariton (SPP) oscillations are the key to breaking down this limit of conventional optics as they allow the compact storage of optical energy at the interfaces of metal and dielectric materials. It opens exciting scientific possibilities such as molecular-scale optics [17] and nano-scale optical circuits [2-7]. Beyond technological incentives, accessing optical length scales well below the diffraction limit allows the enhancement of weak physical processes by orders of magnitude [8-13,17-19].

Results

Optical cavities allow efficient concentration and storage of electromagnetic energy and are consequently used throughout optics for numerous light emission and detection applications [20]. In order to enhance the aforementioned physical processes, it is essential to concentrate light in a small mode volume and store it there for a long time. The cavity quality factor, Q, is a measure of the time that light is trapped inside a cavity and is determined by the optical feedback mechanism (e.g. mirror reflectivity) and the internal loss. While the Q-factors of conventional dielectric cavities can be quite high, [8,14-16] they exhibit relatively weak optical confinement with modal volumes generally larger than the wavelength cubed. Plasmonic cavities on the other hand, can achieve strong mode confinement, but possess intrinsic SPP and scattering losses that in general, reduce the cavity Q-factor well below its dielectric counterpart [5,21- 23].

Here we demonstrate a plasmonic Fabry-Pérot nano-cavity with a Q-factor close to 200. This is obtained by a novel design of closely-spaced high-aspect ratio mirrors, capable of reflecting up to 98% of incident SPPs. Since the cavity length is much shorter than the SPP propagation distance and the mirrors' heights are significantly larger than the SPP penetration depth in air,

the loss per path length and mirror scattering are minimized, respectively. In fact, the SPP propagation loss in these nano-cavities accounts for only a small reduction in the quality factor. The small mode volumes, V_m, achievable with these cavities can exhibit surprisingly large Q/V_m ratios, leading to a strong Purcell effect [9] that is competitive with higher Q diffraction limited Photonic Crystal Cavities [8,16]. Furthermore, the cavity resonance can be tuned over the entire visible spectrum by varying the distance between the mirrors.
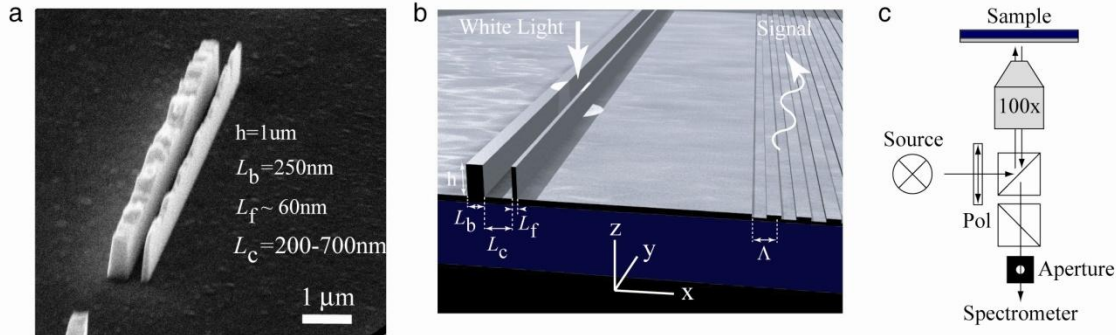
Figure 2.3.1 | The Plasmonic Fabry-Pérot Nano-Cavity. a Tilted scanning electron micrograph of a nano-cavity. Electron beam lithography and electroplating were used to fabricate the vertical Silver fins, which act as mirrors for SPPs bound to the underlying Silver-Air interface. The aspect ratio of the thinner front mirror was close to 20:1, which allows partial transmission of SPP cavity modes. **b** and **c** show schematics of the nano-cavity sample and the optical characterization method. White light (Xe lamp 150W) is focused through a 100x with NA = 0.8 microscope objective onto the nano-cavity, exciting SPP cavity modes. The cavity modes are partially transmitted through the thin front mirror and subsequently propagate approximately 20 μm as SPPs bound to the Silver-Air interface, scattered out of the plane by a grating and collected by the microscope objective. The grating coupler was designed to scatter SPPs across the visible spectrum into the numerical aperture of the microscope objective. An aperture placed in a secondary image plane is used to spatially filter the light scattered from the grating to increase the signal to noise ratio. The incident light is polarized with an electric field along the x-direction. This ensures that SPPs are generated within the cavity. A second polarizer was also used to ensure that only waves originating in SPPs are detected at the grating coupler.

The nano-cavity is made of two parallel Silver fins acting as high quality optical mirrors standing perpendicular to a Silver substrate (Fig. 2.3.1a). While the back mirror, L_b = 250 nm, is 10 times the skin depth of Silver, the front mirror must be sufficiently thin (L_f = 55 - 85 nm) to allow partial out-coupling of resonant surface plasmons in the forward direction. This imposes the requirement of a high aspect ratio (20:1) mirror that cannot be obtained by traditional fabrication techniques e.g. reactive ion etching. This problem, however, has been solved by using a combination of high resolution lithography and electrochemical metal deposition (see methods). Excitation of the nano-cavity can be achieved by focusing white light onto the mirrors, which scatter the light into the various optical modes of the nano-cavity (Fig. 2.3.1b). The SP nano-cavity modes are transmitted through the thin front mirror and, after propagating approximately 20 μm across the metal substrate, are scattered into free-space by a broad-band grating coupler (Fig. 2.3.1b&c).
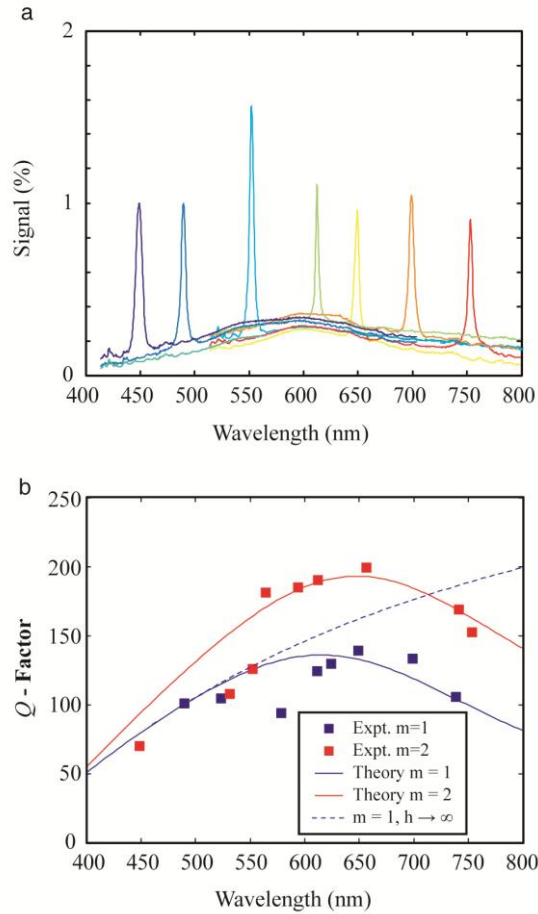
Figure 2.3.2 | Spectral response and *Q*factors of Fabry-Pérot Nano-Cavities of varying length. a Relative signal intensity for seven selected cavity lengths (175 - 700 nm) spanning the visible spectrum. Each cavity length has a single, sharp resonance corresponding to horizontal oscillation between metal mirrors (H-mode). The measured peak signal intensity was about 1% of the excitation intensity. **b** The variation of the nano-cavity *Q*-factors across the visible spectrum. The measured 1st and 2nd order cavity modes (square markers) were fitted with a theoretical model (solid lines, see methods). These trend lines highlight the competition between intrinsic metal and scattering losses. For the hypothetical case of infinitely tall mirrors, $h \rightarrow \infty$, the *Q*-factors are primarily affected by metallic losses (broken line) which increase for shorter wavelengths. Conversely, scattering loss dominates at longer wavelengths due to the larger SPP field extension into the air, that becomes comparable with the finite fin height.

Figure 2.3.2a depicts the spectra collected from the grating coupler for seven nano-cavities with lengths, L_c, ranging from 175 to 700 nm. A sharp resonance that is indicative of a high *Q*-factor mode is observable for each nano-cavity. Aside from the sharp peak, whose spectral position depends on the cavity length, L_c, a weaker and broader background hump is also apparent, which is spectrally similar for all the cavities. By fitting the spectra from Fig. 2.3.2a with two Lorentzians (see methods) the resonant cavity wavelengths and line-widths can be determined. The cavity *Q*-factors, shown in Fig. 2.3.2b, ranging from 100 - 200, are high for any plasmonic

resonator at these frequencies. In fact, the plasmonic losses reduce the Q–factor by less than a half compared to that of a *lossless* dielectric cavity of the same size. This is in sharp contrast to micro-disks cavities with a Q-factor reduction from 10^9 in dielectric [9] to ~1300 in plasmonic cavities at IR frequencies [21]. A theoretical model of the Fabry-Pérot nano-cavity describes the trends of the Q-factors well for the first and second order cavity modes (see methods). The distinctive shape of these trend lines arises from the trade-off between the two cavity loss mechanisms: intrinsic metallic and scattering losses. The Q-factors of cavities resonating at shorter wavelengths are mainly dominated by intrinsic metallic losses including the SPP propagation distance and field penetration into the metallic mirrors. In fact, the Q-factor is not affected at all by the finite height of the mirrors since the field is tightly confined to the metal substrate (Fig. 2.3.2b). Conversely, at longer wavelengths, the plasmonic mode extends further from the metal substrate into the air; hence the Q-factor is clamped by scattering losses from the upper corners of the mirrors (Fig. 2.3.2b).

The measured resonant wavelengths follow the theoretical condition describing surface plasmons resonating in a Horizontal (H) fashion between the metallic mirrors (Fig. 2.3.3a). The observed cavity dispersion deviates from that of free space radiation bouncing between two metal mirrors since the SPP wavelength becomes increasingly shorter than that of free space at higher frequencies. The small cavity size leads to a large free spectral range, so that for each cavity length only one of two possible H-mode orders are observable (blue line = 1ˢᵗ, red line = 2ⁿᵈ H-mode) in our measurements. A Finite Element Method simulation for a cavity length of $L = 325$ nm shows two possible H-modes of the nano-cavity, which lie at opposite ends of the visible spectrum (Figs. 2.3.3b,c). The H-modes have plasmonic character since they are confined in the z-direction with the characteristic exponential decay and are diffraction-limited in the x-direction. The first order mode occurs at the red end of the spectrum and clearly shows penetration into air where scattering from the top of each mirror is appreciable. On the other hand, the second order mode occurs at the blue end of the spectrum where plasmonic confinement is strong and cavity loss is dominated by the SP propagation loss and field penetration into the metallic fins.

Using the Fabry-Pérot model, we can also reveal the cavity's feedback mechanism by extracting the properties of the metallic mirrors; the complex reflection coefficient and the scattering from the top corners of the mirrors (see methods). The phase change upon reflection causes a small wavelength dependent shift corresponding to the finite penetration depth of SPPs into the metal mirrors, which we have determined by comparing the resonance wavelength and physical length of each cavity (Fig. 2.3.4a). The measured penetration depths closely follow the theoretical trend Calculated from the reflection phase of the Fresnel coefficient. The reflectivity of the mirrors is determined from the Fabry-Pérot model and can be as high as 98% (Fig. 2.3.4b).
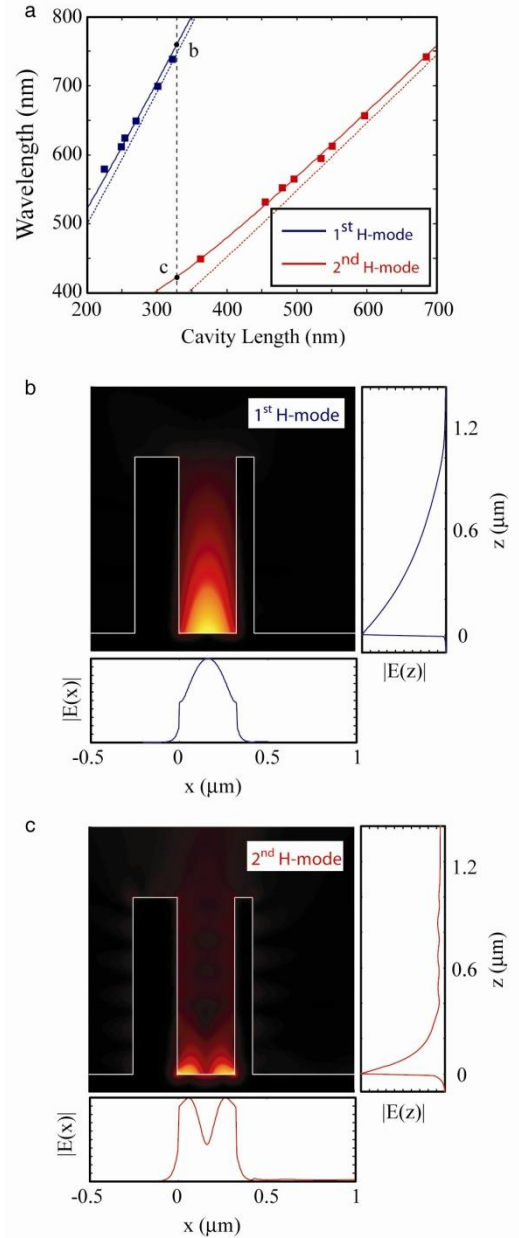
Figure 3.2.3 | Dispersion and field distributions of the Nano-Cavity modes. **a** The measured resonant wavelengths versus cavity length for the 1st and 2nd H-modes (square markers) compared with the Fabry-Pérot model (solid lines, see methods). The dash lines show the linear dispersion of conventional Fabry-Pérot cavities without SPP dispersion. **b & c** The |E|-field distributions of the two nano-cavity modes. The plasmonic character of the modes is evident from the exponential decay along the z-direction while the mode confinement in x direction shows typical sinusoidal variation between the two metal mirrors. The field intensity at the top of each mirror is larger for the 1st order mode than for the 2nd order. Consequently, the Q-factor for the 1st mode is scattering dominated, while that of the 2nd mode is dominated by the intrinsic metallic loss.
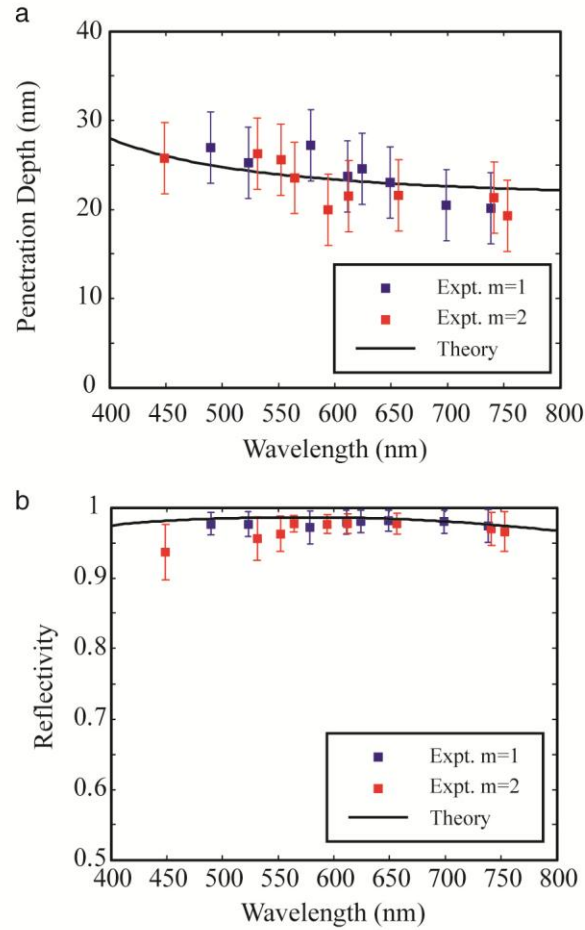
Figure 2.3.4 | Characteristics of the Nano-Cavity mirrors. **a** The penetration of SPPs into the cavity mirrors (square markers) compared with an approximate Fresnel reflection model for SPPs (solid lines, see methods). The experimental penetration depth was calculated by comparing the measured resonant wavelength and physical cavity length. **b** The reflectivity of the nano-cavity mirrors (square markers) compared with a phenomenological SPP reflection model (solid lines, see methods). The reflectivity is limited by intrinsic metal losses (at shorter wavelengths) and scattering due to the finite fin height (at longer wavelengths).

The measured spectral response (Fig. 2.3.2a) shows a broad resonance around $\lambda = 600$ nm consistently for all cavity lengths. This resonance corresponds to an electric field oscillating in the vertical (V) direction (Fig 2.3.5). This V-mode has a non-zero field at the mirror walls, suggesting that it comprises of surface plasmons propagating in the z-direction. The resonator is essentially open at the top of the mirrors, which explains the low quality factor. Feedback is only provided by the small effective index difference at the metal-air interface at the top edges of the cavity mirrors. Furthermore, we found that the resonance frequency of this vertical resonator with a cavity length given by the mirror height, $h = 1$ μm, peaked around 600 nm which coincides with our experimental results.
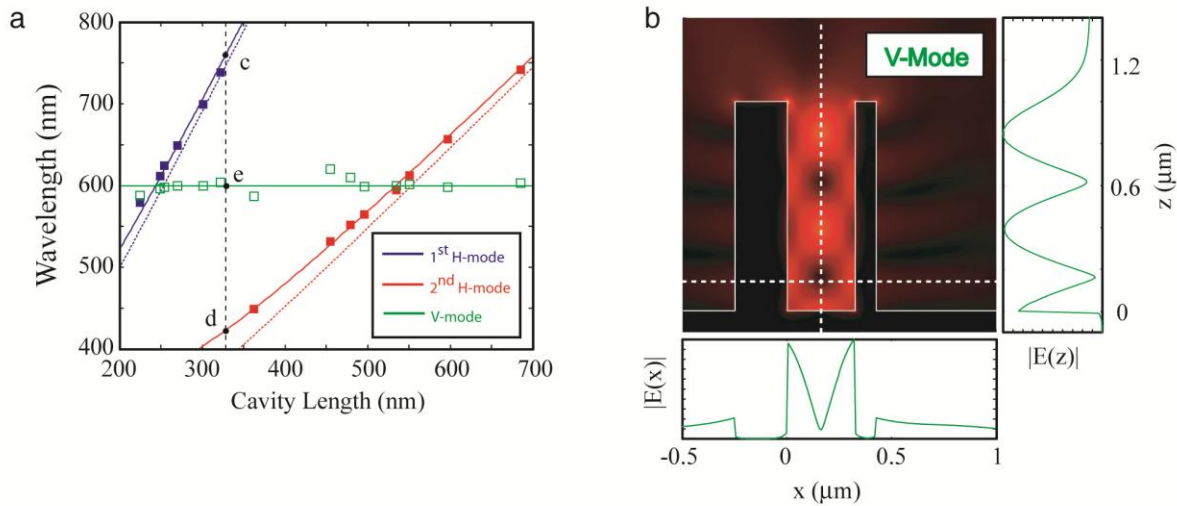
Figure 2.3.5 | Spectral resonance FEM simulation for the E-field vs. position. **a** plot of the nano-cavity's dispersions shows the insensitivity of the V-mode's resonance wavelength on cavity length. **b** For a cavity length of L = 325 nm, a vertical (V) a propagating field in the z-direction forms a standing wave. Here the mirror height, h becomes effectively the cavity length. The *Q*-factor of this cavity is low since the tops of the metal mirrors provide minimal reflection.

Conclusion

In conclusion, we have shown that a Fabry-Pérot nano-cavity utilizing surface plasmon polaritons can exhibit high plasmonic *Q*-factors at visible frequencies. Such high *Q*-factors are achievable when the cavity length is considerably shorter than the SPP propagation distance and the mirrors' heights are significantly larger than the SPP penetration depth into the air. Concurrent high quality factors and small mode volumes allows a strong Purcell effect competitive with higher *Q* diffraction limited Photonic Crystal Cavities and enables numerous applications [24] such as fast and low-threshold lasers [8,12,13].

Experimental Methods

Nano-cavity Fabrication: A series of devices were fabricated on standard Silicon wafers. A wetting layer (4 nm of Germanium) was deposited on a Silicon wafer followed by sputtering of 200 nm Ag (2.5 mTorr, Argon Plasma Gas, 50 mW). The Germanium ensures a film of low surface roughness (RMS = 1.6 nm, measured using atomic force microscopy). A thick layer of Poly-Methyl Meth-Acrylate (PMMA) (A11) was spun onto the sample @ 3000 RPM (~ 1.1 μm) and the solvent was evaporated 180 C for 30 min followed by Electron Beam Lithography (Vistec VB300 @ 100 keV) to pattern the cavities. Cavity mirrors were grown via chemical silver electro-plating (80 μA for 70 seconds) followed by final PMMA lift off in acetone. A post fabrication rapid thermal annealing step in Nitrogen at 400 C for 60 s helps to smooth the metal

surfaces. Finally, the grating coupler (10 grooves: pitch = 247 nm and a depth = 45 nm) was fabricated using focused ion beam milling.

Optical Measurements: A modified reflection mode microscope (Fig. 2.3.1c) was used to characterize the cavity's spectral response. Cavities were illuminated with a white light source (Xe lamp, 150 W) focused onto the sample via a 100X, NA=0.9 objective lens. Surface plasmons generated at the nano-cavity, propagate to a grating coupler at a distance of 20 μm from the cavity, where they are scattered off the surface. An aperture was placed in a secondary object plane to filter the microscope's field of view so that only the grating signal was collected. The signal was recorded using a spectrometer with a liquid Nitrogen cooled CCD detector with a spectral resolution of 0.3 nm.

Theoretical Model: A straightforward Fabry-Pérot model describes the nano cavities effectively. This includes descriptions of four principle phenomena, namely: SPP propagation, attenuation, reflection and scattering. The dispersion relation, $k_{sp}(\lambda) = 2\pi n_{Ag}(\lambda)/\lambda \left[n_{Ag}(\lambda)^2 + 1 \right]^{-\frac{1}{2}} = 2\pi n_{sp}(\lambda)/\lambda$ describes the propagation and attenuation characteristics of surface plasmons at the Silver / Air substrate interface, where the propagation distance, $L_{sp} = \text{Im}\{2k_{sp}(\lambda)\}^{-1}$. The permittivity of Silver is assumed to follow a Drude formula, $n_{Ag}(\lambda)^2 = \varepsilon_b - E_{pAg}^2 \left[E(E + i\gamma_{Ag}) \right]^{-1}$ where, ε_b is the background permittivity, E is the energy, E_{pAg} is the plasma energy and γ_{Ag} is the electron collision energy. The SPP reflection at the mirrors was approximated to the Fresnel coefficient, $r(\lambda) = \left(n_{sp}(\lambda) - n_{Ag}(\lambda) \right)\left[n_{sp}(\lambda) + n_{Ag}(\lambda) \right]^{-1}$. Both the magnitude, $|r(\lambda)|$ and phase, ϕ, of the reflection coefficient, $r(\lambda) = |r(\lambda)|\exp\{i\phi\}$, are relevant to the physics of the nano-cavity. The phase describes the shift of resonance wavelength from a perfect metal reflector due to field penetration, $\delta(\lambda)$, into the metal mirrors (see Fig. 2.3.4a), where $\delta(\lambda) = -\phi\lambda \left[4\pi \text{Re}\{n_{sp}(\lambda)\} \right]^{-1}$. The physical cavity length, L, and optical cavity length, $L_c(\lambda)$, are therefore related by $L_c(\lambda) = L + 2\delta(\lambda)$. However, $|r(\lambda)|^2$ approximates the reflectivity in the absence of scattering due to the non-zero SPP field at the upper corners of the mirrors. Assuming that this scattering is proportional to the electric field intensity at the top corner of the mirror, *i.e.* at a height, h, above the metal surface, the magnitude of the reflection from the metal mirror is $R(\lambda) = |r(\lambda)|^2 - S_0 \exp(-h/L_z(\lambda))$ where $L_z(\lambda) = \lambda \text{Im}\{[1 - n_{sp}(\lambda)^2]^{-\frac{1}{2}}\}/4\pi$ is the SPP penetration depth in air and S_0 is the scattering strength. The Q-factor of the nano-cavity mode at a resonance frequency, $\lambda_R = 2\text{Re}\{n_{sp}(\lambda_R)\}L_c(\lambda_R)$, follows the usual Fabry-Pérot expression

$$Q(\lambda_R) = m\pi \frac{\sqrt{R(\lambda_R)\exp(-2L_c(\lambda_R)/L_{sp}(\lambda_R))}}{1 - R(\lambda_R)\exp(-2L_c(\lambda_R)/L_{sp}(\lambda_R))}$$

where *m* is the order of the cavity mode.

Numerical Fitting Procedure: Each spectrum was fitted to a double Lorentizan distribution plus a constant background using the following formula,

$$S(E) = c_0 + c_1 \frac{c_4^2/4}{(E - c_3)^2 + \gamma_4^2/4} + c_2 \frac{c_6^2/4}{(E - c_5)^2 + \gamma_6^2/4}$$

where c_i are fitting parameters. The resonant energies of the two possible cavity modes are c_3 and c_5, and the Q-factors are c_3/c_4 and c_5/c_6.

The nano-cavity model has 4 unknowns: the Drude parameters of Silver, ε_b, E_{pAg} and γ_{Ag}; and the mirror scattering strength, S_0. We chose ε_b=5 and E_{pAg} = 9.5 eV was determined from the best fit to the cavity mode dispersion, λ_R = 2Re$\{n_{sp}(\lambda_R)\}L_c(\lambda_R)$. The two remaining parameters describe propagation, γ_{Ag} = 0.04 eV, and scattering losses, S_0 = 0.37. To calculate these, we have used a numerical fitting procedure for the function $R(\lambda_R)\exp(-2L_c(\lambda_R)/L_{sp}(\lambda_R))$ that we have extracted from the experimentally determined Q-factors (see Fig. 2.3.2a). While S_0 is a phenomenological constant, it produces a good fit to the reflectivity and Q-factor data from the experiment. The three parameters that define the Drude model describe all characteristics of the nano-cavity's modes well and produce an excellent fit to the various experimental data for the permittivity of Silver [25].

Estimation of Nano-cavity Purcell Factors: The SPP Purcell factor for an emitter placed at a height z_d above a metal-dielectric interface (i.e. without cavity) is,

$$F_{sp} = \pi \, \text{Im}\left\{ \frac{\varepsilon_m \varepsilon_d^{1/2}}{\left(\varepsilon_m + \varepsilon_d\right)^{5/2}} \right\} \exp\left(- z_d / L_z\right) \tag{14}$$

Providing the emitter is located at a distance $z_d \approx 15$ nm from the surface, coupling to the SPPs of a Silver-Air interface dominates and $F_{sp} \approx 1$ across the visible spectrum. As for the achievable quality factors for these nano-cavities, based on the experimental results in the manuscript, we can expect Q-factors as high as 150. In the case of the first order mode of a 2D nano-cavity, the Purcell Factor is given by $F_{nc} \approx 2\sqrt{Q}$ and hence can be as high as 25. The variation with $\sqrt{Q}$ is due to the limited density of states along the degree of freedom in the y-direction. On the other hand, in the case of a 3D nanocavity, the Purcell Factor is approximately $F_{nc} \approx 5Q$ and hence can be as high as 750. This value dramatically exceeds the capabilities of current diffraction limited approaches such as photonic crystal micro-cavities, which typically have Purcell Factors considerably less than 100.

# 3. Deep-Subwavelength Waveguiding with low Loss

3.1 Introduction

Sub-wavelength Optical Modes

In the previous chapter we have reviewed ways of using optical cavities to store electromagnetic energy which can be used to enhance the interaction between electromagnetic waves and matter. An interesting question to ask is, whether such enhancement can also be archived via non-resonant ways. In particular, the question goes further and asks whether an enhancement can be achieved by shrinking the volume of an optical mode and not increasing quality-factor. Regarding sub-wavelength modes, waveguides, open cavities basically, and localized fields can be used (Fig. 3.1.1) [1]. The field localization effect of surface plasmons is a good candidate for such ultra-small mode size waveguides. Here, the spectrum ranges from V-grooves where the optical mode is confined in a narrow metallic groove while the opening angle controls the degree of confinement [2], to the opposite like a metallic wedge. In addition Metal-dielectric-Metal (MIM) waveguides have been explored as well [3]. While this waveguides type can provide sub-wavelength confinement in one dimension, it experiences a cut-off if the second dimension is shrunk as well (see below Figure 3.2.5). In this case the MIM mode becomes a hole inside a metal. Akin to the MIM waveguides are so called channel [4] or slot waveguides [5], however the interesting feature of these waveguides are, that the two metal blocks can be substituted by dielectrics with no ohmic loss. Even though no metals are used, the slot waveguide enables for sub-wavelength optical fields due to the discontinuity of Magnetic field across the high-low-high index boundary.

If a high dielectric waveguide is placed on-top a metal silver film, a deep-subwalength mode is formed [6]. However, since a significant amount of the waveguide mode's energy penetrates into the metal film, the propagation losses are high. An improvement from such design is achieved, when the high dielectric slap is separated from the metal by a small low index gap. This geometry effectively hybridizes the photonic (dielectric) and plasmon mode into a hybrid-plasmon polariton mode (HPP) [7,8]. This mode creates an optical capacitor which pulls the optical field into the low gap region. This is advantageous, because it reduced the ohmic loss significantly compared to the dielectrically-loaded SPP waveguide's mode. In the following two chapters we will discuss the theoretical concept and performance of the HPP mode in detail and demonstrate the first experimental observation of broadband, deep-subwavelength waveguiding, respectively.

Before we do this, let us briefly consider localized optical modes as a potential solution to create strong optical confinement [9]. Unlike waveguides, these schemes utilize local "hot-spots" of concentrated energy to squeeze light into spaces below the diffraction limit. However since these modes do not propagate, their Q-factor is extremely small. On the other hand, light-concentrating

antennae can be deployed as well. For instance the bow-tie antenna (right hand side Fig. 3.1.1) shows a tiny hot-spot in the center of the two metallic tips [10].
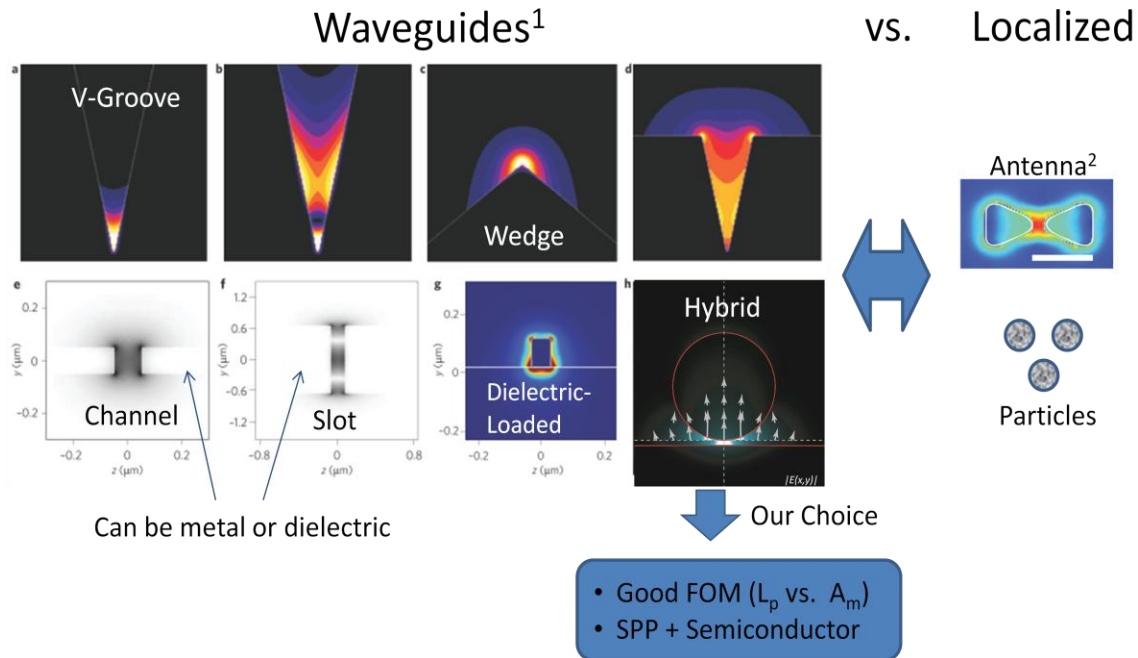
Figure 3.1.1 | Options for Sub-wavelength optical confinement [1]. Most waveguiding approaches featuring sub-wavelength confinement utilize metals to confine the optical mode. However, the slot-waveguide also provides an option for strong confinement with suffering from the parasitic metal loss. The hybrid plasmon-polariton (HPP) mode seem to the superior to other geometries for three reasons; firstly is has ultra-strong optical confinement, secondly it has relatively low loss and thirdly it allows to interfaces metal optics in a unique way with semiconductor technology. The latter is extremely important towards Opto-electronic device applications, as the semiconductor allows providing a viable 2-level system for emission or gain towards lasing action.

The table below (Table 3.1) benchmarks various experimental and theoretical results to the HPP mode studies here. The table clearly shows the superior performance (propagation length vs. optical confinement) of the HPP mode, but also highlights the achievement of measuring such small field sizes directly for the first time as we will discuss in chapter 3.3.

Discussing the table in detail, while the Co-planar waveguide (CPW) structure can theoretically produce strong confinement [11,12], practical realizations of such ultra small metal gaps face fabrication challenges. For instance, Pile et al. showed a FWHM of ~ 300 nm at 633 nm [13],

while Satuby et al. demonstrated a CPW waveguide with only micrometer gap sizes [14]. This is unlike the HPP waveguide and our presented results, where the confinement can be easily controlled by the gap region via thin-film deposition, where Angstrom level accuracy is regularly attainable. In order to bring the extreme confinement of the HPP mode into a broader perspective, we added experimental data from a well known Channel-Plasmon-Polariton (CPP) waveguide design from Bozhevolnyi et al., published in Nature [15].

Reference	Waveguide Type	Mode Width/λ_0	Mode Height/λ_0	Mode Area/$(\lambda_0/2)^2$	L_p (um)	λ_0 (nm)
Wang et. al. Opt. Exp. 13, 10558 (2005) (Theory only)	CPW (Co-planar waveguide)	0.10	0.12	4.8%	1.6 Loss =2.77 dB/um	539
Jung et. al., IEEE Phot. Technol. Lett. 21, 630 (2009) (Theory only)	CPW (Co-planar waveguide)	0.02	0.02	0.2%	20	1550
Pile et. al., APL. 87, 261114 (2005) (experiment)	CPW	~0.47	N.A.	N.A.	18	633
Dionne et. al. Nano Lett. 6, 1928 (2006) (Experiment)	MIM	N. A.	0.2	N. A.	3.4	685
Verhagen et. al. PRL 102, 203904 (2009) (Experiment)	IMI	0.19	~0.19	~14.4%	22	1550
Takahara et. al. Opt. Lett. (1997) (Theory only)	IMI	0.05	0.05	1.0%	0.6 Loss = 3 dB/410nm	633
Bozhevolnyi et. al. Nature 440, 508-511 2006 (Experiment)	CPP	0.65	>0.84[‡] [‡]Groove depth=1.3μm	>216%	~80	1550
[*]**HPP Oulton et. al. Nat. Photo. (2008) (Theory only)** [**]**HPP (Experiment)** [***]**HPP (Experiment)**	HPP	0.02[*] 0.31[**] 0.09[***]	0.02[*] 0.06[**] 0.08[***]	0.1% 6.8% 2.9%	33[*] 17[**] 7[***]	1550[*] 808[**] 633[***]

Table 3.1 | Optical mode size and propagation length comparison for selected publications and to the HPP mode studied here. All values are simulation results, unless noted otherwise.

While this paper claims for subwavelength fields, the degree of confinement is more than an order of magnitude worse per dimension compared to that of the HPP mode. Furthermore, the well known MIM waveguides geometry faces challenges when one wants to confine light in two dimensions (2D), as they lack the ability to provide the same degree of confinement in the lateral direction. For example, Dionne et al. demonstrates a MIM waveguide with subwavelength mode height ($\lambda/5$), but diffraction limited mode width [4]. If one, however, chooses to increase lateral confinement in a thin MIM slab geometry by introducing metal sidewalls, for example, one eventually gets the configuration of a hole in metal, which has a geometrical mode cut-off. MIM based lateral confinement is only possible for limited aspect ratios; otherwise, even this configuration experiences cut-off. This is perhaps the crucial point here: extreme 2D confinement is restricted in a number of metallo-dielectric structures: the challenge is not to find structures that do not experience a cut-off, but to identify those structures that present the optimal confinement conditions with acceptable propagation distances.

3.2 Confinement and Transport in Hybrid Waveguides

Abstract

The emerging field of nano-photonics [1] involves the manipulation of light on scales much smaller than the wavelength, yet practically, very few feasible approaches exist at present. Surface plasmon polaritons (SPP), electromagnetic excitations at metal/dielectric interfaces [2, 3], are one of the most promising candidates for deep sub-wavelength optical confinement [3-8]. However, experiments have only been successful in demonstrating moderate optical confinement comparable to that of conventional dielectric waveguides due to prohibitive fabrication demands and optical losses [9-14]. Here, we propose a new approach fusing conventional waveguide technology with plasmonics to address the trade-off between strong field confinement and propagation distance. We show that "capacitor-like" energy storage allows deep sub-wavelength confinement *in non-metallic regions*. Our approach provides both long propagation distance and strong mode confinement (>100x smaller than the diffraction limit) and opens up the field of semiconductor-based plasmonics.

Introduction

The need for fast, high-resolution and efficient light emission and detection has motivated research into optical structures capable of deep sub-wavelength confinement. Photonic crystals [15-18] are prime examples of facilitating technology for light confinement, yet fundamentally, they only provide confinement on the order of half a wavelength in each direction. Recently, Almeida and co-workers have shown that coupled rectangular dielectric waveguides can provide strong confinement beyond this diffraction limit in one dimension [19]. Although an important geometry, the relatively large portion of energy propagating in the high-index regions imposes the restriction of a thick low permittivity cladding, compromising the overall compactness of the waveguide. While both of these approaches are based solely on low loss dielectric materials, technology's inexorable path to smaller scales requires future nano-photonic devices to comprise of metallic and dielectric components with nanometer size and propinquity. Metal-dielectric waveguide geometries can also provide strong confinement down to sub-wavelength scale by storing optical energy in electron oscillations within dissipative metallic regions [2-14, 20]. This can lead to high optical loss, which is further exacerbated when high permittivity dielectric materials (such as semiconductors) are involved [20]. Consequently, semiconductor based plasmonics is not currently viable at telecommunications or visible frequencies.

Results

Here we report a plasmonic waveguide that supports a single *hybrid* mode of a semiconductor nanowire [21] and metal-dielectric SPP waveguides at the telecommunications wavelength, $\lambda =$ 1550 nm. This mode can be strongly confined to dimensions > 100x smaller than the diffraction limit, while maintaining a propagation distance exceeding that of SPPs on a semiconductor-metal interface. Moreover, by tuning the geometrical properties of this structure, we can increase the

propagation distance (up to millimeter range) while still maintaining moderate confinement. This approach naturally extends the capabilities of both plasmonics and semiconductor photonics and is applicable to nano-scale laser devices [22,23] as well as optically integrated circuits [24].

The hybrid waveguide geometry, shown in Fig. 3.2.1, consists of a high permittivity semiconductor cylinder ("cylinder waveguide") embedded in a low-permittivity dielectric near a metal-dielectric interface ("SPP waveguide"). In the following study, we vary the cylinder diameter, d, and dielectric gap width, h, to control the propagation distance, L_m, mode area, A_m and electromagnetic field distribution of a single hybrid mode.
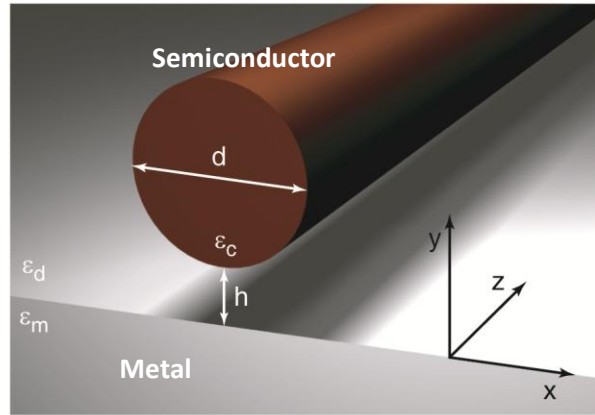
Figure 3.2.1 | The hybrid optical waveguide consists of a dielectric cylinder of permittivity, ε_c, and diameter, d, situated a distance, h, from a metallic half-space of permittivity, ε_m. The host medium is a dielectric of permittivity ε_d. With recent advances in nano-crystal growth technology [21], the dielectric cylinder is readily achievable for a range of semiconductor materials. Here, $\varepsilon_c = 12.25$ (GaAs) and $\varepsilon_d = 2.25$ (SiO$_2$), at the telecommunications wavelength, $\lambda = 1550$ nm. The metallic region is Silver with a permittivity $\varepsilon_c = -129 + 3.3i$ [25]. The center of the cylinder defines the origin x=y=0.

Figures 3.2.2a and 3.2.2b present numerical calculations of propagation distance and normalized mode area, respectively, as a function of d and h (see Methods). For large cylinder diameter and gap width (d > 200nm, h > 20nm) the hybrid waveguide supports a low loss cylinder-like mode with electromagnetic energy confined to the high-permittivity dielectric core (Fig. 3.2.2c). Conversely, a small diameter cylinder (d < 200 nm) results in an SPP-like mode, localized mainly to the metal-dielectric interface and suffering the typical loss of an SPP. At moderate cylinder diameters (d ~ 200nm) the coupling between the underlying modes forms a hybrid mode that features both cylinder and SPP characteristics; namely, its electromagnetic energy is distributed over both the cylinder and adjacent metal-dielectric interface (Fig 3.2.2d). However, when the gap width is reduced towards the nanometer scale, the hybrid mode no longer displays

characteristics of either the cylinder or the SPP mode; instead, it is strongly confined (Figs. 3.2.2e, 2f). Despite this strong confinement, the hybrid mode's propagation length exceeds that of SPPs of the equivalent metal-semiconductor interface (lower broken line in Fig 3.2.2a). Evidently, the gap width provides significant control over the character of the hybrid mode and provides the means to store electromagnetic energy leading to nano-scale optical fields with low mode loss.
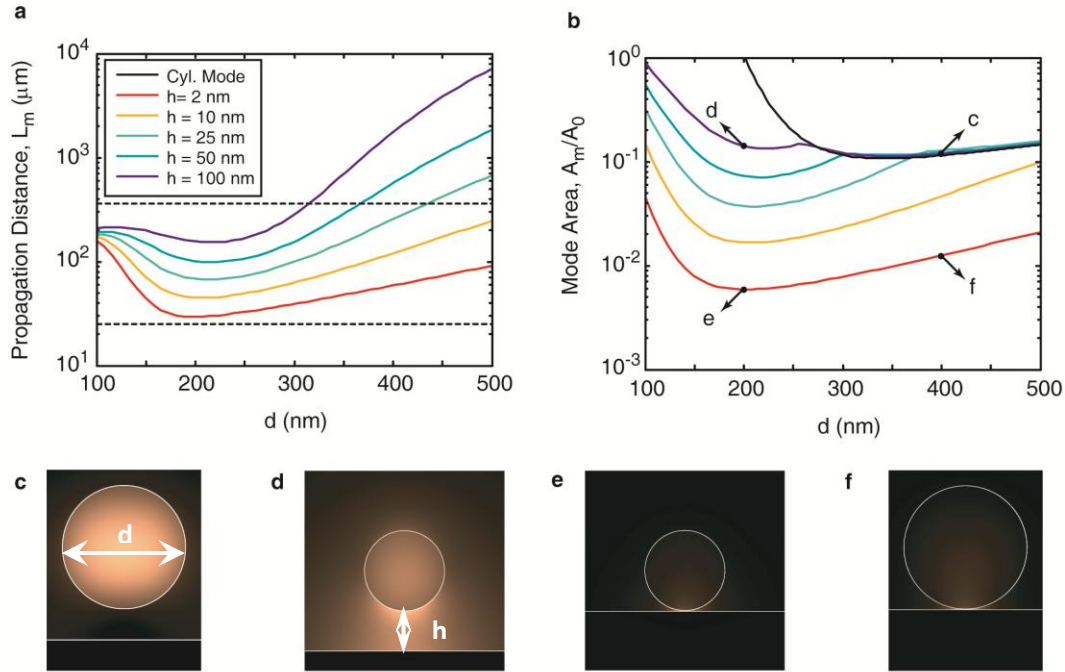
Figure 3.2.2 | Propagation distances and mode areas of the hybrid mode: a Propagation length as a function of cylinder diameter, d and gap, h (colored lines). The upper and lower horizontal broken lines represent the propagation lengths for the uncoupled metal/oxide and metal/semiconductor interfaces respectively (i.e. without cylinder). Note that the uncoupled cylinder waveguide (i.e. without metallic region) is loss-less for the given parameters. **b** Effective mode area, A_m / A_0, (Eq. (5)) as a function of cylinder diameter, d and gap width, h. The cusp features in **b** occur when the position of maximum $W(\mathbf{r})$ shifts from the centre of the cylinder to its edge nearest the metal. Lower panels show electromagnetic energy density distributions for **c**, [d, h] = [400, 100] nm; **d**, [d, h] = [200, 100] nm; **e**, [d, h] = [200, 2] nm; and **f**, [d,h] = [400, 2] nm. Note that the legend in **a** applies throughout this letter and the direction of the arrows indicate increasing h.

On first inspection, the confinement appears to be in the metal; however, the energy density distribution in Fig. 3.2.2d indicates that a significant portion of energy resides in the *low permittivity gap* between the cylinder and the metal-dielectric interface. Figure 3.2.3a resolves the electromagnetic energy density along the $\hat{y}$-axis for $x = 0$ showing that the peak energy

density is in the low index gap between cylinder and metal. Strong sub-wavelength confinement is also evident along the $\hat{x}$-direction (Fig. 3.2.3b). Further calculations (not shown here) indicate that at least 30% of the mode's energy resides in the gap for h = 2 nm (Fig. 3.2.2e) with more than 50% for h = 100 nm (Fig. 3.2.2d).
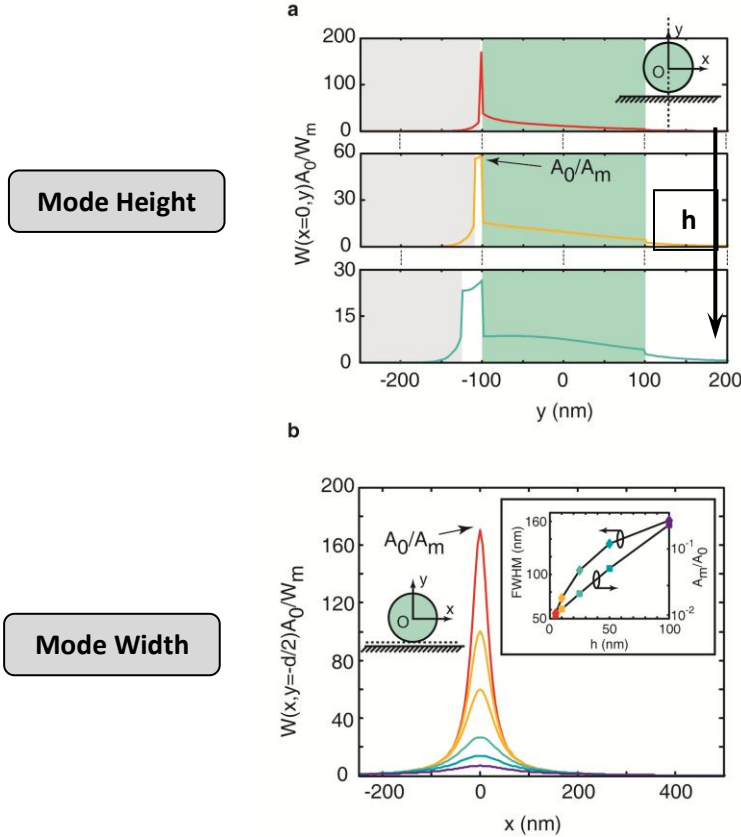
Figure 3.3.3 | Normalized electromagnetic energy density profiles, $W(r)A_0/W_m$, of hybrid modes for d = 200 nm. (Eq. (3)) a Normalized energy density along the y-axis, showing the confinement in the low index dielectric region (no shading). The broken line in the left inset is x=0. The metal and semiconductor cylinder regions are shaded gray and green respectively. **b** Normalized energy density along the x-axis between metal and host dielectric. The broken line in the right inset is y = -d/2. The left inset shows the FWHM of the energy density distribution in the x-direction and the normalized mode area, A_m/A_0, as a function of h. By comparing these two parameters we can see that confinement is stronger in the y-direction for large h and in the x-direction for small h. Furthermore, the near linear increase in gap energy density (reciprocal of A_m/A_0) with decreasing h is indicative of capacitive energy storage of this geometry (inset **b**).

The strong energy density in the gap region occurs for two reasons: firstly, it is directly related to the continuity of the displacement field at the material boundaries, which leads to a strong normal electric field component in the gap [19]; and secondly, in both the uncoupled SPP and

cylinder geometries, the electric field components normal to material interfaces are dominant, amplifying the first effect. Physically, this corresponds to energy storage by polarization and plasma oscillations along the semiconductor/oxide and the metal/oxide interfaces respectively; i.e. the gap region has an effective optical capacitance (Fig 3.2.3). Note that a higher contrast in dielectric permittivity contrast with optimized geometrical parameters can enhance the discontinuity of the uncoupled cylinder's radial electric field component and the hybrid mode confinement.

In order to gain a deeper physical insight we have subsequently analyzed the effective indices associated with the hybrid modes. Figure 3.2.4a depicts numerical calculations of the effective index of the hybrid mode, $n_{hyb}(d,h)$, for the same set of parameters as in Fig 3.2.2. Naturally, in the limits of cylinder-like (d > 200 and h > 10, c.f. Fig 3.2.2c) and SPP-like (d < 200 and h < 10) modes, the effective index approaches those of pure Cylinder, $n_{cyl}(d)$, or SPP, n_{spp}, modes (the black solid and broken lines respectively, Fig 3.2.4a). At the same time, the hybrid mode effective index is *always* larger than that of the underlying dielectric and SPP waveguide modes, indicating a behavior typical of a *coupled mode* system with mode "splitting" into symmetric and anti-symmetric hybrid modes [25] with effective indices, $n_{\pm}(d,h)$ (see Methods). Interestingly, the lower ('anti-symmetric') branch of the system is "cut-off" as the lower index hybrid mode cannot exist for effective indices, $n_{-}(d,h) < n_{spp}$. The high index ('symmetric') mode is the only bound solution in this geometry when a single mode uncoupled cylinder is involved. Using a coupled mode theory, we can describe the hybrid mode to a first approximation as a "superposition" of the cylinder waveguide (without the metallic region) and SPP waveguide (with no cylinder) modes,

$$\psi_{\pm}(d,h) = a_{\pm}(d,h)\psi_{cyl}(d) + b_{\pm}(d,h)\psi_{spp}, \quad (1)$$

where $a_{\pm}(d,h)$ and $b_{\pm}(d,h) = \sqrt{1 - |a_{\pm}(d,h)|^2}$ are the amplitudes of the constituent cylinder, ψ_{cyl}, and SPP, ψ_{spp}, modes respectively (see Methods). The square norm of the cylinder mode amplitude, $|a_{+}(d,h)|^2$, is a measure of the character of the hybrid mode, i.e., the degree to which the guided mode is cylinder-like (or SPP-like).

$$|a_{+}(d,h)|^2 = \frac{n_{hyb}(d,h) - n_{spp}}{(n_{hyb}(d,h) - n_{spp}) + (n_{hyb}(d,h) - n_{cyl}(d))} \quad (2)$$

In this respect, the mode is cylinder-like for $|a_{+}(d,h)|^2 > 0.5$ and SPP-like otherwise (Fig 3.2.3b). While the mode character predicts the transition between cylinder-like and SPP-like modes, it also correlates the point of strongest coupling, near $d = 200$ nm, with the minimum of both mode area and propagation distance (Fig 3.2.2). At this critical coupling diameter, d_c, the hybrid mode has equal SPP and cylinder characteristics ($|a_{+}(d_c,h)|^2 = 0.5$) corresponding to the condition $n_{cyl}(d_c) \approx n_{spp}$. We can now explain the coincidence of the critical diameter with the

maximum energy storage as a phase matching of polarization and plasma oscillations from the underlying cylinder and SPP modes respectively, which maximizes the effective capacitance. Near the critical diameter, mode areas more than two orders of magnitude ($6\times10^{-3}A_0$) smaller than the diffraction limited area of free-space, $A_0 = \lambda^2/4$, are achievable (Fig. 3.2.2b). As the gap width, $h \rightarrow 0$, we can expect the reduction in mode area to continue subject to constraints of non-local effects when h is of the order of a few atomic monolayers [28].
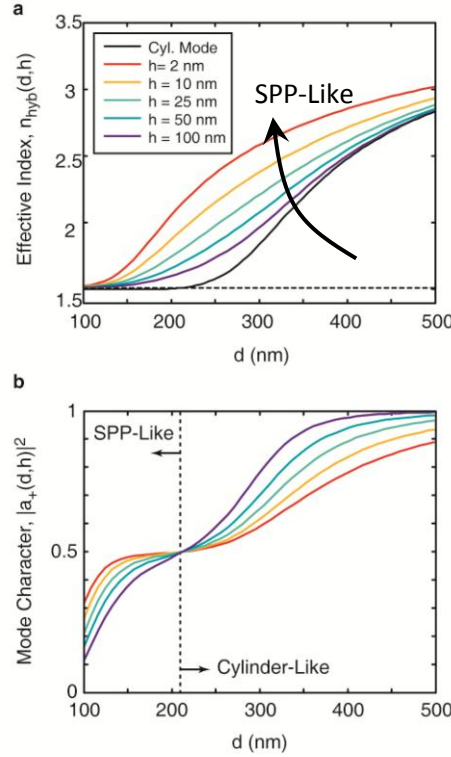
Figure 3.2.4 | The hybridization of dielectric cylinder and SPP Modes. a The effective index of the hybrid waveguide was calculated using the finite element method for gap widths of $h = 2$, 10, 25, 50, 100 nm and cylinder radii in the range $d = [100,500]$ nm (colored lines). The black solid and broken lines represent the uncoupled effective indices of the cylinder (without metallic region), $n_{cyl}(d)$ (calculated using a standard analytical approach [26]), and SPP (without cylinder), $n_{spp} = \sqrt{\varepsilon_m \varepsilon_d / (\varepsilon_m + \varepsilon_d)}$, modes respectively. The cylinder supports a single mode when $k_0 d \sqrt{\varepsilon_c - \varepsilon_d} < 2.405$ (i.e. $d < 375$ nm at $\lambda = 1550$ nm), which is the case of interest here. **b** The calculated cylinder mode character from coupled mode theory as a function of cylinder diameter, d. When $|a_+(d,h)|^2 > 0.5$ the mode is "cylinder-like" and conversely, when $|a_+(d,h)|^2 < 0.5$, the mode is "SPP-like". Maximum coupling occurs near d=200 nm where the hybrid mode consists of equal proportions of cylinder and SPP modes, i.e. $|a_+(d,h)|^2 = 0.5$. According to the coupled mode theory, this point corresponds to the condition, $n_{cyl}(d) = n_{spp}$.

The critical coupling diameter, predicted by the coupled mode theory, is physically interesting since it is invariant with gap width, h. A test of the coupled mode interpretation would be to see if such critical behavior is seen in the numerical calculations, beyond the cursory inspection of Fig 3.2.2. Indeed, Fig 3.2.5 exemplifies the invariance of the critical point by contrasting the variation with h of two waveguide diameters, $d_< = 212$ nm and $d_> = 213$ nm, which lie on either side of d_c. Here, a difference of just 1 nm determines whether the mode becomes cylinder-like or SPP-like as $h \to \infty$. The numerically estimated critical diameter (212 nm $< d_c < 213$ nm) is almost identical to the value predicted by the coupled mode theory, $d_{c,th} = 209$ nm, where the discrepancy is possibly due to the finite computational domain.
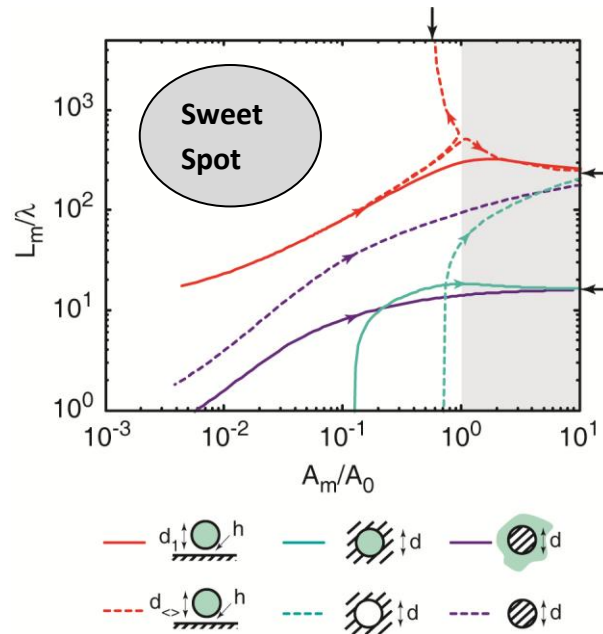
Figure 3.2.5 | Parametric plot of normalized mode area, A_m / A_0, and normalized propagation distance, L_m / λ, for the hybrid waveguide, oxide and semiconductor clad NWs [4-6] and metal clad oxide and semiconductor NWs [5-7]. Each trajectory represents a waveguide for a range of waveguide structural parameters. For the hybrid waveguide, h = [1,10^4] nm for d$_1$ = 200 nm and h = [10^2,10^4] nm for d$_>$ = 213 nm and d$_<$ = 212 nm. The small variation of just 1 nm in $d_{<>}$ illustrates the critical nature of the optimum coupling point in Fig 3.2.4a. For the other waveguides, the diameters, d = [10^1,10^4] nm are used. In all cases an arrow on a trajectory indicates the direction of increasing waveguide parameter (h for the hybrid waveguide and d for the circular waveguides).The plot area is limited to propagation lengths exceeding one wavelength and sub-wavelength mode areas. The shaded region extends these limits only to show the asymptotic behavior of the modes. The arrows on the left hand side show the asymptotic values for the propagation lengths of SPPs at Oxide/Silver and Semiconductor/Silver planar interfaces. The arrow on the top axis shows the mode area for uncoupled cylinder (without metallic region) for a diameter d$_>$.

In order to place the hybrid waveguide's performance in context, we present a parametric plot of normalized mode area versus normalized propagation distance, L_m/λ, for a range of plasmonic waveguides (Fig 3.2.5). This representation is extremely useful for comparing geometries because it is independent of a waveguide's structural parameters and retains the absolute values of L_m and A_m, overcoming the disadvantage of using a single-valued figure of merit [29]. Each trajectory in Fig 3.2.5 represents a plasmonic waveguide over the range of a structural parameter; here, we compare the hybrid waveguide with dielectric clad metal NWs [4-6] and metal clad dielectric NWs [5-7]. Waveguides with the best performance have trajectories towards the top left of the plot. Clearly, the hybrid waveguide out-performs the other geometries considered by at least an order of magnitude in propagation length for comparable mode areas. When compared to other sub-wavelength 2D plasmonic waveguides in the literature, such as Channel SPPs [8,9] the hybrid waveguide also shows superior propagation distance for the same degree of confinement.

In conclusion, we have proposed and examined a new approach to low-loss deep sub-wavelength light confinement. By controlling the hybridization of the fundamental mode of a dielectric cylinder with the SPP of a dielectric/metal interface, we can control confinement and propagation loss, naturally extending the capabilities of both underlying waveguide technologies and their associated applications. We have further shown that the new hybrid waveguide is superior to other plasmonic waveguides discussed in the literature. The potential for single mode operation in conjunction with deep sub-wavelength mode sizes and long propagation lengths suggests application to nano-scale laser devices [22,23], as well as optically integrated circuits [24]. Further studies, not included here; show that the hybrid modes of a rectangular dielectric waveguide and dielectric/metal interface demonstrate similar behavior, making this approach also amenable to Silicon on Insulator technology [30] as well as epitaxial deposition and photolithography techniques.

3.3 Demonstration of Low-Loss Waveguiding at Deep Sub-wavelength Scales

Abstract

Emerging communication applications [1] call for a road-map [2] towards nanoscale photonic components and systems with integrated functionalities [3-5]. While metal-based nanostructures theoretically offer a solution to scale down photonics to the nano-scale [6-10], the key demonstration of optical modes with deep sub-diffraction-limited confinement and significant propagation distances has not been experimentally achieved due to the trade-off between optical confinement and metallic losses. Here we report the first experimental demonstration of truly nanoscale guided waves in a metal-insulator-semiconductor device [11,12] featuring low loss and broadband operation. Nearfield scanning optical microscopy (NSOM) reveals mode sizes down to 50 x 60 nm^2 at visible and near-infrared wavelengths propagating more than 20 times the vacuum wavelength. Interference spectroscopy confirms that the optical mode hybridization between a surface plasmon and a dielectric mode concentrates the hybridized mode inside a nanometer thin gap, which is key for the long propagation of this ultra-small optical mode. This nanoscale waveguide demonstration holds promise for next generation on-chip optical communication systems that integrate light sources [13,14], modulators or switches [15,16], non-linear [17] and quantum optics [18].

Introduction

Photonics has become the key driver in global data communications. The ever growing demand for higher data bandwidth and lower power consumption [19] of photonic devices [1] has set a roadmap for reducing the physical photonic component size down to the nanoscale beyond the diffraction limit of light with integrated functionality [2]. While various compact technologies have been developed for reducing the physical size of devices, [3,8,15,16], strong optical mode confinement offers enhanced light matter interactions [6,15-17] towards low driving power and fast modulation speeds [15,16,20]. Optical confinement in conventional photonic components is restricted by the diffraction limit of the light resulting in weak light-matter interaction that often demands long device sizes to achieve an effect. For example ring resonators [4] and Fabry-Perots [20] often require large cavity lengths of 10 - 1000 microns leading to relatively large footprints, thermal instabilities [6] and high bending induced radiation losses upon downscaling ring resonators [21]. Surface plasmon polaritons (SPPs) [6], collective oscillations of electrons at metal-dielectric interfaces, were proposed as a potential solution for nanoscale photonics since their wavelength can be scaled down below diffraction limit [6-8,22]. However, the direct experimental demonstration of low-loss propagation of deep sub-wavelength optical modes has not been realized due to the rapid increase in the optical mode's propagation loss upon scaling down the optical mode, which pushes the electromagnetic field into the metal [8-10,22-25]. As a result, the use of plasmonics for integrated photonics, in particular for optical interconnects, remains uncertain.

A hybrid plasmon polariton concept has been proposed to overcome this challenge [11,26]. This approach uses a high dielectric constant semiconductor strip separated from a metal surface by a nanoscale low dielectric constant gap. Since the hybridized plasmon energy is concentrated in

the low loss gap, this novel method offers ultra-small mode confinement ($\lambda^2/400$) over a broad range of frequencies and simultaneously allows for reduced optical loss compared to a metal-semiconductor interface design [11]. The physical origin of this quasi-TM highly-confined mode stems from the continuity requirement of the vertical component of electric displacement (D_y) at the high-index contrast interfaces between the high-index material (e.g. semiconductor), the low-index gap region and plasmonic metal.

Results

By utilizing semiconductor and metallic structures in an integrated design, here we report the first observation of long-propagating optical waveguiding revealing mode sizes significantly below the diffraction limit of light visualized by apertureless near-field scanning optical microscopy (a-NSOM) (Fig. 3.3.1a) (see methods). Moreover, unlike other non-resonant plasmonic designs [10,22-25], this HPP concept features both ultra strong optical confinement over a broad wavelength range ($\lambda = 633$ nm $- 1.43$ μm) and relatively low metal losses with propagation distances exceeding 20 times its free space wavelength at near infrared, making it promising candidate for nano-photonics [2]. The measured optical mode sizes down to 53 x 63 nm^2 are in excellent agreement with theoretical simulations. To visualize the extremely small scales of the HPP mode distribution we fabricated HPP-based strips with lateral dimensions of about 200 nm in height, *H*, with varying width, *W* (150 − 800 nm). Figure 3.3.1b shows a topological AFM scan with the shown region being close to the diffraction limit of light around the output of such a strip superimposed with the NSOM image acquired simultaneously at an illumination wavelength of 633 nm. It can be seen that the optical confinement is indeed as small as about 50 nm (Full Width at Half Maximum, FWHM) and is situated at the dielectric constant gap region directly confirming the HPP mode.

The HPP strips are excited by illuminating a metal slit at the input (IN) end of the strip (inset of Fig 3.3.1b) from the substrate side with polarization perpendicular to the slit. Since our nearfield imaging technique is most sensitive to electric fields along the axis of the NSOM detection tip, the z-component of the HPP mode is imaged, which is expected to be strongest in the gap region. To gain access to the internal fields, we sliced the strip open (Fig 3.3.1b) allowing the NSOM tip to probe the HPP mode's cross-section directly (see methods). When the polarization of illumination is parallel to the metal slit, HPP modes are not excited in the strip and only a background signal was measured by the NSOM (see below).
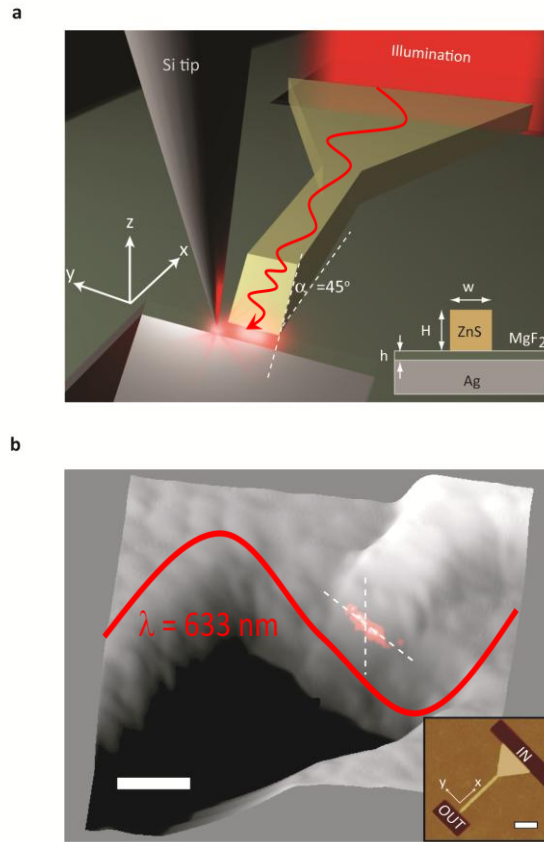
Figure 3.3.1 | HPP mode mapping via near-field scanning optical microscopy (NSOM). a, Schematic of HPP mode size mapping via apertureless NSOM. The HPP strips consist of a semiconductor strip separated from a metallic surface by a nanometer scale low dielectric constant gap and are excited by illuminating a metal slit at the input end. **b**, 3-D image overlap of the deep sub-wavelength HPP mode signal (red spot) offering optical confinement significantly below the diffraction limit of light. This degree of optical confinement indicates the devices' potential to create strong light-matter-interaction for compact and highly functional photonic components. Scale bar = 125 nm. MgF_2 gap $h = 10$ nm, illumination wavelength $\lambda = 633$ nm. Inset: height profile of tapered strip for free-space to HPP strip coupling, scale bar = 1 μm. Focused ion beam (FIB) etching was used to define the illumination-port (IN) and the access point for the NSOM probe of the confined optical mode (OUT) (see methods for fabrication details).

We have compared line-scans of the NSOM field image (broken white lines in Fig 3.3.1b) with numerical simulations. Taking into account the HPP mode's field diffraction along the z-direction, we were able to correlate experiment and theory well at tip-sample separations of about 10 nm (Fig 3.3.2a). A similar correlation is found for the mode-width data along the y-

direction. The optical mode confinement in the y-direction is controllable by the lateral HPP strip width, W, with the smallest measured mode area, $A_{HPP} = 53$ nm x 63 nm, proving a non-resonant, deep sub-wavelength ($<\lambda /10$, $\lambda = 633$ nm) nano-scale mode. Fig 3.3.2b summarizes this property by comparing the FWHM of the HPP mode for varying HPP strip widths. Whereas the mode height in the z-direction remains essentially constant, the mode width follows the strip width. While deep sub-wavelength mode sizes are expected in the z-direction due to the involvement of surface plasmons, lateral confinement can also be strongly sub-wavelength. This arises from the accumulation of polarization surface charges concentrated around the center (y-direction) of the HPP strip [11] (see below). We have chosen to use FWHM as a measure of the mode size as it is representative of where the majority of a mode's power resides. This is particularly relevant to active applications of plasmonics, where interest resolves around achieving high peak field intensities within waveguides. We note that this measure can underestimate the mode size in some plasmonic waveguide systems that involve sharp metal corners or large changes in permittivity [12]. However, in our experiments, diffraction of the confined mode into free space and the point spread function of the NSOM tip smooth out the mode's sharp features making the FWHM a fair representation of where the majority of the mode's power resides. Furthermore, we find the hybrid plasmon mode's confinement to be relatively insensitive to the illumination wavelength [11]. We demonstrate this broadband feature by illuminating the HPP strips with visible and near-infrared light ($\lambda = 633$, 808 and 1427 nm) and find that the vertical mode confinement remains essentially constant at about 50 ~ 60 nm (Fig 3.3.2c). Since the chosen HPP strip height, H, is purposely kept constant thorough all experiments, a subtle mode height increase is expected for changing the illumination wavelength from visible to near-infrared. The confinement of the mode width is also deep sub-wavelength with $\lambda/12$ and $\lambda/7$ for visible and near-infrared wavelengths, respectively, (Fig 3.3.2d). These remarkably small mode sizes are among the smallest for propagating electromagnetic waves demonstrated to date and consequently facilitate reduced waveguide cross-talk (see below).
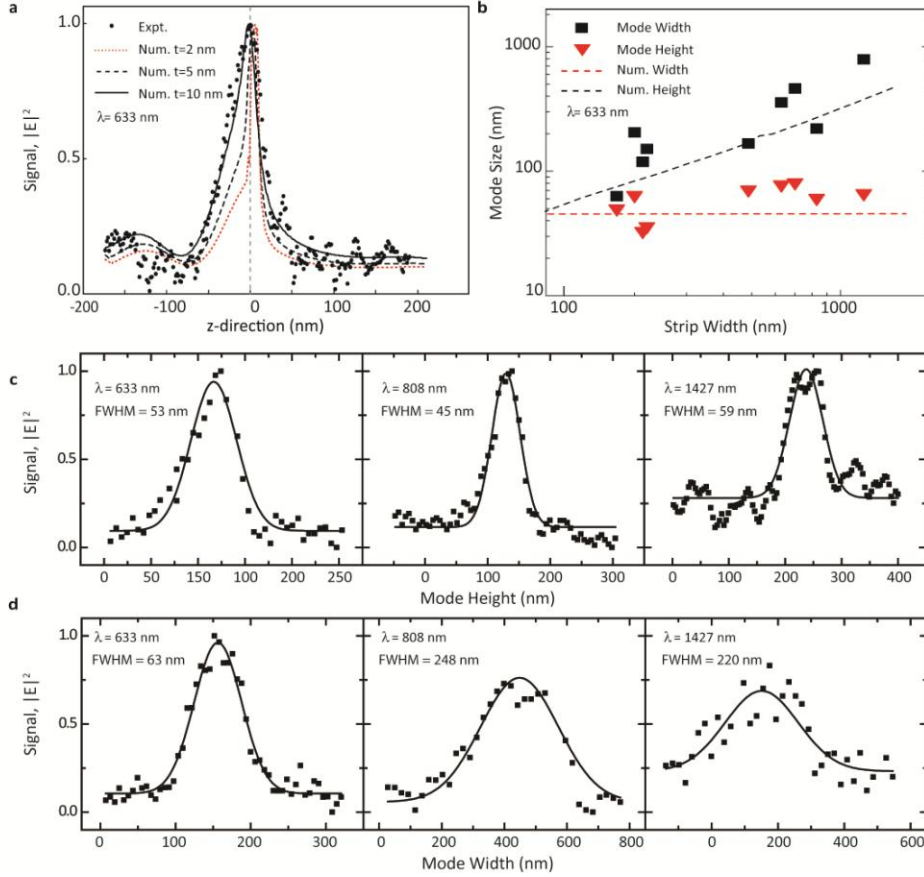
Figure 3.3.2 | HPP mode confinement. a, Experimental field intensity of the HPP mode compared to different tip-sample separations, *t*, from its exiting point. The optical mode height of FWHM$_z$ = 53 nm is deep sub-wavelength for λ = 633 nm, HPP strip dimensions *H* = 230 nm *W* = 174 nm. Note the NSOM operates in tapping-mode having an average separation of *t* = 10 nm, and the simulated mode profile at this distance agrees well with the NSOM result. **b**, Summary of experimental HPP mode dimensions yielding the smallest measured mode area of 53 nm × 63 nm, at λ = 633 nm. The good agreement between experimental data and theoretical simulations (dashed lines) confirms that the optical HPP mode is indeed squeezed into the low dielectric constant gap: the mode height is independent on the strip width (triangles), while the mode width is scaling with the strip width (squares). **c** and **d**, Line scans of the mode height and width, respectively, for wavelengths of the illumination beam of 633 nm, 808 nm and 1427 nm feature broadband, deep sub-wavelength operation of HPP-based devices. The FWHM (solid line) are Gaussian fits to binned data, yielding measured mode areas of λ^2/120, λ^2/59 and λ^2/157, which are deep sub-wavelength modes for all three wavelengths, respectively. Since the strip height, *H*, is optimized for 633 nm, a slightly larger mode height for longer excitation wavelengths is expected.

In addition to providing strong optical confinement, another advantage of the HPP mode, over other non-resonant plasmonic schemes [9,10,24], is reduced optical loss by allocating most of the

optical energy in the dielectric gap instead of inside the metal. We have measured the transmission through HPP strips of varying length under white light illumination (Fig 3.3.3a). The sub-wavelength confined HPP mode propagates more than 10 times its vacuum wavelength at visible wavelengths near 633 nm, which is more than six times further than plasmonic control strips consisting of a metal-semiconductor interface without the low index gap region (Fig 3.3.3b). The propagation length increases with the wavelength, and exceeds 20 times its vacuum wavelength at near infrared (Inset Fig 3.3.3), thus allowing for sufficiently long interaction lengths, which, combined with strong optical confinement, can create strong light-matter-interaction effects for active photonic components [15-17].

In order to gain full insight into the HPP mode physics, we also investigated the mode speed, namely the group index, n_g. The abrupt change in the effective refractive index at the end of the HPP strip acts as a partial reflector for the HPP modes. The resulting optical cavity displays Fabry-Perot interference fringes, corresponding to longitudinal cavity modes. The group index can be determined from the spectral mode spacing, $\Delta\lambda = \left(\lambda^2/2n_g L\right)$, where L is the strip length, λ the wavelength, $n_g = n - dn/d\lambda$ the group index and n is the effective mode index. The increasing group index with photon energy confirms the dispersive, plasmonic mode character of the HPP mode, which manifests itself in the deep sub-wavelength confinement (Fig 3.3.3c). In contrast, an effective mode group index close to one of other SPP-based designs indicates, that most of the field sits outside the metal, thus showing only weak optical confinement [23]. The dispersion of the HPP relation lies between the two extreme cases of gap width, h: namely, a semiconductor strip ($h \rightarrow \infty$) and a semiconductor strip in direct contact with the silver film ($h \rightarrow 0$). This demonstrates controlled hybridization of the modes of a semiconductor strip and a metal-dielectric interface.

Discussion

Plasmonic waveguides can be deployed in two distinct application areas [8]; (1) routing information passively [8-10, 22-25] and (2) actively altering optical signals [15-17]. For the latter, the optical confinement can strengthen light-matter-interactions, thereby reducing the required devices size to utilize a certain effect (e.g. a 2nd, 3rd order non-linearity). Thus, metal optics can produce ultra compact components where propagation distances of the HPP mode are sufficient. The trade-off between enhancing the effect (mode confinement) and the incurred loss form a metric, $(\lambda_0^2/4A_m)exp\left(-\lambda_0/L_p\right)$, where the first term is the device mode area, A_m, normalized by the diffraction limit $(\lambda_0/2)^2$, and the exponential function measures the loss over a given device length in multiples of the wavelength. Applying this metric we find a value of 27 for the HPP strips at $\lambda_0 = 633$ nm. This is about one order of magnitude higher than those of other non-resonant plasmonic light guiding geometries, such as: channel plasmon polaritons [23] metal-insulator-metal (MIM) [24], wedge-plasmon-polariton (WPP) [25] and metal strips [22]. Remarkably, the HPP mode's FOM also outperforms established platforms like silicon-on-insulator (SOI) [27] by a factor of four (see below). In addition, the integration of HPP–based photonics with semiconductor technology is straightforward by placing a metal strip over the semiconductor waveguide, where the optical confinement can be conveniently tuned by varying the low dielectric constant gap thickness.
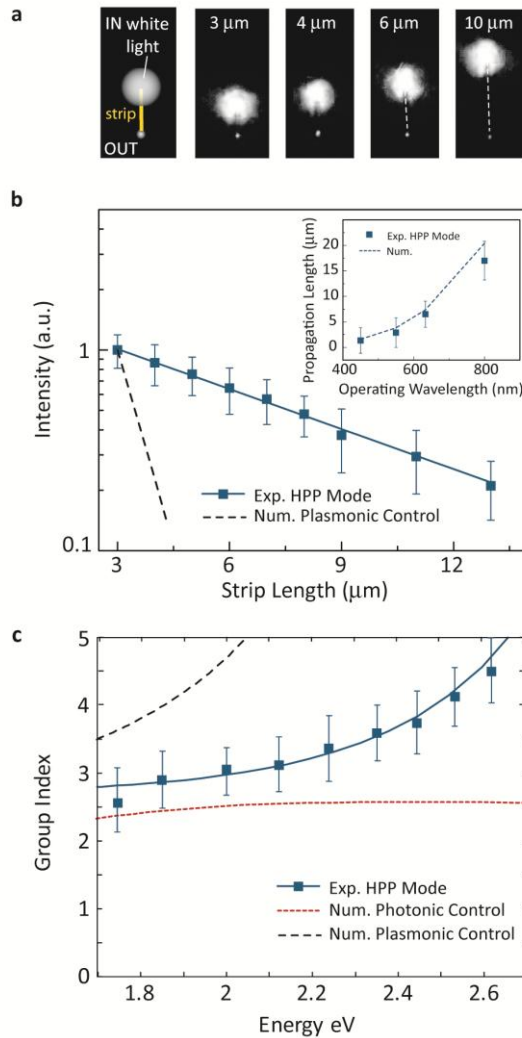
Figure 3.3.3 | HPP mode propagation length and mode speed. a, Far field images of illuminated HPP strips showing incident white light reflected from the strip input and the corresponding emission from the distal strip output facet. The strips lengths, *L*, are indicated on top of each image and dashed lines are a guide the eye to the output signal. **b**, The HPP mode offers propagation lengths of more than 10 times its free space wavelength at $\lambda = 633$ nm. Without the dielectric constant gap-layer (plasmonic control) the propagation length is only about 1 µm (black dashed line). Inset: the HPP mode's propagation length increases with its operating wavelength and exceeds 20 times its vacuum wavelength at near infrared wavelength ($\lambda = 800$ nm). The data are in good agreement with the expected trend from numerical calculations (see methods). **c** HPP mode group index vs. photon energy. Analysis of the HPP strip's transmission spectra, i.e. Fabry-Perot-Interference for a range of strip lengths yields a dispersive group index of the HPP mode falling between the two extreme cases, i.e. photonic (without metal) and plasmonic control confirming the hybrid nature of the HPP mode.

We directly demonstrated waveguiding of ultra-small propagating waves [11] at visible and near infrared frequencies via NSOM imaging. We confirm the appropriate optical field hybridization between a surface plasmon and a dielectric mode by Fabry-Perot interference spectroscopy and find a dispersive group index as a result. This HPP concept has reduced ohmic losses offering reasonably long light-matter interaction lengths, potentially enabling compact and efficient nano-scale photonic components, since it elegantly interfaces plasmonics with semiconductors. This novel mode design holds a great potential for truly nanoscale photonic applications such as intra-chip optical communication [19], signal modulation [15-17], nanoscale lasers [13] and bio-sensing [28].

Experimental Methods

Lithographically defined hybrid plasmon mode strips are prepared by evaporating a high index semiconductor, ZnS, $n = 2.2$ onto an Ag film separated by a thin, $h = 10$ nm, MgF_2 film, both on a quartz substrate followed by lift off in Acetone. The root-mean-square (RMS) of the Ag film roughness is about 1.0 - 1.5 nm, measured via atomic-force-microscopy (AFM). The strip input was chosen to be tapered in order to act as an optical funnel to increase the signal strength and to reduce the impedance mismatch between free space and the HPP mode (Inset. Fig. 3.3.1b). Focused-ion-beam (FIB) milling creates the input and the 45 degree angled output port to enable the scanning NSOM tip to access the HPP mode's field profile. HPP strip illumination for the NSOM experiments is achieved by focusing a laser beam from the sample backside (Quartz) with the following wavelengths: a He-Ne laser at $\lambda = 633$ nm and two solid state diode-lasers at 808 nm and 1427 nm wavelength, respectively (Fig. 3.3.1a). For the mode decay length and speed measurements a white light (Xe lamp, 150W) illuminates the HPP strip in a reflection mode. The signal to noise ratio was increased by placing an aperture in the secondary plane of the image, i.e. over the end of the strip. The transmitted signal is then collected by an objective lens (100X, NA = 0.9), sent to a spectrometer and recorded by a N_2-cooled CCD camera. All measurements were carried out at room temperature. The mode's decay length is measured by the change in the absolute intensity with the variation of the strip length. The experimental results from Fig. 3.3.3b are in good agreement with that obtained by simulation. Data from ref. [29] were used for the wavelength dependent propagation length calculation showing good agreement with the experimental results (Fig. 3.3.3b). In earlier work we found that the permittivity values from Johnson & Christy were overestimations by about 40 % [30], which, together with additional scattering losses, could explain the small difference between experiment and simulation results. For the group index extraction from the measurement data, the Drude-model was employed with the following parameters; the refractive indexes for air, Zinc Sulphide and Magnesium Floride were 1, 2.2 and 1.4, respectively; for Silver we used ε_{Ag} ($\lambda = 600$ nm) = -16.10 - 0.44i [29].

Optical Setups & Measurements

Two different measurement setups were chosen for the near field hybrid plasmon mode (HPP) [1] mode size mapping (Fig. 2.3.4a) and the mode speed and mode decay length tests (Fig.

2.3.4b). For the near-field measurement, we use a home-built scattering type near-field scanning optical microscope (s-NSOM) to map the electric field distribution near the output slit. The basic principle is utilizing a sharp tip in close proximity to a surface to scatter the near-field information of high spatial frequencies into propagating waves. The tapping-demodulation technique is used to differentiate the detected far-field and near-field signals. By assigning the retrieved near-field strength to each point, a full near-field mapping could be compiled. In our setup, a commercial AFM scanner (Veeco, Bioscope) is used to hold and actuate a scattering probe (Fig. 2.3.4a). In addition, a piezo stack on the AFM probe holder drives the cantilevers of AFM probes in the tapping mode, which oscillates at a resonant frequency of about 300 kHz. To launch the HPP mode, a series of laser diodes is focused at the input port of the HPP strip (see inset Fig. 2.3.4b main text) through an objective (Nikon CFI Plan Fluor ELWD DM, 40x, NA = 0.60). The wavelength is chosen to be 633 nm, 808 nm and 1427 nm in order to demonstrate the broadband performances of the HPP mode. When the probe approaches the near-field region of the output port, the light scattered from the sharp tip is collected and collimated to form a signal beam by an aspheric collection lens (Newfocus 5726H, NA = 0.16), which has been aligned to focus exactly at the apex of s-NSOM probe. A polarizer selects the E_z-component of the near-field scattered from the tip. Finally, the collected light is sent into an APD detector.
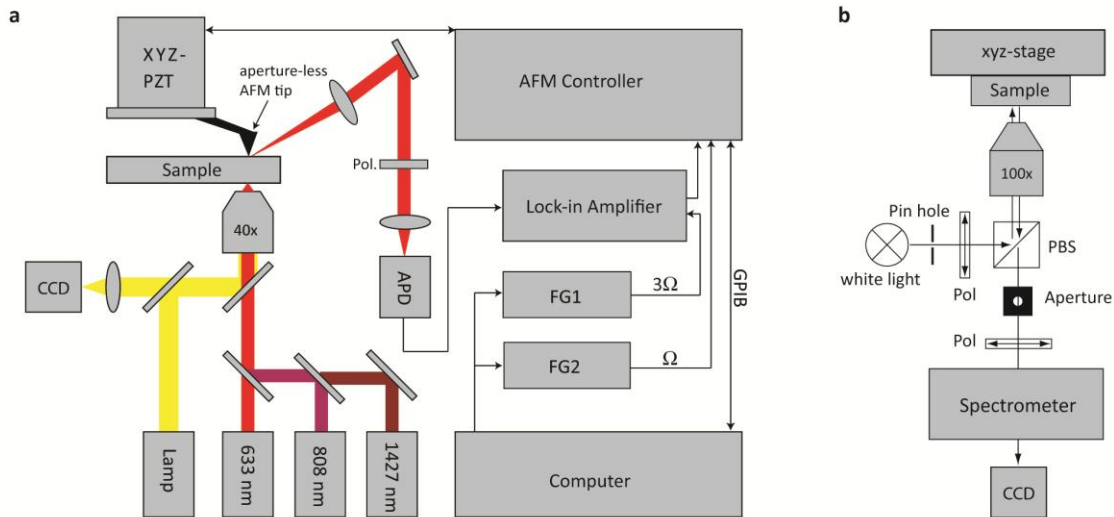
Figure 3.3.4 | The measurement setups. a The NSOM setup utilizes the Silicon tip of an atomic force microscope (AFM), multi wavelength laser sources and Lock-in amplifier for increased signal-to-noise ratios. **b** For the mode speed and propagation length analysis, a reflection mode setup is utilized, featuring, Polarization control, an high NA objective lens (NA = 0.9), a spectrometer with a liquid N_2-cooled CCD camera.

Compared to the far-field, the near-field signal close to the surface has a fast exponential decaying trend due to its evanescent origin. Hence, the Fourier transform of collected near-field signal has many higher harmonic components (n_Ω, with n = 2, 3, 4…) under the sinusoidal modulation from the tapping mode (Ω). By locking in the signal at a high harmonic frequency (n = 3 for all the measurements here), we are able to retrieve the near-field strength of high fidelity.

In our setup, two function generators (FG1 and FG2 in Figure 2.3.41a, Stanford Research Systems, DS345) are used, respectively, to control the vibration frequency and generate the frequency n_Ω for the reference signal of the Lock-in amplifier (Stanford Research Systems, SR844). After the demodulation process, a near-field image of the sample can be reconstructed together with the topography mapping from the AFM system. Note, unlike the conventional metal AFM tip of the NSOM, here a Silicon tip was used to ensure low parasitic field-tip enhancements and measurements artifacts.

A modified reflection mode microscope (Fig. 2.3.4b) was used to characterize the propagation length and mode speed character of the HPP strips. Illumination was done by a white light source (Xe lamp, 150 W) polarized parallel (p-pol) to the HPP strip and focused onto the end of the strip via an objective lens (100x, NA = 0.9). The sharp corners of the strip providing k-vectors beyond the light come facilitate coupling into the HPP mode. An aperture was placed in a secondary object plane at the other end of the strip in order to only collect the propagated signal. The signal was recorded using a spectrometer with a liquid Nitrogen cooled CCD detector with a spectral resolution of 0.3 nm.

HPP Mode Width

The HPP does not only provide strong confinement in the vertical (z-direction), but also laterally (y-direction) as shown in the main text. The plasmonic metal loss and confinement of the HPP mode is not exclusively determined by the field intensity distribution, but rather by the interaction of the surface polarization charge with the metal film. This polarization charge density is not uniformly distributed inside the low dielectric constant gap, but has a maximum at the center (y = 0 nm) of the HPP strip and is weak at the corners (Fig. 2.3.5a). As a result the HPP mode size is deep sub-wavelength in the y-direction. Indeed our experimental results confirm this feature yielding a HPP mode width of $FWHM_y$ = 63 nm, which is deep sub-wavelength ($\lambda/10$) for an operating wavelength of 633 nm (Fig. 2.3.5d, main text). This polarization charge density distribution leads to the sub-wavelength field distribution of the HPP mode as shown in Fig. 2.3.5b).
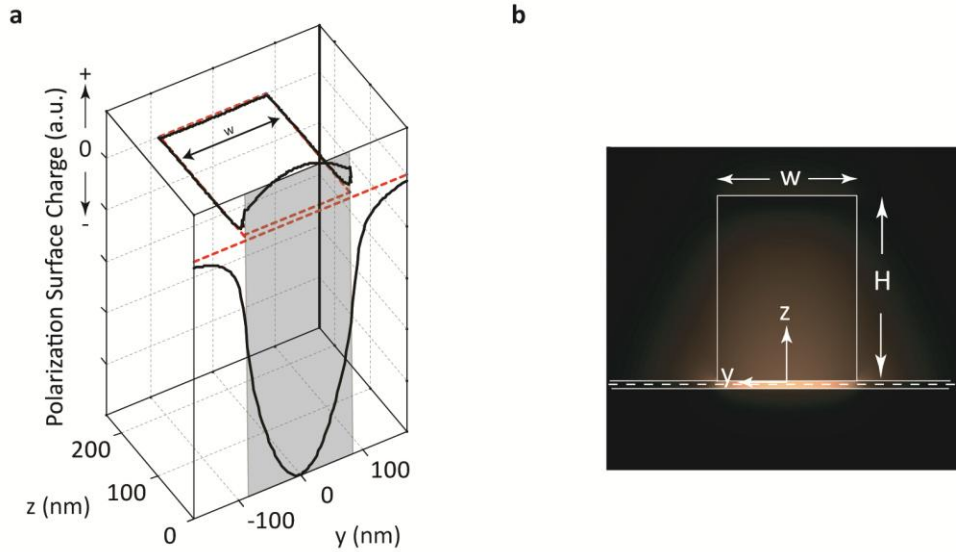
Figure 3.3.5 | Polarization charge and HPP mode width. a, Polarization charge accumulates only at the dielectric boundaries causing an optical energy storage inside the HPP mode. The charge density is strongest in the center of the waveguide (y = 0 nm) and weaker at the corners, thus providing strong confinement of the HPP mode in the y-direction (Simulation). **b,** |E|-field slice through the strip, z-y-plane, (FEM simulation).

Hybrid plasmonic waveguide cross-talk

While hybrid plasmonic waveguides provide scope for compact optical modes, they also have the potential to increase the density of photonic components. The packing density of photonic components is limited by waveguide crosstalk. Hybrid plasmonic waveguides experience reduced cross talk due to their strong confinement. For example Figure 3.3.6 shows the coupling length of 50% energy transfer between two identical hybrid plasmonic waveguides. For comparison, the coupling length for two dielectric waveguides of the same diameter is also shown. These calculations were carried out at the telecommunications wavelength of 1,500 nm. The coupling length between the hybrid plasmonic waveguides is much larger than the dielectric case, suggesting a clear reduction in cross-talk for closely spaced waveguides.

Cross-talk for hybrid plasmonic waveguides can be considerably smaller than what is possible without the metal substrate. Comparing the HPP mode to a photonic mode, we find more than an order of magnitude higher coupling length for the HPP mode for waveguide separations of 250 nm (λ = 1.5 um and high-ε diameter = 250 nm). Note that at this point the HPP coupling length and propagation length are almost equal. We also note that optimal HPP confinement occurs for <200 nm width; here the core width increased is deliberately increased to give the photonic waveguide a chance. At optimal confinement, waveguides could be packed with less space between waveguide cores that their actual width, leading to at least 4 side-by-side waveguides

per wavelength. Furthermore, it is also possible to adjust the aspect ratio of the hybrid plasmon waveguides and maintain confinement. In this way we can increase the packing density by reducing the lateral width, but we must compensate by increasing the waveguide height to ensure optimal coupling. While the FWHM mode measure can be an improper measure of mode field distributions with sharp metal corners, it was not found relevant when considering crosstalk.
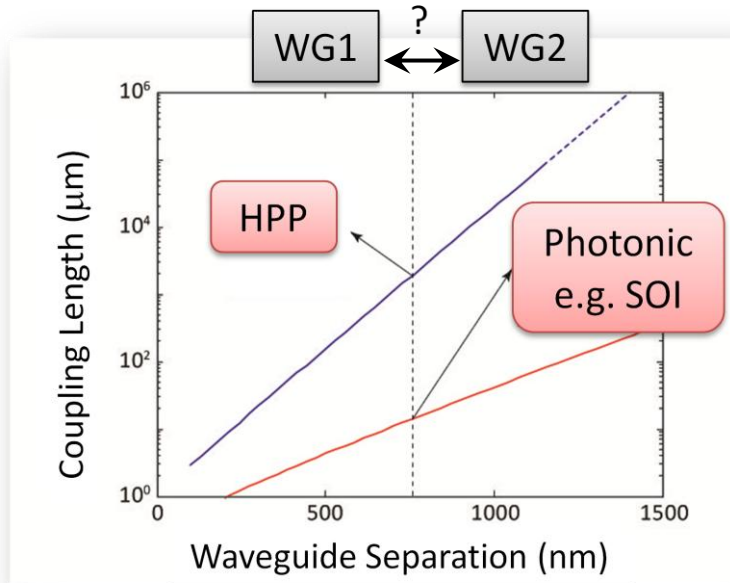
Figure 3.3.6 | The coupling lengths between identical waveguides – HPP vs. Dielectric Waveguides. The refractive indices are: 3.5 for the waveguide cores; 1 for the cladding region; and Johnson & Christy's Silver data [29] was used for the metal substrate. The calculations were performed at a wavelength of 1,500 nm. The solid blue line shows the coupling length between two identical hybrid plasmonic waveguides of size 250x250 nm^2 with a gap of 5 nm from the metal substrate. The solid red line shows the coupling length between two identical dielectric (core = Si) waveguides, without the metallic substrate. The symmetric and asymmetric fields in these two cases are shown as insets. The much weaker field overlaps between nearby hybrid plasmon waveguides leads to a much longer coupling length and greatly reduced cross-talk in this type of waveguide.

4. Plasmonic Nanolasers

4.1 Introduction

Scientific History: Challenges and Opportunities

With the breakthrough demonstration of the first maser and laser devices about 50 years ago an entire new era of science and engineering was born [1]. Since those initial proof-of-concept demonstrations of amplification of stimulated emission, the rich laser physics has been studied with passion. Since then, laser devices have been refined and tailored towards serving as scientific, engineering and even industrial manufacturing tools [2,3]. In certain industries, like the fiber-optical network defining the back-bone of today's world wide web, laser devices are the work horses for sending and routing optical encoded information around the globe [4]. As we will discuss at the end of this chapter, with the exponentially fast growing data demand of the internet, it seems that there is a bright future for laser technology [5,6].

Looking back in time and we do observe a trend leading towards smaller and smaller device sizes. This trend, not unlike to the one from the electronics industry [7] spans from meter size devices initially down to tens of micrometers in the mid 1990's (Figure 4.1.1). Laser physics now dictates, that with shrinking laser cavity (resonator) length and gain (for amplification) volume, that the cavity feedback mechanism, namely the optical mirrors must increase their reflectivity if the same laser threshold power is to be maintained. For instance, Vertical Cavity Surface Emitting Laser (VCSEL) devices already have an extremely high mirror reflectivity, R, approaching 99 - 100% utilizing effective distributed feedback (DBR) mirrors [8]. Leaving aside the question of why, if this scaling trend was suppose to continue it became obvious, that the classical approach of improving the laser cavity mirror quality would not suffice. Fundamental questions arose of whether it might even be possible to shrink a laser below a typical VCSEL size, which was already only tens of micrometer in diameter, let alone to a device of truly nanoscale dimensions with a sub-wavelength mode size. Faced with this challenge, researchers were tasked to explore fundamentally novel approaches in pursing to the smallest lasers ever made.

Before we go further, let us briefly establish the framework for general laser components and what design tasks this implies for Nanolaser devices (Fig. 4.1.2). Starting from the internal mechanism of stimulated emission, the minimum of a 2-level electronic system (e.g. the semiconductor band-gap) is required, provided by the gain material. The required population inversion of electrical carriers can be achieved by either optically or electrically exciting electrons from the lower to the upper level. With increasing photon density inside the laser cavity, stimulated emission events become dominant over spontaneous emission. With a good optical mirror reflectivity the laser cavity provides sufficient feedback, whereas the high density of states of the gain material allows for a high photon density probability, such that the sum of the optical losses can be overcome and lasing operation is possible. Turning the focus back to Nanolasers, design challenges not only limited to the cavity size alone which has to support a

sub-wavelength scale optical mode, but also the feedback mechanism has to be addressed as well as considerations of how to pump the device, what materials are suitable from an optical, electrical and integration point of view. En bloc, the realization of a Nanolaser per se requires a very integrated and 'smart' design, since the design window yielding to photonic, electronic and material demands is quite small.
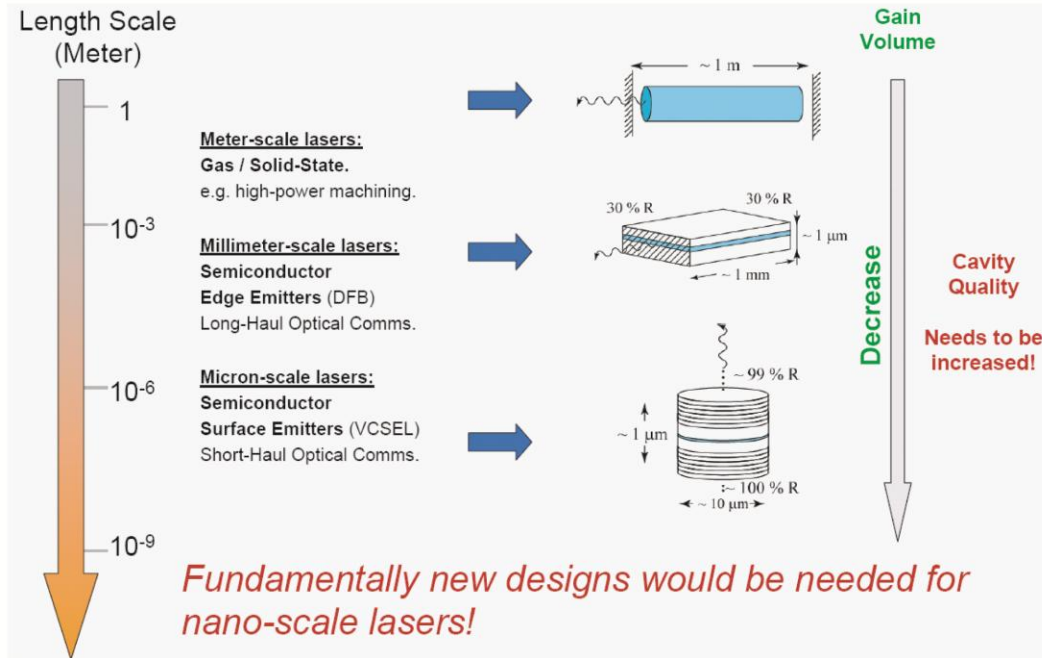
Figure 4.1.1 | Laser length and gain volume down-scaling. As the laser cavity length shrinks the common approach was to increase the photon lifetime inside the cavity, i.e. the quality-factor. However, since the cavity mirror reflectivities for tens of micrometer large VCSELS is within 1% from unity, fundamentally novel approaches must be deployed if further laser shrinking into the sub-wavelength nanoscale regime is to be achieved.

Going back to the discussion of the laser scaling trend (Fig. 4.1.1), we thus far have not talked about the motivation and benefit from scaling laser devices. From the quantum mechanical potential well problem we know, that the number of eigenmodes of such a system depends on the length of the well. Similarly, the laser cavity features a number of potential lasing modes given by $L_c = m\,\pi/2n$, where L_c is the cavity length, n the effective mode index and m and integer counting the mode number. Thus, if the cavity length is short, the number of possible lasing modes decreases, which in term reduces the required threshold power, since the supplied energy or available photon density is efficiently directed towards one mode only and has not to be shared with other potential lasing modes. Note, that in three dimensions the length, L_c, will be a volume. Within this context, a particular goal in laser physics was to demonstrate single mode operation [9]. Such attempts hint already to what we will be discussion in the next chapter 4.4 in detail, namely optimizing and increasing the so called spontaneous emission factor, β [10,11]. The β-factor relates to the fraction of the lasing mode emission to the sum of all available lasing

modes inside the cavity. In other words, increasing the β-factor reduces the number of possible lasing modes leading to an increased pump-laser threshold efficiency.
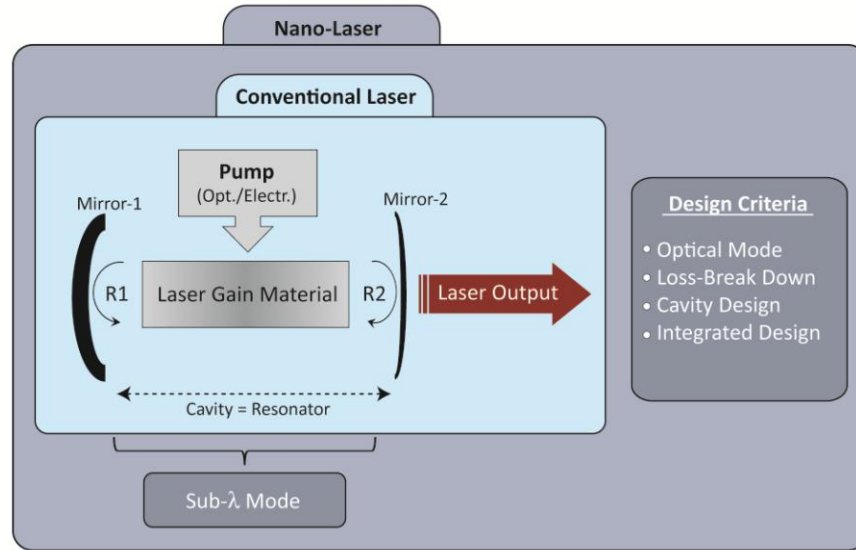

Figure 4.1.2 | Laser Ingredients: Conventional vs. Nano-scale Design. The small cavity length and mode size requires a 'smart' design since the design window (threshold, size, materials, etc) for Nanolasers is very limited.

Yet, the question remained, since single mode lasers have already been demonstrated, why should one attempt to decrease the size of a laser even further? And more, what are the hurdles in doing so and would there be any benefits from it? While we restrict us from giving a hard answer at this point, we encourage the reader to continue reading, since we will try to answer this important underlying question throughout the article. In order to highlight the challenges associated with Nanolaser demonstrations, let us take a look, per exemplum, at the optical loss situation for small laser devices. In general, we know that lasing operation starts at the point where all losses are compensated. A particular loss channel, namely the mirror loss, scales inversely with cavity length, and reaches 10^4 cm^{-1} for a cavity length of 'only' 1 μm, which is not even below the diffraction limit in air for visible frequencies, not to mention higher index materials like semiconductors. Such losses are order of magnitude larger than for conventional lasers. In addition to the mirror losses, there are other loss channels like scattering or quenching, which worsen the situation. Thus with the goal of realizing a Nanolaser, how can one overcome or mitigate these high losses? As previously discussed, since increasing the cavity Q-factor was not an option, a possible answer was seen in increasing the optical confinement, in particular utilizing metal optics or surface plasmon polaritons (SPPs) [12]. While plasmonic cavities can address the mirror loss situation via optically squeezing the lasing mode, they also infer additional loss channels due to metal quenching [9,11,13]. On the other hand the lasing threshold also depends on the overlap of the optical mode inside the cavity with the spatial area where the

gain material resides, which is quantified by the overlap factor, Γ. In typical quantum well laser designs for instance, Γ is on the order of a few percent per quantum well, which lead laser designers to stack many of these well to increase Γ, so called Multiple-quantum well lasers (MQW) [MQW]. Optimizing Γ for a Nanolaser system offers a promising path since the optical mode is spatially quite localized [9,11-13].

One of the first Nanolaser designs was a proposal by Bergman et al., where a laser device was proposed that utilized coherent amplification of localized SPPs [12]. Key point was that the localization of the optical mode can lead to overcome the low feedback system of the lossy metal. The demonstrations of the spaser concept many years after the first spaser proposal indeed showed that it is possible to realize such novel laser concept. With the ultra small optical cavity size, came another advantage of Nanolasers; the ratio of the cavity lifetime (cavity quality) and the cavity volume quantifies the enhancement of the spontaneous emission rate of the pumped gain medium. In other words, a reasonable Q-factor cavity with an ultra small mode volume enhances the spontaneous emission rate, also known as the Purcell Effect [14]. Detailed analysis of this effect in plasmonic Nanolaser systems predicts ultra fast direct laser modulation capabilities ranging into the THz regime, far exceeding conventional systems [15]. Now that we have established a framework of why investing nanoscale laser sources might be appealing, let us look into the differences in laser characteristics of conventional, lasers large or at least with diffraction limited cavity sizes versus Nanolasers, which could be also plasmonic based. Generally the spectral linewidth of a laser collapse upon transitioning from spontaneous emission to lasing (Fig. 4.1.3a). The characteristic 'kink' in the light output vs. pump input graph, however, vanishes with increasing mode selection or β-factor (Fig. 4.1.3b). Thus, the typically expected laser behavior could be smeared out during the experimental tests. Interestingly with the β-factor approaching unity no 'kink' would be observed, which could be referred to as a thresholdless laser [10,11]. The term "thresholdless", however, is somewhat misleading, as the internal aser processes are indeed still quite distinct between the low and high pumping regime, which can be clearly shown in auto-correlation (g^2) measurements.

Thus, key to demonstrating down-scaling laser devices beyond the diffraction limit can be achieved via increasing the optical confinement. The resulting implications are that the fundamental light-matter interaction, i.e. the engine driving the laser, can be engineered and strengthened towards providing viable paths towards actual Nanolaser device demonstrations. The resulting architectures are able to provide unprecedented laser physics in two domains: time and space.
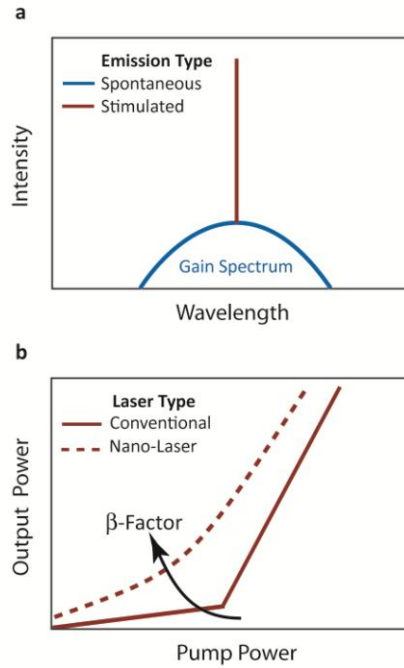
Figure 4.1.3 | Nanolaser Characteristics. a, Typical Laser spectral characteristics; the broad spontaneous emission for low pump power collapses into a narrow line upon crossing the laser threshold pump power. **b**, L-I curve for Conventional (i.e. diffraction Limited) vs. Nano-Lasers. While a large cavity size conventional Laser has a many optical mode the Nano-Laser, due to its small cavity volume, has a reduced number of optical modes, thus a high spontaneous emission factor, β. The elsewise characteristic 'kink' in the L-I diagram is smeared-out in for the Nano-Laser case [11].

Nanolaser Device Landscape

There are already quite a number of papers published on metallic Nanolaser devices including metal-coated photonic laser and plasmon laser (Table 4.1.1), which we will review in the following section.

Metal-coated Photonic laser
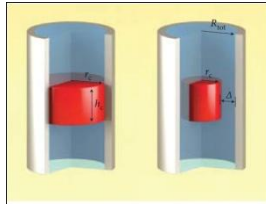
Plasmon laser

Metal-coated disc [16]

Hybrid Nanowire [11]

Particle Spaser [17]

MIM laser [18]

Nano-patch laser [19]
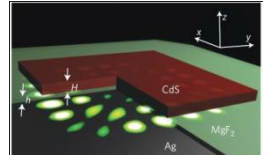
Square [9]
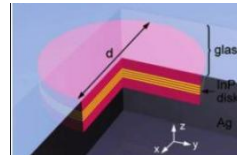
Pan [20]

Table 4.1.1 | Nanolaser Device Zoo. A general device classification based on the optical lasing mode type leading to Photonic and plasmonic laser architectures. The former one can realize mode sizes approaching the diffraction limit of light without the need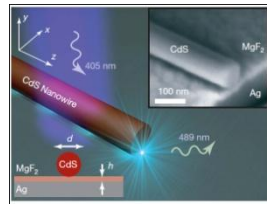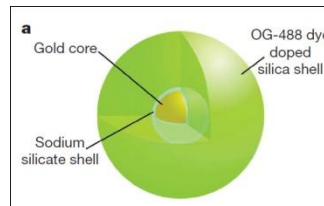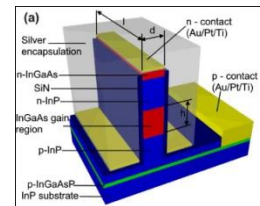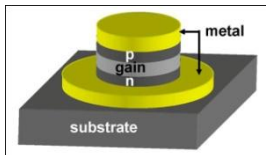 for large footprint mirrors like DBRs in Photonic crystal cavity lasers. Plasmon Nanolaser designs come in different flavors featuring one, two or three dimensional optical confinement.

Metal coated photonic lasers

For a conventional photonic laser cavity, the confinement of the cavity mode inside the gain material is due to the index contrast of the gain materials and surroundings. The overlap of cavity mode and gain material will decrease when one or more dimension of the cavity approach the diffraction limit, which will decrease the mode gain volume and increase radiation loss dramatically. A coated metal layer can shield the cavity modes and thus reduce the radiation loss, though it introduces metal ohmic loss into the system. If the reduced radiation loss is higher than the metal ohmic loss, a coated metal layer can still help to reduce the total loss, which allows for scaling down the photonic cavity close to the diffraction limit of light.

In 2007, Hill et al. reported a metal-coated photonic laser with a diameter semiconductor gain pillar of about 200–300 nm [18]. The pillar is fabricated by etching InP/InGaAsP/InGaAs layers grown via MOCVD epitaxially through electron beam lithography, lift off and an etching process. Then, a silicon nitride layer and metal layers were deposited onto the pillar in sequence. The lasing mode of the metal coated pillar cavity is a HE_{11}-like mode. Since the cavity resonance is below the cutoff frequency for lateral confinement confines the mode effectively in the vertical

direction. The overall optical losses of the device were relatively high, since under electrically pumping, the devices only lased at low (10 K and 77 K) temperatures, with an emission wavelength around 1.4 micrometer. Nezhad et al. adjusted this configuration to operate the laser at room temperature by increasing the diameter of the semiconductor gain core and the thickness of the dielectric layer [16]. The incorporation of a much thicker dielectric layer between the metal and the semiconductor pillar pushed the electromagnetic mode away from the metal walls, thus reducing the mode–metal overlap and hence the ohmic loss. Under optically pumping, lasing emission at 1.43 mm is observed for a gain core diameter and thickness of dielectric layer of about 420 nm and 200 nm, respectively, with the lasing mode being a whispering-gallery mode in the semiconductor core.

Yu et al. reported another configuration of metal coated photonic laser, a nanopatch laser [19, 20]. In the nanopatch laser, a semiconductor disc serving as the gain media is sandwiched between a circular metal patch and a ground metal plane. Here, MOCVD epitaxially grown InP/InGaAsP/InP layers were used as the gain region. Firstly, metal layers were evaporated onto the wafer with a 5 nm of TiO_2 spacer layer. Then, the samples were bonded to a carrier wafer with a 5 nm TiO_2 spacer and the top metal layer after removing InP substrates. Electron-beam lithography was used to define circular hardmask patterns and the top metal, TiO_2 and semiconductor layers were concurrently etched to form the final devices. The semiconductor discs in the devices have diameters of 400 to 620 nm and the thickness being about 200 nm. Under optically pumping at 78 K, the electric- and magnetic- dipole-like modes of nanopatch cavity lase with emission wavelength around 1.3 to 1.4 micrometer.

Plasmon Lasers

Another type of a metallic laser is plasmon laser, which generates and amplifies surface plasmons in a plasmonic cavity directly. Surface plasmons, collective electronic oscillations of metal-dielectric interfaces, are capable of extremely strong confinement well below the diffraction barrier [21]. Such new class of coherent wave source can be considered to be a SPASER (Surface Plasmons Amplification by Stimulated Emission of Radiation) as it was originally introduced by D. J. Bergman 2003 [12]. After being proposed for 8 years, plasmon lasers have been realized in varies kind of plasmon cavities, including metal-insulator-Metal [18], semiconductor-insulator-metal [9,11], semiconductor-metal [20] and localized metal nanoparticle cavities [17]. We will introduce the first three plasmon laser configurations together before talking about the localized metal nanoparticle cavity, since they all share propagating surface plasmon polaritons.

Metal-Insulator-Metal waveguides propagate a well confined transverse magnetic or so called gap plasmon mode [18,22]. Hill et al. incorporated InGaAs gain media into MIM waveguides to overcome loss and realized plasmon gap mode lasing [18]. A rectangular cross-section InP/InGaAs/InP pillar was fabricated through electron beam lithography, lift off and etching process, followed by coating the pillar wall by a 20 nm thick insulating silicon nitride and then silver layer. The index contrast of InGaAs gain layer and InP layers confines the light vertically in the waveguide. The reported thinnest gain medium is about 90 nm thick with a height of 300 nm and a length of 6 micrometer. This device can lase under electrically pumping at 10 K . Increasing the semiconductor core thickness to approximately 310 nm allows for room

temperature photonic mode lasing due to the much lower ohmic loss than the thin gap plasmon MIM mode [18].

In 2009 we reported a hybrid nanowire semiconductor-insulator-metal plasmon laser [9,11]. The high contrast of permittivity at the material interfaces of this structure leads to a strong optical confinement in a few nanometer gap region [13]. The semiconductor (CdS) nanowire in the hybrid configuration has three functions; it serves as the gain media, is part of the confinement mechanism [13] and provides cavity feedback via the high index contrast inside the laser and air. The strong optical confinement in the 5 nm thin low index (MgF_2) region leads to strong electrical field enhancements, this configuration has the unique property of achieving strong confinement and long propagation distance simultaneously. Under optically pumping, lasing of a nanowire with a diameter of just 52 nm and length of about 10 micrometers is observed at 10 K, which only feasible with hybrid plasmons and cannot occur in purely dielectric nanowires. This device we will discussed below in sub-chapter 4.3.

Recently, we developed the HPP concept further for an improved laser cavity enabling room temperature plasmon laser [9]. Here, total internal reflection of surface plasmons is adopted to mitigate the radiation loss, while utilizing the hybrid semiconductor-insulator-metal [13] design in a nano-squares cavity configuration. This laser design features strong confinement while simultaneously having low metal and radiation loss enabling the first semiconductor plasmon laser operation at room temperature and with a much shorter cavity length than the reported cryogenic temperature ones, though it sacrifices optical confinement in one dimension [9]. The device consists of a 45 nm thick, 1 micrometer length Cadmium Sulphide nano-square atop a Silver surface separated by a 5 nm thick Magnesium Fluoride gap layer. By lowing the structural cavity geometry symmetry, the number of cavity modes can be reduced to achieve single mode lasing. This device we will discussed below in sub-chapter 4.4.

Another plasmon Nanolaser design by Kwon et al. utilizes a confined whispering-gallery at a semiconductor-metal interface in a configuration of InP/InAsP/InP disk coated by silver [20]. In this geometry lasing was observed up to liquid nitrogen temperatures upon optical pumping the device . The 235 nm thick InP/InAsP/InP disk were formed on the glass substrate using electron-beam lithography and a dry etching process. After that silver was evaporated on the disk to form a pan-shaped metal coated cavity. The whispering-gallery plasmon mode can lase under optically pumping with increasing threshold from 8 K to 80 K while no lasing was observed at 300 K. Distinguishing between the threshold value for the plasmonic and the photonic mode was achieved by monitoring the temperature dependence for each mode type.

In 2009, Noginov et al. reported a localized surface plasmon laser [12] in solution [17]. The device is composed of a 44-nm-diameter nanoparticles with a gold core and dye-doped silica shell. The gold core provides for surface plasmon oscillations and the surrounded silica shell containing organic dye molecules (Oregon Green 488) provides the gain material. Under optically exciting, the energy of recombination of excitons in dye molecular will transfer to the collective oscillations of electrons of the gold nanoparticle. When the loss of the localized surface plasmons is totally compensated by the gain supplied by dye-doped silica shell, the lasing occurs. The authors claimed, that the stimulated emission was produced by single nanoparticles.

4.2 Nanowire-based Plasmon Nanolaser

Abstract

Laser science has tackled physical limitations to achieve higher power, faster and smaller light sources [1-9]. The quest for ultra-compact laser that can directly generate coherent optical fields at the nano-scale, far beyond the diffraction limit of light, remains a key fundamental challenge [10, 11]. Microscopic lasers based on photonic crystals [3], metal clad cavities [4] and nanowires [5-7] can now reach the diffraction limit, which restricts both the optical mode size and physical device dimension to be larger than half a wavelength. While surface plasmons [12, 13] are capable of tightly localizing light, ohmic loss at optical frequencies has inhibited the realization of truly nano-scale lasers [14, 15]. Recent theory has proposed a way to significantly reduce plasmonic loss while maintaining ultra-small modes by using a hybrid plasmonic waveguide [16]. Using this approach, we report an experimental demonstration of nano-scale plasmonic lasers producing optical modes 100 times smaller than the diffraction limit, utilizing a high gain Cadmium Sulphide semiconductor nanowire atop a Silver surface separated by a 5 nm thick insulating gap. Direct measurements of emission lifetime reveal a broad-band enhancement of the nanowire's exciton spontaneous emission rate by up to 6 times due to the strong mode confinement [17] and the signature of apparently threshold-less lasing. Since plasmonic modes have no cut-off, we show down-scaling of the lateral dimensions of both device and optical mode. As these optical coherent sources approach molecular and electronics length scales, plasmonic lasers offer the possibility to explore extreme interactions between light and matter, opening new avenues in active photonic circuits [18], bio-sensing [19] and quantum information technology [20].

Introduction

Surface plasmon polariton (SPP) are the key to breaking down the diffraction limit of conventional optics as they allow the compact storage of optical energy in electron oscillations at the interfaces of metals and dielectrics [11-13]. Accessing sub-wavelength optical length scales introduces the prospect of compact optical devices with new functionalities as it enhances inherently weak physical processes, such as fluorescence and Raman scattering of single molecules [19] and non-linear phenomena [21]. An optical source that couples electronic transitions directly to strongly localized optical modes is highly desirable as it would avoid the limitations of delivering light from a macroscopic external source to the nano-scale, such as low coupling efficiency and difficulties in accessing individual optical modes [22].

Achieving stimulated amplification of SPPs at visible frequencies remains a challenge due to the intrinsic ohmic losses of metals. This has driven recent research to examine stimulated SPP emission in systems that exhibit low loss, but only minimal confinement, which excludes such schemes from the rich new physics of nanometre scale optics [14, 15]. Recently, we have theoretically proposed a new approach hybridizing dielectric waveguiding with plasmonics, where a semiconductor nanowire sits atop a metallic surface, separated by a nano-scale insulating gap [16]. The coupling between the plasmonic and waveguide modes across the gap

enables energy storage in non-metallic regions. This hybridization allows SPPs to travel over larger distances with strong mode confinement [23] and the integration of a high quality semiconductor gain material with the confinement mechanism itself.

Results

Here, we utilize the "hybrid plasmonics" approach to experimentally show the laser action of SPPs with mode areas as small as $\lambda^2/400$. The truly nano-scale plasmonic laser devices consist of Cadmium Sulphide (CdS) nanowires [24] on a silver film, where the gap layer is Magnesium Fluoride (MgF_2, Fig. 4.2.1a). The close proximity of the semiconductor and metal interfaces concentrates light into an extremely small area as much as 100 times less than a diffraction limited spot [16] (Fig. 4.2.1b). To show the unique properties of hybridized plasmon modes, we compare the plasmonic lasers directly with CdS nanowire lasers on a quartz substrate, similar to typical nanowire lasers reported before [5-7]. In what follows, we will refer to these two devices as *plasmonic* and *photonic* lasers respectively.
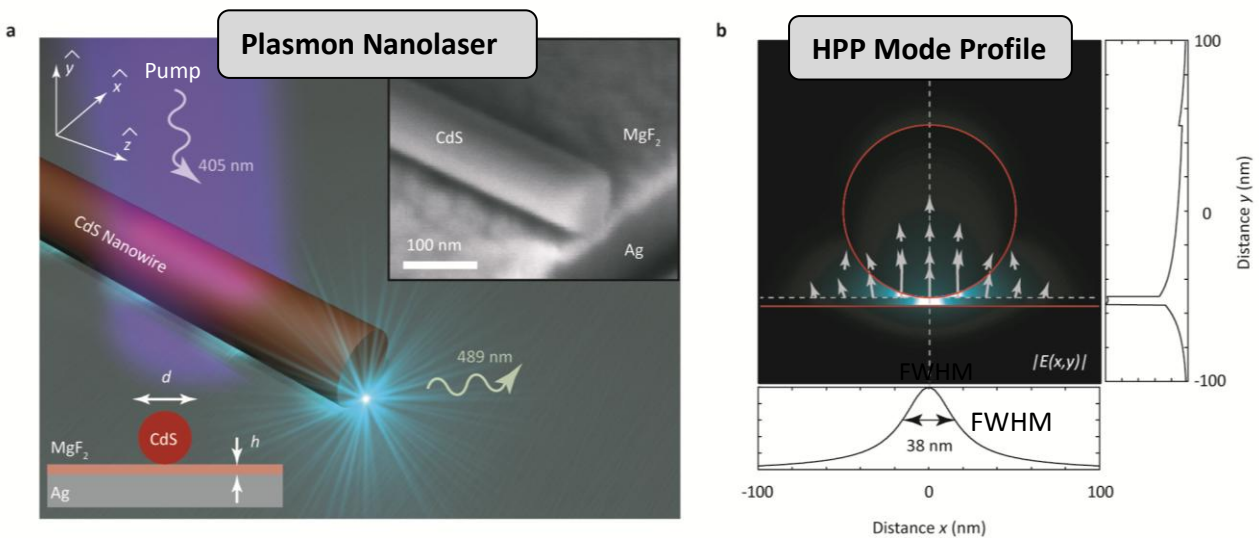
Figure 4.2.1 | The deep sub-wavelength plasmonic laser. a The plasmonic laser consists of a Cadmium Sulphide semiconductor nanowire atop a Silver substrate, separated by a nanometre scale MgF_2 layer. This structure supports a new type of plasmonic mode [16] whose mode size can be 100 times smaller than a diffraction limited spot. The inset shows a scanning electron microscope image of a typical plasmonic laser, which has been sliced perpendicular to the nanowire's axis to show the underlying layers. Panel **b** shows the electric field distribution and direction $|E(x,y)|$ of a hybrid plasmonic mode at a wavelength $\lambda = 489$ nm corresponding to the CdS I_2 exciton line [25]. The cross-sectional field plots (along broken lines in field map) illustrate the strong overall confinement in the gap region between the nanowire and metal surface with sufficient modal overlap in the semiconductor to facilitate gain.
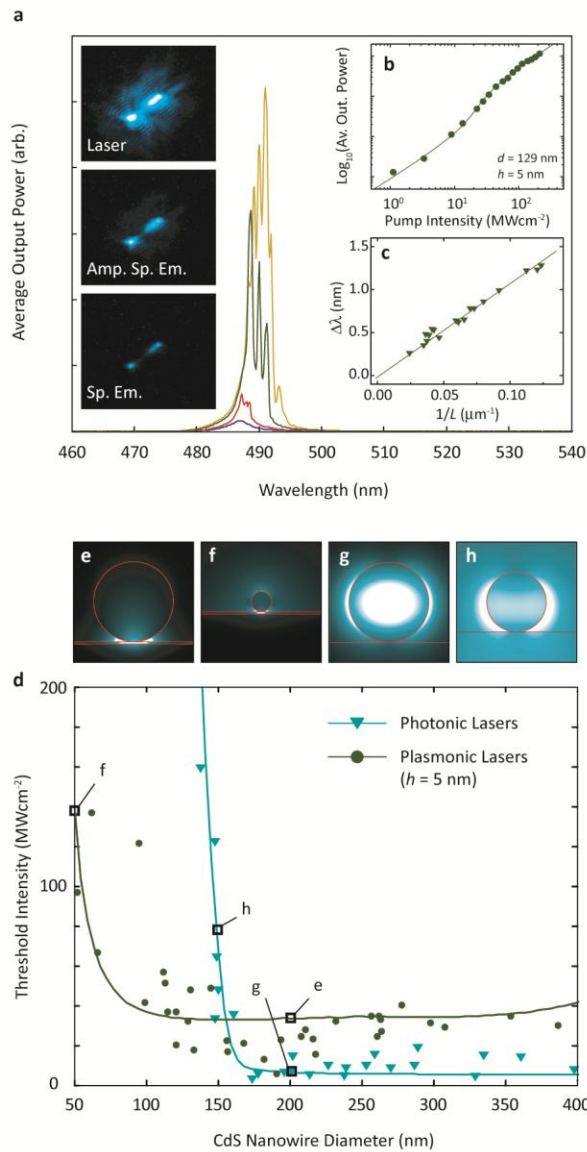
Figure 4.2.2 | Laser oscillation and threshold characteristics of plasmonic and photonic lasers. a Laser oscillation of a plasmonic laser, $d = 129$ nm, $h = 5$ nm (longitudinal modes). The four spectra for different peak pump intensities exemplify the transition from spontaneous emission (21.25 MWcm^{-2}) via amplified spontaneous emission (32.50 MWcm^{-2}) to full laser oscillation (76.25 MWcm^{-2} & 131.25 MWcm^{-2}). **b** Shows the non-linear response of the output power to the peak pump intensity. The relationship between mode spacing, $\Delta\lambda$, and nanowire length, in **c** indicates a high group index of 11 due to the high material gain. The pictures on the left correspond to microscope images of a plasmon laser with $d = 66$ nm exhibiting spontaneous emission, amplified spontaneous emission and laser oscillation, where the scattered light output is from the end-facets. **d** Threshold intensity of plasmonic and photonic lasers versus nanowire diameter. The experimental data points correspond to the onset of amplified spontaneous emission, which occurs at slightly lower peak pump intensities compared to the threshold of gain saturation. Amplified spontaneous emission in hybrid plasmonic modes occurs at moderate pump

intensities of 10-60 MWcm^{-2} across a broad range of diameters. Plasmonic lasers maintain good mode confinement over large range of diameters as shown in **e** (d = 200 nm) and remain confined even for a 50 nm diameter wire as shown in **f**. While the photonic lasers have similar threshold intensities around 10 MWcm^{-2} for all nanowires larger than 200 nm shown in **g**, a sharp increase in the threshold occurs for diameters near 150 nm, due to the loss of confinement within the nanowire and subsequent lack of overlap with the gain region [7] shown in **h**. The solid lines show a numerical fit to a simple rate equation model. Below 140 nm, the photonic mode is *cut-off* and lasing could not be observed at all. In contrast, plasmonic lasers maintain strong confinement and optical mode-gain overlap for diameters as small as 52 nm, a diameter for which a photonic mode does not even exist. The relatively small difference in the thresholds of plasmonic and photonic lasers can be attributed to high cavity mirror losses, which are on the same order of magnitude as plasmonic losses.

We optically pump these laser devices at a wavelength of 405 nm and measure emission from the dominant I$_2$ CdS exciton line at 489 nm [25]. At moderate pump intensities (10-60 MWcm^{-2}), we observe the onset of amplified spontaneous emission peaks. These correspond to the longitudinal cavity modes that form when propagation losses are compensated by gain allowing plasmonic modes to resonate between the reflective nanowire end-facets (Fig. 4.2.2a). The large amount of gain needed to compensate both cavity and propagation losses produces a strong *frequency pulling* effect [26] causing the Fabry-Perot modes to be much more closely spaced than expected for a passive cavity (Fig. 4.2.2c). The clear signature of multiple cavity mode resonances at higher pump powers demonstrates sufficient material gain to achieve full laser oscillation, shown by the non-linear response of the integrated output power with increasing input intensity (Fig. 4.2.2b). The occurrence of these cavity resonances indicates that the laser mode's *plasmonic coherence* is determined by cavity feedback and not by its propagation distance.

Surmounting the limitations of conventional optics, plasmonic lasers not only support nano-scale optical modes, their physical size can also be much smaller than conventional lasers, i.e., plasmonic lasers operate under conditions where photonic modes cannot even exist [7]. Plasmonic lasers maintain strong confinement and optical mode-gain overlap over a broad range of nanowire diameters (Fig. 4.2.2e - f) with only a weak dependence on the nanowire diameter. While hybrid modes do not experience mode cut-off, the threshold intensity increases for smaller nanowires due to the reduction in the total gain volume. Conversely, photonic lasers exhibit a strong dependence of the mode confinement on the nanowire diameter (Fig. 4.2.2g - h), resulting in a sharp increase in the threshold intensity at diameters near 150 nm due to a poor overlap between the photonic mode and the gain material. Moreover, actual photonic lasers suffer mode cut-off as the leakage into the quartz substrate prevents lasing for nanowire diameters less than 140 nm [7]. This is to say, the observation of plasmonic lasing for nanowire diameters of just 52 nm confirms the role of the hybrid plasmonic mode where a purely dielectric nanowire mode cannot exist.

Plasmonic modes often exhibit highly polarised behaviour as the electric field normal to the metal surface binds most strongly to electronic surface charge. We have detected the signature of lasing plasmons from the polarisation of scattered light from the nanowire end-facets, which is in

the same direction as the nanowire. Conversely, the polarisation of scattered light from photonic lasers is perpendicular to the nanowire. This distinction provides a direct confirmation of the plasmonic mode.

We find a strong increase of the spontaneous emission rate when the gap size between the nanowire and metal surface is decreased. Lifetime measurements reveal a Purcell factor of more than 6 for a gap width of 5 nm and nanowire diameters near 120 nm (Fig. 4.2.3), where hybrid plasmonic modes are most strongly localized [16]. This enhancement factor corresponds to a mode that is 100 times smaller than the diffraction limit, which agrees well with our mode size calculations. While the enhanced emission rate, or Purcell effect [17], is usually associated with high quality micro-cavities [3, 4], we observe a broad-band Purcell effect arising from mode confinement alone without a cavity [20].

We next examine the physics underlying the gain mechanism in the plasmonic lasers, which combines exciton dynamics, the modification of spontaneous emission [17] and mode competition. While photo-generated excitons have intrinsic lifetimes of up to 400 ps [25], they recombine faster at the edge of the nanowire near the gap region due to strong optical confinement mediated by the hybrid plasmon mode (Fig. 4.2.3). The exciton diffusion length in bulk CdS is about a micrometer [27], which is much larger than the nanowire diameter. Therefore, the distribution of exciton recombination quickly adjusts itself to match the hybrid mode's profile (see Fig. 4.2.1b). The fast diffusion and the enhanced emission rate into the hybrid plasmonic mode lead to preferential plasmon generation. In this way, the proportion of light that couples into the laser mode, known as the *spontaneous emission factor, β* can be high (Fig. 4.2.3b) [28]. The measured emission rates and a simple emission model show that the β-factor of the plasmonic mode is as high as 80% for a gap width of 5 nm. For gap widths below 5 nm, the exciton recombination is too close to the metal surface, causing rapid non-radiative quenching [29]. While nanowires placed in direct contact with the metal surface show the highest spontaneous emission rates, these devices exhibit weak luminescence and do not lase. Our calculations support these observations indicating a sharp reduction in the β-factor below gap widths of 5 nm.
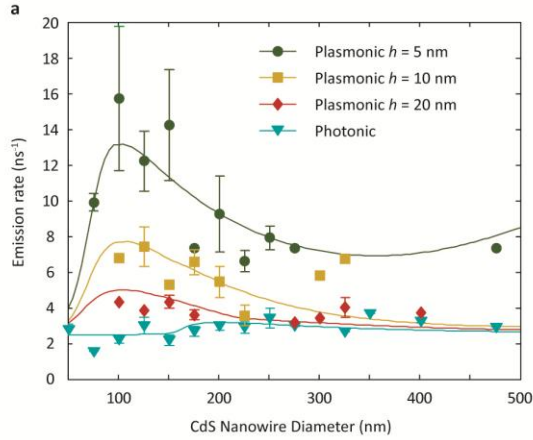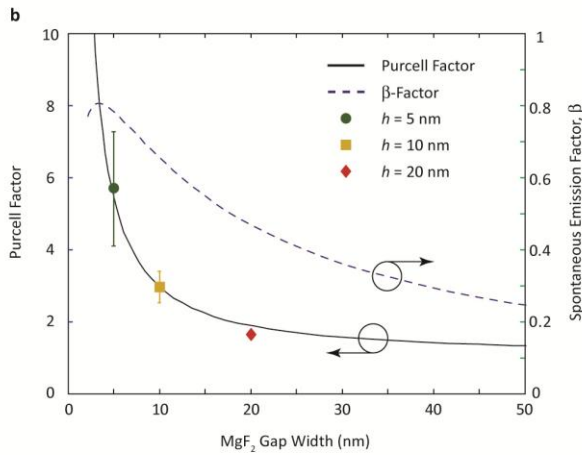
Figure 4.2.3 | The Purcell effect in plasmonic and photonic lasers. a The emission rates of photonic and plasmonic nanowire lasers with different MgF$_2$ gap widths as a function of the nanowire diameter following the calculated trend. The optimal confinement condition of hybrid plasmonic modes is found near d = 120 nm, where the hybridization of nanowire and SPP modes is strongest giving the highest emission rate [16]. Panel **b** shows the Purcell factors determined from a numerical fit of the emission rate measurements to a simple emission model. Near optimal confinement (d = 120 nm ± 20 nm), the average Purcell factor for devices with 5 nm gaps is more than 6, which is considered high for a broad band effect. We have also calculated the β-factor from the emission model fit by accounting for the possible emission pathways. The β-factor reaches a maximum of 80 % for a gap width near 5 nm. At gap widths smaller than 5 nm, non-radiative quenching to the metal surface causes a sharp drop in the hybrid plasmon β-factor, which subsequently eliminates the possibility for lasing. The error bars show standard deviation of emission rates from data collected within 25 nm nanowire diameter ranges.

The laser threshold is commonly manifested as a *kink* between two linear regimes of the output power versus pump intensity response (log-log scale). However, it is known that lasers with strong mode confinement do not necessarily exhibit such behaviour so that the laser threshold may be obscured [28, 30]. Since the plasmonic lasers exhibit strong mode confinement, we indeed observe this *smearing* of the threshold pump intensity (Fig. 4.2.4). The photonic lasers

that we have measured, on the other hand, show the distinctive kink in the output power, which is in agreement with recently reported Zinc Oxide nanowire lasers [7]. Since both plasmonic and photonic lasers in this work utilize the same gain material, we conclude that the smeared response in output power arises from local electromagnetic field confinement. We therefore attribute this distinct behaviour to the increased spontaneous emission factor of the hybrid plasmon mode. A high spontaneous emission factor is often associated with low threshold laser operation where undesired emission modes are suppressed. While the linear response, shown in Fig. 4.2.4 for a nanowire diameter of 66 nm, may therefore give the impression of a lower threshold [28], in reality, the laser threshold only occurs once cavity losses are compensated.
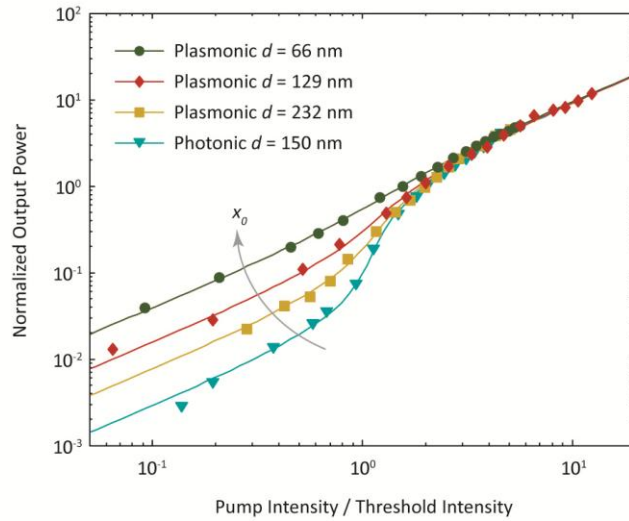
Figure 4.2.4 | Nearly *threshold-less lasing* due to high spontaneous emission factor. The dependence of measured output power over pump intensity highlights clear differences in the physics underlying the plasmonic ($h = 5$ nm) and photonic lasers using a multi-mode lasing model [30]. In particular, our fitting parameter, x_0, is related to the gain saturation of individual longitudinal laser modes and their lateral mode area. A higher value of x_0 corresponds to a smaller mode area and a higher β-factor. Photonic lasers exhibit a clear transition between spontaneous emission and laser operation characterized by a change in the gradient of input peak pump intensity versus output power, corresponding to the laser threshold. For a 150 nm diameter nanowire, the parameter $x_0 = 0.026$ is in agreement with a recent nanowire laser study [7]. Plasmonic lasers, however, show a strong dependence of x_0 on the nanowire diameter; a large multi-mode plasmonic laser ($d = 232$ nm) shows a somewhat smeared transition region ($x_0 = 0.074$), while smaller single mode plasmonic lasers ($d = 129$ nm and $d = 66$ nm) have much less visible changes in gradient ($x_0 = 0.150$ and $x_0 = 0.380$ respectively). The large value of x_0 observed in the plasmonic lasers is associated with so-called *threshold-less* operation and attributed to the strong mode confinement giving rise to a high spontaneous emission factor. Nevertheless, the onset of amplified spontaneous emission peaks in all devices occurred at non-zero threshold intensities as shown in Fig. 4.2.2d.

Conclusion

The demonstration of deep sub-wavelength plasmonic laser action at visible frequencies paves the way to new sources that produce coherent light directly far below the diffraction limit. Extremely strong mode confinement, which is evident from the increase of the spontaneous emission rate by up to 6 times, and the resulting high spontaneous emission factor are key aspects for the operation of deep sub-wavelength lasers. We have also shown that the advantage of plasmonic lasers is the ability to down-scale the physical size of devices, as well as the optical modes they contain, unlike diffraction limited lasers. Furthermore, the use of metals in plasmonics could provide a natural route toward electrical injection schemes that do not interfere with mode confinement [6]. The impact of plasmonic lasers on optoelectronics integration is potentially significant as the optical fields of these devices rival the smallest commercial transistor gate sizes and thereby reconcile the length scales of electronics and optics.

Experimental Methods

The technical challenge of constructing the plasmonic lasers is ensuring good contact between the nanowire and planar optical film. Low film roughness (~1 nm rms) and accurate deposition (~10%) allow <2 nm gap width. Crystalline CdS nanowires exhibit extremely low surface roughness, hence the contact is limited by film roughness. Nanowires were grown using chemical vapour deposition of CdS powders on Si substrates by self assembly from a 10 nm Au film seeding layer leading to random nanowire diameters, d = 50 - 500 nm. CdS nanowires were deposited from solution by spin coating onto pre-prepared films with varying MgF_2 thicknesses of 0, 5, 10 and 20 nm, along with control devices of nanowires on a quartz substrate.

A frequency doubled, mode-locked Ti-Sapphire laser (Spectra Physics) was used to pump the plasmonic and photonic lasers (λ_{pump} = 405 nm, repetition rate = 80 MHz, pulse length = 100 fs). An objective lens (20x, NA = 0.4) was used to focus the pump beam to a 38 μm diameter spot on the sample. All experiments were carried out at low temperature, T < 10 K, utilizing a liquid-He cooled cryostat (Janis Research). Individual spectra were recorded using a spectrometer with a resolution of 0.25 nm and a liquid-N_2 cooled CCD (Princeton Instruments). The lifetime measurements were conducted under very low pump conditions to avoid heating and exciton-exciton scattering effects using time-correlated single photon counting (PicoQuant: PicoHarp 300, Micro Photon Devices APD 40 ps timing resolution). A 490 ± 10 nm band pass filter was used to filter out ambient light and pass light from the I_2 CdS exciton line near 489 nm. An emission model was used to describe the enhanced lifetime data (Purcell effect), which relates to deep sub-wavelength mode confinement.

## 4.3 Enhancing the Feedback of a plasmon Cavity

Plasmon lasers are a new class of coherent optical amplifiers that generate and sustain light well below its diffraction limit [1-4]. Their intense, coherent and confined optical fields can enhance significantly light-matter interactions and bring fundamentally new capabilities to bio-sensing, data storage, photolithography and optical communications [5-11]. However, metallic plasmon laser cavities generally exhibit both high metal and radiation losses, limiting the operation of plasmon lasers to cryogenic temperatures, where sufficient gain can be attained. Here, we present room temperature semiconductor sub-diffraction limited laser by adopting total internal reflection of surface plasmons to mitigate the radiation loss, while utilizing hybrid semiconductor-insulator-metal nano-squares for strong confinement with low metal loss. High cavity quality factors, approaching 100, along with strong $\lambda/20$ mode confinement lead to enhancements of spontaneous emission rate by up to 18 times. By controlling the structural geometry we reduce the number of cavity modes to achieve single mode lasing.

Lasers are ideal for optical communications, information storage, accurate metrologies and sensitive spectroscopies as they present the means to deliver powerful, coherent and directional high frequency electromagnetic energy. However, the diffraction limit of light imposes fundamental constraints on how compact such photonic devices can be and their potential for integration with electronic circuits, which are orders of magnitude smaller. While recent efforts in photonic crystal, whispering gallery and metal-coated photonic cavities have succeeded in confining light to less than the vacuum wavelength, they remain limited by diffraction [12-16]. On the other hand, surface plasmon polaritons (SPPs) [17], the collective electronic oscillations of metal-dielectric interfaces, show great promise for an exciting new class of light source capable of reconciling photonic and electronic length scales. Furthermore, SPPs are capable of extremely strong confinement in one or two dimensions [2, 4, 18, 19], enabling plasmon lasers to deliver intense, coherent and directional optical energy well below the diffraction barrier. Such lasers can drastically accelerate the scalability of photonics to catch up with Moore's law for electronics and will naturally introduce new functionalities and applications.

Notwithstanding the growing body of work on metal-based lasers, the demonstration of sub-diffraction limited semiconductor plasmon lasers operating at room temperature remains a major hurdle owing to the problem of mitigating both the high absorptive loss of metals and the low cavity feedback of propagating surface plasmons in small metallic structures. This has restricted such lasers to working at cryogenic temperatures in order to attain sufficient gain [2, 4]. Recent efforts in semiconductor plasmon lasers were only able to partially tackle these obstacles and the design stratagems remain mutually exclusive: improved feedback was obtained in devices capped in metal at the expense of high metal loss resulting in limited mode confinement [2]; whereas nanowire lasers on planar metal substrates achieved reduced metal loss but had limited feedback that required cavity lengths much longer than the wavelength [4]. Room temperature plasmon laser operation below the diffraction limit demands effective cavity feedback, low metal loss and high gain; all within a single nano-scale device.

Here, we report the first realization of cavity-enhanced coheren plasmon light source (laser) operating at room temperature with $\lambda/20$ optical confinement. An ultra-thin Cadmium Sulphide

(CdS) nanosquare atop a Silver surface separated by a 5 nm thick Magnesium Fluoride gap layers provides the subwavelength mode confinement and low metal loss [20]. Surprisingly, although the high-index material is only 45 nm thick, the surface plasmons of this system carry high momentum, even higher than light waves in bulk CdS or plasmonic nanowire lasers [4]. This leads to strong feedback by total internal reflection of surface plasmons at the cavity boundaries.
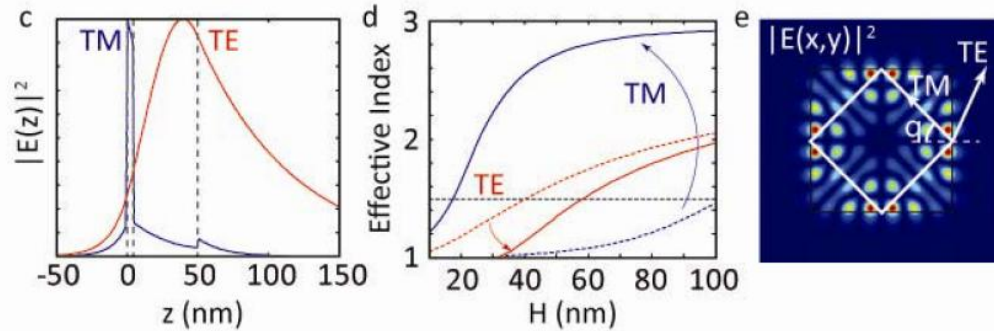
Figure 4.3.1 | Mode Selection of Cavity. (left) The electric field intensity distribution of the two modes of the system along the z direction. While TM modes are localized in the gap layer, TE modes are delocalized from the metal surface. **(middle)** The effective index of TM and TE waves with (solid line) and without (dashed line) the metal substrate. TM waves strongly hybridize with SPPs resulting in the strong confinement within the gap region (blue line in **left**) accompanied by a dramatic increase in momentum (blue line in **middle**) with respect to TM waves of the CdS square alone (blue dashed line in **middle**). However, the delocalized TE waves (red line in **left**) show decreased momentum (red line in **middle**) with respect to TE waves of the CdS square alone (red dashed line in **middle**). **(right)** Electric field intensity distribution of a TM mode in the x and y directions. While both mode polarizations are free to propagate in the plane, only TM modes have sufficiently large mode index to undergo efficient total internal reflection providing the feedback for lasing.

The room temperature plasmon laser and is 45 nm thick, 1 μm length sitting atop a Silver substrate with a 5 nm MgF$_2$ gap. The close proximity of the high permittivity CdS square and silver surface allows modes of the CdS square to hybridize with SPPs of the metal-dielectric interface, leading to strong confinement of light in the gap region (middle Fig. 4.3.1) with relatively low metal loss [20]. The coupling is extremely strong and causes a dramatic increase in the momentum with respect to the modes of the CdS square alone (middle blue arrow in Fig. 4.3.1). Since the dominant magnetic field component of the waves is always parallel to the metal surface we call these transverse magnetic (TM) waves [21]. On the other hand, waves with dominant electric field parallel to the metal surface (transverse electric, or TE) cannot hybridize with SPPs. Consequently, they become increasingly de-localized as the gap size decreases and are effectively pushed away from the metal surface (left Fig. 4.3.1c) with a corresponding decrease in momentum with respect to TE waves of the CdS square alone (middle red arrow in Fig. 4.3.1). While both wave polarizations are free to propagate in the plane, only TM waves have sufficient momentum to undergo total internal reflection and achieve the necessary

feedback for lasing as shown in Fig 4.3.1e [22, 23]. Although CdS squares thicker than about 60 nm can support TE waves with sufficient momentum to undergo total internal reflection, they are scattered out of the plane more effectively than TM waves since they are delocalized from the metal surface. While long lived eigenmodes of square cavities are achievable [24], the finite size of the cavity leads to imperfect internal reflection causing in-plane scattering of surface plasmon waves and volume scattering of radiation waves, which we use to measure the response of the plasmon laser.
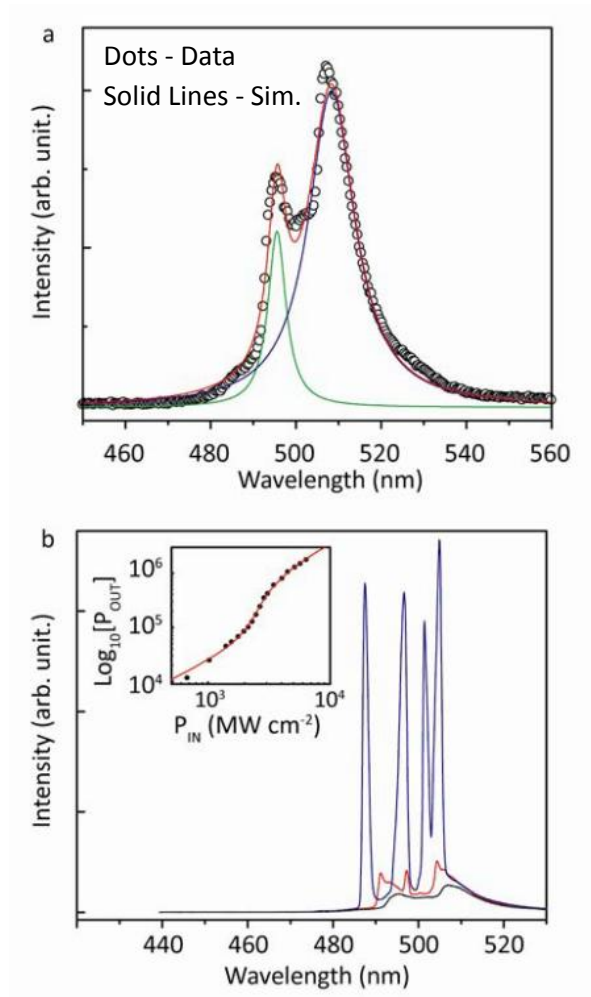
Figure 4.3.2 | Laser spectra and integrated light-pump response a plasmon laser below and above threshold. a The spontaneous emission spectrum at a peak pump intensity of 1960 MW cm-2 shows obvious cavity modes albeit being below the threshold which indicates the excellent cavity feedback. Measured at room temperature. **b** room temperature laser spectra and integrated light-pump response (inset) showing the transition from spontaneous emission (1960 MW cm-2, black) via amplified spontaneous emission (2300 MW cm-2, red) to full laser oscillation (3074 MW cm-2, blue).

The feedback mechanism of totally internally reflected SPPs is extremely effective as shown by the well-pronounced cavity modes in the spontaneous emission spectrum below threshold in Fig.

4.3.2a. The Q factors of the two apparent modes are 97 and 38 at the resonant wavelengths of 495.5 nm and 508.4 nm, respectively. We have identified these as plasmonic total internal reflection modes using a numerical model. While the Q of the 495.5 nm resonance is close to numerical predictions, the other Q value is an underestimate because that resonance is composed of several modes that are too close to be resolved. For larger pump intensities, multiple cavity modes appear with orders of magnitude higher coherence than the underlying spontaneous emission, as shown in Fig. 4.3.2b. The emission spectrum is completely dominated by these high coherence peaks when collecting the light at large collection angles. This is a signature of the plasmonic cavity modes, which preferentially scatter into large angles to conserve their in-plane momentum. The nonlinear response of the integrated output power with pump intensity confirms the observation of laser oscillation well above threshold (inset of Fig. 4.3.2). This laser can be considered to be a spaser (Surface Plasmons Amplified by Stimulated Emission of Radiation) as it was originally introduced in Ref. 1, since it generates plasmonic cavity eigenmodes and only emits light to the far-field as a side effect of scattering.
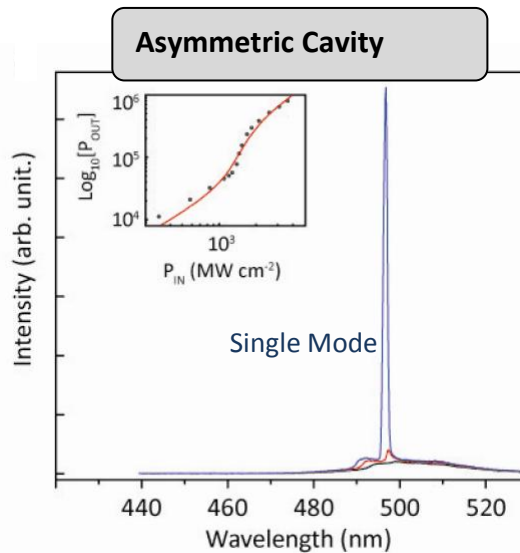
Figure 4.3.3 | Laser spectrum and integrated light-pump response of a single mode room temperature plasmon laser. The room temperature laser spectra and integrated light-pump response (inset, top) showing the transition from spontaneous emission (1096 MW cm-2, black) via amplified spontaneous emission (1280 MW cm-2, red) to full single mode laser oscillation (1459 MW cm-2, blue) and the spectral narrowing of the single laser mode.

The current device exhibits multiple laser peaks attributed to the number of available modes in the square cavity configuration. However, we have also observed single mode plasmon lasing in irregularly shaped devices with lower symmetry where only a limited number of modes can undergo total internal reflection. Figure 4.3.3 shows the spectrum and power response of a single mode room temperature plasmon laser of the device with 75 nm thick, 1.1 µm length. Lasing in

such ultrathin devices is viable solely due to the plasmonic confinement and strong total internal reflection feedback. This was verified from control samples; consisting of similar CdS squares on quartz substrates, none exhibited laser action due to the lack of both mode confinement and cavity feedback.
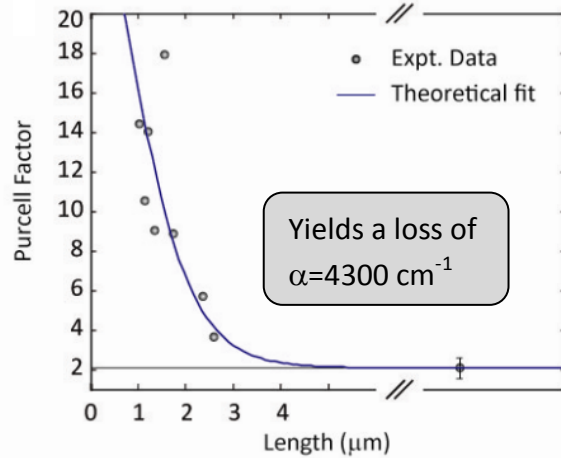
Figure 4.3.4 | Observation of the Purcell effect in cavity enhanced plasmon lasers. The figure shows the increase in Purcell effect with the decrease of the cavity side length as a result of the mode volume reduction accompanied by a high quality factor. Very large cavities do not benefit from cavity feedback and exhibit a Purcell effect of 2 due to confinement along the z-direction alone. This agrees well with a simple theoretical model taking into account the numerous emission processes (see Methods). This indicates the ability of these plasmon lasers to strongly enhance light matter interactions. The variations in the CdS thickness (45 to 88 nm) do not play a major role in the emission enhancement.

The intense fields that are generated and sustained in the gap region (left Fig. 4.3.1) make such lasers highly useful for investigating light-matter interactions. Namely, an emitter placed in this gap region is expected to interact strongly with the laser light. Such light-matter interaction enhancements are also observable to a lesser extent in the CdS gain medium; under weak pumping, the CdS band edge transitions of this plasmon laser show a spontaneous emission lifetime reduced by a factor of 14. The Purcell effect [25] is apparent in all the laser devices measured. The smaller devices show Purcell factors as large as 18 due to the combination of both high cavity quality factors (Q) and strong mode confinement. On the other hand, for devices larger than the surface plasmon propagation length, the cavity feedback no longer plays a role and an average 2-fold reduction in lifetime is obtained due to the strong confinement of SPPs alone. A theoretical formula describing the observed lifetime reduction is shown in Fig 4.3.4 and predicts SPP losses of 6,323 cm-1, in good agreement with the numerical estimate (see Methods). We note that this plasmon loss can be compensated by gain available in CdS [26]. Since the electric field intensities in the gap region are 5 times stronger than in the CdS, we anticipate Purcell factors as high as 90 for light-matter interactions within the gap. We note that despite sub-diffraction limited confinement in only one dimension, this value is even higher than the highest simulated Purcell factors of 60 for the recently reported metal-coated photonic cavities [14-16].

A semiconductor plasmon lasers with strong mode confinement, which is much smaller than the diffraction limit operating at room temperature has been demonstrated. The mode is generated inside a nanoscopic gap layer of 5 nanometers and remains bound by strong feedback arising from total internal reflection of surface plasmons. The small mode size and high quality factor gives rise to a strong Purcell effect, resulting in demonstration of up to 18 times enhancement of the natural spontaneous emission rate of CdS band-edge transitions. This indicates that these sub-diffractional laser modes have the potential to enhance light-matter interactions. Moreover, with tight confinement on the nanometer scale, plasmon lasers can reconcile the scales of photonics and electronics, opening a new door in optoelectronics. The room temperature plasmon lasers enable new possibilities in applications such as single molecular sensing, ultra-high density data storage, nano lithography and optical communications.

Experimental Methods

The CdS squares were made by a solution based sonication cleaving process of CdS nanobelts, which were synthesized via the chemical vapor deposition method [27]. The squares were then deposited from solution on MgF_2/Ag (5 nm/300 nm) substrates. A frequency-doubled, mode-locked Ti-sapphire laser (Spectra Physics) was used to pump the squares (λ_{pump}=405 nm, repetition rate 10 KHz, pulse length 100 fs). A 20x objective lens (NA=0.4) focused the pump beam to ~ 5 μm diameter spot on the sample. All experiments were carried out at room temperature. Figure 4.3.5 shows the experimental low temperature setup. A Spectrometer and an single photon counting system have been utilized.
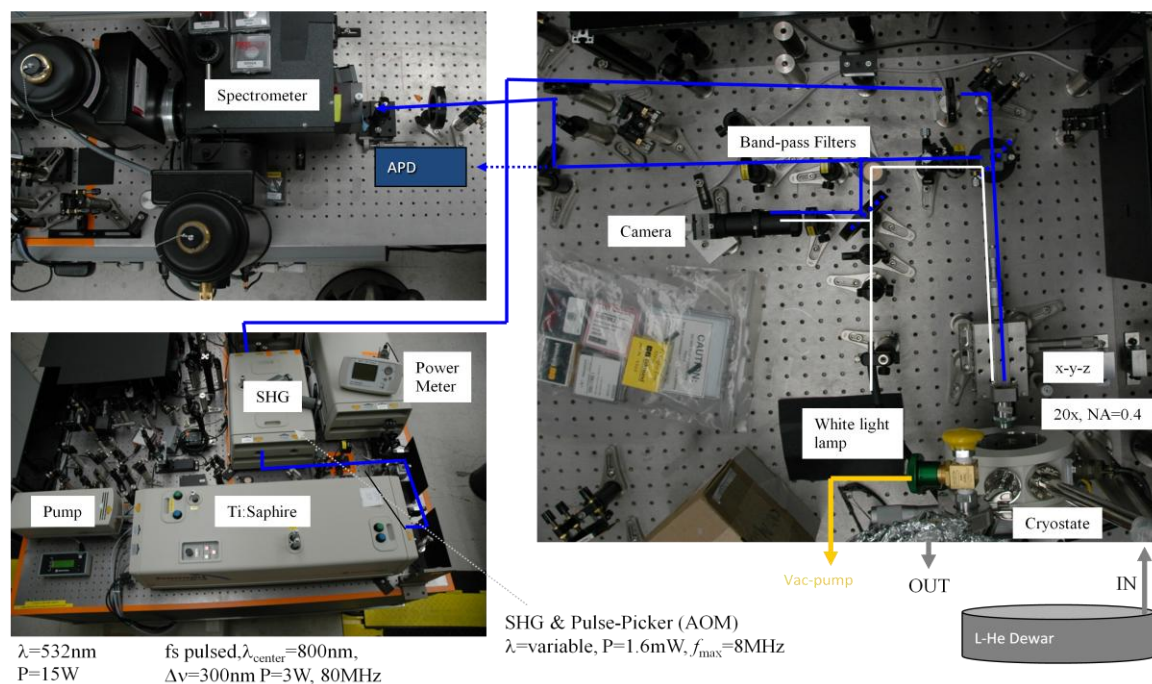
Figure 4.3.5 | Experimental Setup. Notice a Time-correlated Single Photon Counting Setup (Pico-harp from Picoquant) was used for the lifetime measurements.

4.4 Plasmonic Laser Physics and Operational Characteristics

Introduction

The general trend to miniaturize lasers in past decades has led to clearly observable differences in their operational characteristics compared to conventional devices. In particular, small lasers suffer loss of beam directionality as their cavities approach the diffraction limit [1-9] and enhanced spectral noise due to the modification of spontaneous emission [3,6]. While the loss of directionality is generally manageable using suitable out-coupling optics, the additional laser noise is generally unavoidable as spontaneous emission is an integral part of a laser's operation. As the dimensions of a laser cavity approach the operating wavelength, the rate of spontaneous emission between an excited electronic state and an optical mode can either be enhanced [3,6,10-12] or inhibited [13], an effect first pointed out by Purcell [14]. While this can affect a number of processes within a laser, most importantly it also leads to a drastic spatial redistribution of spontaneous emission; that is to say, light can be preferentially coupled to the laser mode. While this can significantly reduce the pump conditions for the onset of laser action, this is at the sacrifice of increase spontaneous emission noise in the laser mode. In plasmonic laser systems, we seek to make extremely small devices where increased spontaneous emission rates are inevitable. In this sub-section, we discuss the Purcell effect in the context plasmonics and describe how it modifies the characteristics of plasmonic lasers.

The Purcell Effect in Plasmonic Systems

The Purcell effect is commonly associated with Fermi's Golden rule, which quantifies the rate, Γ_D, at which weakly coupled systems can exchange energy with an optical mode. The Purcell factor, F, is the emission rate enhancement into all possible modes of an optical structure relative to the emission rate in the absence of that structure. Accounting for all the possible modes of an optical structure is not a trivial task so here we account only for the competition between radiation modes, which are assumed to be unaffected by the Purcell effect, and a single plasmonic mode, such that

$$F = \frac{\Gamma + \Gamma_D}{\Gamma} = 1 + \frac{\pi}{2\Gamma}|g_D(\boldsymbol{r}_a)|^2 G_D \qquad (1)$$

where the first and second term respectively account for emission into radiation and plasmonic modes; $g_D(\boldsymbol{r}_a) = \langle \psi_1|\boldsymbol{d}.\boldsymbol{E}(\boldsymbol{r}_a)|\psi_2\rangle/\hbar$ is the emitter-to-plasmonic mode coupling strength depending on the overlap of the dipole moment $\boldsymbol{d}$, induced by transition between electronic states ψ_2 and ψ_1, and the local electric field, $\boldsymbol{E}(\boldsymbol{r}_a)$; $\boldsymbol{r}_a$ is the dipole position; G_D is the density of optical states (number of modes per unit frequency and volume); and $\Gamma = n_a\omega^3|\boldsymbol{d}|^2/3\pi\varepsilon_0\hbar c^3$ is the natural spontaneous emission rate of the emitter in an open lossless medium of refractive index n_a.

In most cases, an optical structure does not influence the electronic wavefunctions and only the local electric field and the density of optical states affect the spontaneous emission rate. While

the Purcell effect is often associated with cavity modes confined in all three dimensions, the effect can also be observed in plasmonic systems exhibiting confinement in fewer dimensions. Here we have modified Fermi's Golden Rule to account for confinement in D dimensions and we have averaged over the possible emitter dipole orientations so that,

$$g_D(\boldsymbol{r}_a) = \sqrt{\frac{2}{\pi^2}\omega\Gamma C_D(\boldsymbol{r}_a)\left(\frac{\pi c}{n_a\omega}\right)^{3-D}} \tag{2}$$

where the confinement factor is,

$$C_D = f(\boldsymbol{r}_a)\frac{\text{Max}\{2u_E(\boldsymbol{r})\}}{\int d^D r u_{EM}(\boldsymbol{r})}\left(\frac{\lambda}{2n_a}\right)^D = \frac{f(\boldsymbol{r}_a)}{V_D}\left(\frac{\lambda}{2n_a}\right)^D \tag{3}$$

Here, the electromagnetic energy density, $u_{EM}(\omega,\boldsymbol{r}) = u_E(\omega,\boldsymbol{r}) + u_M(\omega,\boldsymbol{r})$ $= (d\omega\varepsilon(\omega)/d\omega)|\boldsymbol{E}(\omega,\boldsymbol{r})|^2/2 + \mu_0|\boldsymbol{H}(\omega,\boldsymbol{r})|^2/2$, is normalized to the vacuum energy $\int d^D r u_{EM}(\omega,\boldsymbol{r}) = \hbar\omega$; V_D is the mode volume ($V = V_3$), mode area ($A = V_2$) or mode width ($W = V_1$); and we will assume that the position dependence of the coupling strength is optimal, i.e. $f(\boldsymbol{r}_a) = u_E(\boldsymbol{r}_a)/\text{Max}\{u_E(\boldsymbol{r})\} = 1$.

For free space radiation modes ($D = 0$), the density of optical states is $G_0 = n_a^3\omega^2/\pi^2 c^3$, hence $\Gamma_0 = \Gamma$. Increasing the confinement dimensionality modifies the density of states such that $G_1 = n_p n_g\omega/2\pi c^2$ for confinement in 1D and $G_2 = n_g/\pi c$ for confinement in 2D (propagation along a metal wire), where n_p and n_g are respectively the phase and group indexes of SP modes. The Purcell factors for confinement in one and two dimensions are respectively,

$$F_1 = 1 + \frac{n_p n_g}{2n_a^2}\frac{(\lambda/2n_a)}{W}$$
$$F_2 = 1 + \frac{n_g}{\pi n_a}\frac{(\lambda/2n_a)^2}{A} \tag{4}$$

Such plasmonic systems are capable of emission enhancements over a broad range of frequencies since they do not rely on a cavity with a well defined resonant frequency and are therefore widely broadband in nature [15]. Generally only when the mode width or area drop below the diffraction limit does the effect become pronounced, however, the group index of the waves can potentially have a significant effect in some configurations. Conversely, 3D cavity systems exhibit a resonance condition and must be tuned to match the emitter's spectrum. Furthermore, the optical feedback onto the emitter can introduce both irreversible and reversible energy exchange between light and matter states, the so-called strong coupling regime [12]. However, the high metal loss encountered in most plasmonic systems results in irreversible coupling with a Purcell effect [14],

$$F_3 = 1 + \frac{2}{\pi}\left(\frac{\lambda}{2n_a}\right)^3\frac{Q}{V} \tag{5}$$

where the 3D cavity density of optical states, $G_3 = 2/\pi\gamma = 2Q/\pi\omega$, is the peak value of the Lorentzian cavity line shape function. This is the well-known Purcell enhancement factor for a cavity with volume V and quality factor Q [14,15].
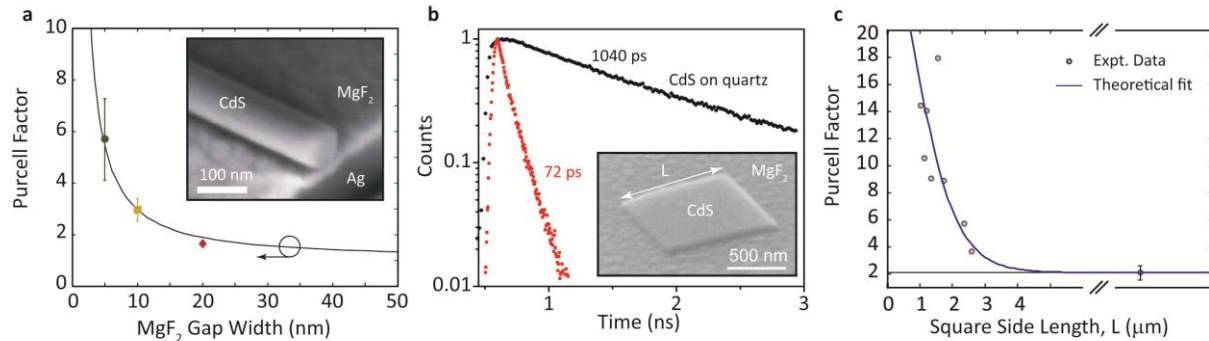
Figure 4.4.1 | Observation of the Purcell effect in plasmonic lasers. a Purcell factors of CdS I_2 exciton emission from nanowires on a metal surface separated by a thin MgF2 gap layer (see inset), for diameters near optimal confinement (d = 120 nm ± 20 nm). The average Purcell factor for devices with 5 nm gaps is more than 6, which is considered to be high for a broad band effect (i.e. without cavity enhancement). b Time resolved spontaneous emission of a related laser devices consisting of thin CdS squares placed on metal with a similar MgF_2 gap layer (see inset) shows a dramatic reduction in lifetime compared with CdS placed on quartz. The combination of both high cavity quality and strong confinement enhances the spontaneous emission rate by 14 times. c shows the increase in the Purcell effect with the decrease of the square cavity side length (inset of b) as a result of the mode volume reduction accompanied by an increasing cavity quality factor. Very large cavities do not benefit from cavity feedback and exhibit a Purcell effect of about 2 due to confinement along the z-direction alone. This agrees well with a simple theoretical model taking into account the numerous emission processes [6]. The variations in the CdS thickness (45 to 88 nm) for this data set do not play a major role in the emission enhancement.

There are many example of spontaneous emission rate enhancement that have been observed in plasmonic systems [12,16-19]. Here, we focus on those systems that also exhibit laser action. The first example are plasmonic nanowire lasers [3]. These truly nanometer-scale plasmonic laser devices consist of Cadmium Sulphide (CdS) nanowires [20] on a silver film, where a gap layer of Magnesium Fluoride (MgF_2) creates a highly localized transverse mode, as shown in the inset of Figure 4.4.1a. The close proximity of the semiconductor and metal interfaces concentrates light into an extremely small area as much as a hundred times smaller than a diffraction-limited spot (Figure 4.4.1) [20]. The second example is related, but instead of nanowires, the active region and confining geometry is very thin CdS square, as shown in the inset of Figure 4.4.1b. The intense fields that are generated and sustained in the gap region make such lasers highly useful for investigating light-matter interactions. Namely, an emitter placed in this gap region is expected to interact extremely strongly with the laser light. Such light-matter interaction enhancements are also observable to a lesser extent in the CdS gain medium. In both examples, the emission rate was measured by time correlated single photon counting, by weak optical excitation from a 100 fs pulse centered at a wavelength of 405 nm [3,6]. In the first case, emission was collected from the sample at 10 K, where the signal was dominated by I_2 excitons at a wavelength of 489 nm with a natural lifetime of about 400 ps [3]. In the second example,

emission was collected from the sample at room temperature, where the band edge emission near 515 nm has a lifetime of approximately 1 ns.

Plasmonic nanowire lasers show a strong increase of the spontaneous emission rate when the gap size between the nanowire and metal surface is decreased, as shown in Figure 4.4.1a. Lifetime measurements reveal a Purcell factor of more than six for a gap width of 5 nm and nanowire diameters near 120 nm, where hybrid plasmonic modes are most strongly localized [3]. This enhancement factor corresponds to a mode that is a hundred times smaller than the diffraction limit, which agrees well with our mode size calculations, based on the Purcell factor for 1D plasmon waves, given by Eqn. (4).

The Purcell effect is also apparent in the square laser devices operating a room temperature despite a loss of lateral confinement compared to the nanowire case, as shown in Figure 4.4.1b and 4.4.1c. Figure 4.4.1b shows a time correlation histograms for a laser device exhibiting a 14 fold increase in the spontaneous emission rate compared to the natural rate of CdS band edge transitions. While sacrificing the lateral confinement, surface-plasmons undergo total internal reflection at the device boundaries forming an effective cavity with strong feedback. It is this combination of both high cavity quality factors (Q) and strong mode confinement in only one dimension that leads to Purcell factors as large as 18 in the smaller devices. We can describe the spontaneous emission rate in these devices using a combination of both 1D and 3D expression for the Purcell factor. Here, we must sum over contributions to the emission rate including: radiation modes (assumed to be negligible due to thin CdS film in proximity to metal surface); 1D confined plasmon modes that are not cavity enhanced; and 1D confined plasmon modes that are cavity enhanced such that,

$$F_{Sq} \approx F_1 + \sum_i \frac{2}{\pi} \left(\frac{\lambda}{2n_{CdS}}\right)^3 \frac{Q_i}{V_i} \tag{6}$$

where $Q_i = m_i \pi e^{-\alpha L_i}/(1 - e^{-2\alpha L_i})$ is the quality factor and m_i is the mode order. It is difficult to derive an exact formula to compare with the experiment, as we do not know the quality factors or mode volumes of all of the possible cavity modes. We can, however assume an approximate functional form for the dependence on the square circumference, L. We first assume an average mode order $\bar{m} \propto L$; cavity volume, $\bar{V} \propto L^2$; cavity length $\bar{L} = L/\sqrt{2}$; quality factor $\bar{Q} = \bar{m}\pi e^{-\alpha \bar{L}}/(1 - e^{-2\alpha \bar{L}})$; and approximate number of cavity modes, $N \propto L^2$, in the CdS emission bandwidth, we find a Purcell factor with functional form,

$$F_{Sq} = F_1\left[1 + \beta L \operatorname{csch}\left(\alpha L/\sqrt{2}\right)\right] \tag{7}$$

This rough and simple estimate agrees quite well with observed trend in Fig. 4.4.1c. For devices larger than the surface-plasmon propagation length, the cavity feedback no longer plays a role and an average twofold reduction in lifetime is observed owing to the strong confinement of SPPs alone, i.e. $F_1 = 2$. However, for smaller devices, the improved feedback leads to an increased Purcell factor, which provides an estimate of the round trip cavity losses, $\alpha \approx 4,300$ cm^{-1}. This agrees quite well with our theoretical estimates and with the losses of plasmonic

nanowire lasers. Depending on the size of the CdS square, these devices therefore exhibit both 1D and 3D Purcell factors.

The observed enhancements are extremely large when compared with non-plasmonic state of the art optical devices. However, the electric-field intensities in the gap regions of these type of device are at least five times stronger than in the CdS, so we anticipate Purcell factors as high as 100 for light-matter interactions within the gap.

Static Rate Equations

In order to gain at least a basic theoretical understanding of the characteristics of small lasers, we start with a simple steady state rate equation picture of the photon number of a single laser mode, s, and electronic excited state population, n, within a small single mode laser device under continuous pumping, p. The form of these equations is reminiscent of much of the work from the 1990's on microcavity lasers [21]. Particular attention should be paid to the fact that both spontaneous and stimulated processes are proportional to the spontaneous emission rate, A, and are thus both modified by the optical environment through the Purcell effect, where the Purcell Factor, $F = A/A_0$ where A_0 is the natural spontaneous emission of the material and the corresponding modal redistribution of emission. While the Purcell effect can dictate the rate of electronic transitions within a laser, it does not have as strong an effect as the corresponding spatial re-distribution of spontaneously emitted light. A faster spontaneous emission rate into the laser mode mode, A_i, relative to the total spontaneous emission rate into all modes, A, increases the probability of light coupling into that mode, quantified by the spontaneous emission factor, $\beta = A_i/A$. The rate equations are [21]:

$$\frac{dn}{dt} = p - An - \beta\Gamma As(\alpha n - n_0)$$
$$\frac{ds}{dt} = \beta An + \beta\Gamma As(\alpha n - n_0) - \gamma s \tag{8}$$

Here p is a pump rate, Γ is the overlap factor quantifying the spatial distribution of gain relative to the laser mode, γ is the total cavity mode loss rate and n_0 and α are parameters that accounts for the energy level configuration of the gain medium. For example, in a 3-level system with a maximum inversion of n_T, the ground state population is $n_g = n_T - n$, so that $n_0 = n_T$ and $\alpha = 2$, while for a 4-level system, $n_0 = p/A_l$ and $\alpha = 1$, where A_l is the spontaneous decay rate of electrons out of the lower level of the laser transition. A semiconductor laser with a linear gain model is also described by these rate equations where one would choose $\alpha = 1$ and interpret n_0 as the excited state population at transparency. Note that we have assumed an non-depleting pump rate, p, and rapid decay from an upper level to fill the upper laser transition. It is relatively straightforward to apply a similar analysis for systems where the finite number density of excited states depletes the pump.

In steady state, the emitted laser mode photon number, s, and excited state population, n, are related by, $p = (1 - \eta\beta)An + \gamma s$, and the photon number is described by the quadratic equation,

$$\gamma s^2 - s\left[p - p_{th}^{(n)}\right] - [p/\alpha\Gamma] = 0 \tag{9}$$

where, $\alpha p_{th}^{(n)} = \gamma/\beta\Gamma + (1-\beta)An_0$, with solutions of the form,

$$\gamma s = \frac{1}{2}\left(p - p_{th}^{(n)}\right) + \frac{1}{2}\left(p + p_{th}^{(n)}\right)\left[1 - \frac{4}{p}\frac{(1-\beta)An_\infty}{\left(1 + p_{th}^{(n)}/p\right)^2}\right]^{1/2} \tag{10}$$

Where $\alpha n_\infty = (\gamma/\beta\Gamma A + n_0)$. In the limits of very high and very low pump rates, one finds the distinct linear responses for the photon number exhibited by all lasers,

$$s(p \to \infty) = \frac{p}{\gamma} - \frac{(1-\beta)An_\infty}{\gamma}$$
$$s(p \to 0) = \frac{p}{\alpha\Gamma p_{th}^{(n)}} \tag{11}$$

and, correspondingly for the excited state population,

$$n(p \to \infty) = n_\infty$$
$$n(p \to 0) = \frac{n_\infty p}{\alpha p_{th}^{(n)}} \tag{12}$$

It is possible to discern the threshold behaviour of lasers from these linear trends. However, for small lasers with large spontaneous emission factors, the manifestation of a laser threshold is quite distinct from conventional lasers. When the usual but essentially *ad hoc* definition of laser threshold is taken as the pump rate where $s(p \to \infty) = 0$, we find

$$\alpha p_{th}^{(s)} = \frac{(1-\beta)}{\beta\Gamma}(\gamma + \gamma_g) \tag{13}$$

where $\gamma_g = \beta\Gamma An_0$, is the absorption loss due to the gain medium. This definition has given rise to the concept of *thresholdless* laser operation since when $\beta \to 1$, we find that $p_{th}^{(s)} \to 0$ [21]. Some caution is advised here: the term "thresholdless" should be understood to mean "lack of a threshold", as opposed to "an onset of laser action for infinitely small pump rates". Indeed, a great deal of care must also be taken when measuring the threshold of a laser from the corresponding characteristic kink in the light output versus pump response in Fig2a, which is smeared out as $\beta \to 1$. A more detailed analysis shows that the disappearance of the kink can also arise as a manifestation of directionality of the laser relative to the background spontaneous emission. To show this, consider a power meter collecting light from a small laser: emission from the laser mode leaves the cavity at a rate γ_r and is collected with an efficiency η_m, while spontaneous emission is collected with an efficiency η_{se}. Above threshold, the power meter registers a signal,

$$I(p) = \eta\eta_m p - (\eta\eta_m - \eta_{se})(1 - \beta)An_\infty \tag{14}$$

where the amount of spontaneous emission detected from the cavity is $\eta_{se}(1 - \beta)An_\infty$ and $\eta = \gamma_r/\gamma$, is the maximum laser cavity efficiency given by the ratio of radiative, γ_r, and total cavity losses. One can see that if it were not for the directionality of the laser mode relative to the spontaneous emission, ensuring $\eta_m \neq \eta_{se}$, the characteristic kink would also be smeared out, even when $\beta < 1$. This illustrates the point that monitoring the threshold behaviour of a laser by the extrapolated detected response at $I(p) = 0$, can give a subjective measure of threshold that depends on how the light is detected.

$$\alpha p_{th}^{(I)} = \frac{\eta\eta_m(1 - \beta)}{\eta\eta_m - \eta_{se}}(\gamma + \gamma_g) \tag{15}$$

This is extremely important to consider in plasmonic laser systems with high β, since the laser signal often strongly diffracts into the far-field making it difficult to spatially distinguish laser light from spontaneous emission. When measuring laser threshold according to the extrapolated response of the light-pump (L-I) curve, one must take care to ensure effective spatial filtering of the laser mode from the spontaneous emission. However, spatially filtering spontaneous and stimulated emission is impossible when $\beta \to 1$ since all spontaneous and stimulated emission is directed into the same spatial mode. For this reason, this measure of threshold is inappropriate in small laser cavities with low internal losses.

An alternative measure of the transition between spontaneous and stimulated emission dominated operation is to monitor the onset of gain clamping where we know that laser action begins. When defining the threshold in this way, i.e., where $n(p \to 0) = n_\infty$, we find a different expression,

$$\alpha p_{th}^{(n)} = \frac{1}{\beta\Gamma}(\gamma + (1 - \beta)\gamma_g) \tag{16}$$

The two definitions are illustrated in Fig for an ideal 4-level system ($\alpha = 1, n_0 \to 0$). This response shows quite clearly that there is a reduction in the onset of laser action due to an increased β factor that is also consistent with the tenet that threshold should be commensurate with the internal losses of the laser device. While this second definition, $p_{th}^{(n)}$, exhibits a more consistent behavior, notice that as $\beta \to 1$, $p_{th}^{(n)} \to \gamma/\Gamma$, suggesting that at this pump level only the cavity losses are compensated. This would be fine for an ideal 4-level gain medium, but would provide a severe underestimate of the threshold of a 3-level gain medium. Furthermore, it is still difficult to determine the precise onset of laser action for large β due to the smearing of the laser transition. In the next section we show how laser emission at this threshold pump rate can still be quite incoherent.
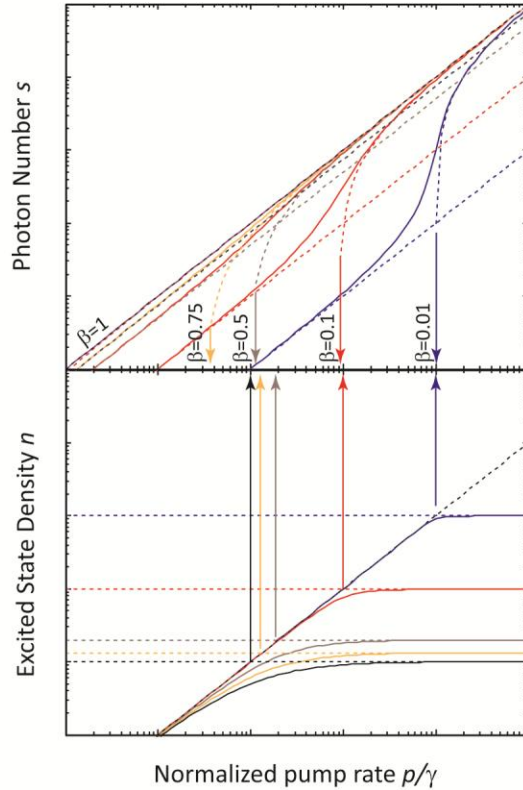
Figure 4.4.2 | Characteristics of the onset of laser action in small lasers modified by the Purcell Effect. The photon number and excited state population are plotted versus the normalized pump rate. Here we assume conditions that are characteristic of plasmonic lasers, where the cavity loss rate is much larger than the spontaneous emission rate, $A = 10^{-4}\gamma$. As mode selectivity increases due to the beta factor the transition from spontaneous to stimulated emission dominated response becomes smeared.

These definitions of threshold highlight an important aspect of plasmonic laser systems – generally stimulated emission begins to dominate when the pump rate is close to the ratio of total cavity loss rate and β. While conventional lasers have relied on relatively low cavity losses to ensure realistic thresholds, since $\beta \ll 1$ [22], plasmonic lasers can operate at much higher cavity loss rates provided there is a substantial improvement in β stemming from a strong Purcell effect and effective mode selection. This behavior has already been seen in plasmonic nanowire lasers [3,6]. Figure 4.4.1 shows normalized light output versus pump curves and laser thresholds for a selection of Cadmium Sulfide nanowire lasers on Quartz and Metallic substrates under the same optical pumping conditions [3]. While the plasmonic nanowire lasers have internal cavity losses estimated to be about 10x larger that the photonic nanowire lasers ($\eta \sim 0.1$), the average plasmonic laser has a threshold no more than a factor of 3 larger than a photonic nanowire laser of the same diameter, as shown in Figure 4.4.1b. We attribute this to the much larger β factors of the plasmonic lasers, as shown in Figure 4.4.1a.

It is quite clear that either a more detailed theory is needed to define the laser threshold or we should change our assertion that the onset of laser action in small devices is a critical phenomenon. To shed more light on this point, we discuss the onset of lasing in more detail with respect to both the spectral, photon and excited state population responses. In the next section, we discuss the origin of this smearing out of the laser threshold due to spontaneous emission noise
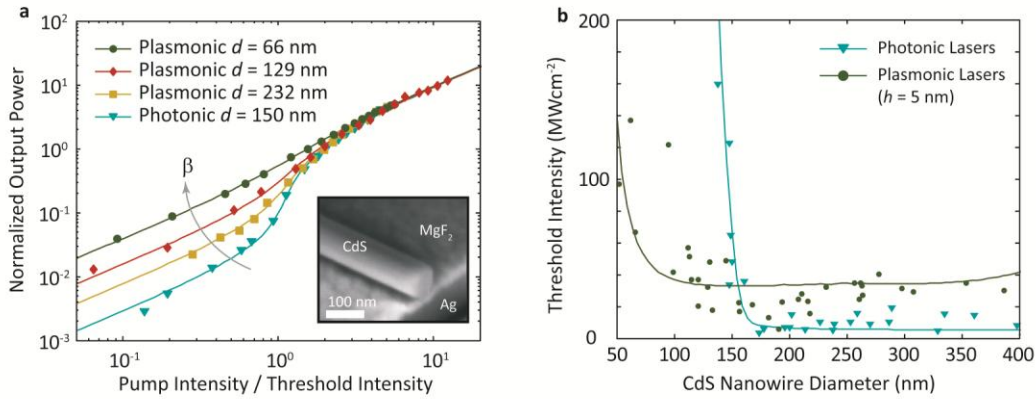
Figure 4.4.1 | Modification of conventional laser characteristics by the Purcell Effect in plasmonic nanowire lasers [3]. a The dependence of measured output power over pump intensity highlights the clear differences in the physics underlying the plasmonic and photonic lasers using a multi-mode lasing model [24]. In particular, our fitting parameter, x_0, is related to the gain saturation of individual longitudinal laser modes and their lateral mode area. A higher value of x_0 corresponds to a smaller mode area and a higher β-factor. Photonic lasers exhibit a clear transition between spontaneous emission and laser operation characterized by $x_0 = 0.026$ for a 150 nm diameter nanowire, in agreement with a recent nanowire laser study [23]. Plasmonic lasers, however, show a strong dependence of x_0 on the nanowire diameter producing much larger values between $x_0 = 0.074$ for larger wires up to $x_0 = 0.380$ for the smallest. b Threshold intensity of plasmonic and photonic lasers versus nanowire diameter. The experimental data points correspond to the onset of amplified spontaneous emission, where coherent peaks start to appear in the laser spectrum. Amplified spontaneous emission in hybrid plasmonic modes occurs at moderate pump intensities of 20-50 MWcm^{-2} across a broad range of diameters, while photonic nanowire lasers, with much lower losses, require 5-20 MWcm^{-2}. Note also, that while plasmonic lasers maintain good mode confinement over large range of diameters as shown in e (50 < d < 500 nm), photonic lasers exhibit a sharp increase in the threshold for d < 150 nm, due to the loss of confinement within the nanowire and subsequent lack of overlap with the gain region [23] shown in h.

Noise in plasmonic Laser Systems

We have seen in the last section how the modification of spontaneous emission can help to control the apparent threshold of plasmonic lasers. This is important as the high losses in such devices can otherwise make the necessary pump rates inhibitive. However, while the increase in β factor serves to lower threshold, this comes at the expense of laser mode coherence. In the following we analyze the noise characteristics of plasmonic lasers based on their expected

linewidth due to residual losses at finite pump rates above threshold. For large pump powers the photon rate equation shows that,

$$\frac{ds}{dt} = \beta\gamma An_\infty - \gamma's = 0 \tag{17}$$

According to this expression, the photon number in the laser mode is fed by spontaneous emission (first term), while light escapes from the cavity at a modified rate γ' (second term), which accounts for both the loss compensation by stimulated emission and underlying cavity losses. The reader will immediately notice that in steady state, the laser mode losses must still be finite depending on the rate of spontaneous emission. If more spontaneous emission couples to the laser mode due to a high β, the laser mode's loss rate, or indeed spectral linewidth $\Delta\nu = \gamma'/\pi$, must also be larger. In steady state, the output power, $P_{out} = h\nu\gamma_r s$, is

$$\Delta\nu = \frac{h\nu}{\pi}\frac{\gamma_r(\gamma + \gamma_g)}{\alpha\Gamma P_{out}} = \frac{\pi h\nu\Delta\nu_r}{\alpha P_{out}}\left(\frac{\Delta\nu_t}{\Gamma} + \beta An_0\right) \tag{18}$$

Where γ_r is the radiative out-coupling rate from the cavity, $\Delta\nu_r$ is the equivalent radiative linewidth and $\Delta\nu_t$ is the equivalent total cavity linewith. The first term in the bracket generates the Schawlow-Townes linewidth limit [25] modified by a factor $\eta = \gamma_r/\gamma$, while the second is the additional spontaneous emission noise arising from a non-zero ground state population. The first term is in agreement with the original formula by Schalwlow and Townes for an ideal 4-level gain system in a cavity with only radiative mirror losses, where $\alpha = 1, n_0 \to 0$.

It is most interesting to observe that the Schawlow-Townes term is independent of modifications to the spontaneous emission rate and represents the underlying laser noise limit for ideal 4-level laser systems. The modification from the usual expression, by the factor η, leads to a higher coherence for lossy cavities than we might have expected. This is entirely consistent with formulations of the laser line-wdith for lasers with parasitic cavity losses [3] and for experimental observations of plasmonic laser line-widths. For example, in a plasmonic laser cavity (i.e. $\eta \ll 1$), the line width should be, $\gamma'\sim\gamma_r$, just above threshold. In the case of plasmonic nanowire lasers, despite a cavity loss of 10,000 cm^{-1}, laser lines are clearly observable just above threshold with a line-width similar to that of Fabry-Perot modes of a lossless nanowire, as shown in below (Figure 4.4.5). Note that strong dispersion within the gain medium, especially in semiconductors, also modifies the line-width formula [3,26].

On the other hand, the Purcell effect does modify the spontaneous emission noise significantly, predominantly through β, which can be many orders of magnitude larger in plasmonic lasers compared to conventional ones [3,6]. We also note that the noise of a 4-level laser system has a lower limit given by the power broadening phenomenon, dictated by the decay rate, A_l, of electrons out of the laser transition's lower level. In this case, the noise is limited by $\gamma' > \gamma_r\beta A/A_l$, which could severely limit the performance of plasmonic laser systems based on 4-level gain media.
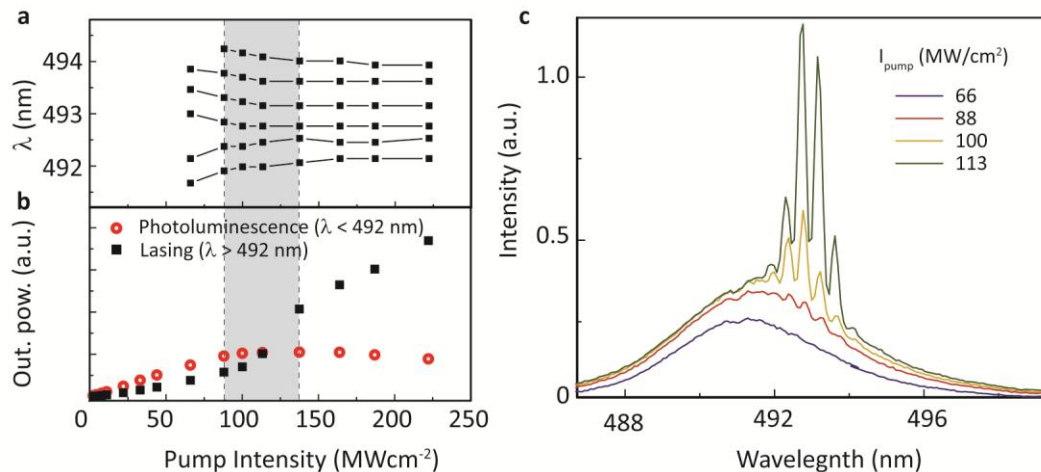
Giant Frequency Pulling

The very high material gain needed to compensate for the losses of metal generates extremely strong cavity mode dispersion. This behavior has been reported in a number of plasmonic lasers with Fabry-Perot type cavities with single transverse laser modes [5], as illustrated in Figure 4.4.2. The longitudinal mode spacing, $\Delta\lambda$ is governed by the expression, $\Delta\lambda = \lambda^2/2n_gL$, where L is the wavelength and n_g is the effective laser mode group index. For plasmonic nanowire lasers [3], the mode spacing of all measured devices above threshold followed an approximately linear relationship of $\Delta\lambda$ vs. $1/L$, confirming that the single transverse mode Fabry-Pérot cavity responses all exhibited essentially the same internal gain (red line in Figure 4.4.2a). The corresponding average group index for theses plasmonic nanowire lasers is about 11, much higher than expected for passive waveguides, which would be approximately 3. For example, photonic nanowire lasers (without metal substrate) have a group index of around 3-4 [26]. Similarly, Martin Hill et al. have observed high mode group indexes in metal-insulator-semiconductor-insulator-metal structures [5]. In this work, the authors report a group index that increases with decreasing semiconductor core width, shown in Figure 4.4.2b. Since the core width of these devices strongly affects laser cavity mode propagation loss, it is highly likely that this observation also reflects the high internal gain, necessary to make these lasers operate. The high group index for plasmonic nanowire lasers has been attributed to the strong frequency pulling effect, arising from the large amount of gain required to achieve lasing in the lossy plasmonic system. The nanowire is consequently highly dispersive across the narrow gain spectrum. A more detailed study of this "Frequency Pulling" effect, as it is more widely known [27] is presented in the next section.
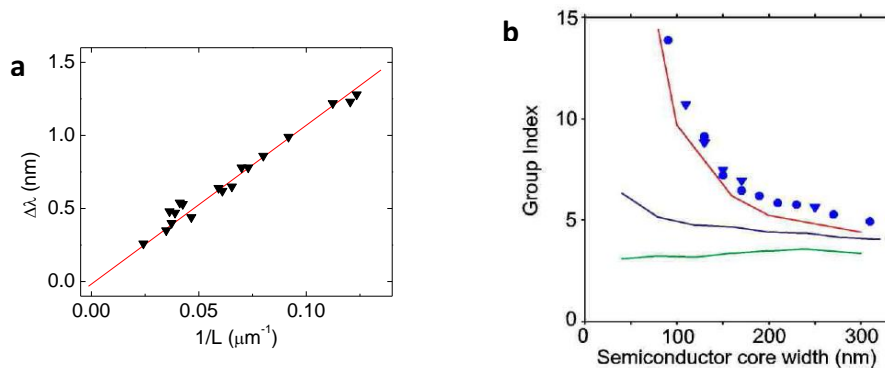
Figure 4.4.2 | Observations of large group indexes in plasmonic lasers. a Longitudinal mode spacing versus inverse nanowire length. The data confirms the Fabry-Pérot like cavity behaviour for the plasmonic laser. The red line is a linear fit to the data giving an effective index of 11. **b** Group index, estimated from mode spacing in laser spectra, versus semiconductor core width for metal-insulator-semiconductor-insulator-metal (MISIM) plasmon lasers [5]. Blue circles are estimates from 6 micron long devices and blue triangles are estimates from 3 micron long devices. All measurements at 78K except for the two smallest, which were at 10K. Blue, green and red curves are simulated group indexes. Blue - semiconductor only filled MISIM structures (no insulator). Green - including the insulator layers. Red – include SiN layers and varying dispersion for the InGaAs core. InGaAs dispersion was varied from $d\varepsilon/d\omega = 2 \times 10^{-13}$ s for the thinnest device to $d\varepsilon/d\omega = 2 \times 10^{-14}$ s for the thickest.

In the following can see the effect of high gain in plasmonic nanowire lasers in the region where amplified spontaneous emission transitions to lasing. In Figure 4.4.5 we show the results of resolving the spectral and light output properties of a plasmonic nanowire laser as a function of the pump power. Amplified spontaneous emission is deemed to start when Fabry-Perot ripples are discernable, in this case near a pump intensity of 88 MWcm^{-2}. The laser threshold is associated with clamping of the internal gain, known as "gain saturation". We therefore expect the frequency pulling effect to "clamp" at the threshold as the gain saturates. At the same time, the spontaneous emission saturates as the stimulated process starts to dominate. At this point, laser emission is expected to further increase linearly with the pump intensity. In Figure 4.4.5b we can see the increase in frequency pulling throughout the amplified spontaneous emission regime and subsequently, a constant frequency pulled response once lasing has been achieved. At the same time, by comparing those parts of the spectrum that show spontaneous emission, with those that show laser lines, we can see that the underlying photoluminescence saturates, in this case somewhere between 100 MWcm^{-2} and 113 MWcm^{-2}.

Figure 4.4.5 | Frequency pulling in a plasmonic nanowire laser with diameter, d = 112 nm, and length, L = 33.7 μm [3]. The shaded area in a and b indicates the blurred transition from amplified spontaneous emission to lasing, characteristic of small lasers. **a** Positions of Fabry-Perot resonances against the peak pump intensity extracted from the spectra in c. For lower pump intensity, the effect of frequency-pulling is clearly seen. At the threshold (on-set of lasing), the frequency pulling becomes constant, indicating that the gain is clamped. **b** shows evidence of gain saturation associated with such gain clamping. Here for wavelengths less than 492 nm, only photoluminescence occurs, while lasing occurs for wavelengths greater than 492 nm. While the photoluminescence clearly saturates, the power in the Fabry Pérot modes continues to increase. **c** Emission spectra of the studied plasmonic nanowire laser exhibiting clear Fabry-Pérot peaks.

Monitoring Gain

We saw from the large frequency pulling effect in Figure 4.4.5 that the gain in plasmonic laser systems can be extremely strong. It is particularly interesting to explore this relationship further

as it provides an additional means to study the onset of laser action despite the blurring of the laser threshold. In particular, we can identify that coherence rapidly appears in the emission spectrum of a plasmonic laser, well before the gain is fully clamped. This suggests that the concept of threshold of small lasers is no longer appropriate, since the onset of laser action is no longer a critical phenomenon.

The frequency pulling effect allows us to estimate the material gain of lasers simply by measuring the Fabry-Pérot mode spacing. In conventional lasers this is quite difficult to do as the effect is extremely small; however, in plasmonic lasers the effect is extremely pronounced, as illustrated by Figure 4.4.5. As an example, we have analysed the spectra of a 112 nm diameter, 33.7 um long plasmonic nanowire laser [26] as a function of peak pump pulse intensity, shown in Figure 4.4.5. The process of estimating the material gain starts from evaluating the average group index, which is related to the nanowire length, L, and cavity mode spacing, $\Delta\lambda$, by $n_g = \lambda^2/2L\Delta\lambda$. Figure 4.4.3 shows the group index extracted from the peak positions in Figure 4.4.5c. To extract the material gain, we have used a simplified description of the gain from I_2 excitons in bulk CdS, which dominate the emission over a wide range of pump intensities. The CdS permittivity is described by,

$$\varepsilon_{CdS}(E) = \varepsilon_{CdS}^\infty + \frac{2E_{CdS}\chi}{E^2 - E_{CdS}^2 - 2i\gamma_{CdS}E} \tag{19}$$

Where $E_{CdS} = 2.53$ eV and $\gamma_{CdS} = 0.013$ eV is the CdS I_2 exciton energy and linewidth respectively and $\varepsilon_{CdS}^\infty = 5$ is the background permittivity of CdS. The group index, n_g, of the mode is then calculated using a finite element method mode solver with a nanowire permittivity, $\varepsilon_{CdS}(E)$, where the population inversion and gain is parameterized by χ. The relationship between the group index and peak material gain, g_{CdS}, in the CdS nanowire is shown in Figure 4.4.3. The modal gain, $g = \Gamma g_{CdS}$, within this particular plasmonic nanowire laser is in reasonable agreement with the expected modal losses, α,

$$\alpha = \frac{1}{L_m} - \frac{1}{L}\ln R \tag{20}$$

where $R \approx 20\%$ is the reflectivity of the nanowire facets, $1/L\ln R \approx 500$ cm^{-1} is the cavity loss and $L_m^{-1} = 4{,}100$ cm^{-1} is the propagation loss of the plasmonic mode, based on the data of Johnson & Christy [28]. While the material gain, estimated from the frequency pulling experiment, reaches a maximum of about 10,000 cm^{-1}, the actual modal gain is nearer 5,000 cm^{-1} for an estimated gain-mode overlap factor of $\Gamma = 50$ %. This matches quite closely with the theoretical losses of $\alpha \approx 4{,}600$ cm^{-1}, from the losses of Silver predicted by Johnson and Christy. However, the quality of the Silver film is likely to play an important role and in the overall losses and this estimate is significantly less than that predicted by the data of Palik [29], which places the theoretical losses at $\alpha > 15{,}000$ cm^{-1}. We also note, that while our estimate is relatively crude, the losses are unlikely to be as high as suggested by the data of Palik.
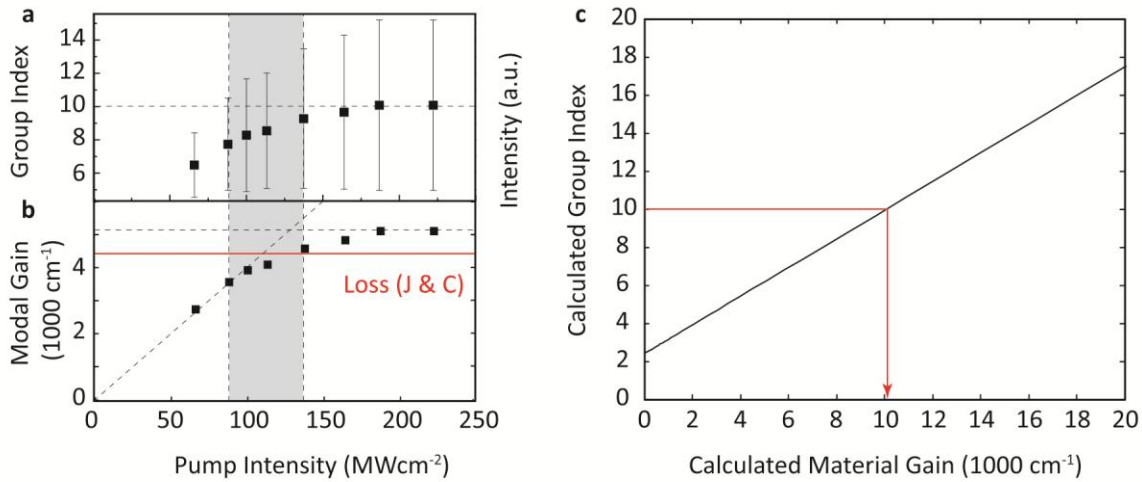
Figure 4.4.3 | Estimating material gain for a plasmonic nanowire laser with a diameter, *d* = 112 nm, and length, *L* = 33.7 μm. The shaded area in **a** and **b** indicates the transition from amplified spontaneous emission to lasing. **a** The average group index calculated from the average mode spacing and the nanowire length. Error bars are mainly due to limited spectrometer resolution (~0.25 nm). **b** The high group index arises from strong dispersion as a result of the gain and can be used to estimate the internal material gain. In this case, the material gain clamps at about 10,000 cm⁻¹, which concurs well with the estimated losses of this plasmonic cavity. **c** Calculated relationship between the modal group index and the material gain.

Directionality and polarization in plasmonic lasers systems

Plasmonic lasers generate highly confined light in the near field. This light is only visible in the far field via scattering from the boundaries of the laser cavity. For example, in our work [3] and the works of Hill et al. [4,5], light is scattered from these lasers by the sharp edges of the finite cavity [4,5, 30] into a diffracting beam. In contrast, dipole-like cavities [8] scatter light in a much broader range of directions. Without some form of near field control over the out-coupling of light from these lasers, the poor directionality renders them of little use compared to conventional lasers. To date, all plasmonic lasers systems have relied on weak scattering into the far-field. However, there is the potential to achieve good control over the near field out-coupling from these devices since they have very well defined modal structure and polarization. In this section we discuss studies of the polarization of scattered light from plasmonic lasers and the diffraction that arises from their small cavities. Such studies have been extremely useful in determining which modes are lasing and for unraveling the well-defined mode structure of plasmonic lasers systems.

In the first example, we consider again plasmonic nanowire lasers [3,6], where we have looked in detail at the polarisation properties of the laser mode. In this work we have observed different polarisations of scattered light from plasmonic lasers and non-plasmonic (i.e. purely photonic) ones. In the majority of cases, the scattered light polarisation of photonic lasers was perpendicular (x-direction) to the nanowire axis, while for plasmonic lasers, the scattered light polarisation was parallel (z-direction) to the nanowire axis. Figure 4.4.4a and Figure 4.4.4b show results of polarisation angle resolved emission spectra for plasmonic and photonic lasers

respectively. This information is critically important as we can identify the internal mode structure of a small laser by its predominant polarization. In this case, a hybrid plasmon mode, whose dominant field components are perpendicular to the metal surface and parallel to the nanowire (Figure 4.4.4c,e and Figure 4.4.4d,f), would produce scattered light that is predominantly polarized in z-direction. The field distribution is highly localized between the nanowire and metal surface, with a modal area that can be as small as $\lambda^2/400$. Lasers exhibiting polarization along the nanowire axis, therefore lase in highly confined plasmonic modes. For nanowire diameters less than 150 nm, this is the only scatter polarization that is supported by the plasmonic lasers. However, plasmonic lasers with diameters larger than 150 nm can also support a photonic mode, which is not bound to the metal surface and, in rare cases, leads to lasing that scatters x-polarized radiation in the far field. On the other hand, the dominant electric field components of the photonic modes of the nanowire lasers are parallel to the quartz substrate (**Error! Reference source not found.**d and 4.4.6f), producing scattered light that is predominantly olarized in the x-direction. These photonic modes exhibit diffraction limited confinement and are 'cut-off' for diameters smaller than 140 nm, inhibiting laser action [3].
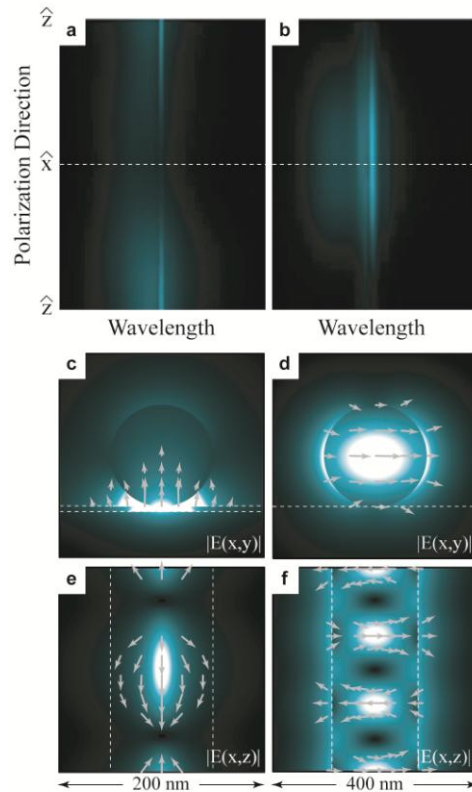
Figure 4.4.4 | Nanolaser Polarization dependency [3]. Left: a & b experimental maps of emission polarisation of scattered light from the nanowire end-facets of a plasmon laser and a control photonic laser, respectively. A dependence on polarisation direction is apparent for both the narrow laser lines as well as the broad background spontaneous emission. While plasmon laser emission is polarised parallel to the nanowire axis, nanowire emission is polarized perpendicular to the nanowire axis. c, d, e & f are maps of |E| fields of the plasmonic and photonic lasing modes in the x/y (c & d) and x/z (e & f) planes, where the arrows indicate the direction of the |E| field. The |E| field of the plasmon laser mode is predominantly polarised along the nanowire axis and scatters most effectively to radiation with a similar polarisation. and circularly polarized nature of the modes.
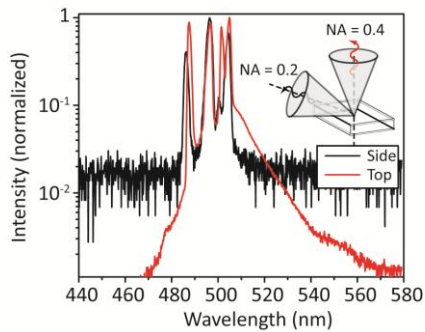
Figure 4.4.5 | Laser emission angle dependency [6]. Emission spectrum above threshold for a multi-mode plasmonic laser for different collection angles. Light collection at large angles from the surface normal (black line) is dominated by the scattering from the lasing cavity modes, while near the surface normal direction a much larger spontaneous emission signal is observable. The modes of the laser diffract significantly after out-coupling.

To date, there have not been any detailed studies examining the extent of diffraction from plasmonic lasers. However, to illustrate the relevance of diffraction, we refer to the recent work on room temperature plasmonic lasers based on semiconductor nano-squares. Figure 4.4.5 Shows the light collected from a plasmonic laser from the surface normal into and NA = 0.4 and at an angle to the surface normal into an NA = 0.2. The same clear laser lines are observable over the broad range of angles indicating strong diffraction of the light from the near field. Furthermore, light collected along the surface normal shows a strong spontaneous emission background, while at an angle, the spontaneous emission is strongly suppressed, as one would expect a Lambertian-like profile from spontaneous emission near a metal surface.

It is apparent that the scattered light from plasmonic lasers exhibits poor directionality, which is of limited use. For this reason, plasmonic lasers are more suitable for applications of light in the near field, for example when light is coupled out of them into waveguides for use in Optical Circuits, for example as we will discuss in sub-chapter 4.5. However, another possible application of these devices is to use the light within the laser cavities. Light within the laser has the potential to enhance interaction between light and matter providing for a new form of near field spectroscopy for extremely sensitive detection [12].

Dynamic rate equation analysis

All plasmonic Nanolasers demonstrated to date have operated under pulsed pumping [2,3,6]. In some cases, the pulses are long enough to be considered quasi-continuous and are describable using a static rate equation analysis. Here, we explore the properties of plasmonic lasers pumped with pulses that are short relative to the spontaneous emission lifetime. While extremely fast pump pulses do not significantly modify the characteristic threshold behaviour of plasmonic lasers, the internal dynamics can be extremely fast due to short cavity lifetime, i.e. high cavity loss, the Purcell effect and large β factors. This may be of considerable interest toward new applications area of these laser devices, in particular, high intensity laser physics.

Figure 4.4.6 Light-pump curve and transient response of dynamic rate equation analysis. a, Non-linear light-pump curve highlights the onset of lasing. We can identify laser action from the dependence on the spontaneous emission factor, β, Which shows the laser's ability to couple directly to the laser mode. Note that the horizontal axis is labeled in physical units and is about an order of magnitude less than the threshold observed in the experiments. This is due to the omission of the unknown exciton population at transparency from the calculation. **b**, shows the saturation of the calculated time averaged gain within the laser for $\beta = 0.5$ according to Eqn (21). The corresponding transient laser responses are shown in c **-** h**.** Here, the effect of gain switching can be observed. The gain switching leads to a fast output pulse that can be as fast as the pump pulse since the cavity photon lifetime is much shorter than the pump laser pulse.

We have solved the rate equations using parameters according to the experimental conditions of the plasmonic nanowire laser work [3]: the incident pump laser pulse, $p(t) = p_0 \exp\left(-4\ln2(t - t_0)^2/\Delta t^2\right)$ has a full width half maximum pulse width, $\Delta t = 100$ fs; the natural lifetime of bulk CdS I$_2$ exciton emission is $A_0^{-1} = 400$ ps [31]; the Purcell factor is $F = 5$, giving a spontaneous emission lifetime of $A^{-1} = 80$ ps [our-nature]; the photon lifetime in the cavity is, $\gamma^{-1} = 13$ fs, corresponding to a Fabry-Perot modal cavity loss of 5,000 cm^{-1} [3]; the mode confinement factor, $\Gamma = 0.5$; the pump beam has a spot size of 40 µm and we assume complete absorption of light within the nanowire cross section of 40 µm long and 100 nm diameter; and we have varied

the spontaneous emission factor $\beta = [0.1 - 1]$. In the following simplified treatment we have had to set $n_0 = 0$ as the exciton population at transparency is unknown, which would give at least an order of magnitude underestimate of the threshold intensity. Figure 4.4.9**Error! Reference source ot found.**a shows the output power versus peak pump intensity for the simulated devices. In this case, we can see that the pump intensity necessary to reach threshold is between 1 - 10 MWcm^{-2}, which is within the expected order of magnitude of what we observed in the plasmonic nanowire laser experiments [our-nature]. When examining the corresponding light-pump curves, one can also immediately see the same effect of the spontaneous emission factor, β, which smears the transition kink between spontaneous dominated and stimulated dominated emission processes, in a similar manner to the static case.

We have also examined the transient response of the output laser pulse. As expected, this exhibits the traits of gain switching due to the rapid turn on time of these devices, as shown in Figure 4.4.6c-h. In particular, it is important to note that gain switching, occurs on the time scale of the plasmon lifetime, which can be as small as 10 fs. This suggests that plasmonic lasers could be modulated at extremely high speeds, since relaxation oscillations will have characteristic frequencies as high as 10 THz. Furthermore Figure 4.4.6c-h reveals the changing shape of the pump pulse for various pump powers above threshold; just above threshold, a gain switching effect leads to a narrowing laser pulse. Finally, at very large pump powers, the output photon pulse starts to resemble the shape of the pump pulse. The appearance of transient effects indicates the achievement of laser threshold and this can be corroborated with the saturation of the time averaged gain over the pulse duration (Figure 4.4.6b),

$$g = \frac{\int \beta \Gamma As(\alpha n - n_0)dt}{v_g \int sdt} \tag{21}$$

The fast transient dynamics within these plasmonic lasers could provide the means to deliver energy to the nanoscale on femtosecond timescales, and thus achieve extremely high intensities in the near field.

4.5 Technological Impact & Outlook

Since the invention of the laser in the middle of the last century laser devices have been utilized in a vast number applications. They range from various scientific and industrial applications to medical and military usages to commercial and even the private sector [1]. The driver behind this success story is, certainly, the underlying physical processes creating and sustaining the laser light itself; the temporal coherency, high monochromaticity, and ability to reach extremely high powers and power densities are all properties which allow for a variety of applications.

	Nanolaser	Conventional Laser
Cavity Size	Below diff limit – Tiny	Above diff limit – large
Power Output	Less power (but high Power density)	Higher power
Usage Range	Near field	Far-field
Laser Threshold Level	Medium	Low
Emission Profile	Non-directional	Directional
Modulation Speed	Ultra fast (THz+)	< 50GHz

Table 4.5.1 | Qualitative comparison of Nanolasers with Conventional Devices.

This leads to the question, what usages are potentially possible for Nanolasers in particular plasmonic-based devices? In addressing this question, let us summarize the very physical specialties of the plasmon Nanolaser as introduced in chapter 4.4 and demonstrated in chapters 4.2 and 4.3. The often feared high ohmic metal losses, which could increase the lasing threshold beyond usability, are effectively mitigated by either deploying low-loss mode design architectures [2,3] and increasing the optical mode selection via the Purcell effect and high spontaneous emission factor as introduced in chapter 4.4.

Photonic Integrated Circuits (PIC)

Relatively soon after the introduction of electrical circuit interaction (ICs) in the 1950's and 60's a similar scheme of circuit integration was proposed by D. Miller in 1969 [4], on-chip lasers create photons, modulators encode the data signal onto the light stream, waveguides route these optical data and integrated photo-receivers convert the optical signal back into the electrical domain (Fig. 4.5.1).

Optical Network Technology

Traditional   vs.   Photonic Integration

Laser   Mod.   MUX   DMUX   λ-lock
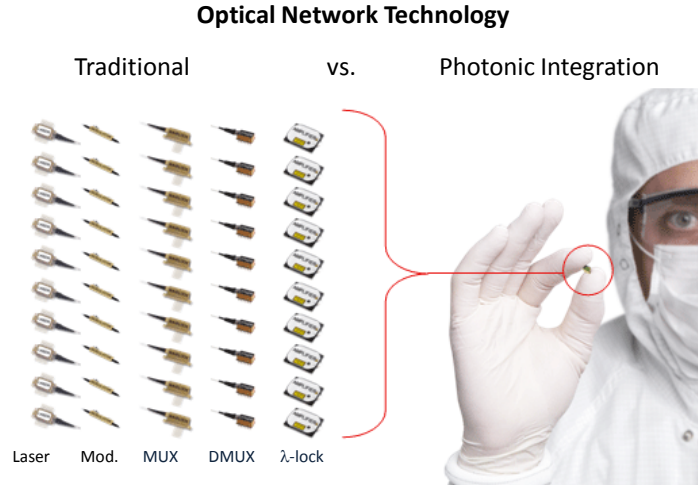
Figure 4.5.1 | Photonic Integration. Traditionally discrete optical components becoming integrated onto a chip towards improving speed, efficiency and reliability [5].

With the race of products based on PICs having already started (Infinera, Luxtera, Intel), the question arises of what the next step after these initial demonstrations will be? The logical answer would be, these currently developing PIC solutions will have to be become significantly smaller and more efficient. In other words, with the end of electronic Moore's Law coming in sight (~2020) [6], there is a photonic-electronic hybrid scaling law emerging that seems to be driven not by transistor scaling, but data bandwidth routing [7]. Like any exponential scaling trend, it is just a matter of time when photonic circuit functionality and thus the individual device footprint and performance will enter the regime of the nanoscale.

However, one of the main bottle-necks for down scaling photonic circuits was and still is the realization of an integrated and efficient light source on the chip. The problem starts with the material choice. The ideal laser material, from an industry standpoint, would be a group IV semiconductor (e.g. Si, Ge) due to the mature existing processing infrastructure, however, the indirect band-gap of these materials prohibits efficient light creation [8]. Current solutions of on-chip light sources are either a monolithic integration of a laser device into a costly III-V wafer [9] or to growth the laser device on a separate (still costly) III-V wafer and transfer it (e.g. via wafer bonding) onto a prefabricated low-cost photonic routing platform (e.g. SOI technology) [10,11]. Both methods, while doable and possibly economical now, are unlikely to be profitable in the mid to far future due to the exponential scaling trend of data bandwidth and device footprint (Fig. 4.5.2).
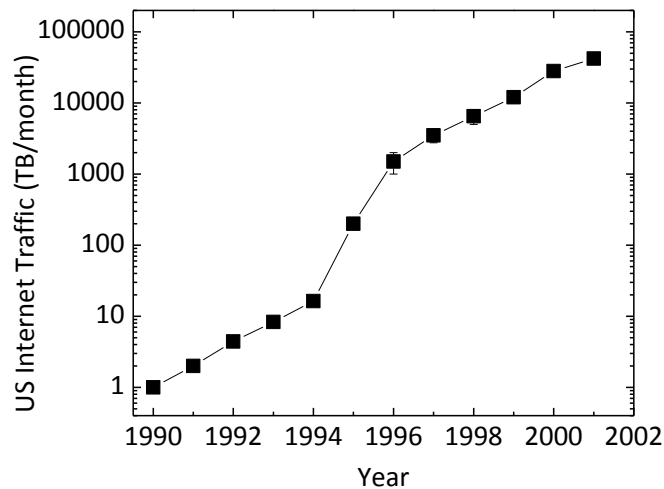
Fig. 4.5.2 | Internet Bandwidth vs. Time. The data bandwidth growths exponentially over time, requiring for stringing technology that is able to keep up with this fast pace – the solution is photonic integration. Because of its parallism (WDM-wavelength division multiplexing), PICs are able to provide this demand.

Plasmon Nanolasers could offer a solution for a light source towards ultra-scaled photonic circuits; the high optical lasing mode selectivity due to a large spontaneous emission and Purcell factor can compensate for the higher cavity loss arising from high mirror losses due to small size and metal quenching losses [2,12,13]. Furthermore, with integration space and footprint becoming more and more tangible not only the small physical size of Nanolasers in general will become a critical differentiation, but also the synergies between electronic and photonics are becoming key design factors. For instance, the very same metal structure of a plasmon-based Nanolaser that confines the optical field and typically also defines the optical cavity, can now conveniently be used to electrically address the laser; for driving or modulating the laser or temperature stabilizing it [14,15].

Furthermore, with the tremendous increase in computing power over the last decades, the input/output (I/O), transmittance (Tx) and reception (Rx) of the high bandwidth data streams especially in and out of the processor core to outside systems (mother board, internet, …) is becoming more and more bandwidth limited [16]. A solution to this challenge is to bring the optical domain, which is capable of delivering high bandwidths, closer to the computational core [17]. In such a scenario the photonic elements could be implemented onto the same electronic core chip and thus had to yield to similar footprint laws as electronic components. Thus, with typical telecommunication wavelengths being on the order of 1.5 μm, the optical components have to be sub-wavelength in mode size.

Lastly, the aforementioned exponential data or bandwidth increase of the internet and other telecommunication methods (e.g. smart phones, ipads, connected cars, homes, etc …) can be generally addressed from two fronts; increasing the speed per channel, increasing the number of channels or a combination of both. The step from TDM to WDM to DWDM created a boost in

data bandwidth [18,19]. However, increasing the speed of a single channel is challenging and requires precise device design of the laser system including the WDM mode spacing, modulators wavelength stabilizers etc. Here, conventional (non diffraction limited and non plasmonic) laser sources face speed limitations given by their cavity loss (see chapter 4.4) and gain compression effects [21, 22]. Unconstrained from both these limitations, plasmon Nanolasers are proposed to provide unprecedented direct modulations speeds into the THz region, which is far beyond conventional laser performance capabilities.

With application opportunities arising for Nanolasers there are also challenges to overcome [22-24]. For instance due to the small modal size, the 'squeezed' (sub-wavelength) laser light typically strongly diffracts from the laser source into free space. In particular in PIC applications the laser light needs to be efficiently coupled into a waveguide bus. However, high symmetrical cavities [12-14], and/or the conversion of surface-plasmon waves into photon laser light [3] thus far resulted in light propagation in all directions prohibiting the collimation for the reported Nanolasers. Furthermore, for metal coated plasmon laser designs, the emission is shielded by a metal layer reducing outcoupling efficiencies significantly [14,25]. Another challenge towards to on-chip integration is to realize electrical connections to Nanolasers without dramatically increasing the footprint and disturbing the optical mode, which is a critical step towards direct modulation and electrically pumping of the Nanolaser [news and focus papers about Nanolasers]. Lastly for large scale integration, the assemble of Nanolasers into light-source arrays is necessary [22-24]. While electrical injection and room temperature operation has been demonstrated thus far, directional emission and direct and efficient coupling into a waveguide bus without introducing high losses is still to be explored. After the pioneering plasmon Nanolaser work of the Berkeley group of Prof. Zhang, the group recently utilized a cross-bar plasmon Nanolaser design demonstrating all of the above challenges, except electrical pumping [15, chapter 7.].

The nanoscale gain material volume of Nanolasers does produce a limited amount of optical light power. Current PIC platforms, however, have much higher optical power demands than what Nanolasers can probably ever produce. Is this a show-stopper for future Nanolaser PIC integration? The answer is probably no, since the ultimate PIC photon level (power density) limits are set by the sensitivity of the photodetector on the receiver end of the photonic circuit [26,27]. Thus, the photon-to-electron conversion sensitivity limiting the photodetector is governed by the electrical shot noise and the operating temperature (Fig. 4.5.3). The minimum optical power in the circuit must therefore be larger than $40k_BT$, where k_B is the Boltzmann constant and T the operation temperature, which already includes a 10x safety margin in terms of signal-to-noise. Notice, that $40k_BT$ equals to 1eV or the energy of a single photon with the wavelength being on the order of a micrometer, the typical wavelength for telecommunication. We thus see, that the overall power level of a scaled photonic integrated circuit could be down to a single photon per bit, a level certainly attainable by Nanolasers. In contrast, current PIC and optical fiber technology operate with bit sizes on the order of 10^4 - 10^5 photons [26,27].

$$\left(\Delta I\right)^2 = 2qI \times BW$$

$$Signal - to - Noise = \frac{I}{\sqrt{2qI \times BW}}$$

$$Thus: I > 2q \times BW \quad and \quad qV > energy @ 300K = 2kT$$

$$Min.\,Required\,Power = P = IV = 2qBW \times \frac{2kT}{q} = 4kT \times BW$$

$$Say\,as\,a\,safety\,margin\,40kT \doteq 1eV\,(Single\,Photon\text{-}level)$$

Figure 4.5.3 | PIC sensitivity limits. The photon detection sensitivity at the receiver of the PIC is limited by the electrical shot of the photoreceiver and can approach a single photon level, which opens possibilities for low power Nanolaser devices as light source.

Sensors & Bio-Medical Applications

Optical metrology and in particular, sensing applications, are becoming extremely important in the bio-medical arena. Interfacing and sensing biological as well as chemical substances for health treatments and/or chemical trace detections need to be carried out with the highest sensitivity and selectivity via optical detection and analysis. With emerging lab-on-the-chip technology platforms [28], a small, integratable and efficient light laser source is on demand. Plasmon Nanolasers could be integrated with micro-fluidic channels for future lab-on-chip applications as outlined in Figure 4.5.4. The unique optical sub-wavelength mode feature of the plasmon laser approaches single molecular scales, which enables such a bio-sensor to become extremely sensitive. Furthermore, the aforementioned HPP mode system could be utilized with a small air-gap between the metal and the semiconductor laser part where a molecular gas or specimen could be flowed through or channeled by towards various sensing and bio-molecule detection applications such as DNA sequencing. With the high photon density and small optical mode size, plasmon Nanolasers could also become useful as manipulators and cutting tools of biological tissues, e.g. affected cancer cells, with unprecedented chirurgical precision for health care treatments.
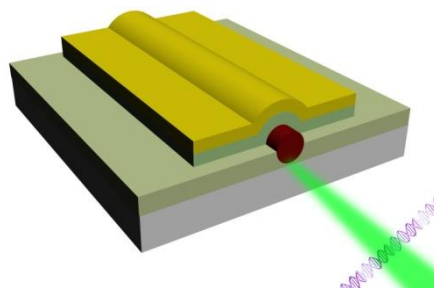
Figure 4.5.4 | Plasmon lasers as Bio-molecule sensors. Bio sensor scheme highlighting the length scales of the optical signal, which can approach the ise of individual protein molecules (~5 nm).

Ultra-Fast Spectroscopy

As established in chapter 4.4, plasmonic Nanolasers are potentially able to provide ultra-fast (fs-scale or faster) optical processes [29], which is possible to the unique internal laser processes inside such devices and the high-loss cavity system. Even though the absolute optical power provided by these lasers is small, the optical intensity can be quite high due to the small size. These Nanolasers can therefore be envisioned to become a platform for ultra-fast spectroscopy with unprecedented footprint, energy and cost functions. Again, the lossy (low Q-factor) character of plasmonic systems Fourier-transformed into the time domain, provides for ultra-fast optical processes which can be utilizes for various spectroscopic techniques and studies.

Outlook

The above described technological opportunities and challenges for plasmon Nanolasers are summarized in Table 4.5.2. However, as history had shown with the demonstration of the first laser, the exact technological scope and more importantly the sociological impact of such inventions is often difficult to predict and might even take many years since its discovery to become sought out to become implemented towards a concrete product or solution.

So, what are the practical limitations of these lasers? Generally, Nanolaser devices rely on stringent fabrication control on sub-100 nm length scales (e.g. line-edge roughness). With state-of-the-art processing technology becoming more and more precise, these length scales are becoming more and more feasible. Secondly, the extreme high optical field intensities inside the optical confinement of plasmonic Nanolasers, which can approach $\lambda^2/400$ [2,3] place clear limitations on material choices, in particular for the laser gain material. But also the best choices for metals in plasmon lasers, i.e. the inert noble metals like Silver and Gold, can face challenges due to reduced melting temperatures arising from thin metal film sizes where the bulk meting temperature is reduced or fabrications defects. Furthermore, Nanolaser arrays or laser reliability tests have not been demonstrated to and will show the maturity of this still young technology.

Opportunities	Device Challenges
Tele-communication/ IT	Directional Emission
Scaled Photonic Integration	I/O Coupling Efficiencies
Bio / Medical Applications	Electrical Pumping
Sensitive Sensors	Optical Losses
Ultra-Fast Spectroscopy	Arrays and Integration

Table 4.5.2 | Technological Opportunities and Challenges for Nanolasers

However, with progressing processing technology, device and chip integration skills and expanding knowledge about the internal Nanolaser processes on a fundamental level, what are we to expect to achieve if we were to invest in this technology for the next 10 years? While the

answer is certainly quite unclear at this moment, there already exist various leaps-of-faith that above mentioned technologies and sociological impacts are under way. For instance certain US government agencies and industrial corporations are heavily investing recently in nanophotonic R&D. Such programs for instance invest in the exa-scale (10^{18} bits/sec) bandwidth computing era [30] or into hybrid circuit architectures of nanoelectronics and nanophotonics [31]. Such global and vicious goals are likely only attainable with ultra-scaled light sources like Nanolasers such that economy of scale rules can be applied to drive this technology.

5. Photonics and Logic

5.1 Introduction

Opportunities for Photonic and Logic

With the tremendous success of the Silicon transistor and very large scale integration (VLSI) [1], the laws of transistor scaling predict the end of the roadmap in the year 2020 with transistor gate lengths on the order of 10 or less nanometers [2]. Currently there are many research projects involved in exploring a logic devices that can continue the performance trend of Moors' Law [1,3]. Among those are classical transistors with improved performance like a steeper switching performance (steeper sub-threshold swing), spin-based electronic switches, electrically driven MEMS-like mechanical switches, cryo-electronics, electro-chemical switches and photonic elements [3]. Here, we would like to focus on the latter for two reasons: firstly photonics offers the opportunity for large data bandwidths due to the weak photon-photon interaction and consequently multiplexing technologies for instance in terms of wavelength (WDM). The second argument is an efficiency argument, namely, the fundamentals of electromagnetism and solid-state physics allow for a single photon to induce a relatively strong voltage change up to 1eV, which could trigger or switch a signal. This is provided optical absorption and the internal quantum efficiency is high enough [4].
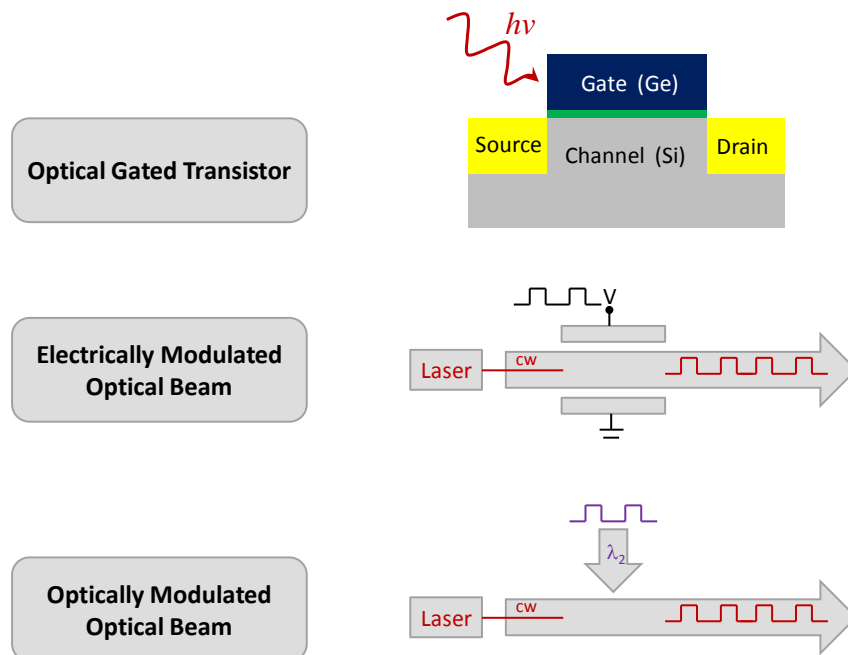
Figure 5.1.1 | The three possible ways of realizing a switch utilizing photons. (top) A classical electrical transistor is gated optically. (middle) An optical light beam is altered electrically, for instance via the non-linear electro-optical effect. (bottom) Third-order non-linearities can be utilized to realize an all-optical transistor.

In this work, we are particularly interested in opto-electronic solutions for a switching element with footprints on the order of a wavelength down to the nanoscale. Here, light-matter-enhancement effects allow driving this technology forward to novel devices with unprecedented performance and energy consumption benchmarks. Figure 5.1.1 highlights possible methods realizing a switch using optics. Here, the optical beam can be utilized to switch an electrical transistor (optically gated Transistor) (top) or an electrical signal is used to encode the data onto an optical light beam leading to so called electro-optical-modulation (middle). A particular interesting switch is the all-optical transistor, where a light beam is actively switched by a second light beam via third-order non-linear effects.

In the following we like to look into some details of each switching-scheme introduced in Fig. 5.1.1. Starting with the optically gated transistor, a tiny Germanium (Ge) island placed on top of a classical Si-based transistor creates a quantum well in the band-diagram (left panels Fig. 5.1.2) (Fig. 5.1.2). Thus, the optically induced (via absorption) electron-hole pairs drift apart and holes accumulate at the quantum well near the Ge-Si interface. This in turn leads to an attraction of electrons inside the Si-channel. Applying a bias between the source and the drain can now amplify these carriers leading to a detectable electronic signal. Notice due to the small capacitance the switching speed can potentially reach THz. In addition if the internal quantum efficiency (i.e. the photon-to-electron conversion efficiency) is high, a single photon is able to induce a 25 meV potential foe the device schematic shown on Fig. 5.1.1.
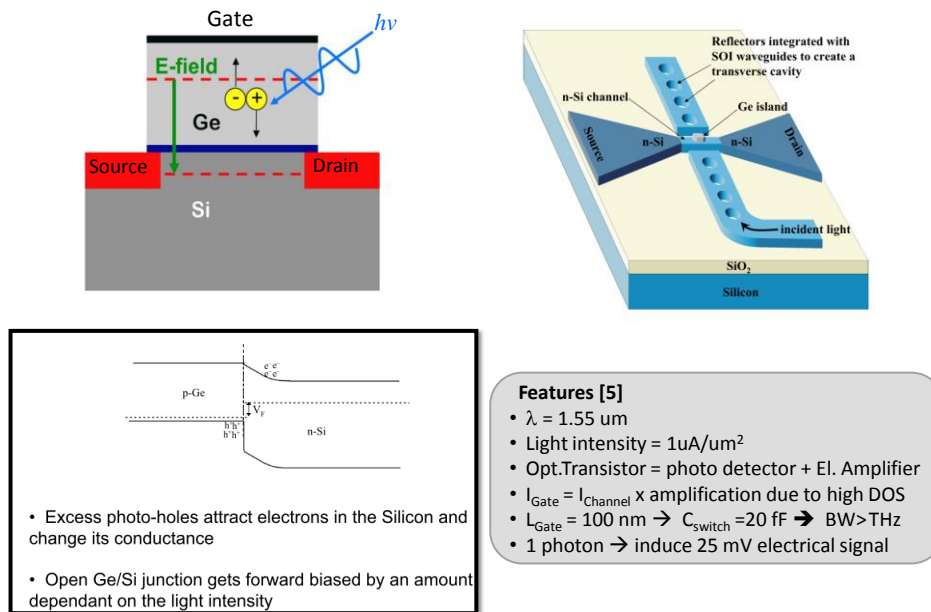
Figure 5.1.2 | The Optical Transistor. (top-left) Schematic of the optically gated Si-transistor. (bottom-left) The band gap of the Ge-Si interface creates an electronic quantum well attracting carrier in the Si-channel which can be amplified via an applied S-D bias. (top-right) The absorption of the Ge-island can be enhanced with a cavity, e.g. a 1-D photonic crystal which elegantly connects to a Silicon-on-insulator waveguide. (bottom-right) Performance measures of an experimental demonstration of an optical transistor after Ref. 5 with estimations of the switching speed.

The inverse to the optically gated transistor is the electro-optical modulator (middle Fig. 5.1.1) [6,7]. Here the second-order electro-optical non-linear effect is deployed where either in real (Δn) or the imaginary part ($\Delta \kappa$) refractive index is changed (Fig. 5.1.3). This is can be achieved via two means: carrier depletion and change of the free carrier concentration (plasma effect) [6]. In a nut-shell these effects change the dispersion of the material which chances the phase or the loss. Although one should point out that a change in n always induces a change in κ as well, because of the Kramer-Kroenig-Relations, which tie a change of the real part of the electric permittivity, ε', to the imaginary part ε''. Interestingly, both types of index change can be deployed towards electro-optical modulation. Whereas the change in κ facilitates a linear absorption-type modulator, a phase-modulator , i.e. an Mach-Zender Interferometer, is achieved by modulating the real part of the index. For the first one, the change in the imaginary part of the index leads to a change in the optical loss and thus to a change in the optical transmission (ΔT) which researchers named extinction ratio (*ER*) (left panel Fig. 5.1.3). Ideally an extinction ratio exceeding 10 dB is achieved in the static DC limit, because the modulation depth decreases as the switching speed is increased, because of capacitive delays of the device. The Mach-Zender modulator is characterized by the product of the applied voltage to achieve a π-phase change (V_π) over the required device arm length (*L*) to achieve the effect (right panel Fig. 5.1.3). Thus the Figure-of-Merit for a Mach-Zender electro-optical modulator is given by FOM = V_π x *L*.

In terms of materials a variety of choices are available, ranging from the originally explored Lithium Niobate (NiNbO$_3$) [8], over Silicon-based modulators by the Cornell group from M. Lipson [7] and Intel's photonics group [6] to novel materials like polymers, which are reported to have strong non-linear potentials [9] and graphene [10].

However, the electro-optical effect is often quite weak requiring devices to be on the millimeter to even centimeter size [6]. Solutions to this large footprint come in two ways; the first approach is to store the electromagnetic energy inside an optical cavity which simultaneously increases the effective length of the modulator by the cavity quality factor. However the trade-off is the limited bandwidth due to the cavity resonance. A second approach which we will follow in this chapter is to utilize optical confinement to boost the electro-optical effect. The idea is to utilize the field enhancement of the broadband deep-subwavelength propagating modes of the hybrid plasmon waveguide design discussed in chapter 3 to strengthen the induced electro-optical effect [11]. For instance the field-enhancement of the hybrid-plasmon mode of 30 times utilized in an 2nd order non-linearity like the electro-optical effect, results in an effective single enhancement of $30^2 \approx 1000$ [11]! Thus a millimeter size device can now be scaled down to the single digit micrometer scale, allowing for single wavelength active nano-plasmonics. Another advantage over the cavity approach is, that the effective bandwidth is not resonance limited, however the insertion loss can be high due to plasmonic losses and impedance mismatches between the photonic and plasmonic mode.

Linear (Absorption)

$$ER = \Delta T = \exp(-\alpha L_{WG}) \overset{!}{=} \dots \mathrm{dB} > 10\mathrm{dB} \; @ \; DC$$

$$\Delta\kappa = \frac{\alpha\lambda}{4\pi}$$

Mach-Zender (Phase)

$$\Delta\Phi = \frac{2\pi}{\lambda}\Delta n_{eff}(V_D)L_{WG}$$

$$L_{WG}(\Delta\Phi = \pi) = \frac{\lambda}{2\Delta n_{eff}(V_D)}$$

$$FOM = V_\pi \times L$$

Large Devices (0.1-10 mm size)

1. Rings/Resonances

input   output
Ring resonator, doped n⁻   Waveguide
n⁺   p⁺   n⁺

Lipson et. al. *Opt. Expr.* **17**, 5118 (2009)

2. Hybrid Plasmonics[1]

Solutions

IN   V   EO-Material   Out
Metal
Silicon
Oxide

HPP E-field Enhanc. = 30x
EOM - |E|² → 30² ~ 10³
Strong LMI → lower V
Smaller Devices

[1] V. J. Sorger, D. Kimura, R.-M. Ma in progress

Figure 5.1.3 | Two ways to design an Electro-Optical-Modulator (EOM). (Left) electrically altering the imaginary part of the refractive index ($\Delta\kappa$) leads to a change in the transmission (ΔT) or extinction ratio (*ER*) of the optical signal. (right) Phase changed interferometer-type EOM and figure of merit. (bottom) Due to the intrinsically weak EO-effect solutions to enhance the effect and reduce the device footprint are to deploy cavities [7] and plasmonic-ally enhanced fields leading to strong effect enhancements without sacrificing the bandwidth [11].

From a bandwidth and speed point of view the ultimate goal is to switch an optical beam optically i.e. all-optical transistor or switch (bottom Fig. 5.1.1). While progress in this field has been made with non-linear materials incorporated into fiber optics [12] and quantum-dot materials [13] plasmonic nanophotonic building blocks have not explored much yet. In chapter 5.3 we will discuss a plasmonic all-optical switch that elegantly interfaces with SOI technology, thus has great potential to make an impact in next generation's photonic circuit switching elements [14].

5.2 Plasmonic Electro-Optical Modulator

Device Design

As described in the previous sub-chapter the electro-optical (EO) effect can be influenced and altered by a change in the carrier concentration inside the EO-material. For instance, a Drude-Lorentz model [1] (Eqn. 1) can be used to describe the change in the complex refractive index
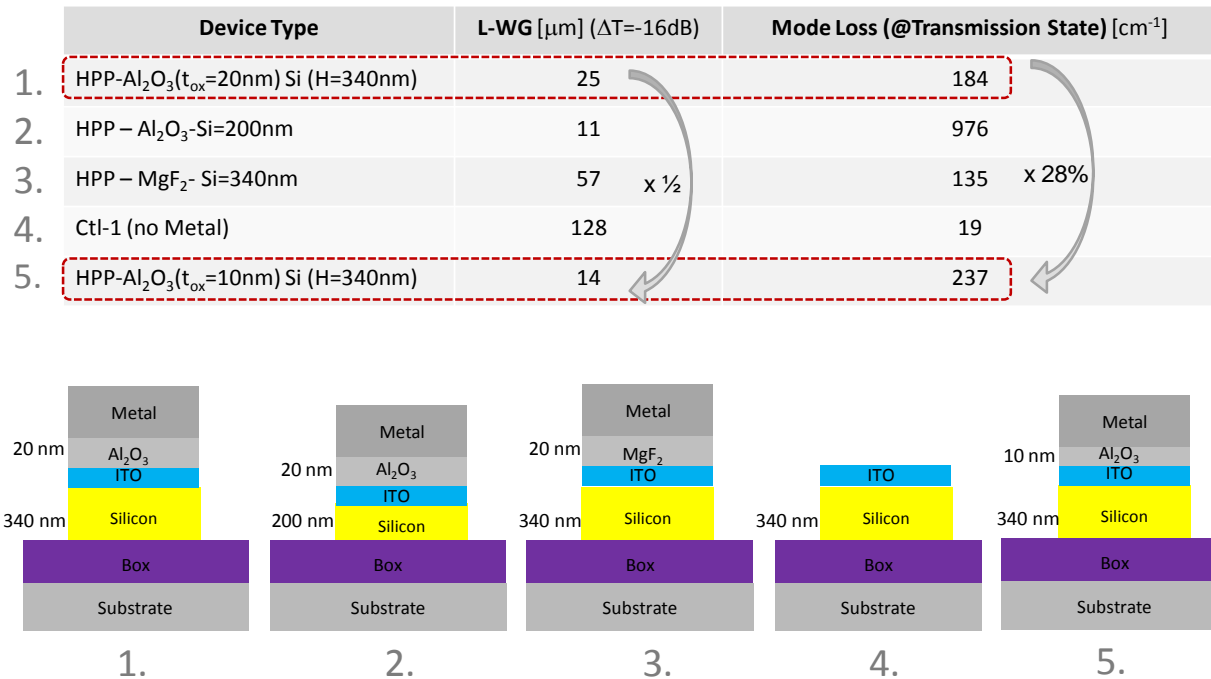
$$\Delta n = \frac{-e^2 \lambda_0^2}{8\pi^2 c^2 \varepsilon_0 n}\left(\frac{\Delta N_e}{m_e^*} + \frac{\Delta N_h}{m_h^*}\right) \tag{1}$$

where ΔN_e and ΔN_h represent the electron and hole densities, e is the electronic charge; λ_0 is the free space wavelength; c and ε_0 are the speed of light and permittivity in vacuum, respectively; m_e^* and m_h^* are effective electron and hole masses, respectively. The required carrier densities are determined using the Drude model [1] for the permittivity (Eqn. 2)

$$\varepsilon = \varepsilon_\infty - \frac{\omega_p^2}{\omega^2 + i\omega\Gamma} \quad \text{with } \omega_p^2 = \frac{Ne^2}{\varepsilon_\infty m^*} \tag{2}$$

where ε is the material permittivity, ε_∞ is the high frequency permittivity, ω is the angular frequency, ω_p is the plasma frequency (corresponding to $\varepsilon = 0$), and Γ is the relaxation frequency. Using Eqn (1) and (2) we can compute the permittivity as a function of operation frequency or wavelength. While a De at visible wavelengths requires a carrier change of 5×10^{21} cm^{-3}, at telecommunication wavelengths this change is about 1/5 of that value [2]. Furthermore, Feigenbaum et al. recently showed that the refractive index of an Indium Tin Oxide (ITO) layer inside a metal-insulator-metal geometry can be altered electrically by unity via the above described carrier modulation [2].

Extrapolating the response of an ITO film to an applied bias at telecommunication wavelengths and solving for the eigenmode profile allows us to determine the effective mode index change as a function bias. Via the left-panel equation from Fig. 5.1.2 we can compute a required device length, L, in order to achieve a desired extinction ratio, say 16 dB. Following this approach we simulated various designs of an EOM utilizing the hybrid-plasmon mode, where the gap layer has been substituted by a thin ITO and oxide layer, whereas the latter is needed in order to prevent electrical shorting (Fig. 5.2.1).

	Device Type	L-WG [μm] (ΔT=-16dB)	Mode Loss (@Transmission State) [cm^{-1}]
1.	HPP-Al$_2$O$_3$(t$_{ox}$=20nm) Si (H=340nm)	25	184
2.	HPP – Al$_2$O$_3$-Si=200nm	11	976
3.	HPP – MgF$_2$- Si=340nm	57 x ½	135 x 28%
4.	Ctl-1 (no Metal)	128	19
5.	HPP-Al$_2$O$_3$(t$_{ox}$=10nm) Si (H=340nm)	14	237

Figure 5.2.1 | Eigenmode simulation results for various EOM designs. The imaginary part of the refractive index was computed after a data extrapolation from Ref. 2. From here, the transmission ratio of 16 dB was taking into account to solve for the required device interaction length. Two cases stand out (marked red) which have been explored experimentally (see below).

Device Fabrication

The process flow is sketched in Figure 5.2.2. Wire bonding onto prefabricated pads was used to electrically connect the sample.
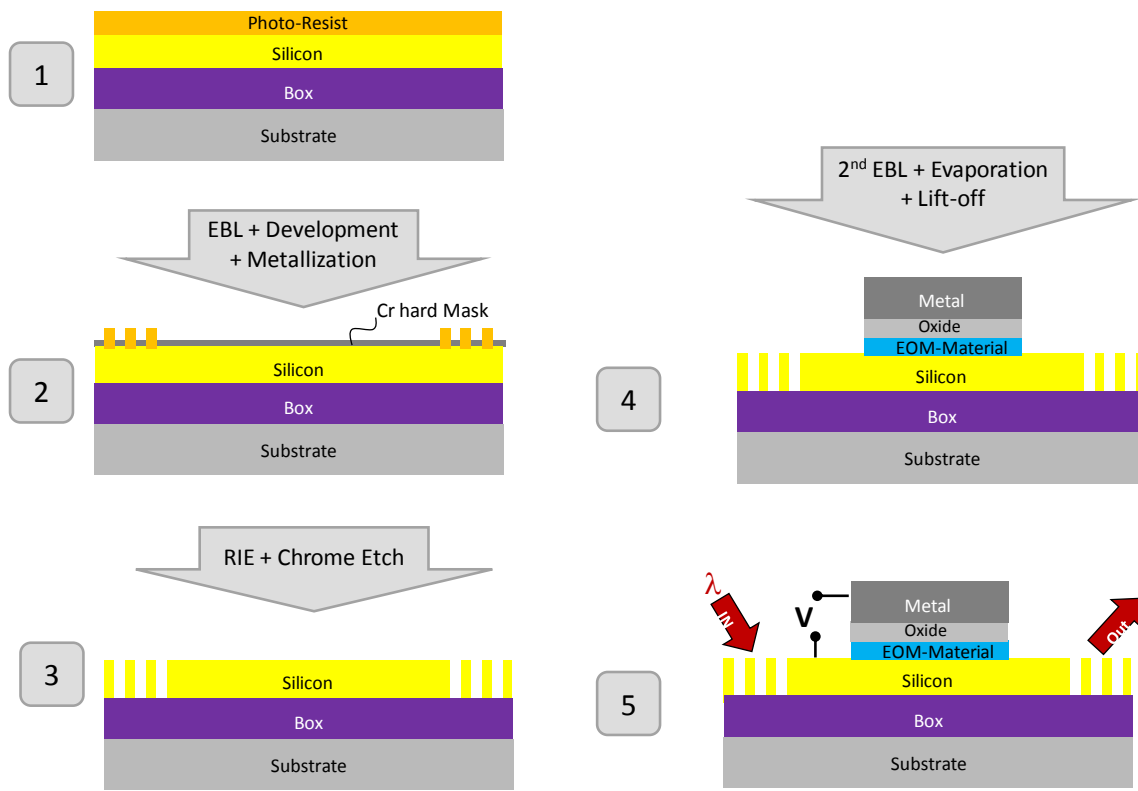
Figure 5.2.2 | Process flow for fabricating the HPP-based plasmonic EOM. SOI (Soitech, Box = 3 μm, Si device layer = 340 nm, doping: n-type, ρ = 1-10 Ωcm) wafers were cut and cleaned prior to starting the process. The photoresist for the 1st and 2nd Electron-Beam-Lithography (EBL) step was PMMA A5 (4000 rpm, 1 min) and PMMA A8 (2600 rpm, 1 min), respectively. The 1st and 2nd development step was carried out at low and room temperature respectively. Cr-7 was used for 3 minutes to remove the Chrome hard mask. All evaporation steps were carried out using a electron-beam thin film evaporator (CHA).

Experimental Results

Before the samples were tested for modulation performance, we checked the silicon-on-Insulator (SOI) grating coupler without the EO-oxide-metal layer on top (Fig. 5.2.3). While the total transmission through the SOI waveguide normalized to the reflected signal from the pump beam was on the order of 5%, that signal was sufficiently large enough for the following EOM measurements and significantly below the damage threshold for the SOI waveguide (the pump power on the grating coupler was on the order of 100 μW). Critically important for the 500-fold improvement in the total transmission was precise lithography as well as a low pressure reactive ion etcher (Lam Research). The optimized grating coupler had a Si-to-Si pitch of 590 nm and an air gap of 210 nm operating at 1300 nm wavelength.
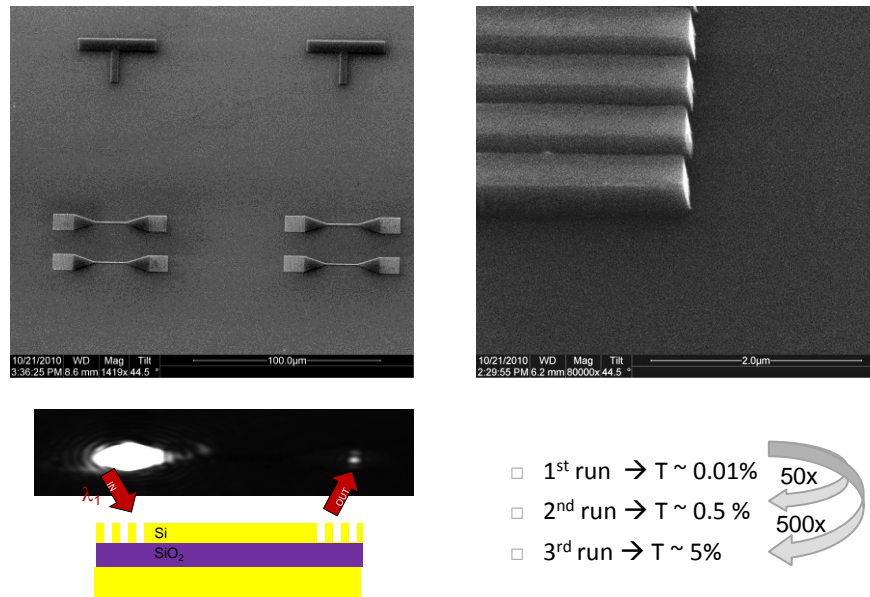
Figure 5.2.3 | SOI waveguide Grating Coupler Optimization. Best results were achieved with low-pressure reactive ion etching instead of atmospheric pressure etching.

Next, we tested the transmission performance after the EO-Oxide-Metal stack had been deposited (Fig. 5.2.4). As expected the total transmission decreases after the hybrid-plasmon mode was introduced, due to both the increased ohmic plasmon loss and the impedance mismatch between the HPP mode and the SOI waveguide mode. The decrease from about 5 to 2 % for the total transmission for a HPP-stack length of 5 μm corresponds well to the expected propagation length. Even though no impedance between the SOI and the HPP mode was used, calculations have shown that the transmission can be about 60-80% depending on the HPP-modes confinement. Notice however, that the SOI waveguide thickness was 340 nm, which theoretically allows for photonic mode to coexist alongside the HPP mode. Ideally one would utilize a thinner SOI waveguide whose thickness is closer to the cut-off of the eigenmode. With the eigenmodes effective mode index for the SOI waveguide being close to 3 (finite element eigenmode simulation, Comsol Multiphysics), cut-off would be achieved for a SOI thickness of about 220 nm if an operation wavelength of 1300 nm is used.
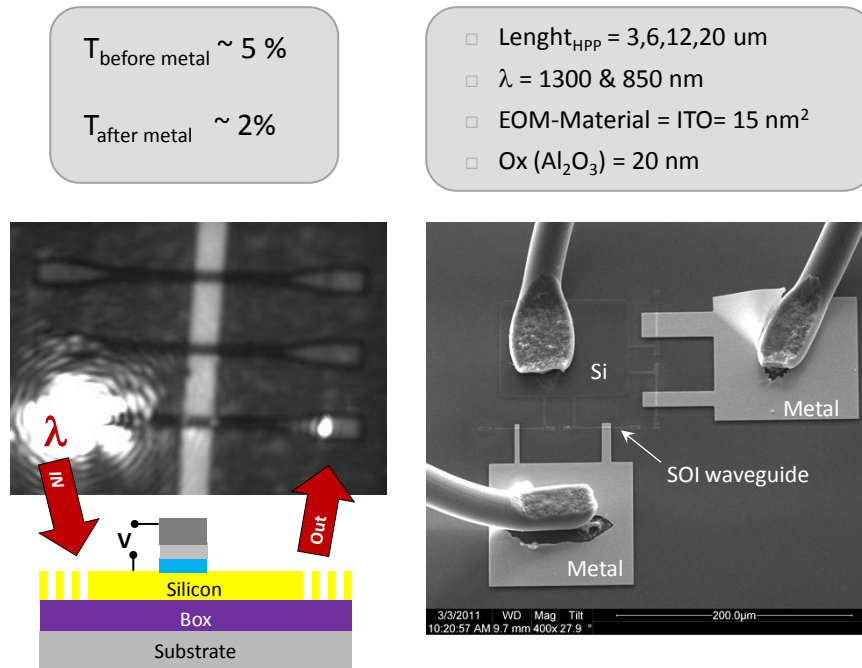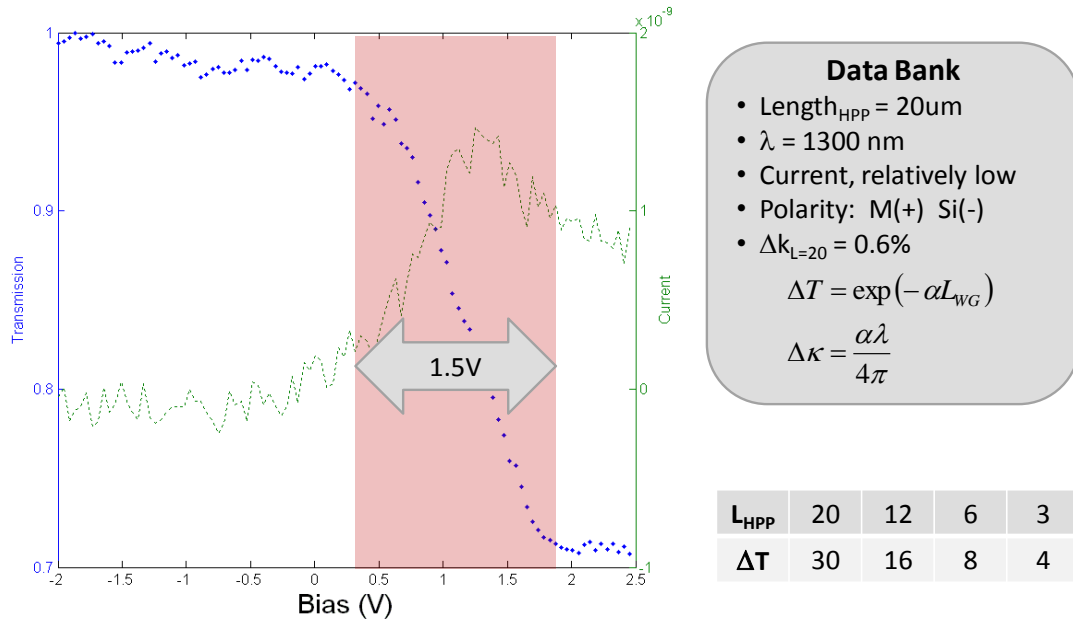
Figure 5.2.4 | Finished HPP-based plasmonic EOM devices. (Left) Transmission through Silicon-on-insulator (SOI) – hybrid-plasmon – SOI waveguides. (Right) Scanning electron micrograph of four modulators with varying length, L_{HPP}. Wire bonding (Aluminum wires) is used to electrically contact the sample which was mounted onto a chip carrier.

Testing the HPP-based plasmon EOM for its extinction ratio shows a 30% change in the transmission for an applied bias change of only 1.5 V for a length of L_{HPP} = 20 μm suggesting that the ITO layer has been influencing the optical mode. Shorter lengths result in a smaller transmission change as expected (see table Fig. 5.2.5). The current of the device is relatively low (single digit nano ampere range) indicating that the device is not shorted. We fabricated control samples where a complete device was fabricated but the ITO layer was left out. None of these devices showed any optical intensity modulation upon changing the applied bias which suggests that the ITO indeed changes its optical properties, i.e. κ. The strong effect of the HPP-based ITO EOM modulator comes into the picture when we compare the transmission change observed from the control samples (no ITO, but oxide and metal) to the EOM samples (ITO-oxide-metal). Our control samples are effectively the EOM modulator from the Intel group which utilizes the Si-plasma effect (MOS EOM) [3] which required centimeter long device lengths. Thus Intel's EOM has a 2000 times weaker modulation potential compared to our 20 μm long plasmonic EOM modulator.

In understanding the results shown in Fig. 5.2.5, the question arises why the modulation stops (levels off) with increasing bias voltage. There are two possible answers; Firstly, the capacitor might be fully charged at this point, which is possible considering the small capacitance of the HPP-stack. The second answers lies in the mode architecture; with the relatively thick SOI waveguide (340 nm) a photonic SOI mode and the hybrid plasmon mode coexist underneath the

HPP-stack. Thus, even if the effective mode index of the HPP part is changes completely, the SOI-photonic mode is unchanged with applied bias. The obvious choice to increase the modulation depth performance of the plasmon EOM is to decrease the silicon device layer of the SOI wafer.

Data Bank
- $Length_{HPP}$ = 20um
- λ = 1300 nm
- Current, relatively low
- Polarity: M(+) Si(-)
- $\Delta k_{L=20}$ = 0.6%

$$\Delta T = \exp\left(-\alpha L_{WG}\right)$$

$$\Delta\kappa = \frac{\alpha\lambda}{4\pi}$$

L_{HPP}	20	12	6	3
ΔT	30	16	8	4

Figure 5.2.5 | HPP-based plasmonic EOM Results. A maximum of 30% transmission change was achieved over about 1.5volts of applied bias for a HPP-stack length of 20 μm. This corresponds to a Δκ of 0.6%.

Critically important for an electro-optical modulator, and by that any switching device, is the modulation speed performance. The time response of our plasmon EOM depends on two factors; the time it takes the electrons to for an accumulation layer at the ITO-oxide interface and the RC-delay time (Fig. 5.2.6). The form depends on the geometry, the amount of applied bias change and the carrier mobility, we estimate the time for the electrons to drift through the thin ITO layer to be 0.1 ps, corresponding to 10 THz. The mobility was measured with a electrical 4-probe test and determined to be 6 cm^2/Vs, which is close to the reported 15 cm^2/Vs [2]. From a network point of view the estimated energy consumption per bit is an interesting benchmark whose attention to is growing [4]. With a 2 Volts of applied bias to switch the plasmon EOM and a capacitance of only 13 f*F*, we estimate the required per consumption to be 5 fJ/bit. This is only 5% of the estimated power requirements for future photonic modulation schemes [4] and about 4 orders of magnitude lower than current EOM energy/bit functions [3].
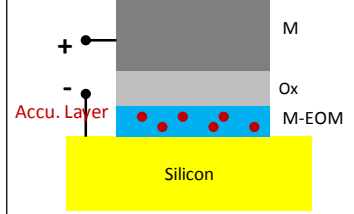
Active Carrier Speed (Time to drift through EOM layer?)

$$drift\text{-}speed = \frac{length}{time\,(\tau)} \to \tau = \frac{t_{EOM}}{v_{drift}}$$

$$with: v_{drift} = \mu E \ \ and \ \ E = V_{bias}/t_{tot} = V_{bias}/(t_{EOM} + t_{oc})$$

$$\tau = \frac{t_{EOM} \times t_{tot}}{\mu V} = \frac{10nm \times 30nm}{15\,cm^2/Vs \times 2V} = \frac{10 \times 10^{-7}\,cm \times 30 \times 10^{-7}\,cm}{15\,cm^2/Vs \times 2V} = 0.1ps$$

$$Mod - Speed = 10THz$$

$$\left(\mu_{measured} \approx 6\,cm^2/Vs, \mu_{Lit} \approx 15\,cm^2/Vs\right)$$

M

Ox

Accu. Layer   M-EOM
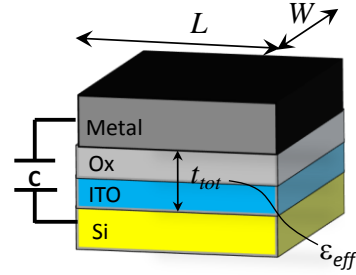
+

−

Silicon

2.   Device Capacitance

$$C = \varepsilon_0 \varepsilon_r \frac{LW}{d} = \varepsilon_0 \varepsilon_{eff} \frac{L_{Device}W_{SOI-WG}}{t_{ox} + t_{EOM}} = \varepsilon_0 1.8 \frac{25\,\mu m \times 1\,\mu m}{30nm} = 13fF$$

$$BW = \frac{1}{\tau} = \frac{1}{R_{50\Omega}C} = \frac{1}{R_{50\Omega}\varepsilon_0\varepsilon_{eff}\dfrac{LW}{t_{tot}}} = \frac{1}{50\Omega \times 13fF} = 1.5THz$$

$$\frac{P_{dissipated}}{bit} = \frac{P_{stored} \times BW}{bit} = \frac{\frac{1}{2}CV_{bias}^2 \times BW}{BW/2} = CV^2 = 5fJ/bit^*$$

L   W

Metal

Ox

ITO t_{tot}

Si

C

ε_{eff}

Figure 5.2.6 | Modulation Speed Performance of HPP-based plasmonic EOM. From both the active carrier time to drift through the active ITO layer and the RC-delay time constant, an modulation speed in excess of THz can be expected.

Experimental Setup

The experimental Setup is shown in Figure 5.2.5. While the setup shows the option for speed-tests, only the DC has been tested thus far. As an optical source a pulsed fs-laser (Spectra Physics) (λ = 900, 1300 nm) and a laser diode were used (λ = 1310 nm). The optical intensity response as a function of applied bias voltage was recorded with an infrared camera (Goodrich), where for each voltage step 10 frames were averaged.
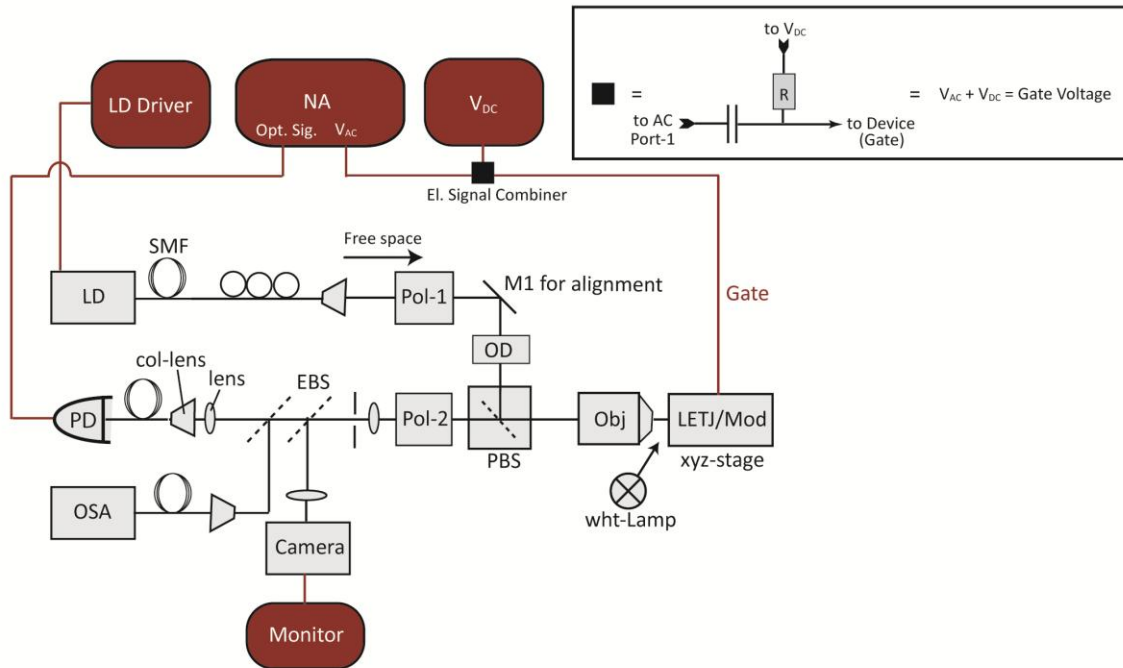
Figure 5.2.7 | The EOM characterization setup. LD = laser diode, PD = photo diode, OD = optical density filter, PBS = polazing beam splitter, OSA = optical spectrum analyzer, SMF = single mode fiber, M1 = mirror, NA = network analyzer.

Future Directions

The electro-optical modulation effect can be enhanced by placing the HPP-stack inside a cavity, which increases the time of the interaction of the optical mode with the ITO, effectively folding a long linear EOM device into a small footprint (Fig. 5.2.8). We analyzed a particularly interesting and feasible cavity candidate, namely a 1-D photonic crystal cavity (left-top Fig. 5.2.8). combining the 1-D cavity with the HPP-based plasmon EOM allows for high extinction ratios (strong signal modulation) for ultra-low voltage biases. Figure 5.2.9 shows the 2-D simulation results for a 1-D photonic crystal cavity. Each distributed feedback (DBR) mirror consists of seven narrow grooves etched into a SOI waveguide. The interference of each DBR reflects a certain percentage of the mode. Photonic crystal stop-band is clearly visible in the spectrum (shaded red) with the cavity resonance (high transmission) in its center. The cavity Q-factor is about 130. If even only $1/10^{th}$ of this Q-factor can actually be deployed towards enhancing the EO effect, then the cavity had shown its potential. However, there are some fabrication challenges with this approach, since it requires relatively precise etching processes of the Si grooves. Alternatively it is possible to place a DBR on top of the waveguide. Yet, the photonic mode of the thick SOI waveguides used here has only a small amount of field sitting in on top of the silicon, thus the expected modulation will be weak.
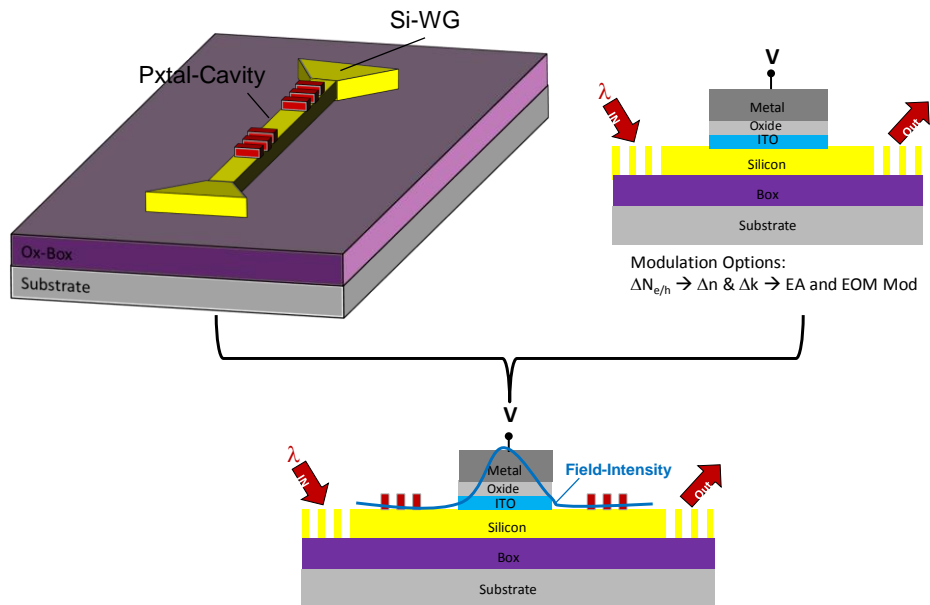
Figure 5.2.8 | The plasmonic EOM Roadmap. With the successful demonstration of the ITO HPP-based plasmon EOM (top right), a 1-D photonic crystal cavity can deployed to boost the EO effect. The cavity will built up an electric field as shown in the bottom schematic.

Cavity Design

- Bragg reflector: Air / Si grating
- Air width 100 nm
- Period = 251.7 nm (7 each side of cavity)
- L_c = 960 nm (Si)
- Grating depth = 120 nm deep
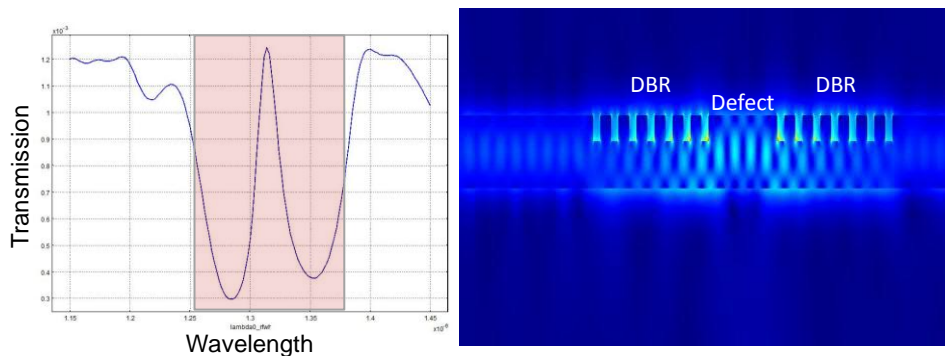
Figure 5.2.9 | The plasmonic EOM Photonic Crystal Cavity. 2-D Finite-Element-Method simulation results for a cavity design with two distributed feedback (DBR) mirrors and a cavity defect. The photonic stop-band is highlighted (red) in the spectrum on the left. The cavity resonance has a linewidth of about 10 nm corresponding to a quality of 130 for a wavelength of 1310 nm. Thus the EO effect could be enhanced by roughly the cavity's quality factor.

The HPP-based plasmon EOM can be improved even mode as we will discuss next. 2-D simulations results of a single HPP-stack (L_{HPP} = 2.12 μm) result in an ON-to-OFF state ration of 0.9/0.7 = 1.3 (top Fig. 5.2.10). However, if the single stack is divided into 4 individual ones such that the total HPP-stack length is the same as in the single-stack case, the modulation ON-to-OFF increases to 0.7/0.1 = which is a 5.5-fold increase. The underlying effect is that each SOI-HPP interface the mode can be reflected or transmitted with a certain probability. Modulation of the ITO index which in turn changes the effective mode index, creates an interference effect between the pure SOI mode and the HPP mode. Thus the length of the HPP-stack effectively acts as a linear phase-modulator, where each SOI-HPP interface adds to the modulation depth. The lower overall transmission for the multi-stack case results from additional scattering losses at each interface and the DBR effect due to the modulation of the index of refraction in the system. In the end these two effects determine the overall transmission and the modulation depth and can be optimized according to the required design.
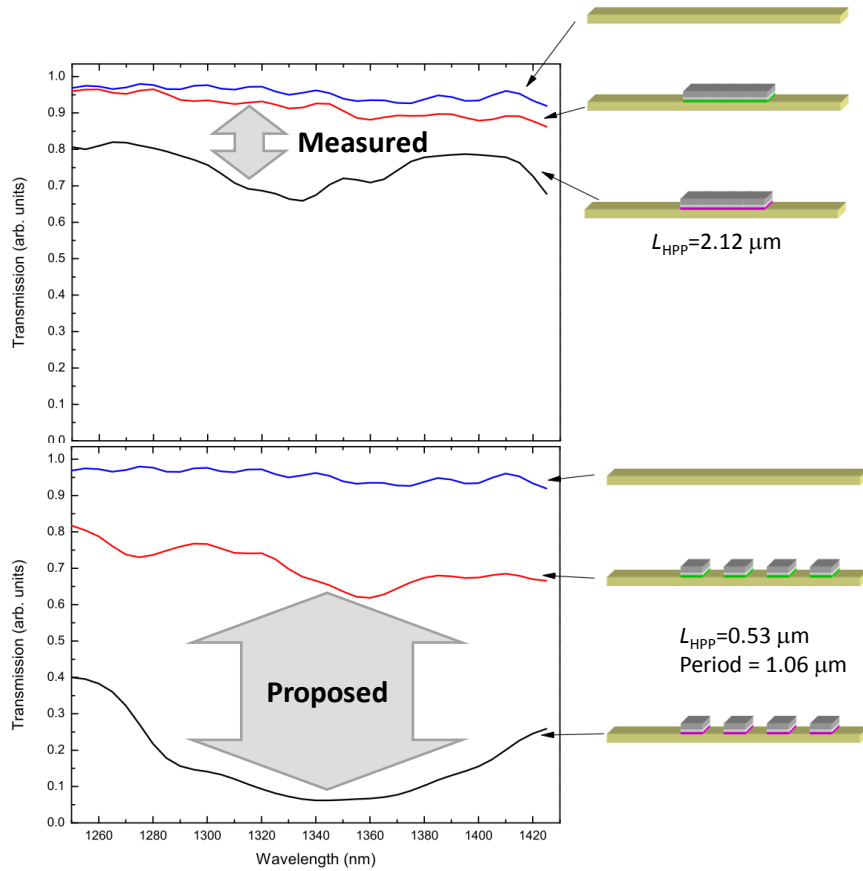
Figure 5.2.10 | Proposed "multi-finger" EOM Interferometer. (Top) The transmission change (modulation depth) for a single HPP-stack at the ON-state (red) is about 25% higher than the OFF-state (black). This modulation ratio of ON-to-OFF state (90%/70%=1.3) can be significantly increased (70%/10% = 7) if a multitude of shorter HPP-stacks is deployed a modulated. The overall transmission is lower for the multi-HPP case due to additional scattering loss from each stack interface. Photonic SOI mode as a control (blue).

5.3 All-Optical-Switches

As briefly mentioned in the introduction, the ability to switch an optical signal optically is very appealing. However, while the prospect of staying entirely in the optical domain seems appealing, the concerning question of how efficient is such process is well stated. As we have briefly discussed in this chapter, the energy per bit function is becoming more and more strict allowing less and less room for device flexibilities. All optical devices have been explored before. An interesting example was provided by M. Hochberg et al. where an on-chip SOI waveguide with a non-linear polymer cladding was used to create a 3-terminal all-optical transistor (top Fig. 5.3.1) [1]. While the device functions exactly like an optical version of a transistor with a source, drain and gate, the device footprint and switching depth as well as power requirements were research demonstration level at best (see top box Fig. 5.3.1). However, the device switching speed was verified to be in the THz regime far exceeding what electronics can provide [2]. This example elegantly shows the potential for ultra-high speed all-optical networks.
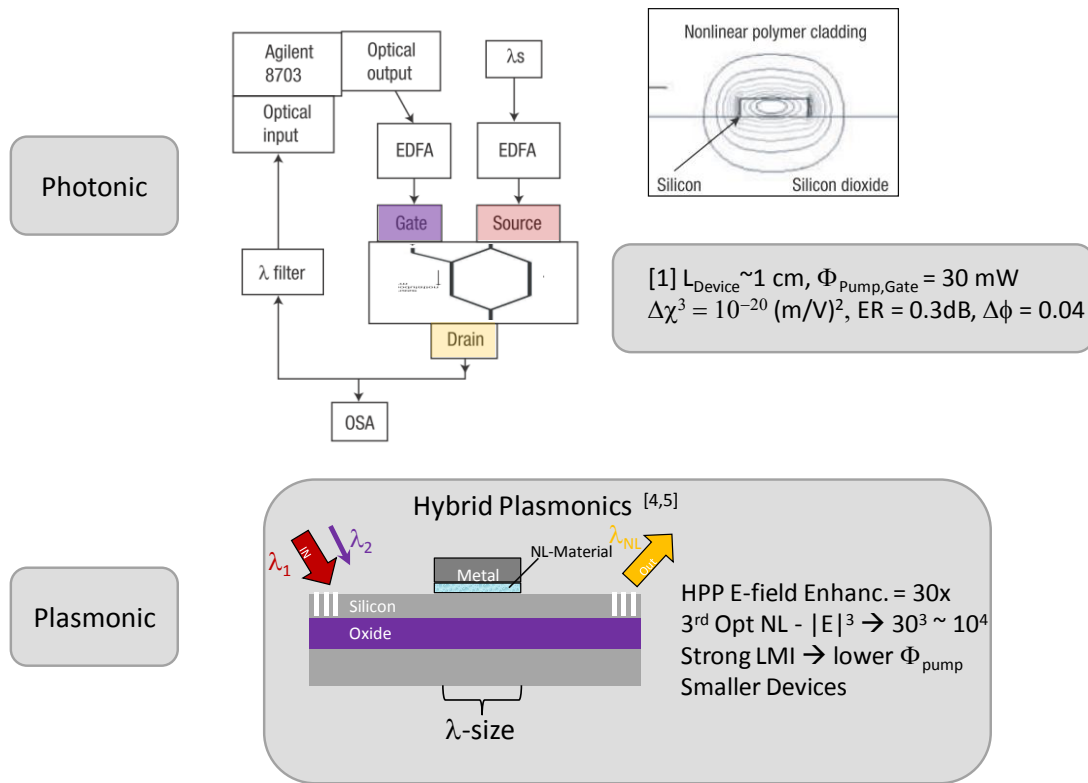
Figure 5.3.1 | All-optical-Switches. (top) A SOI waveguide with a non-linear polymer cladding can function as an all-optical switch [1]. The weak interaction of the SOI mode with the non-linear polymer requires millimeter to centimeter interaction lengths a low extinction ratio. (bottom) The enhanced field of the HPP mode on the other hand allows for strong non-linear effects. A 3rd order non-linearity effect which is proportional to the cubed electric-field amplitude gets boosted by the HPP mode to 10^4. Thus a centimeter device can now on the order of a single wavelength. Such enhanced light-matter-interaction (LMI) therefore allows for small and efficient nanophotonics building blocks like an all-optical switch.

On the other hand, the hybrid plasmon polaritons (HPP) modes' unique ability to enhance propagating field intensities for a relatively low propagation length cost penalty opens up opportunities in all-optical devices [2,3]. As we had briefly introduced in chapter 3.3, the HPP mode has a clear advantage in terms of non-linear nanophotonics, because of its strong confinement and low loss. Here, optical confinement can strengthen interactions between light and matter and thereby reduce the required devices size to utilize a certain effect (e.g. a 2nd, 3rd order non-linearity). Thus, metal optics can produce more compact components provided propagation losses do not exceed the necessary device interaction length. Here the relevant metric is the trade-off between light matter interaction enhancement (mode confinement area, A_m, relative to the diffraction limit) and the loss incurred (propagation length relative to desired interaction length). The mode confinement area measures the enhancement strength, whereas the ratio of propagation length and interaction length tells us about the loss. Key is here, that the strong confinement can outweigh the propagation length limitation in terms of producing the desired effect ratifying the use of the exponent function. For instance: the HPP mode has an electric field enhancement of 30x, thus if a 3rd order non-linear effect is been used to, say switch a signal, then the effective non-linear effect enhancement of the HPP mode is close to 10^4. In other words, the signal strength of a non-linear effect that usually takes millimeter of even centimeter to "build up", can now be created within only a few wavelengths.

In order to quantify this non-linear potential we simulated the eigenmode the HPP waveguide with two different optical confinement measures and compared the results to a SOI waveguide (Fig. 5.3.2). We picked a 3rd order non-linearity where the electrical field comes in as the third power of the electric field. Since the electric field is distributed over the entire SOI waveguide, the maximum field strength is relatively low (top Fig. 5.3.2). However, the strong electric field enhancement of the HPP mode can yield 4-fold stronger fields compared to a SOI waveguide (bottom Fig. 5.3.2). In addition, the non-linear material (e.g. As_2Se_3) is carefully placed inside the highest field location of the HPP mode. The net effect is that such a plasmonic waveguide has the potential to provide two orders of magnitude higher non-linear signals than an SOI waveguide (Fig. 5.3.2). Comparing these results to SOI waveguide with the non-linear cladding [1] the HPP mode performs $3 - 4$ order of magnitude better, because the electric field outside the high index SOI waveguide is quite low [1].

Such a strong enhancement reduced the optical input and gating power and allows for ultra-small footprint devices. Interestingly if a plasmonic non-linear switch can now be realized within a few wavelengths only, the higher plasmonic losses become secondary. Thus plasmonic non-linear based devices lit all-optical switches can indeed attack the research space of non-linear optics.
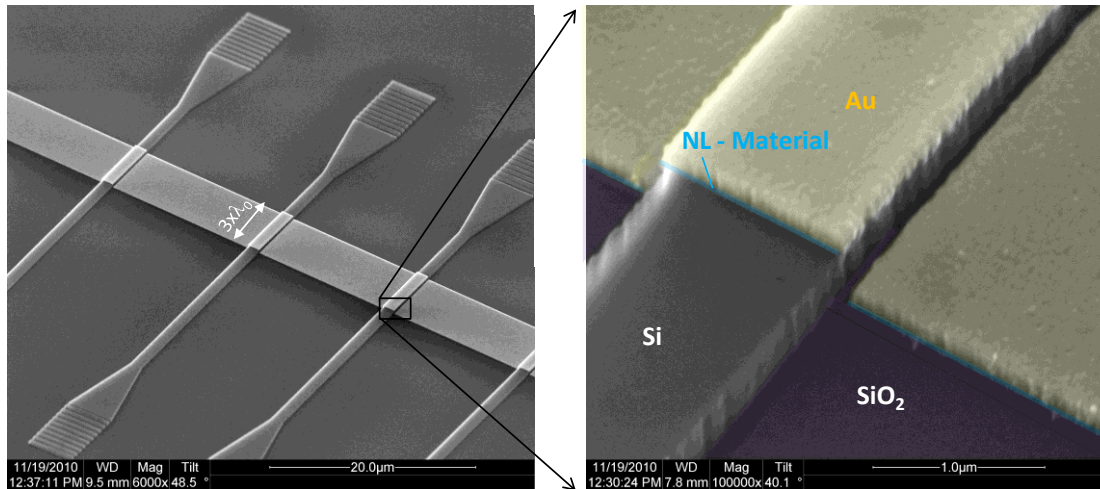
WG-Type	Max-Field	Non-linear coefficient, n_2	Non-linear Signal Strength (3rd order)
SOI	0.3	440	11.8
HPP (h-30nm)	0.8	1200	610
HPP (h=10nm)	1.2	1200	2070

x50

x175
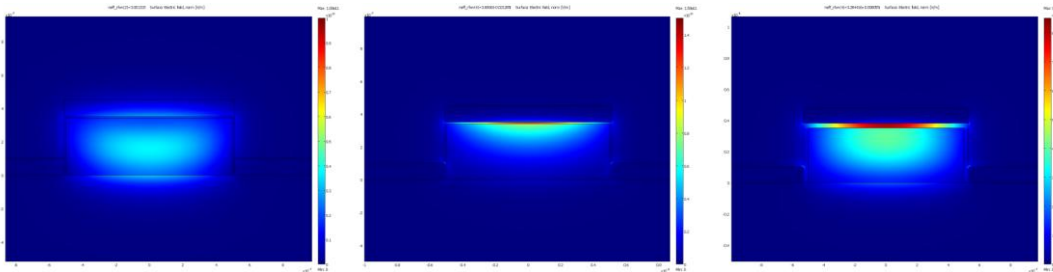
Figure 5.3.2 |Third order non-linear effect comparison of HPP mode vs. SOI photonic waveguide. (top) Comparison 3rd order non-linear effect strengths for integrated photonics. The reference is a SOI on-chip waveguide's ability to create a 3rd order non-linear signal. The hybrid plasmon polariton (HPP) strong field enhancement allows for more than 150 times the potential for 3rd order non-linearities compare to the SOI waveguide. The HPP mode was assumed to be filled with the Chalcogenide material, As_2Se_3 [5.6]. (bottom) Field profiles of the SOI waveguide (left), HPP with gap height = 10 nm and 20 nm in (middle) and (right), respectively.

Based on our SOI-HPP-SOI system we fabricated first prototypes of such all-optical switches (top panels Fig. 5.3.3). The SOI waveguide is 800 nm wide and 340 nm in height and is fabricated in a similar way as outlined in chapter 5.2. Even the HPP-stack is similar to the EOM with the differences of no oxide layer and a highly non-linear material instead of ITO. The non-linear material was chosen carefully, based on non-linear index (n_2), refractive index and processing (i.e. deposition) compatibility. The group of Chalcogenide materials is of particular interest, because they provide extremely high non-linearities, yet have a relatively low loss function (table in Fig, 5.3.3) [5.6].

The top panels in Figure 5.3.3 show the finished devices with an HPP-stack of only 3λ, where λ = 1.3 μm. Based on our previous studies of the SOI grating couplers and HPP-to-SOI mode coupling expect a relatively strong output signal, which was confirmed in transmission measurements. The devices are currently under experimental study and further research will show whether the HPP mode can indeed provide such strong non-linear signals.

Material	n_2 [x10^{-20} m^2/W]	Loss [10^{-12} m/W]
As$_2$S$_3$	290	<0.01
As$_2$S2$_3$	1200	1
Si	440	8.4
SiO^2	2.2	NA
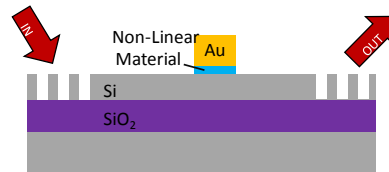
Figure 5.3.3 | Plasmonic Non-Linear Device Concept. (top) SEM micrograph of finished device and inset highlighting the different material layers (false color). The Non-linear material is 15 nm thick As$_2$Se$_3$. (bottom) Table after Ref. 5 & 6 highlighting the strong performance of Chalcogenide materials. n_2 is the non-linear coefficient. The higher the ratio of this coefficient and the loss, the stronger will the non-linear effect be.

6. Metal-Oxide-Semiconductor Tunnel Junctions

6.1 Introduction & Basic Idea

Conventional microprocessor interconnect performance cannot keep pace with semiconductor device scaling. Since the 130nm lithography node, more than half the power to the microprocessor is dissipated in interconnects. In addition to power loss, interconnect delay now dominates that of transistor by a factor of 250 for a 1mm line (Figure 6.1.1). Reducing feature sizes at the regimented pace of Moore's Law has only worsened the situation. Continued scaling increases device density and decreases the copper conductivity due to grain and boundary scattering. The semiconductor industry has long recognized the fact that traditional solutions will not satisfy performance requirements in the long term [1]. The input-output pins for inter-chip connections are already approaching their delay limits. Space wise, no more pins can be integrated on the chip and electromagnetically no higher data-rates can be transmitted with this architecture. With today's increasing connectivity of people, consumer electronics and military operations electronic a major shortfall in processing and communicating the raw data gathered is insight [2]. To continue the pace of processor development critical towards this data-driven demand, interconnect technology must move beyond the inefficient charging and discharging of metal wires.
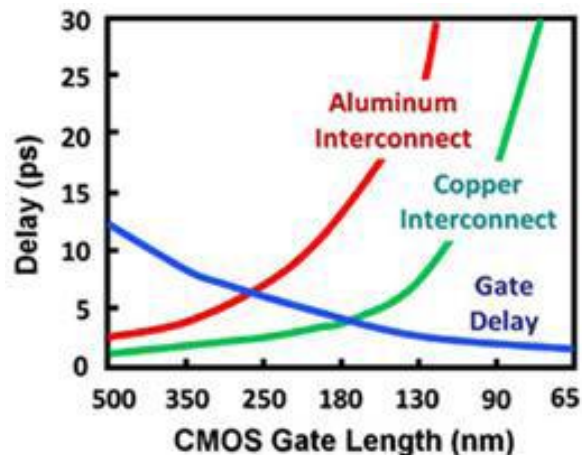
Figure 6.1.1 | The communications bottleneck imposed by metallic interconnects [1]. The capacitive speed delay from the electrical interconnects severely limit the chip performance. This effect worsens as the technology node is being shrunk down.

The case for implementing optical interconnects has been made and the benefits are manifest [3]. The large bandwidth of optical waveguides can accommodate densely multiplexed signals. While an electrical line is limited to signaling at the clock frequency, an optical line can support channel capacities beyond terabits per second [4]. Optical signals provide speed-of-light signaling, mitigation of skew and voltage isolation problems, and near-ideal impedance matching

at the photo-detector [3]. In addition to large performance gains, silicon photonics is a mature industry with detectors, modulators, waveguides and filters routinely fabricated with CMOS processing. The missing element in the realization of optical Si-based photonic circuitry is the silicon light source [6]. Development of that critical device is the subject of this manuscript.

Here, we outline a CMOS-compatible light source solution employing inelastic electron tunneling (Fig. 6.1.2) as experimentally discussed in chapter 6.2. The underlying physical processes are elastic and inelastic electron tunneling controlled by bias voltage. In the elastic tunneling picture, a conduction electron in highly doped silicon approaches a biased, nanometer-scale oxide barrier. With each scattering event at the barrier, there exists a finite probability that the electron will tunnel into the conduction band of the metal counter-electrode, conserving electron kinetic energy. After tunneling, the hot electron achieves thermal equilibrium with the electron sea, giving up its energy as heat. Inelastic electron tunneling, in contrast, does not conserve electron energy. Instead, a photon or phonon is created as the electron transfers to a lower energy state in the metal counter-electrode. Herein, we refer to this light emitting device as 'light-emitting-tunnel-junction' (LETJ).
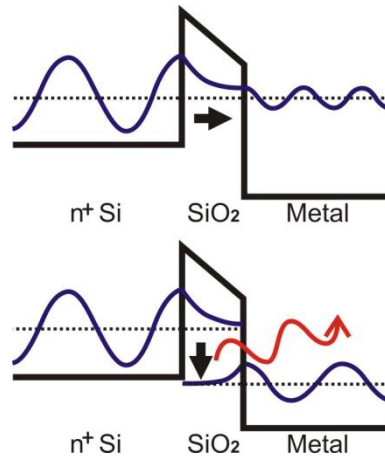
igure 6.1.2 | Illustrations of Light-emitting tunnel junction (LETJ) operation. (top) elastic and (bottom) inelastic electron tunneling mechanism.

The first experimental evidence demonstrating light from such a junction was published in 1976 [7]. These early devices are representative of those in the literature in their simple planar geometry of a metal or doped semiconductor substrate with a thin dielectric layer followed by a thin (10s of nm thick) metallic layer on top. Light is typically scattered to free space from the plasmonic bound mode confined the dielectric by the surface roughness of the thin metal layer. Figure 6.1.3 | Spectra from early Observations MIM Tunnel Junction [7] shows the emitted optical bandwidths to be in the mainly visible.
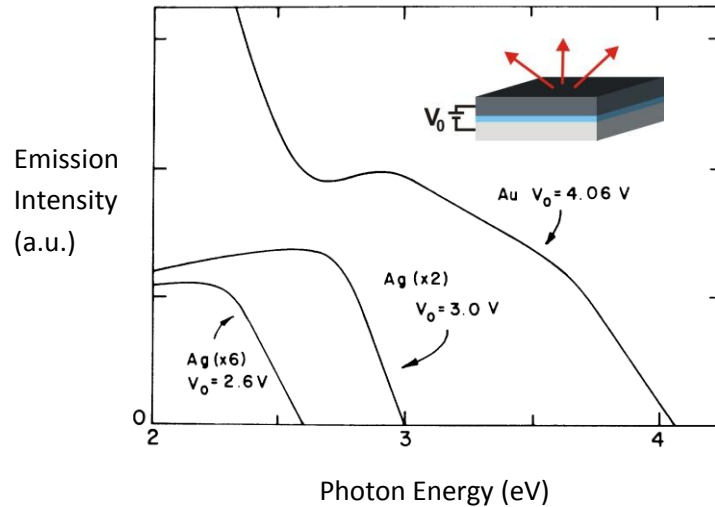
Figure 6.1.3 | Spectra from early Observations MIM Tunnel Junction [7]. The strongest Emission Intensity was obtained if Gold contact was used.

The dominance of elastic tunneling over inelastic tunneling remains the crux of the efficiency problem. Preliminary numerical analyses calculated inelastic tunneling could be 10% of tunneling processes when optimized for materials and bias [8]. To make inelastic tunneling dominant, the process must be made favorable through the introduction of a cavity. Note that the bound mode in the MIS system is sub-wavelength, thus allowing for a nano-scale cavity. From the Purcell enhancement could result a factor of up to 50 gain in inelastic tunneling [9-11]. The process of stimulated emission could even further enhance the quantum efficiency. Because the stimulated emission is from the rapidly-thermalized Fermi-sea of a conductor and into the conduction band of a metal, the limiting processes do not follow from the standard rate equations.

From quantum theory we know that any spontaneous process can also be stimulated. There has yet, however, to be an experimental effort demonstrating stimulated emission from electron tunneling beyond the early theoretical work [12-14]. In the near term, this must be demonstrated and the limiting physical mechanisms must be quantified.

6.2 Experimental Tunnel Junctions

Introduction

Computer systems in the 1960's were set-up by thousands of individual components and were therefore not only slow in computing power, but also bulky failure prone and needed a medium size staff to support their operation. The advent of integrating such components on a single chip (IC) solved many of these problems and ultimate led to the IT revolution as we know it today. The photonic counterpart to large scale IC, namely the Photonic Integrated Circuit (PIC) was proposed by Miller in 1969 [1], however until now has not yet showed its full potential due to two main reasons; Photonic components are subject to the diffraction limit of light and the Silicon is a weak optical light emitter. The diffraction limit, however, has been shown to be surpassed by using surface plasmon polaritons (SPP) [2], name oscillating electromagnetic waves on metal interfaces, demonstrating sub-wavelength components such as waveguides [3] and laser devices [4,5]. Yet, many of these devices are incapable of being integrated onto an IC chip since there are material incompatibilities. For the second reason, here we argue that even though Silicon is an indirect band gap semiconductor and relies on phonon assisted exciton generation, the mount of photons created by Si-based light emitters can be sufficient for a novel Photonics platform that utilizes a lower photon/bit rate than used for current communication.

Under voltage bias Metal-insulator-metal (MIM) tunnel devices have been shown to emit light due inelastic electron scattering [6]. However, most of the MIM structures were not stabile at room temperature and had to be cryogenically cooled. Improved stability was found from metal-insulator-semiconductor (MIS) junctions operating at room temperature under continuous (cw) voltage bias [7,8].

Here we report on a Silicon-based plasmonic light source utilizing a tunnel junction with sub-wavelength field confinement. Both simulation and previously found near-field-scanning-optical microscopy (NSOM) results prove extremely high optical intensities inside the device due to a plasmonic-hybrid mode [9, 10]. We show that the out-put coupling efficiency of such a MIS-based light emitting tunnel junction can be significantly enhanced due to surface grating couplers.
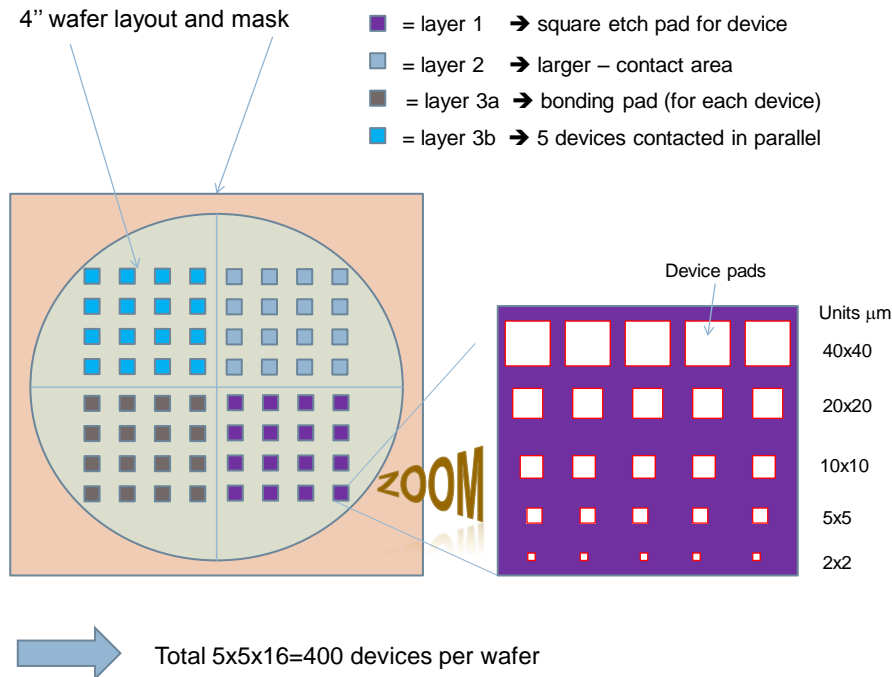
Figure 6.2.2 | Mask Layout for LETJ Processing. A total of 4 optical lithography steps is used. The space distance between each neighbor device is 1000 um. This effectively produces: 16 chips (0.5x0.5 cm^2) with 25 devices each. Sophisticated alignment marks allow for alignment within ~ ±1um (Karl-Suess Aligner).

Figure 6.2.1 shows the process mask layout highlighting the 4 individual optical lithography steps, while Figure6.2.2 shows the details of the overall CMOS fabrication process flow of the LETJ. In particular, the LETJ is comprised of a p-Silicon substrate (ρ = 50 Ωcm) with a nanometer thin (~2 nm) native oxide (NOX) and a metal (Gold or Silver, 100-200 nm) top electrode (Fig. 6.2.3**a**). Such a metal/low-dielectric/high-dielectric generally structure supports a hybridized mode between a classical photonic waveguide and a surface plasmon polariton (Fig. 6.2.3**b**) [4,5,9,10]. This geometry acting as an optical capacitor, is able to confine light below the diffraction limit of light down to λ/15 at visible wavelengths.

However we note that, since the Silicon layer is thick (wafer), the hybridization is relatively weak, due to the majority of the light residing inside the high index Silicon region. In an optimized device layout, a thinner Silicon layer like in SOI technology should be used. The Si-SPP light source emission area (square shape) is designed to range from 0.0625 μm^2 (250 nm side length) to 1600 μm^2 (40 μm side length) and show uniform electro-optical characteristics (Fig. 6.2.1 and 6.2.3).

Tool Name	Type
Sink 8	Etch
Sink 8	Etch
Oxford	PCVD
Nanospec	/
SVG - Coat	SVG -DEV
KS Aligner	Litho
Sink 8	Etch
PR revome/Sink 2	Aceton/Pirahana
Sink 6	Pirahana
Tystar 2 (11 down till Feb-2010) Or Evap	Dry oxidation (no pin holes, but not stabile below 20nm) (LPCVD)
Nanospec	/
SVG – Coat	SVG -DEV
KS Aligner	Litho
Edwards	Sputter
SVG - Coat	SVG -DEV
KS Aligner	Litho
Edwardseb3/Torr	Ebeam

□ Piranha clean

□ BOE (1:5 or 1:10) on n+ Si wafers to remove native oxide

□ Grow ~SiO_2 ~ t_{ox}<300nm.

□ Verify oxide thickness

□ Photo-pattern oxide, BOE etch (etch rate = 70nm/s, 20% over-etch)

□ Grow 3-5nm tunnel oxide. About 1.5 hrs at 700C in O_2 flow. Add a clean (oxideless) monitor wafer to the oxidation run. Or dry-ox, 1hr in O2 flow

□ 10min Aceton soak (oxide stipper?)

□ Clean Pirahana

□ Verify oxide thickness using nanospec on monitor wafer.

□ Deposit PR and pattern. The pattern should allow for Au all around the square to maximize the chance of electrical contact

□ Sputter ~30nm of Au or Ag.

□ Lift-off

□ Another PR and pattern step for bond pads. Should be large enough to wire bond

□ Deposit 120nm Au and liftoff

Figure 6.2.3 | Process flow of LETJ Fabrication. This most critical step is creating the thin tunnel oxide. General processing options include CVD, LPCVD or growing thermal oxide. However, CVD is too fast and the oxide quality poor. Thus a simple solution is to utilize the natural forming native oxide (NOX) of a Silicon interface which is about 2 nm thick.

Electro-optical Experimental Results

Upon biasing the Si-SPP light source junction a double exponential increase in current flow was observed (Fig. 6.2.4**a**). Fitting I-V curve to a tunnel current model [11] gives a diode ideal factor of 1.35 corresponding to a tunnel oxide thickness, t_{ox}, of 2.6 ± 0.4 nm, which is within the expected range of native oxides for Silicon [11]. Notice, the effective voltage drop across the junction is about half a magnitude lower that the total series resistance (R_s ~ 50 kΩ) of the bulk Silicon wafer and measurement setup including chip carrier-Silicon wafer interface resistances (Fig. 6.2.4**a**). Figure 6.2.4**b** shows the overall light-pump characteristic revealing a relatively linear trend.
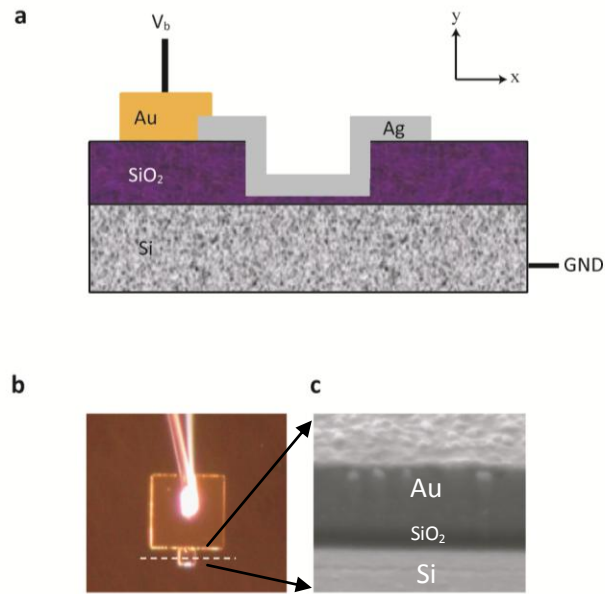
Figure 6.2.3 | Light Emission Tunnel Junction. **a** Schematics of Light-Emission-Tunnel-Junction. Standard Lithography (optical and electron beam) as well as wet-etching and metal deposition techniques have been used to fabricate the device. **b** Sub-wavelength Plasmon-Hybrid Mode inside the junction. Highest $|E_y|$-Field strength is inside the thin native oxide. [9,10] **c** SEM crossection of the junction area.

For negative voltage bias the semiconductor bands bend upwards at the Si-SiO$_2$ interface, thus allowing for holes (majority carrier in p-Si) to accumulate (Inset, Fig. 6.2.3**c**). If the oxide between the metal and semiconductor is thin enough, $t_{ox} < 4$ nm, electrons can tunnel from the metal to the semiconductor. For positive bias the silicon bands are bending downwards, leading to a depletion of holes close to the Si-SiO$_2$ interface and an inversion layer of electrons at the Silicon surface, which allows electrons to tunnel through the thin oxide barrier. This leads to a low current independent of V_b, since the electrons are minority carrier in the p-type Silicon substrate. The Si-SPP light source square emission area is designed to range from 0.0625 μm^2 (250 nm side length) – 1600 μm^2 (40 μm side length) and shows a typical current density of about ~10^{-2} Acm^{-2}, suggesting a native oxide thickness of about 2 nm [11]. Ellipsometry measurements, $\bar{t}_{ox} = 2.1 \pm 0.4\ nm$, match this thickness.
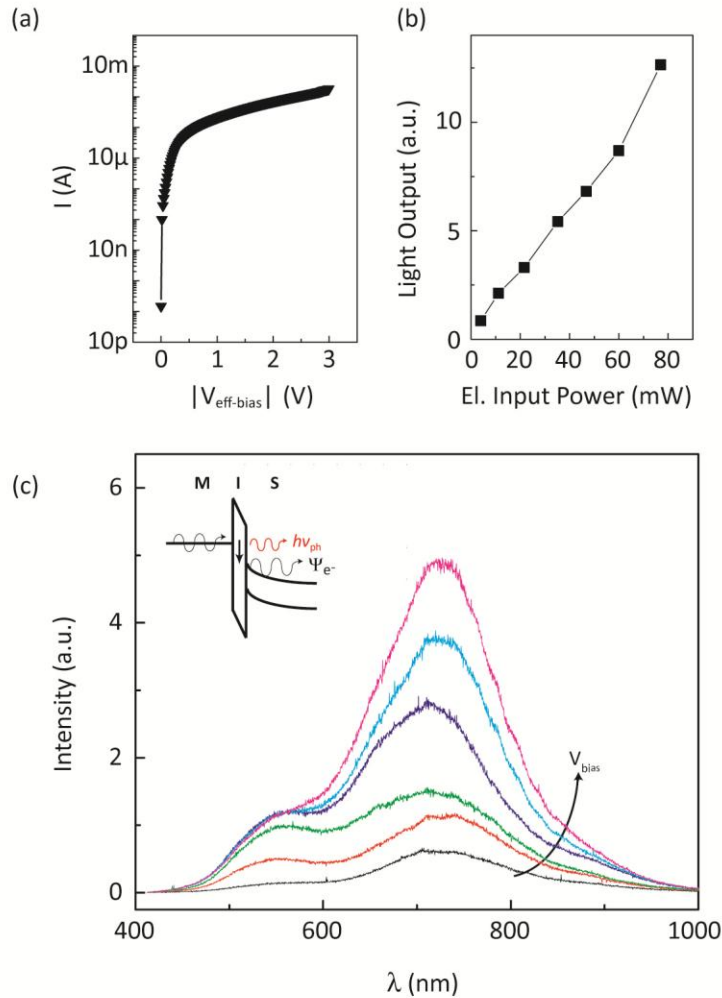
Figure 6.2.4 | Electrical and optical characteristics of the LETJ. **a**, I-V_{bias} characteristic shows a bi-exponential growth. Fitting the current to a tunnel model yields an oxide thickness, $t_{ox} = 2.6 \pm 0.4$ nm. **b** The light output was found to increase roughly linearly with current. **c**, The spectrum centered around 720 nm increases with junction bias. T = 300 K. Inset: The inelastic electron tunneling mechanism is source of the photon generation. **d**, The optical light output shows a linear dependency with electrical pump power as expected from energy the conservation law.

The broadband emission is centered at 700 nm (FWHM = 250 nm) and increases with bias voltage in intensity, but does not spectrally shift with V_b (Fig. 6.2.4**c**). This observation can be explained by spectral surface plasmon creation due to current fluctuations inside the device [8,12]. Calculations of the power-density in similar devices show a maximum around 700 nm for a Gold top-contact on Al/Al$_2$O$_3$ devices [12]. The emission was collected via a free space objective (50X, NA=0.8), send to a Spectrometer and recorded via a liquid N$_2$ cooled CCD.
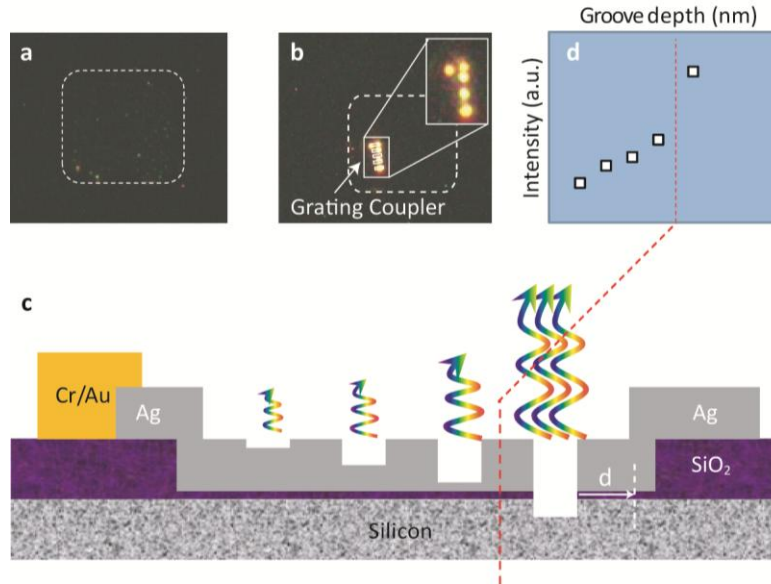
Figure 6.2.5 | Outcoupling enhancement. **a**, EL output though the top metal contact yields low intensity due to strong metal absorption and low scattering rates arising from the surface roughness of the metal film. **b**, A grating coupler can increase the outcoupling EL by both decreased metal absorption and increased far-field scattering contribution. **c,d** Schematic illustrating the expected increased EL with grating depth due to reduced metal absorption.

The generated photons are kept inside the device due to the hybrid-plasmon mode. In order to couple this light out into free space, attempts with thin (~ 30 nm) top metal contacts were made, where light from inside the device leaks to the metal/air interface, from where surface roughness provides the additional k-vectors for the plasmons to scatter into free-space [6-8]. However, this method yields in low efficiencies on the order of $\eta = 10^{-5}$ [6,7]. In order to improve the out-coupling ratio and gaining further inside into the Si-SPP light source, we etched gratings (via FIB) into the device accessing the sub-λ hybrid-plasmon-mode and facilitating coupling into free space. Figure 6.2.5 compares the far-field collected electro-luminescence (EL) intensities of an as-fabricate (panel **a**) with an etched device (5 thin grating lines) (panel **b**), clearly showing the increase in collected emission. This effect is schematically illustrated in Figure 6.2.5**c** and **d**. Here, the EL increases due to the reduced metal losses and due to the increased momentum addition from the grating edges.

In order to quantitatively measure this EL enhancement with grating depth, we etched gratings with varying depth via focused-ion-beam milling (FIB) into the junction and correlated the measured EL from these samples with for various bias voltages. We found that when the metal loss incurring metal thickness is reduced, EL increases exponentially (top region A Fig. 6.2.6). This trend can be understood of an increasing extraction efficiency due to reduced metallic absorption. However the maximum EL is not reached for a zero metal thickness (corresponding to a grating depth of 100 nm), but for a metal thickness of about the skin-depth of the material, here ~ 20 nm for Gold. This is intuitive, because if the metal is removed, the top contact is lost and photon creation is prohibited. If the edge depth is increased to a grating depth of about 100-130 nm the EL decrease sharply because, no photon creation can take place above the silicon

(top region B Fig. 6.2.6). The eventual saturation effect (EL around 200k counts) grating depths of greater than 150 nm is probably a result of the parasitic doping of the Silicon due to the extended Gallium bombardment from the focused-ion-milling process. The EL trend curves for changing grating depths and voltage bias indicate a significant increase in EL for medium voltages and optimized grading depths (bottom Fig. 6.2.6).
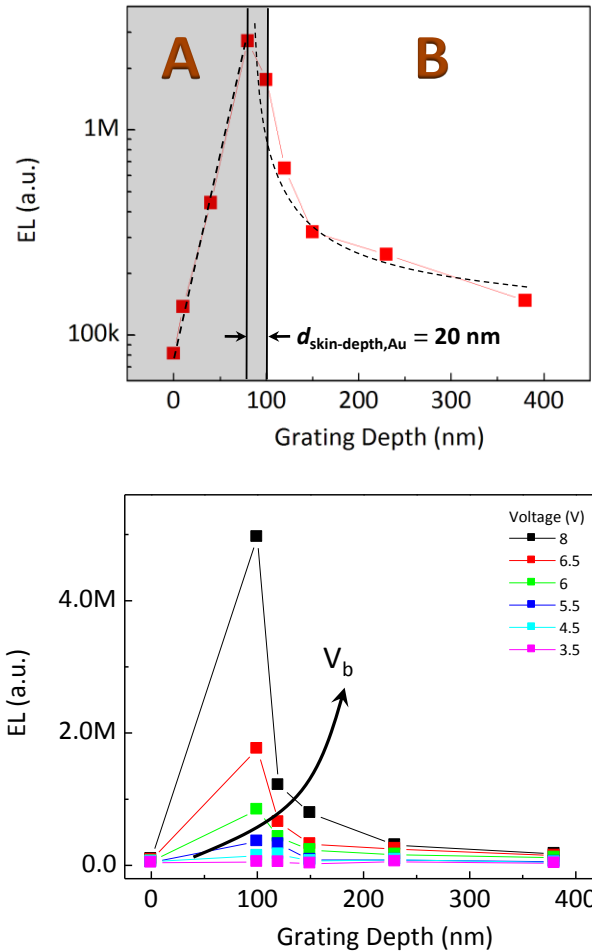
Figure 6.2.6 | EL - Grating Depth Correlation. (top) the grey shaded area is the thickness of the top-metal contact of the MIS-LETJ with a maximum thickness of 100 nm. If the metal thickness is reduce or grating thickness increased, the metal loss is consequently reduced exponentially as expected. The maximum EL occurs not at zero metal thickness, because then it cannot function as an electrical contact any more. EL_{max} is however found at about a metal thickness equivalent to the skin-dept of Gold. (bottom) EL trend curves for changing grating depth and voltage bias indicating a significant increase in EL for medium voltages and optimized grading depths.

Comparing our experimentally tested and grating-optimized MIS-based LETJ to un-optimized, as-fabricated junctions, we define the EL enhancement ratio as the collected signal from the grating samples minus the background signal and divide this product by the EL signal from the un-etched metal pad minus its background (upper left Fig. 6.2.7). A square-shaped grating yields a medium EL enhancement of up to around 50 times (middle Fig. 6.2.7). However, a sinusoidal

grating-shaped grating yields en enhancement of up to 450 times (bottom Fig. 6.2.7). The additional EL performance for the latter could come from a more homogeneously provided momentum addition to the hybrid plasmon mode, yielding to a higher out-coupling efficiency.
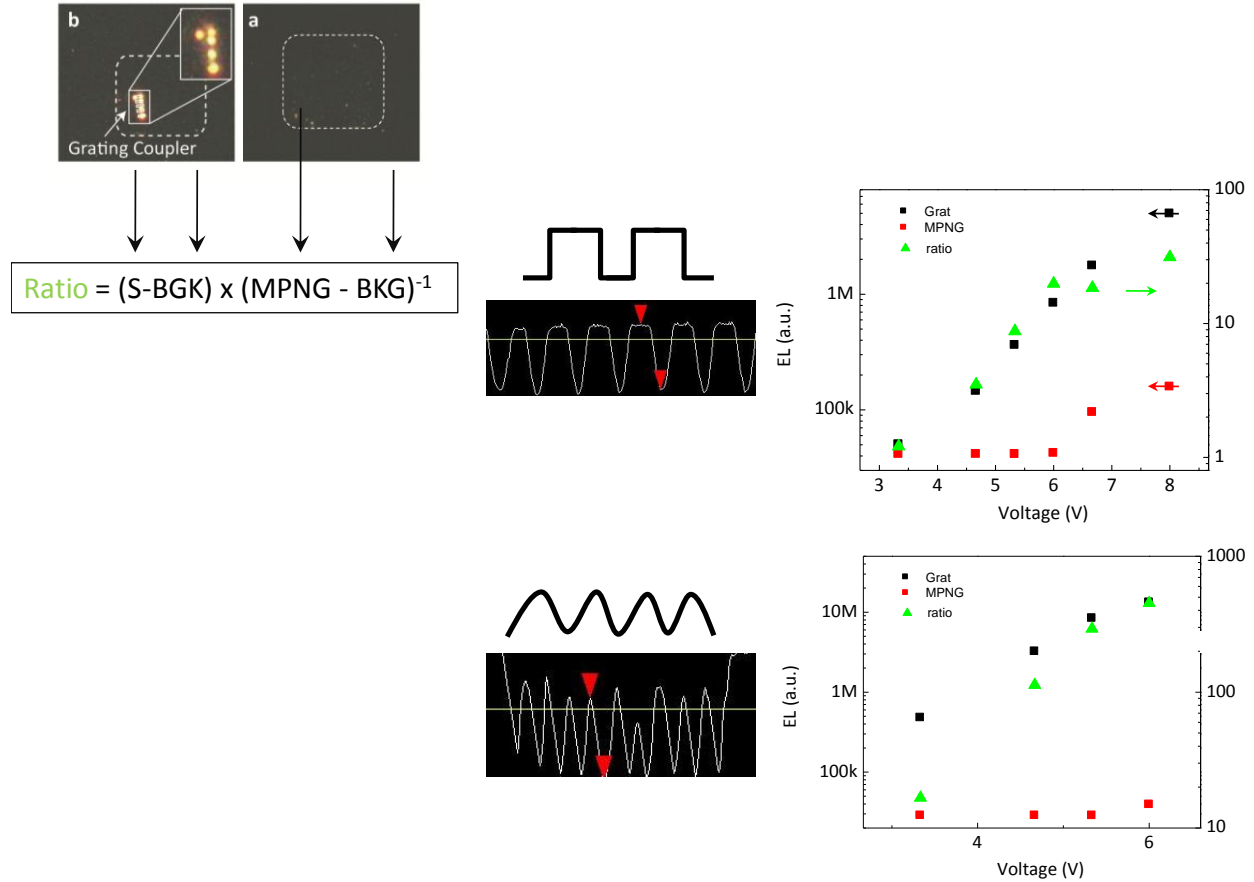
Figure 6.2.7 | Outcoupling Enhancement and comparison to un-etched samples. (top-left) Formula and indications for enhancement ratio (green) calculation. S = Signal, BGK = background, MPNG = Metal-pad-No-Grating. (middle) Square-grating shape and EL enhancement ratio showing an up to 50 times increased EL for this grating compared to samples without. (bottom) The EL enhancement for a sinusoidal grating yields an enhancement of up to 450 times. The degradation of the EL curve for high bias voltages is due to imperfect MIS-junction.

Lastly, we analyzed experimental data in order to confirm the underlying light-creating mechanisms. IV and L-I curves from more than 10 devices were normalized and averaged to show the voltage trend of junction current and light creation (top Fig. 6.2.8). The result shows that the current and the EL track each other almost perfectly. This confirms that the tunneling electrons are indeed the source of the photon creation. However, the question is what the external quantum efficiency of the junction is. For this we need to calibrate the EL from the LETJ with a known light source, for which a He-Ne laser as used. The resulting EL vs. electrical power input curves are shown in the bottom panel of Figure 6.2.8 for three different grating depths, d. As previously discussed the highest light output and also efficiency is measured for grating

thicknesses of about 80 nm, thus 20 nm of metal resides on top of the junction. For such high EL samples the external quantum efficiency is 10^{-4}.
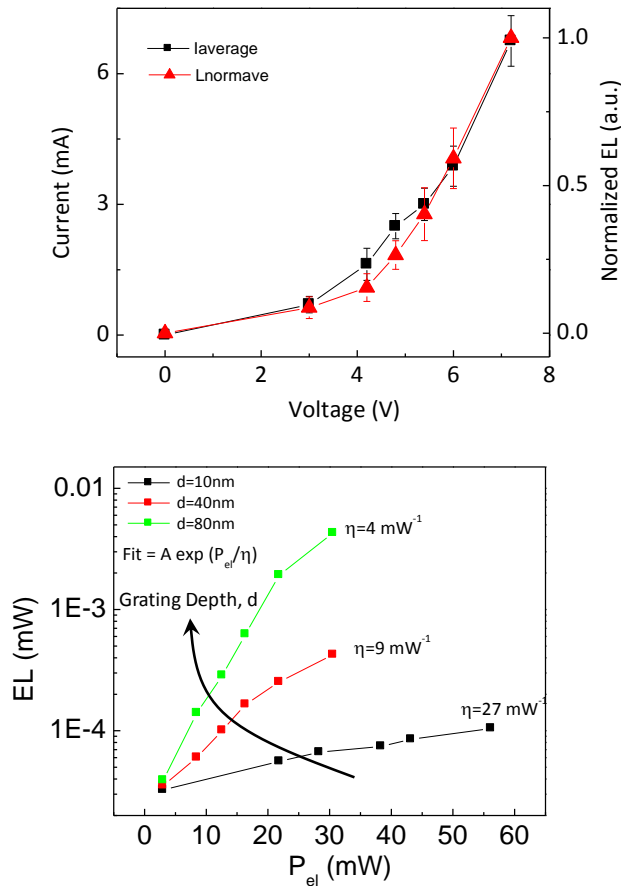
Figure 6.2.8 | LETJ Performance Characteristics. (top) The I-V (black squares) and L-I (red triangles) curves track each other almost perfectly. Data from more than 10 devices were normalized and averaged. The finding that these two trends match each other confirms that the source of the photon creation lies in the electrical current. (bottom) the EL from the LETJ with a grating showing a maximum external quantum efficiency of $\eta = 10^{-4}$.

6.3 Modulation Speed Simulations

Of great interest is the modulation speed of such light emitting tunnel junctions. From Heisenberg's Uncertainty principle, large optical bandwidths imply inelastic tunneling speeds on the order of 10 fs [1] and tunneling events have been measured on the order of 100 as [2. Comparing this to recombination lifetimes of direct and indirect bandgap semiconductors such as GaAs and Si [2,3], which are on the order of ns and ms, respectively, we find a clear advantage in terms of modulation speed for the LETJ. Thus the fundamental photon generation process can yield 6 or more orders of magnitude improved direct modulation bandwidths. The speed of inelastic tunneling, then, is effectively negligible. In the case of optical modulation, then, device bandwidths on the order of THz would be expected. For electrically driven devices to achieve large direct modulation rates, the limiting factor would then fall to RC effects of the junction itself. Representative metal-insulator-semiconductor (MIS) devices are planar structures that act as parallel plate capacitor (inset Figure 6.3.1). The relevant resistance in this case is not the line impedance but the tunneling resistance. For inelastic tunneling to be efficient, electron tunnel current must dominate the displacement current across the capacitor.

<div align="center">Standard Thermionic Emission Current + Tunneling</div>

$$J_{Tunnel} = A^* T^2 \exp\left(-\alpha_T \Phi_T^{0.5} t_{ox}\right) \exp\left(-q\Phi_B / k_B T\right)\left[\exp\left(qV_{bias}/k_B T\right) - 1\right]$$

$$A^* = 4\pi m_t^* q k_B^2 h^{-3} \text{ (effective Richardson constant)}$$

$$\Phi_T = \chi_{Si} - \chi_{SiO2} = 4.05 - 0.95 = 3.1 eV$$

$$\Phi_B = \chi_{Si} + E_g - \Phi_M = 4.05 + 1.12 - 4.2 \approx 1eV$$

$$C = \varepsilon_0 \varepsilon_r \frac{A}{t_{ox}} = 8.8 \times 10^{-12} \frac{F}{m} \cdot 4 \cdot \frac{1\mu m \cdot 1\mu m}{2nm} = 20 fF$$

$$U = RI, J = IA^{-1} \Rightarrow R_{tunnel}^{-1} = J_{tunnel} A U^{-1}$$

$$BW = \frac{1}{\tau} = \frac{1}{R_{tunnel} C} = \frac{t_{ox} J_t(t_{ox}, U) A}{\varepsilon_0 \varepsilon U A} = \frac{t_{ox} J_t}{\varepsilon_0 \varepsilon U}$$
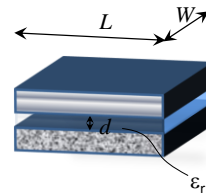
Figure 6.3.1 | Equation Tool-Set for simulating the modulation speed of the LETJ. The current inside the LETJ can be modeled by a current with two components; thermionic emission and tunneling. Taking the junction as a parallel plate capacitor (Inset) the capacitance can be easily estimated. The final bandwidth (BW) depends only on the RC delay time which interestingly does not depend on the device area any more.

Note, that tunneling resistance scales inversely with area and capacitance scales linearly with area, yielding an RC time constant invariant to area. The resistance scales exponentially with thickness, while the capacitance only scales inversely, meaning that a very high bandwidth can

be achieved with a sufficiently thin dielectric. A plot of this RC limited bandwidth is given in 6.3.2 for the case of 2V bias across the junction.
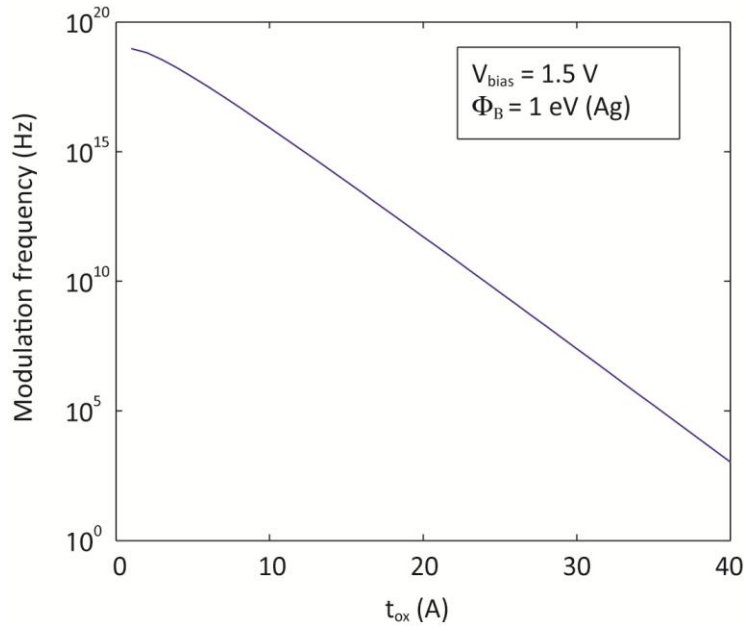
Figure 6.3.2 | Speed Simulation of a LETJ. The modulation speed is a strong function of the tunnel oxide thickness, t_{ox}, which dominates the speed characteristic of the junction.

Although tunnel junction light sources have the potential for unprecedented modulation rates, low wall-plug efficiencies have limited their utility. Typical reports demonstrate less than 10^{-5} electrical to optical conversion [3]. This problem stems from two sources: the poor methods of out-coupling from the lossy, tightly-bound plasmon mode to a free-space photon and the quantum efficiency of elastic over inelastic tunneling. As our recent theoretical and experimental advances in LETJ as shown above and nano-lasers have demonstrated the first of these problems can be overcome by modern nanofabrication tools and educated design [4-6].

In conclusion in this chapter we discussed theoretical and preliminary experimental results on light emitting Tunnel Junctions. Their novel physics of stimulated emission from electron tunneling and speed analysis seems a promising path towards 100% CMOS compatible light sources suitable for full-scale production. In addition, they can be directly modulated at high speeds, while also scalable below the micron size by employing plasmonic mode character. This provides a superior match to the transistor, reducing the footprint on chip by several orders of magnitude compared to conventional light sources.

7. Photonic Integration

7.1 Motivation for Photonic Integrated Circuits

Components Integration

With the electronic advances during World War I and II, various industries took on a path to shrink-down (scaling) individual components. For instance the very successful amplifier of its time, the vacuum-tube, was replaced by an electronic, solid-state device, namely the transistor. However, circuit design first looked quite different from what we know today from pictures from e.g. Intel. That was, individual components e.g. a single transistor or a single capacitance were mounted on some sort of printed circuit board. These discrete components are for example shown in the top left panel of Fig. 7.1.1. While it was possible to set up running computers with such discrete circuit architecture, resulting computers were not only huge and slow, but also power-hungry and failure prone (top Fig. 7.7.1).

Empirically one finds a relation between the critical device length scale of a technology and its maximum operation speed limit. Figure 7.1.2 for instance shows such a relationship of various technologies as areas on such a comparative scheme. The previously described discrete-component circuits fall in the lower right corner of fig. 7.1.2. The semiconductor industry took a path to move along one axis of Figure 7.1.2, namely from the lower right to the lower left corner. That is, devices, namely transistors were integrated to the billions onto the same chip platform. The fundamental limitation of this approach are the capacitances created by such densely packed circuits which ultimate limit electronic circuits to about 15 GHz switching speeds for these on-chip circuits [1-5]. From the 'old' lower right (large & slow) corner the parallelism of photonics, namely bosonic nature of photons, allows sending enormous amounts of information. Thus Photonics allows advancing along the speed (vertical) axis of the Figure. This potential has been realized in the 1980's and 90's by various telecommunication, former telephone, companies leading to ultra-fast (at the time) optical networks. Yet, similar to 1st generation IC's such optical networks deployed discrete components, namely a laser module, a MUX, a DE-MUX, a wavelength stabilizer, selector, add-drop filters and signal photodetector (middle Fig. 7.1.1). And again, while these optical networks were fast, they suffered from being power hungry and failure prone. Naturally, a solution is to integrate such photonics circuits and move to the upper left corner (bottom). The obvious show-stopper then soon is the diffraction limit of light, prohibiting further scaling.

The realization to combine optics with metals leads to the field of plasmonics, also known as metal optics. Here, a unique synergy is created between high-speed bosonic light and ultra-small electronic foot-prints (upper-left corner of Fig. 7.1.2). This chapter addresses the integration potentials of such future hybrid circuit.
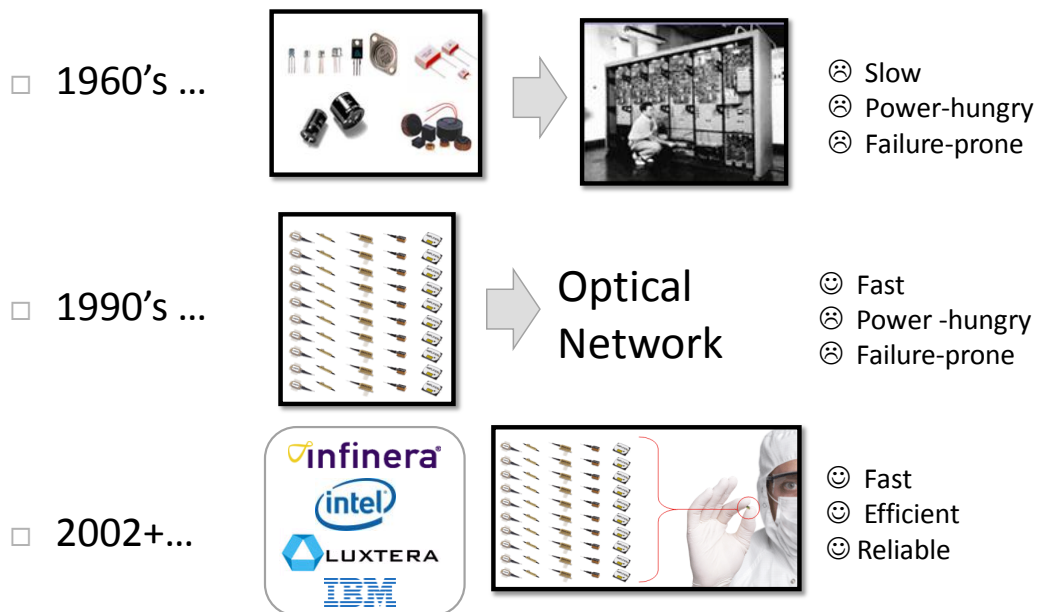
Figure 7.1.1 | Time-line and Performances of electrical and optical networks and circuits. (top) Electrical discrete components and first computers leading to low performing networks. (middle) The discrete-components based optical network revolutionized the general network architecture towards high speed, yet other parameters are similar to the electronics versions. (bottom) Integrating optical components onto a single chip lead to the photonic integrate circuit (PIC) taking all advances of ICs but adding the fast bandwidth contribution from photonics. Companies working on PICs are shown on the lower left side.

Future Hybrid Circuits

The International Technology Roadmap for Semiconductors [1] predicts a continuing advance of CMOS electronic technologies towards fabricated dimensions on the scale of 10 nm or smaller within the next 10 – 12 years. In addition to making better transistors, such a technology opens unprecedented opportunities for sophisticated nanoscale structures combining semiconductors, dielectrics and metals. In particular, the combination of two opportunities enabled by such technology – 10 nm-scale quantum-confined semiconductor structures and 10 nm-scale concentration of light by nanometallic and plasmonic metal structures – opens a new field of possibilities. Semiconductors on such size scales show strong quantum mechanical effects even at room temperature – essentially, we will be able of manufacturing quantum dots. Such quantum confinement opens new opportunities for optical effects, such as the very strong electroabsorption recently observed in CMOS-compatible Ge nanostructures [2] that has recently been applied to optical modulators [3]. The concentration of light on 10 nm scales into semiconductors offers radical possibilities, such as ultralow capacitance (e.g., < 10 aF) ultrafast

(e.g. < 1 ps) photodetectors integrated with transistors; quantum dot light emitters; nonlinear optics, possibly to the single photon level; ultralow energy (e.g. < 100 aJ) optical modulators; and even hybrid optoelectronic logic [4].

Such a new technology of hybrid nanophotonics could solve significant and growing problems in electronic information processing. In general, information processing is becoming limited by power dissipation [5], both for small mobile devices or devices on mobile platforms that have limited power sources and for large systems that will reach environmental limits. In electronics, even down to the level of individual gates, the energy of interconnects can dominate over logic energies themselves [4]. That interconnect energy is primarily the charging and discharging of electrical lines, a process fundamentally avoided in optics. Efficient nanoscale hybrid optical-electronic technology could therefore eliminate the major source of power dissipation in information processing. When coupled with the efficient dielectric optics and guides that enable long distance optical communications, such nanophotonic approaches also eliminate the interconnect bandwidth density problems that are the other major constraint on scaling in information processing. Optics too can solve other information processing limitations such as timing precision for clocking high speed systems. Analog-to-digital conversion is limited by sampling time precision, especially for high conversion rates [6], and optics has already been shown to provide a possible solution [7,8]. High-speed integrated nano-photodetectors would reduce the optical triggering energy requirements to make such optoelectronic sampling practical.

Requirements	Examples			
Active Components	Photo-Detector[8]	Modulator	SPP/Light-Emitter	Optical Transistor
Passive Components	Waveguides	Couplers	Splitters	Antennae
Fabrication Techniques	Tolerances < 10 nm		Electrical Contacting & Passivation	
Systems	Coupling to all components		Ultra-low capacitance devices	
	Ultrafast sampling systems		Efficient/fast interconnects	

Table 7.1 | Device and System Requirements for future electro-optical hybrid circuitry. The overall design scheme is governed by speed or bandwidth requirements as well as cost and efficiency functions [5].

For all of these information processing applications, integration of devices is critical, both to generate the numbers and densities to impact real applications and to achieve the necessary level of performance (avoiding any stray or interconnect capacitance). The key is to generate the specific ideas and nanostructures to enable this vision.

There is a broad range of possible hybrid nanophotonic devices that could be enabled by such a technology base and that could impact applications. In particular Table 7.1 summarizes requirements for nanoscale future ultra-fast and energy efficient hybrid circuits. While many components named in table 7.1 are generic devices, care has to be taken in performance and benchmark measures such as energy consumption, fabrication feasibility and system

compatibilities. Many of these components will include metal optics or plasmonic elements since they hold great promise for efficient and fast IT technology [9-17].

Operating Speed and Critical Dimensions

While the photonic integrated circuit (PIC) was proposed shortly after the invention of the electronic integrated circuit (IC), the absence of an optical transistor hindered the advance of optical circuits for many years [18]. However, with unique properties of metal optics new momentum is currently (the year 2011 that is) present in the research community. Primarily these advances are due to the possibility to scale down various components and hence circuits on the on hand. On the other, the novel synergies are being made by combining the fields of optics and electronics to gain the best from both worlds [9-19]. In particular the plasmonics allows to strengthen light-matter interactions, creating unprecedentedly strong effects [10-13,19-21].

Figure 7.1.2 highlights a particular interesting viewpoint on this matter, that is the generic relation between the scaling trend of various technologies and their corresponding operating speed. While in the past components or critical dimensions of components were rather large and also slow, the huge success of the semiconductor industry demonstrated the feasibility of integrating billions of building blocks onto a single die (piece of wafer). However, due to the strong capacitive interconnect delay which worsens with each advance in technology node (=smaller devices), the maximum achievable operating speeds are limited to ~ 10 GHz [1,5].
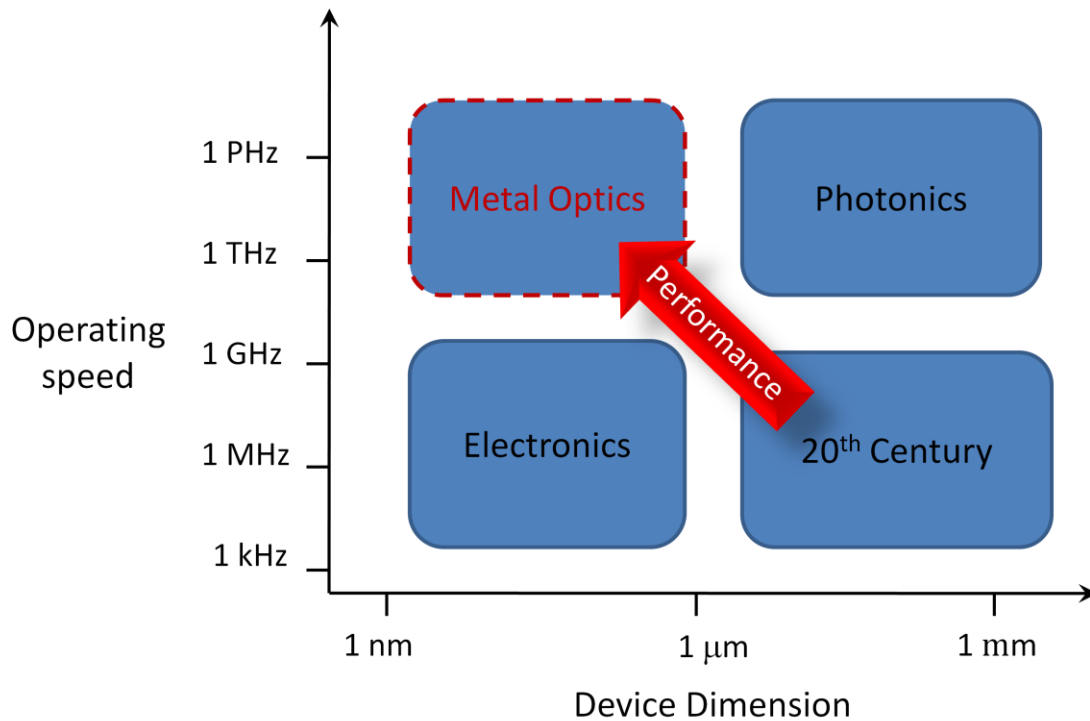
Figure 7.1.2 | The Trend of device performance. Components shrink in size, the operating speed increases allowing for faster and more efficient architectures [17].

Requirements for Optical and Opto-Electronic Devices

Above we argue that nanoscale metal-optics-based hybrid circuits comprised smart synergies between electronic and optical components including novel plasmonics & metal-optics structures can open a road for next generation circuits. In particular energy requirements are not only becoming important from a performance (hard number) point of view, but also from a socio-political (soft numbers) one. With the raised awareness for energy-scarceness in developed countries, the US government also tool on a policy roadmap to reduce the countries CO_2 production by 83% until 2050 [22]. Such policies therefore also penetrate into the IT sector and influence corporation future decision making. Coming back to the PIC, let us analyze what direct influence and requirements this would require for photonic and opto-electronic components for future hybrid circuits [5].

i.   To be competitive with the current state of the art in electrical off-chip interconnects, the system energy per bit should be <1 pJ, and to offer sufficient energy advantage for optics, it should be 100 fJ/bit or lower.

ii. To meet the demands of off-chip interconnects out to the ITRS projections of 2022, system energies per bit of 100 fJ/bit may sufficient, but to sustain the number of bytes in the later years will require 50 fJ/bit or lower system energy.

iii. To be competitive with near-future electrical global on-chip interconnects, the system energy per bit should be significantly lower than 50–200 fJ/bit.

iv. Lastly, to meet global on-chip interconnect demands until 2022 will require system energies per bit of 30 fJ/bit on ITRS projections. This is assuming the global on-chip bandwidth is 5 times the off-chip bandwidth; and to sustain the number of bytes/ FLOP in the later years will require 10 fJ/bit system energies.

7.2 Demonstrations and Trends

Introducing the status of current photonic integration Figure 7.2.1 provides an overview of the history until 2011, see references in figure for detailed information on the particular demonstration [18]. For the first decade or so after the demonstration of the CW laser in the GaAs system, lasers in compound semiconductor system started to mature. In mid 1980s, there was active work in the area of Opto-Electronic Integrated Circuits where the integration of electronic devices like the heterojunction bipolar transistor and field effect transistor with laser diodes and photodetectors was pursued. In the late 1980s three section tunable Distributed Bragg Reflector lasers were introduced. Electro-absorption modulators (EAMs) integrated with distributed feedback (DFB) lasers were also demonstrated during this period. The trend continued with more complicated tunable laser sources which were also integrated with an EAM or a semiconductor optical amplifier (SOA). The next step was the demonstration of the Arrayed Waveguide Grating (AWG) or PHASAR (Phased Array) router integrated with photodetectors for multi-channel receivers or with gain regions and EAMs for multi-frequency lasers and multi-channel modulated sources. One of the most complex PICs reported in the last century was a 4-channel optical cross-connect integrating 2 AWGs with 16 MZI-switches.
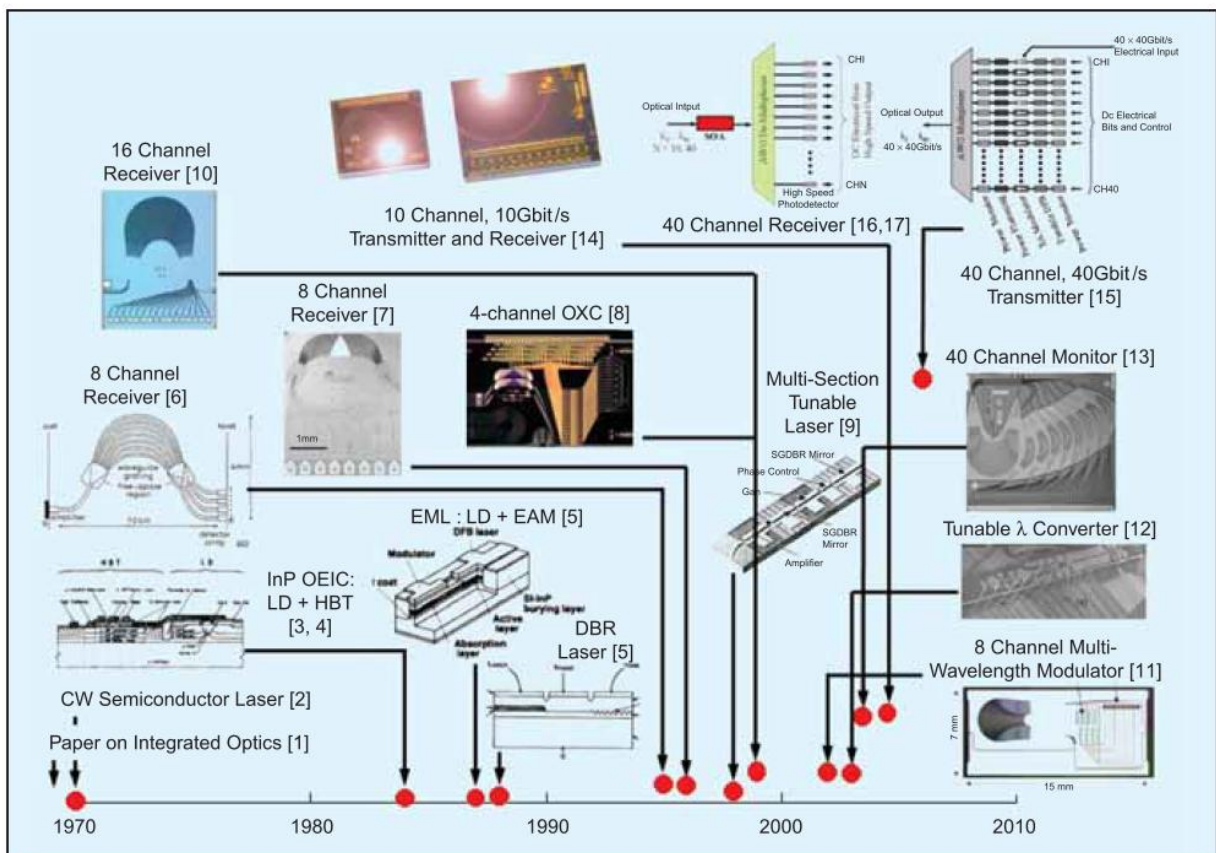
Figure 7.2.1 | History of Photonic Integrated Circuits showing increasing performance and circuit complexity with advancements in various technologies on a component level [18]. See references in figure for details on the device or demonstration.

At this stage, the most sophisticated laboratory devices still had component counts below twenty while those in the field had component counts of about four. The trend in low-level photonic integration continued into the first few years of the 21st century. The first integrated chip was made in 2004 when Infinera introduced a 10-channel transmitter, with each channel operating at 10 Gbit/s. This device with an integration count in excess of 50 individual components was the first large-scale PIC device deployed in the field to carry live network traffic. This demonstration was quickly followed by a 40-channel monolithic InP transmitter, with each channel operating at 40Gbit/s, with a total component count larger than 240, and a complementary 40-channel receiver PIC. As a further step in complexity, the 40-channel receiver PIC also had an integrated, polarization independent, multi-channel SOA. The upper right corner of Figure 7.2.1 shows the architecture of the 40-channel transmitter PIC. Each transmit channel consists of a tunable DFB, a back facet power monitor, an EAM, a power flattening element, and a front power monitor. The 40 different wavelength channels are then combined using the AWG multiplexer. The normalized, power flattened, fiber coupled, output power spectrum of the 40-channel PIC channel AWG was designed to match the 50GHz channel spacing of the DFB array.

With many device concepts and first nanoscale PICs are emerging, the circuit functionalities per footprint is still rather small. In order to drive such performance measures further, scaling of such circuits is mandatory. Ongoing research in this direction seems to have already shown promising results. For instance the Harvard group from H. Park recently crossed a semiconductor nanowire with a metallic one showing electrical single surface plasmon detection. Our group has very recently theoretically calculated that the coupling from a plasmon hybrid mode laser into a semiconductor waveguide when a metal-strip and the waveguide are crossed can surprisingly high. The crossing junction constitutes the photon source in form or a plasmon laser. While the transverse magnetic mode of this coherent source allows for deep sub-wavelength confinement in form of the hybrid mode discussed in chapter three, the transverse electric mode is able to couple from the laser cavity quite efficiently into the waveguide where it can be routed anywhere desired. This coupling efficiency is about seventy percent over a wide range of geometric parameter of the device. It is straight forward to envision utilizing multiple such crossing towards increasing the functionality of such emerging scaled circuits.

8. Outlook and Conclusion

8.1 Future Directions

Bringing the research described in this dissertation into a perspective from an information technology-to-market point of view we yield an order like the one shown in Figure 8.1.1. While research activities are found on all six fields, the technology frontier of actual products deploying this technology is at the Integrated-Photonics box. Companies like Intel, Infinera and Luxtera are selling (or are just about to) products including photonic integrated circuits.

My dissertation looked into solutions beyond such diffraction limited integrated photonics solutions. As I have outline in the previous chapters, beating the diffraction limit of light via metal optics or plasmonics can lead to Opto-electronic building blocks that are not only on the same order like electronic devices or biological viruses, but also are able to introduce novel efficient effects. Similar to the trend of ICs to reduce the overall driving voltage of individual components and circuits level biases, we can expect the optical "voltage" namely the light intensity inside photonic circuits to be reduced. Thus, the natural next stepping stone after the Nano-Photonics era will be to reduce the optical power level to the extreme, namely to the single photon level. From here, the bridge to quantum optics is a small one. The unique difference here will be to utilize Q-bits instead of traditional bits towards computation. While a computation on bit is comprised of a series of zeros and ones, the Q-bit utilizes the four linear combinations of a bit; namely the quantum mechanical states of 1+1, 0+0 and the cross terms 1+0 and 0+1. Such technology will enable not only enhance computing power usage through 'clever' quantum algorithms, but also introduce a new era of IT security. The latter is possible because a Q-bit is going to be changed be even measuring its state. Or in other words, if a spy, typically called an eve's dropper, is extracting data from a information send between two parties, e.g. Alice and Bob, the eve's dropper would change the quantum state by simply 'listing in'. This additional security level is currently of great research interest.

Other future directions include single molecular optical elements and finding bridges with or to the life-sciences. As mentioned before, plasmonics allows shrinking optical field (almost) to molecular level. Here sensors or detecting applications could find a strong partner in optics. Furthermore, with the current rising awareness of 'green-living', optically enhanced fields on a nanoscale are holding promise to allow for instance ultra-thin, yet high efficient photo-voltaic applications. Such novel solar cells could be very investment cost effective, due to low processing and material costs of such tens of nanometer thin solar cells.

In the following chapter we will go back to experimental results as an example of strongly enhanced light-matter interactions. Here, molecular emission is coupled into a deep-subwavelength waveguide, resulting in strong emission rate enhancements and an enhanced photon flux or brightness of the emitter. The strong coupling of molecule or atom like emitter is a stepping stone to single-photon devices like a single photon transistor [1].
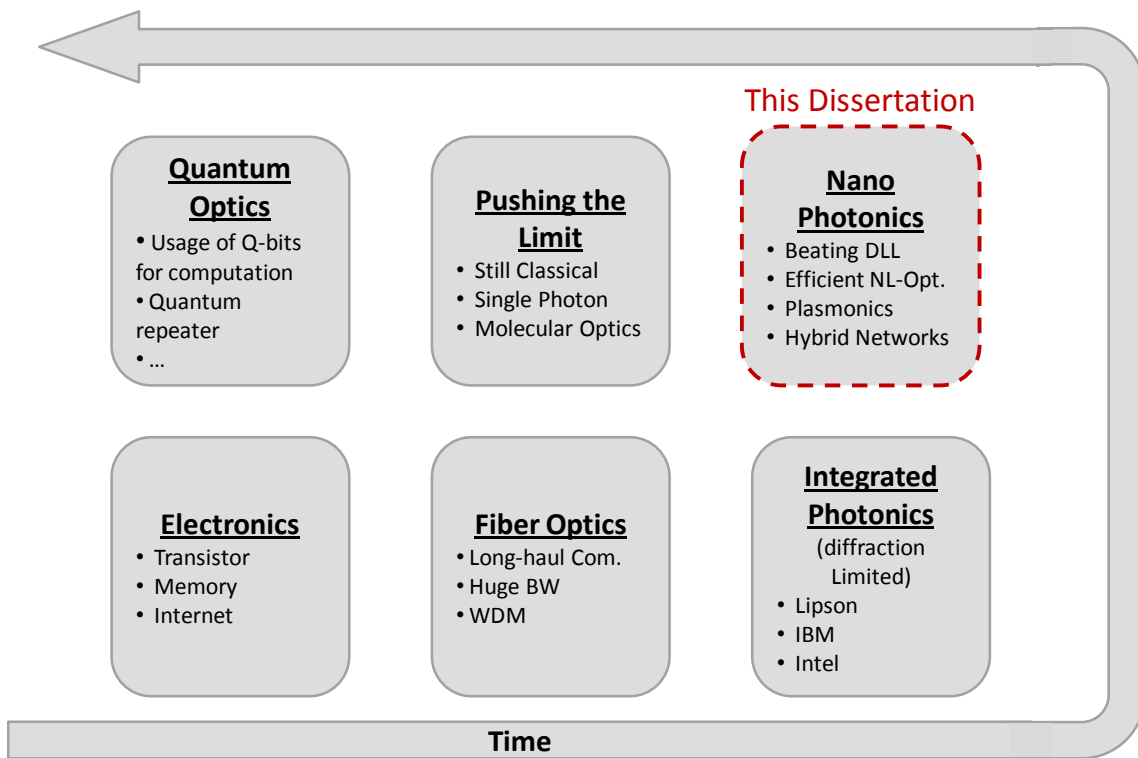
Figure 8.1.1 | The Time Advancement of the Research Frontier of Information Technology. While there is active research in all of the six sectors shown above, the frontier of information technologies in terms of commercialization follows the time outline shown. The next big impact will come from Integrated photonic solutions, e.g. Intel's Silicon Photonics labs or IBM. This dissertation targets the technology beyond pure photonic integration, namely a scaled version of it. As I have shown, metal optics can lead to strong non-linear effects with optical modes beating the diffraction limit of light (DLL). Nano-Photonics, however is just a stepping stone to quantum optics.

8.2 Enhancing Light-Matter Interaction

Abstract

We present an experimental study of spontaneous emission rate and photoluminescence (PL) intensity enhancement from dye molecules strongly coupled to the deep-subwavelength mode of a metal-dielectric hybrid plasmon polariton (HPP) waveguide. The rate of broadband dye spontaneous emission in the waveguide was found to be up to 65 times higher compared to uncoupled, intrinsic dye emission. We quantitatively verify the competing mechanisms of non-radiative energy transfer to the metal and, emission coupling into the guided mode. Up to 85% of the molecular emission couples into the waveguide mode due to the strong Purcell enhancement, resulting in a five-fold enhancement in the far field PL intensity.

Introduction

Most interactions between light and matter are inherently weak due to the vast difference in the characteristic wavelengths of light and electrons. A well known solution is to place emitters within an optical cavity with a small optical mode volume and high Q-factor [1]. However, as long as optical cavities remain diffraction limited, strong light-matter interactions will rely on high quality-factors (Q-factors) [2-5], which impose intrinsic limits on emission rates, bandwidths and often require painstaking tuning of emitter and cavity resonances [6]. The remaining strategy, to utilize electromagnetic field enhancement by reducing the spatial size of optical modes beyond the diffraction limit, is appealing because it allows for strong light matter interactions with extremely low Q-factor systems [7-9]. Hence, even the low densities of states of confined propagating waves are sufficient to significantly strengthen light matter interactions [10-13].

Results

Here, we report large enhancements of the spontaneous rate of molecular emission by strong coupling to a deep sub-wavelength propagating plasmonic waveguide mode [14,15]. We measure a reduction in emission lifetimes by as much as 65 times relative to the intrinsic lifetime of dye molecules over the broad spectral bandwidth of emission (> 70 nm). We attribute the high Purcell factors to a number of generated emission modes since the molecules probe the local density of states of the waveguide. Our experiments reveal a high probability that emission couples into the waveguide mode, which competes successfully with other emission channels. The fraction of emission coupling to the waveguide can be expressed by the spontaneous emission factor, β, which is as high as $\beta = 85\%$ in this work. The remainder of the emission is lost to free space, in-plane surface plasmon waves and non-radiative quenching [7-9]. Furthermore, we observe a 5-fold enhancement of the overall PL rate arising from the spontaneous emission rate enhancement into the waveguide mode and subsequent out-coupling. The efficient coupling of emission into waveguiding structures holds promises in the transfer of

quantum information technology [16], efficient light extraction [17,18] beyond the cavity-limited bandwidth and the speed of photonics [19,20].

In our experiments, we fabricated waveguides consisting of high permittivity ZnO semiconductor nanowires [21] with diameters between $d = 80 - 160$ nm (n = 2, [22]) separated from a silver substrate by a low permittivity PMMA layer (n = 1.46) of controllable nano-scale thickness containing Oxazine dye molecules [22,23], as shown in Figure 8.2.1(a) [14,15]. The silver was evaporated onto a quartz substrate while the Oxazine/PMMA and nanowires were spin-coated from solution. The resulting deep sub-wavelength confinement in the gap layer arises from the hybridization of the photonic mode of the nanowire and a surface plasmon polariton; polarization surface charge on the semiconductor nanowire and collective electron oscillations on the metal interface sustain a strong electric field in the dye region that is perpendicular to the substrate [14,15], as shown in Fig. 8.2.1(b). Note, that the key to the fabrication is the placement of the dye emitters in the waveguide mode's region of highest electric field intensity, as described above [14,15]. Since we are measuring emission from a small number of molecules beneath the nanowire, we had to ensure that the photoluminescence from defect states of the large-bandgap nanowire material was insignificant. We verified this by placing the nanowires on a quartz substrate and measured the emission for comparable excitation powers. The first evidence of efficient coupling between the dye molecules and the guided mode is fluorescence from the waveguide ends; emission (left inset Fig. 8.2.1(a)) from optically excited molecules beneath the middle of the waveguide propagate and subsequently scatter from the two nanowire ends (right inset Fig. 8.2.1(a)).

We measured the spontaneous emission lifetime using time-correlated single photon counting, where the dye molecules were excited by femtosecond laser pulses focused to a spot of about 1 μm diameter through an objective lens onto the centre of each waveguide [22]. Emission from the dyes was collected from the nanowire ends with the same objective lens and registered by an avalanche photodiode, which built up a histogram of time delays between laser pulses and detected photons (Fig. 8.2.2) [22]. Spontaneous emission lifetimes were extracted by fitting the time response histogram to a bi-exponential lifetime model, which was sufficient to describe the spatial and dipole orientation heterogeneity between the optical mode and background dye emission.

To gain insight into the emission coupling to the various decay channels, we fabricated two control samples consisting of a 10 nm thick Oxazine/PMMA layer spin-coated onto: (i) quartz; and (ii) silver (300 nm thick film on quartz). Control (i) serves as a reference for the average intrinsic spontaneous emission lifetime of dye molecules in PMMA coupled to free space, which was found to be $\tau_{(i)} = \tau_0 = 2$ ns, as shown in Fig. 8.2.2(a). Control (ii), on the other hand, quantifies coupling to in-plane surface plasmons and the non-radiative quenching to the metal, which dominate over the coupling to free space and result in much shorter lifetimes of about $\tau_{(ii)} = 0.45$ ns, as shown in Fig. 8.2.2(b). The spontaneous emission lifetimes of the control samples are in sharp contrast to those of dye emission from the waveguide mode configuration with a 10 nm Oxazine/PMMA layer, which yields much shorter lifetimes of $\tau_m = 48 \pm 12$ ps (Fig. 8.2.2(c)). The enhancement beyond that of control (ii) arises from the strong mode confinement and suggests that the majority of emitted photons couple to the waveguide mode. This is

supported by our calculations, which show that quenching and surface plasmon coupling are not significantly modified by the presence of the nanowire [22].
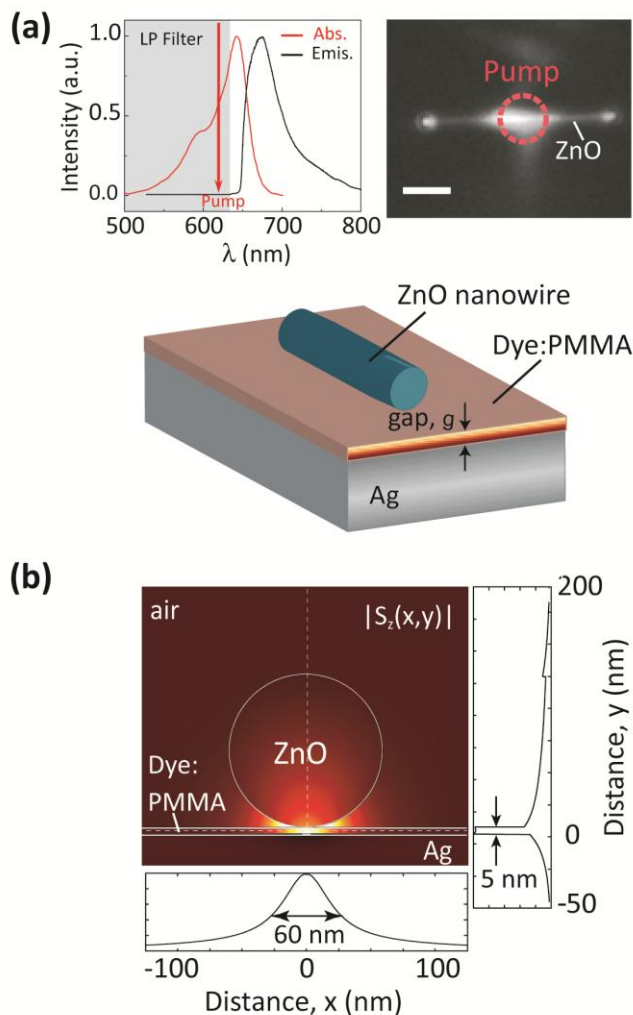
Figure. 8.2.1 | Schematic of the Experiment to couple molecular Emission into a plasmonic Waveguide. (a) Schematic of the HPP waveguide with dye-doped PMMA films (nanowire diameter = 80 − 160 nm, length about 5 μm). Dye to PMMA ratio = 0.06 wt% = constant. Insets: (Left) Spectral absorption of the Oxazine dyes and measured emission [22,23]. (Right) PL image of emission from dye molecules excited at the center of the nanowire (red circle) coupling to the HPP waveguide and scattering to far field at the ends of the wire, scale bar = 2 μm. (b) HPP mode pointing vector, $|S_z(x,y)|$ supporting a deep sub-wavelength propagating mode (full width at half maximum = 5 and 60 nm in x and y-direction, respectively) [14,15].
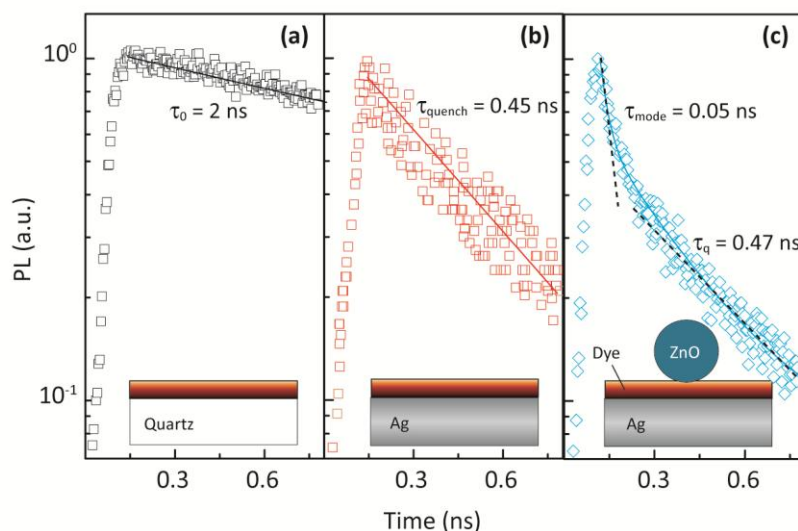
Figure. 8.2.2 | PL decay histograms with insets showing corresponding sample schematics (Dye:PMMA thickness, $g = 10$ nm). (a) and (b) show control samples (i) and (ii) serving as the intrinsic decay and quenched decay references, with average count rates of about 10^4 and 10^3 s^{-1}, respectively. (c) The HPP waveguide sample yields a shorter lifetime component due to coupling to a sub-wavelength waveguide mode (non-resonant Purcell effect), while the longer lifetime is due to background molecules near the metal surface, which is consistent with the lifetimes observed in (b). Average count rate was about 10^3 s^{-1}. Dashed lines are guides to the eye for the two exponential dependencies.

Further evidence for the role of the waveguide mode in the emission process is seen in the shapes of the time delay histograms in Fig. 8.2.2. While both histograms for the two control samples display single exponential decays, the waveguide's histogram is bi-exponential. In the control samples, we observed little dependence on the dipole orientation of the dye molecules or their position on the substrate. However, the coupling of dye molecules to the waveguide mode depends both on position beneath the nanowire and the dipole orientation since the mode is both laterally confined and highly polarized perpendicular to the metal surface (Fig. 8.2.2(c)). We therefore attribute the observed bi-exponential decay of dye emission in the waveguide structure to the different decay rates of molecules coupled (fast decay) and uncoupled (slow decay) to the HPP mode [22]. This conclusion is supported by the observation that the slower decay rate is comparable to the decay rate of dyes in control (ii).

To understand the mechanism of strong coupling of dye emission to the waveguide mode in more detail, we have conducted the experiments above for various Oxazine/PMMA layer thicknesses, g. Figure 8.2.3(a) and (b) show a schematic of the possible decay channels and the measurement results, respectively. The results clearly show that the emission rate into the waveguide mode and non-radiative quenching to the metal follow two distinct trends with changing g. Our analysis is therefore greatly aided by the following analytical formula for the modal Purcell factor $F_m(\boldsymbol{r}_0)$ [4,9,22,24]

$$F_m(\boldsymbol{r}_0) = \frac{\gamma_m(\boldsymbol{r}_0)}{\gamma_0} = \frac{3\lambda_0^2}{4\pi} \left(\frac{c/n}{v_E}\right) \left[\frac{\varepsilon_0 |\boldsymbol{E}(\boldsymbol{r}_0)|^2}{2 \int w(x,y)dA}\right] \qquad (1)$$

where the emission rate to the mode $\gamma_m(\boldsymbol{r}_0)$ is normalized by the unmodified emission rate of dipoles γ_0 within an unbounded (intrinsic) host medium of index $n = \sqrt{\varepsilon}$; $|\boldsymbol{E}(\boldsymbol{r}_0)|^2$ is the waveguide mode's electric field at the dipole position $\boldsymbol{r}_0 = [x_0, y_0]$; $w(x,y)$ the mode's energy density; ε_0 and λ_0 are the free space permittivity and wavelength, respectively; and c/n and v_E are the phase and energy velocities, respectively. Following Eqn. (1) we interpret the Purcell effect for the waveguide mode as a combination of strong electrical energy concentration and deceleration of power flux. Using this, we have estimated the Purcell factor for our system, $F_p(g) = F_m\left(0, \frac{g}{2}\right) + F_q(g) + F_{SPP}(g) + 1 = \left(\gamma_m(0, g/2) + \gamma_q(g) + \gamma_{SPP}(g) + \gamma_0\right)\gamma_0^{-1}$ as a function of the gap width, g (Fig. 8.2.3(b)). Here, a dye molecule emitter is simulated as a vertical dipole situated mid-gap ($y_0 = g/2$) directly beneath the center of the nanowire ($x_0 = 0$), yielding the modal Purcell factor $F_m(0, g/2)$ (Fig. 8.2.3(b), green dotted line). We have confirmed this analytical description of the emission in these waveguides by 3D full vectorial Finite-Element Method simulations giving the contributions of control (ii), $F_{(ii)}(g)$, (Fig. 8.2.3(b), red dashed line) and the total Purcell factor, $F_P(g)$ (Fig. 8.2.3(b), black solid line).

The experimental data from the spontaneous lifetime measurements for varying Oxazine/PMMA thickness, g, agree well with the predicted total decay rates based on a single dipole for both control (ii) (red squares) and nanowire samples (black squares), as shown in Fig. 8.2.3(b). In comparing the nanowire and control (ii) samples, the calculated modal Purcell factor, $F_m(0, g/2) \approx F_p(g) - F_{(ii)}(g)$, suggests that emission into the hybrid plasmon mode dominates over all the other emission channels for a large range gap sizes, g [14,15]. However, for gaps smaller than about 5 nm, non-radiative quenching should start to dominate over emission into the waveguide mode (red squares).

An improved theoretical description should consider the whole molecular ensemble and account for the probability of detecting emission from each dipole. This is particularly important in our experiments due to the difference in areas beneath the nanowire (~ 5 μm x 100 nm) and the pumping area (~ 1 μm radius). Fast decaying dipoles beneath the nanowire can have a higher PL yield and therefore contribute more to the collected signal in the time decay histogram, especially when background molecules couple predominantly to non-radiative channels for thin gap layers. However, the small number of fast decaying molecules beneath the nanowire can be masked by the much stronger background from molecules in the collection area when the Dye/PMMA gap layer is thick and quenching processes are much weaker. Consequently, both the mode confinement and molecular ensemble affect the observed spontaneous emission rate as a function of the gap thickness, as shown in Fig. 8.2.3. For strong confinement, light is collected predominantly from the vertically oriented dipoles near the waveguide center with a high modal Purcell factor, which gives good agreement with our theory (Fig. 8.2.3(b), $g < 20$ nm, black squares). However, for low confinement, background emission, from uncoupled molecules in the thicker gap layer, overshadows the HPP mode emission leaving almost no observable Purcell effect (Fig. 8.2.3(b), $g > 20$ nm, black squares). This hypothesis is confirmed by selectively removing molecules contributing to the background signal with oxygen plasma etching using the

nanowire as an etch mask [22]. Successful removal of the background signal exposes the strong Purcell effect of molecules beneath the nanowire, even for quite large gap thicknesses (Fig. 8.2.3(b), black triangles). However, strong Purcell enhancements at low g strengthen the fast channel to the HPP mode leaving an insignificant contribution from the background signal (Fig. 8.2.3(b), black triangle at $g = 5$ nm). The above observations can be used to identify three different regimes highlighting the shift in dominance of competing decay channels. While quenching and the background signal from uncoupled molecules dominate the emission process for $g < 8$ nm (region **Q**) preferential coupling to the HPP waveguide mode is achieved for $g > 8$ nm (region **M**). On the other hand, the data from control (ii) (quenching contribution) match the theory excellently due to the lateral uniformity and a much weaker dependence of emission rate on dipole orientation (Fig. 8.2.3(b), red squares).
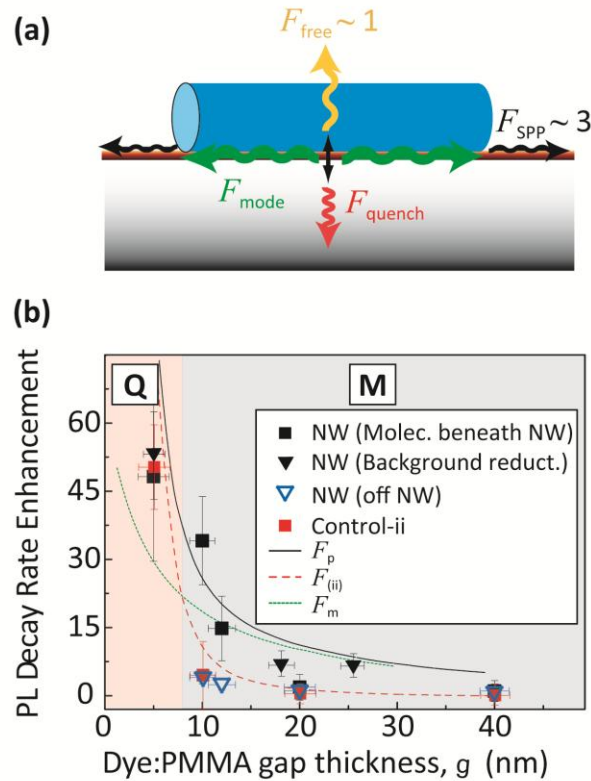
Figure. 8.2.3 | Possible Decay Channels and Emission Rate Analysis. (a) The decay channels accounted for in this study, the confined waveguide mode, free space and surface plasmon and quenching channels. (b) Average measured and calculated (after Eqn. (1)) spontaneous decay rate enhancements ((Purcell Factors [1]) versus gap thickness, g, highlighting competition between the various decay channels. While, quenching and the background signal from uncoupled molecules dominates for $g < 8$ nm (region **Q**), preferential coupling to the HPP waveguide mode is achieved for $g > 8$ nm (region **M**). An average (highest) Purcell enhancement of 48 (65) is observed at $g = 5$ nm. For large g the theoretically predicted trend of F_p is found by reducing the molecular background emission signal via O_2-plasma etching using the nanowire as a mask (black triangles) [22]. In the calculations, the emitting dipole (black vertical arrow in panel (a)) is positioned midgap ($g/2$) and the nanowire diameter =120 nm.

The competition between waveguide mode coupling and non-radiative quenching can be further examined by measuring the overall PL rate enhancement. While the Purcell factor of control (ii), $F_{(ii)}(g)$, describes the contributions from coupling to free-space, surface plasmons and non-radiative quenching, the measured Purcell factor from NW samples also includes the contribution from the waveguide mode coupling $F_p(g) \approx F_m(g) + F_{(ii)}(g)$. This provides an estimate of the waveguide mode coupling probability, $\beta(g) \approx 1 - F_{(ii)}(g)/F_p(g)$ (Fig. 4(a)). As expected, with decreasing gap, g, the β-factor approaches zero due to an increased quenching contribution. For thicker gaps, $\beta(g)$ increases to about 85%. It will eventually tend to zero again for very gaps much larger than those considered in this work.
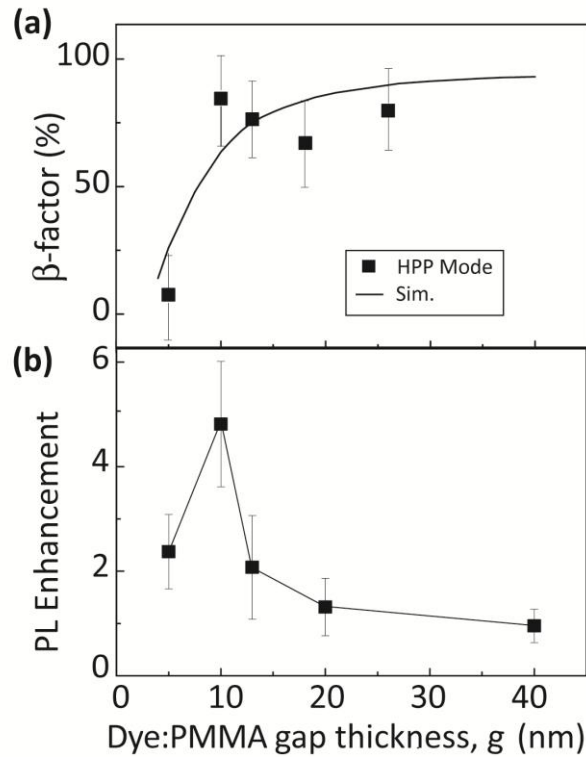
Figure. 8.2.4 | Emission Coupling Strength and PL Enhancement. Experimentally determined spontaneous emission factor (β) and Photoluminescence (PL) enhancement. (a) The waveguide modes β-factor increases monotonically with increasing gap thickness, g, and fully dominates over coupling to other emission channels, including quenching, for $g > 8$ nm. Note, for data points at $g = 18$ and 26 nm, we have interpolation between neighbouring data points from control (ii) samples. (b) The measured PL enhancement (on vs. off nanowire) shows directly the successful competition of the HPP mode over other emission channels, including quenching, resulting in a 5-fold increase at $g = 10$ nm.

In addition to the enhancement of the spontaneous emission lifetime, the PL brightness, or photon flux, at the detector is important from a practical device standpoint. We measured the total photon flux values from dyes beneath the waveguide (pump on nanowire) and the metal (pump on control-ii) samples as a function of the gap thickness and remarkably observed a 5-fold PL enhancement (Fig. 8.2.4(b)). This enhancement of PL extraction from dye molecules beneath

the wire is related to the product of the spontaneous emission rate enhancement (F_p), the hybrid mode spontaneous emission factor (β) and the far field photon out-coupling efficiency from the hybrid mode. Since $\beta F_p = F_m$, it must monotonically increase and for smaller gaps. Indeed, down to $g = 10$ nm the measured PL enhancement does increase as expected. However, below $g = 10$ nm, the decrease in the PL enhancement is attributed to a reduction in photon out-coupling efficiency from the hybrid mode, most likely due to limited propagation distance of hybrid plasmons. The directly measured photon flux is also affected by numerous additional factors small gaps including: modification of the excitation rate of dye molecules beneath the nanowire relative to uncoupled dye molecules; propagation losses of the hybrid mode; scattering of hybrid plasmons from the nanowire end facets; re-absorption of the propagating hybrid plasmon mode by other dye molecules; and the effect of background dye emission masking any enhancement due to dyes coupled to the nanowire. The effect of background dye emission is particularly strong; 15 times as many dye molecules are excited within the illumination spot (radius ~ 1 μm) compared with dye molecules beneath the 100 nm diameter nanowire; and we have already pointed out that the background emission in samples for $g > 20$ nm completely masks the signal from out-coupled nanowire modes. If dye molecules were accurately positioned beneath the nanowire we could expect to observe much larger enhancements in the PL rate away from the regime where quenching mechanisms dominate.

Conclusion

To summarize, we have quantitatively measured the spontaneous decay rate and PL intensity enhancement of dye molecules, which sample the sub-wavelength mode area in the gap region of a hybrid plasmon waveguide. We show that about 85% of the molecular emission can be coupled to an optical waveguide with deep sub-wavelength confinement. In addition, we verify the metal quenching contribution in the PL decay data by comparing with theory and PL intensity data. Furthermore, we find a PL brightness enhancement up to 5-fold for an optimum gap height of about 10 nm, implying that good photon extraction efficiency can be achieved. These results are important for the understanding and control of emission coupling into nano-plasmonic waveguide structures towards the development of rapid transfer of quantum information [16] and efficient light extraction [17,18] beyond the cavity-limited bandwidth [2,3,5,20].

Experimental Details

To demonstrate strongly coupled the dye molecule emission into the deep sub-wavelength guided HPP mode, we choose to utilize a time-resolved spontaneous emission spectroscopy. The Oxazine (O1 perchlorate 750, Fig. 8.2.5(a)) dye molecules were excited by a Ti:Sapphire fs-pulse laser ($\lambda = 620$ nm, spot radius ~ 1 μm, fs-pulse length ~ 100 fs) through an objective lens (63x, NA = 0.95). Spontaneous emission of the dyes was collected by the same objective, filtered within the spectrum bandwidth of 633 - 700 nm and registered by an avalanche photodiode. The measurement setup in a microphotoluminescence setup with schematic shown in Fig. 8.2.5(b). A reference pump laser triggers a diode (TD) and the Oxazine photon emission signal are the start and stop signal, respectively, in this time-correlated single photon counting system (TCSPC system PicoQuant) (Fig. 8.2.5(a)). Note, the detector's (APD, MicroPhotonicDevices, PDM-

series) dark count rate is one tenth of the photon collection rate from samples with dye molecules, thus no instrument response artefacts are expected in the single photon counting data (Fig. 8.2.2(b),(c)).
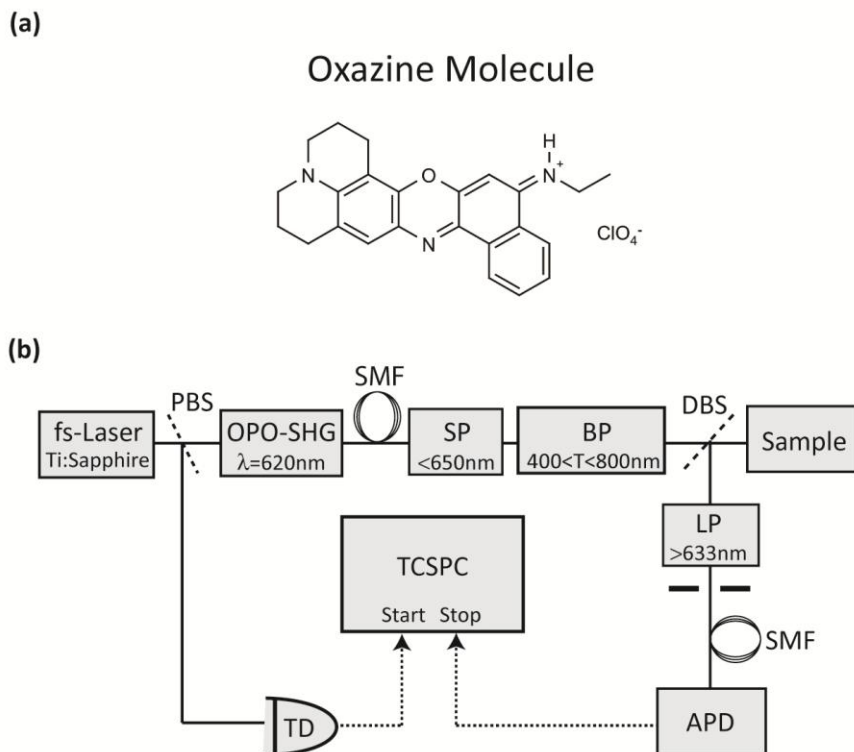
Figure 8.2.5 | Dye Molecule used and Experimental Setup. (a) Chemical Structure of Oxazine (O1 perchlorate 750) dye molecule. (b) Schematic of the microphotoluminescence time-correlated-single-photon-counting (TCSPC) setup: Ti:sapphire fs-pulse laser, pulse width ~ 100 fs, OPO: Optical Parametric Amplifier, SHG: second harmonic generation, PBS: polarizing beam splitter, SMF: single mode fiber for spatial filtering, SP/BP/LP: shortpass/bandpass/longpass filters, DBS: dichroic beamsplitter (long pass edge = 625 nm).

Effect of background dye emission vs. Purcell effect

Figure 8.2.3b in the main text highlights two different regions where the molecular emission is dominated, i.e. quenching and the background signal from uncoupled molecules for $g < 8$ nm (region **Q**) and preferential coupling to the waveguide mode for $g < 8$ nm (region **M**). The contribution of the background for larger gap sizes stems from uncoupled emission reaching the detector from molecules having a lateral offset to the nanowire. The origin of this is the size discrepancy between the collection area (~ 1 μm) and the nanowire diameter (~ 100 nm). In order to test this background emission dominance for large g we etched those offset dye molecules away, by deploying a mild oxygen plasma treatment using the nanowires as an etch mask (Inset Fig. 8.2.6). Lifetime measurements of samples before and after etching showed single exponential decay histogram with $\tau_{before} = 1.0$ ns and $\tau_{after} = 0.4$ ns, respectively, e.g. for g

148

= 20 nm (Fig. 8.2.6). Eliminating the overshadowing background signal contribution for large g, we are able to extract the total Purcell factor (Fig. 8.2.3(b)), black triangles), which now matches the predicted curve well (Fig. 8.2.3(b), black solid line). In contrast, repeating the etch process step for small gap sizes did reveal a bi-exponential decay before and after etching, showing the contributions of the vertical dipole and quenching. The reason behind these two different displays is the very strong Purcell factor at low gap sizes. In other words, the background contribution is too weak in this low-g-regime, which confirms the proper operation of the HPP mode concept; providing strong Purcell enhancements due to the sub-wavelength scale optical mode.
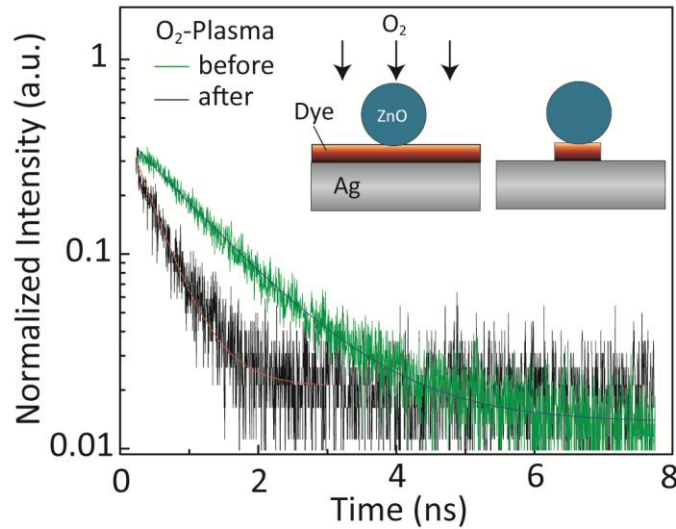
Figure 8.2.6 | Effect of plasma oxygen (O$_2$) etching on molecular emission into HPP-based waveguides. The nanowire is used as a shadow mask selectively etching the dye layer (Inset). For large gap sizes, the decay histograms show a single exponential decay before and after etching, however, with long (short) lifetimes before (after) etching. The long lifetime response before etching stems from uncoupled molecular emission creating a background signal overshadowing the HPP mode channel.

8.3 Large Scale Integrated Hybrid Nanophotonics

As an outlook into the future, the question comes up where this research field is leading to and what hurdles or challenges have to be overcome for a successful implementation. In particular, the merger between electronics and photonics seem to have already started. In the following we will discuss a particular interesting prospect that is the large scale integration of hybrid nano Photonic circuits.

In recent years great progress has been made in the field of nanophotonics. Within this trend the combination of photonics with nano electronics and the emerging prospect of chipscale optical networks. Novel waveguiding structures, such as slot, gap, MIM and hybrid waveguides, as well as the metal-optical modes of surface plasmons in particular allow for manipulation of light at ultra-small scales [1-11]. Although a wide set of both passive and active nanophotonic components have been achieved, it is expected that merging these two technologies will lead to opportunities and synergies unattainable by each technology separately [12]. However, fundamental questions will have to be answered in this new field and will require new theories and computational tools to address the interaction of intense and rapidly varying fields with metals, semiconductor and organic materials operating in both linear and non-linear regimes. Such fundamental development of novel near and far-field optical characterization tools will be required to help answer fundamental questions and optimize performance benchmarks on a device level [6]. Taking all advantages of both technologies, new building blocks allowing for simultaneous electronic and optical functions will be demonstrated. The component-span to be investigated in future research will include novel light sources [14-24], waveguides [1-11], antennas [25] and detectors [26], frequency converters, modulators [27-30], cavities [13], quantum optical devices [14] as well as high-speed devices [22,24,31] and circuits.

It is already foreseeable, that hybrid nanophotonics will also require the development of novel nano-manufacturing techniques to facilitate the large scale deployment of the technology and to allow for its integration with existing microelectronic and optoelectronic platforms. Although the recently emerging deep ultra-violet CMOS fabrication has allowed for a variety of Silicon-based photonic building blocks [27], the device performance can be severely reduced due to line-edge roughnesses of the critical dimension attainable in commercial operations. Thus, the fabrication of hybrid nanophotonic integrated circuits will require new high-throughput and large-area fabrication process. Apart from deep UV lithography, continuing development in electron beam lithography, focused ion beam milling, nano-imprint lithography and potential bottom up approaches will push the realization of large scale hybrid nanophotonics integration further. In the event of success of such circuitry, components could form the basis of a low-power, high-speed, lightweight optical technology that takes advantage of the synergy between semiconductor optoelectronics and metal optics operating at similar dimension. Table 8.3 summarizes various requirements for the research areas needed toward successful realization of such future large scale integrated hybrid Nanophotonic circuits and platforms [12].

Research Areas	Requirements
Materials & Fabrication	Novel Processing Techniques with minimum Roughness
Overall-design Format	Large-scale & high-throughput
Data-Routing	Novel hybrid Waveguide & Interconnect Concepts towards enhanced Interactions
Device Level	Sub-λ Photonics including Detectors & Light Sources
Light-Harvesting	Hybrid optical & plasmonic Cavity Effects; extreme light concentration
Non-Linear Optics	Hybrid Structures & Incorporation of non-linear Materials towards Devices & Subsystems based on non-linear effects
Tools & Support	Characterization Tools, computational Support & analytic Design Strategies Device & Sub-System level
Integration	Integration of these novel hybrid Circuits into exciting platforms like CMOS for higher functionality

Table 8.3 | Research areas and their Requirements for a realization of large scale integrated hybrid Nanophotonics [12].

The somewhat unforeseeable questions however is, what the industrial and sociological impact of such novel hybrid nanophotonic platforms will allow, incentivize or inhibit. Quite likely is the influential effect of the increased functionality of devices and components leading to impact a wide variety of sensing, security, communication and computing systems. Thus, integrated on-chip systems with unprecedented levels of integration, boasting digital, analog, power electronics with optical in-and-outputs, therefore can become reality [12]. Furthermore, the simultaneous integration of electronics and photonics will most likely result in significant speed and power advantages with subsequent overall system performance improvements. The exploration into nano manufacturing processes should allow realizing such novel platforms. Finally, on a more fundamental, physical level, the exploration of large scale integrated hybrid Nanophotonics will allow for a deeper understanding of the ultimate limitations and capabilities of future information technology.

8.4 Concluding Remarks

Concluding this dissertation, I have shown how synergies between photonics and electronics in particular metal-optics lead to novel device physics. In particular the enhancement of optical fields has a strong influence on the emission processes of optical emitters in terms of emission rate or speed and brightness. Furthermore, I have demonstrated that nanoscale hybrid-plasmon waveguides can be fabricated and utilized towards nanoscale plasmon laser sources and light-emitting tunnel junctions, ultra-dense & high-bandwidth waveguide elements, efficient non-linear devices like electro-optical modulators and potentially all optical switches. The concepts established in this dissertation establishes a framework and robust basis for large scale integrated nano Photonics, that manifest a hybrid between state-of-the-art electronic and photonic circuits for future information technology as shown in this last chapter.

The proven possibilities of bridging the gap between electronics and photonics length scales as demonstrated here, has great potential, and further research will show what this young field will finally enable.

References

Chapter-1 (Part-1)

[1] S. Murugesan 'Understanding Web 2.0' *IEEE Computer Society* **9**, 4, 34 (2007).

[2] J. L. Stieglitz 'Global Positioning System receivers in space applications' *Digital Avionics Systems Conference, 1999. Proceedings* **2** (1999).

[3] P. Enge, T. Walter, S. Pullen, C. Kee; Y.-C. Chao; Y.-. Tsai 'Wide area augmentation of the Global PositioningSystem' *Proceeding of IEEE,***84**, 8, 1063-1088 (1996).

[4] B. Huhnke www.vwerl.com (2010).

[5] M. Venables 'Smart Meters makes smart Consumers' *IEEE Engineering & Technology* **2**, 4, 23 (2007).

[6] U.S. department of Energy http://www.energy.gov/energyefficiency/transportation.htm (2011).

[7] www.tivo.com (2011).

[8] R. Pool 'Setting a new Standard' *Science* **7**, 29-31 (1988).

Chapter-1 (Part-2)

[1] E. Purcell 'Spontaneous emission probabilities at radio frequencies' *Phys. Rev.* **69**, 681 (1946).

[2] H.-J. Miesner, D. M. Stamper-Kurn, M. R. Andrews, D. S. Durfee, S. Inouye and W. Ketterle 'Bosonic Stimulation in the Formation of a Bose-Einstein Condensate' *Science* **279**, 553, 1005-1007 (1998).

[3] V. R. Almeida, C. A. Barrios, R. R. Panepucci and M. Lipson 'All-optical control of light on a silicon chip' *Nature* **431** 1081 (2004)

[4] R. F. Oulton, V. J. Sorger, D. F. P. Pile, D. A. Genov and X. Zhang 'A hybrid plasmonic waveguide for subwavelength confinement and long-range propagation' *Nature Photonics* **2**, 496-500 (2008).

[5] V. J. Sorger, Z. Ye, R. F. Oulton, Y. Wang, G. Bartal, X. Yin and X. Zhang *accepted at Nature Communications* (2011).

[6] *R.-M. Ma, R. F. Oulton, V. J. Sorger, G. Bartal and X. Zhang Nature Materials* **10**, 110-113 (2010).

[7] S. A. Maier 'Plasmonics, Fundamentals and Applications' (Springer, New York, 2007).

[8] W. L. Barnes, A. Dereux and T. W. Ebbesen 'Surface plasmon subwavelength optics.' *Nature* **424** 824-830 (2003).

[9] E. Yablonovitch 'Inhibited Spontaneous Emission in Solid-State Physics and Electronic' *Physical Review Letters* **58**, 2059 (1987).

[10] K. J. Vahala 'Optical Microcavities' *Nature* **424**, 839-846 (2003).

[11] V. J. Sorger, R. F. Oulton, J. Yao, G. Bartal and X. Xiang, *Nano Lett.* **9**, 3489-3493 (2009).

[12] V. J. Sorger et al. In review at *Physical Review Letters* (2011).

Chapter-1 (Part-3)

[1] J. Rattner 'The Future of Silicon Photonics' *Integrated Photonics Research OSA*, Monterey July (2010).

[2] R. Beausoleil 'CMOS-Compatible Microring Modulators for Nanophotonic Interconnect' *Integrated Photonics Research OSA*, Monterey July (2010).

Chapter-2 (Part-1)

[1] M. Cai, O. Painter and K. J. Vahala *Phys. Rev. Lett.* **85**, 74-77 (2000).

[2] J. Shainline, G. Fernandes, Z. Liu and J. Xu, *Frontiers in Optics,* FWZ4 San Jose (2009).

[3] Purcell, E. 'Spontaneous emission probabilities at radio frequencies.' *Phys. Rev.* **69**, 681 (1946).

Chapter-2 (Part-2)

[1] J. Shainline, G. Fernandes, Z. Liu and J. Xu, *Frontiers in Optics,* FWZ4 (2009).

[2] K. J. Vahala 'Optical Microcavities' *Nature* **424**, 839-846 (2003).

[3] Purcell, E. Spontaneous emission probabilities at radio frequencies. *Phys. Rev.* **69**, 681 (1946).

[4] Miyazaki, H & Kurokawa, Y. Squeezing Visible Light Waves into a 3-nm-Thick and 55-nm-Long Plasmon Cavity. *Phys. Rev. Lett.* **96**, 097401 (2006).

[5] Weeber, J.-C., Bouhelier, A., Colas de Francs, G., Markey, L. & Dereux, A. Submicrometer In-Plane Integrated Surface Plasmon Cavities. *Nano Lett.* **7**, 1352-1359 (2007).

[6] Min, B., Ostby, E., Sorger, V.J., Ulin-Avila, E.,, Yang, L., Zhang, X. & Vahala, K. High-Q surface-plasmon-polariton whispering-gallery microcavity. *Nature* **457**, 455 - 458 (2009).

[7] V. J. Sorger, R. F. Oulton, J. Yao, G. Bartal and X. Xiang, *Nano Lett.* **9**, 3489-3493 (2009).

Chapter-2 (Part-3)

[1] Maier, S.A. Plasmonics, Fundamentals and Applications (Springer, New York, 2007).

[2] Barnes, W. L., Dereux, A., & Ebbesen, T. W., Surface plasmon subwavelength optics. *Nature* **424** 824-830 (2003).

[3] Takahara, J., Yamagishi, S., Taki, H., Morimoto, A., & Kobayashi, T., Guiding of a one-dimensional optical beam with nanometer diameter. *Optics Lett.* **22** 475-477 (1997).

[4] Oulton, R. F., Sorger, V. J., Pile, D.F.P., Genov, D.A. & Zhang, X. A hybrid plasmonic waveguide for subwavelength confinement and long-range propagation. *Nature Photonics* **2**, 496-500 (2008).

[5] Miyazaki, H & Kurokawa, Y. Squeezing Visible Light Waves into a 3-nm-Thick and 55-nm-Long Plasmon Cavity. *Phys. Rev. Lett.* **96**, 097401 (2006).

[6] Ditlbacher, H., Krenn, J. R., Schider, G., Leitner, A. & Aussenegg, F. R. Two-dimensional optics with surface plasmon polaritons. *Appl. Phys. Lett.* **81**, 1762–1764 (2002).

[7] Bozhevolnyi, S. I., Volkov, V. S., Devaux, E., Laluet, J. -Y. & Ebbesen, T. W. Channel plasmon subwavelength waveguide components including interferometers and ring resonators. *Nature* **440**, 508–511 (2006).

[8] Stoltz, N., Rakher, M., Strauf, S., Badolato, A., Lofgreen, D., Petroff, P.; Coldren, L. & Bouwmeester, D. High-quality factor optical microcavities using oxide apertured micropillars. *Appl. Phys. Lett.* **87**, 031105 (2005).

[9] Armani, K., Kippenberg, T. J., Spillane, S. M., Vahala K. J. Ultra-high-Q toroid microcavity on a chip. *Nature* **421**, 925 – 928 (2003).

[10] Akahane, Y., Asano, T., Song, B.-S., & Noda, S. High-Q photonic nanocavity in a two-dimensional photonic crystal. *Nature* **425** 944-947 (2003).

[11] Altug, H., Englund, D. & Vuckovic, J. Ultrafast photonic crystal nanocavity laser. *Nature* **2**, 484 (2006).

[12] Purcell, E. Spontaneous emission probabilities at radio frequencies. *Phys. Rev.* **69**, 681 (1946).

[13] Akimov, A. V., Mukherjee, A., Yu, C. L., Chang, D. E., Zibrov, A. S., Hemmer, P. R., Park, H. & Lukin, M. D. Generation of single optical plasmons in metallic nanowires coupled to quantum dots. *Nature* **450**, 402-406 (2007).

[14] David J. Bergman, D. I., & Stockman, M. I., Surface Plasmon Amplification by Stimulated Emission of Radiation: Quantum Generation of Coherent Surface Plasmons in Nanosystems *Phys. Rev. Lett.* **90** 027402 (2003).

[15] Yu, N., Cubukcu, E., Diehl, L., Belkin, M. A., Crozier, K. B., Capasso, F., Bour, D., Corzine, S. & Höfler, G., Plasmonic Quantum Cascade Laser Antenna *Appl. Phys. Lett.* **91** 173113 (2007).

[16] Baba, T. & Sano, D. Low-threshold lasing and Purcell effect in microdisk lasers at room temperature. *IEEE* **9**, 1340-1346 (2003).

[17]Lal, S., Link, S., & Halas, N. J. Nano-optics from sensing to waveguiding. *Nature Photonics* **1**, 641-648 (2007).

[18] Liu, Y., Bartal, G., Genov, D. A. & Zhang, X. Subwavelength Discrete Solitons in Nonlinear Metamaterials. *Phys. Rev. Lett.* **99**, 153901 (2007).

[19] R. Hillenbrand, T. Taubner & F. Keilmann, Phonon-enhanced light–matter interaction at the nanometre scale. *Nature* **418**, 159-162 (2002).

[20] Vahala, K. J. Optical microcavities. *Nature* **424**, 839-846 (2003).

[21] Min, B., Ostby, E., Sorger, V.J., Ulin-Avila, E.,, Yang, L., Zhang, X. & Vahala, K. High-Q surface-plasmon-polariton whispering-gallery microcavity. *Nature* **457**, 455 - 458 (2009).

[22] Oulton, R.F., Pile, D. F. P., Liu, Y. & Zhang, X. Scattering of surface plasmon polaritons at abrupt surface interfaces: Implications for nanoscale cavities. *Phys. Rev. B* **76**, 035408 (2007).

[23] Weeber, J.-C., Bouhelier, A., Colas de Francs, G., Markey, L. & Dereux, A. Submicrometer In-Plane Integrated Surface Plasmon Cavities. *Nano Lett.* **7**, 1352-1359 (2007).

[24] Kirchain, R. & Kimerling, L. A roadmap for nanophotonics. *Nature Photonics* **1**, 303-305 (2007).

[25] Johnson, P. B and Christie, R. W. Optical Constants of the Noble Metals. *Phys. Rev. B* **6** 4370-4379 (1972).

Chapter-3 (Part-1)

[1] A. Gramotnev and S. I. Bozhevolnyi *Nature Photonics* **4** (2010).

[2] S. I. Bozhevolnyi, V. S. Volkov, E. Devaux, and T. W. Ebbesen *Phys. Rev. Lett.* **95**, 046802 (2005).

[4] J. A. Dionne, H. J. Lezec and H. A. Atwater, *Nano Letters* **6**, 9, 1928-1932 (2006).

[4] D. F. P. Pile, T. Ogawa, D. K. Gramotev, T. Okamoto, M. Haraguchi, M. Fukui and S. Matsuo *Applied Physical Letters* **87**, 061106 (2005).

[5] L. Chen, J. Shakya,and M. Lipson *Optics Letters* **31**, 14, 2133-2135 (2006)

[6] A. Krasavin, A. Zayats *Optics Express* **18,** 11, 11791-11799 (2010).

[7] R. F. Oulton, V. J. Sorger, D. A. Genov, D. F. P. Pile, and X. Zhang, *Nature Photonics* **2**, 495-500 (2008).
[8] V. J. Sorger, Z. Ye, R. F. Oulton, Y. Wang, G. Bartal, X. Yin and X. Zhang *accepted at Nature Communications* (2011).

[9] S. A. Maier *Plasmonics, Fundamentals and Applications*; Springer: New York, 2007.

[10] A. Kinkhabwala, Z.Yu, S.Fan, Y. Avlasevich, K. Muelen and W. E. Moerner *Nature* **443**, 1062 (2008).

[11] B. Wang and G. P. Wang *Optics Express* **13**, 10558 (2005).

[12] Jung et al.. *IEEE Phot. Technology Letters* **21**, 630 (2009).

[13] D. F. Pile et al. *Applied Physics Letters* **87**, 261114 (2005).

[14] Y. Satuby and M. Orenstein *Optics Express* **15**, 4247 (2007).

[15] Volkov, V. S., Devaux, E., Laluet, J.-Y., Ebbesen, T. W. and Bozhevolnyi, S. I. *Nature* **440**, 508-511 (2006).

Chapter-3 (Part-2)

[1] R. Kirchain and L. Kimerling, "A roadmap for nanophotonics." *Nature Photonics* **1,** 303 (2007).

[2] A. D. Boardman, *Electromagnetic Surface Modes*, (Wiley, New York, 1982)

[3] W. L. Barnes, A. Dereux & T. W. Ebbesen "Surface Plasmon Sub-Wavelength Optics" *Nature* **424** ,824 (2003).

[4] J. Takahara, S. Yamagishi, H. Taki, A. Morimoto, and T. Kobayashi, "Guiding of a one-dimensional optical beam with nanometer diameter." *Optics Letters* **22,** 475 (1997).

[5] L. Novotny and C. Hafner, "Light propagation in a cylindrical waveguide with a complex, metallic, dielectric function." *Phys. Rev. E* **50,** 4094 (1994)

[6] J. Takahara and T. Kobayashi, "Nano-Optical Waveguides Breaking Through Diffraction Limit of Light." Optomechatronic Micro/Nano Components, Devices, and Systems, edited by Yoshitada Katagiri, *Proc. of SPIE* Vol. **5604** (SPIE, Bellingham, WA, 2004).

[7] R. Waele, S. Burgos, A. Polman and H. Atwater "Plasmon Dispersion in Coaxial Waveguides from Single-Cavity Optical Transmission Measurements" *Nano Letters* **8**, 2832-2837 (2009).

[8] D. F. P. Pile and D. K. Gramotnev, "Channel plasmon– polariton in a triangular groove on a metal surface." *Optics Letters* **29,** 1069 (2004)

[9] S. I. Bozhevolnyi, V. S. Volkov, E. Devaux, and T. W. Ebbesen, "Channel Plasmon-Polariton Guiding by Sub-wavelength Metal Grooves." *Phys. Rev. Lett.* **95,** 046802 (2005)

[10] A. Karalis, E. Lidorikis, M. Ibanescu, J. D. Joannopoulos and Marin Soljaucic, "Surface-Plasmon-Assisted Guiding of Broadband Slow and Sub-wavelength Light in Air." *Phys. Rev. Lett*. **95**, 063901 (2005)

[11] R. Zia and M. L. Brongersma, "Surface plasmon polariton analogue to Young's double-slit experiment." *Nature Nanotech*. **2,** 426 (2007)

[12] F. Kusunoki, T. Yotsuya, J. Takahara and T. Kobayshi, "Propagation of guided waves in index-guided two-dimensional optical waveguides." *Appl. Phys. Lett*. **86,** 211101 (2005)

[13] F. Kusunoki, T. Yotsuya and J. Takahara, "Confinement and guiding of two-dimensional optical waves by low-refractive-index cores." *Optics Express* **14,** 5651 (2006)

[14] B. Steinberger, A. Hohenau, H. Ditlbacher, A. L. Stepanov, A. Drezet, F. R. Aussenberger, A. Leitner and J. R. Krenn, "Dielectric stripes on gold as surface plasmon waveguides." *Appl. Phys. Lett*. **88,** 094104 (2006)

[15] R. F. Cregan, B. J. Mangan, J. C. Knight, T. A. Birks, P. St. J. Russell, P. J. Roberts and D. C. Allan, "Single-Mode Photonic Band Gap Guidance of Light in Air." *Science* **285**, 1537 (1999)

[16] G. S. Wiederhecker, C. M. B. Cordeiro, F. Couny, F. Benabid, S. A. Maier, J. C. Knight, C. H. B. Cruz and H. L. Fragnito, "Field enhancement within an optical fibre with a subwavelength air core." *Nature Photonics* **1**, 115 (2007)

[17] S. Noda, "Seeking the Ultimate Nanolaser." *Science* **314,** 260 (2006)

[18] H. Altug, D. Englund and J. Vuckovic, "Ultrafast photonic crystal nanocavity laser" *Nature Physics* **2** 484 (2006)

[19] V. R. Almeida, Q. Xu, C. A. Barios and M. Lipson, "Guiding and confining light in void nanostructure." *Optics Letters* **29** ,1209 (2004)

[20] D. A. Genov, M. Ambati, and X. Zhang, "Surface Plasmon Polariton Amplification in Planar Metal Films", *IEEE Journal of Quantum Electronics* **43,** 0018 (2007).

[21] Y. Huang and C. Lieber, "Integrated nanoscale electronics and optoelectronics: Exploring nanoscale science and technology through semiconductor nanowires." *Pure Appl. Chem.* **76** ,2051 (2004)

[22] M. H. Huang, S. Mao, H. Feick, H. Yan, Y. Wu, H. Kind, E. Weber, R Russo, P. Yang, "Room-Temperature Ultraviolet Nanowire Nanolasers." *Science* **292,** 1897 (2001)

[23] M. T. Hill, Y.-S. Oei, B. Smalbrugge, Y. Zhu, T. de Vries, P. J. van Veldhoven, F. W. M. van Otten, T. J. Eijkemans, J. P. Turkiewicz, Huug de Waardt, E. J. Geluk, S.-H. Kwon, Y.-H. Lee, R. Notzel and M. K. Smit, "Lasing in metallic-coated nanocavities" *Nature Photonics* **1,** 589 (2007)

[24] E. A. Ash, C. W. Pitt and M. G. F. Wilson, "Integrated optical circuits for telecommunications." *Nature* **261,** 377 (1976)

[25] E. Prodan, C. Radloff, N. J. Halas, P. Nordlander, "A Hybridization Model for the Plasmon Response of Complex Nanostructures" *Science* **302**, 419 (2003)

[26] P. B. Johnson and R. W. Christie, "Optical Constants of the Noble Metals." *Phys. Rev. B* **6,** 4370 (1972)

[27] A.W. Snyder and J.D. Love, *Optical Waveguide Theory*. (Chapman and Hall, 1983)

[28] Non-local response from thin films.

[29] R. Buckley and P. Berini, "Figures of merit for 2D surface plasmon waveguides and application to metal stripes." *Optics Express* **15**, 12174 (2007)

[30] V. R. Almeida, C. A. Barrios, R. R. Panepucci and M. Lipson, "All-optical control of light on a silicon chip." *Nature* **431,** 1081 (2004)

Chapter-3 (Part-3)

[1] D. F. Welch, F. A. Kish, R. Nagarajan, C. H. Joyner, R. P. Schneider, V. G. Dominic, M. L. Mitchell, S. G. Grubb, T.-K. Chiang, D. Perkins and A. C. Nilsson *IEEE Journal of Lightwave Tech.* **12** 4674 - 4683 (2006).

[2] R. Kirchain and L. Kimerling *Nature Phot.* **1**, 303 (2007).

[3] M. L. Brongersma and V. M. Shalaev, *Science* **328**, 440-441 (2010).

[4] L. Liao, D. Samara-Rubio, M. Morse, A. Liu, D. Hodge, D. Rubin, U. D. Keil and T. Franck, *Optics Express* **13**, 8, 3129-3135 (2005).

[5] B. Guha, B.B.C. Kyotoku and M. Lipson *Optics Express.***18**, 15 (2010).

[6] S. A. Maier *Plasmonics, Fundamentals and Applications*; Springer: New York, 2007.

[7] A. L. Pyayt, B. Wiley, Y. Xia, A. Chen, L. Dalton *Nature Nanotech.* **3**, 660 - 665 (2008).

[8] D. K. Gramotnev and S. I. Bozhevolnyi *Nature Phot.* **4**, 83 - 91 (2010).

[9] S. A. Maier, P. G. Kik, and H. A. Atwater *Appl. Phys. Lett.* **81**, 1714-1716 (2002).

[10] A. V. Krasavin and A.V. Zayats *Optics Express* **18**, 11791-11799 (2010).

[11] R. F. Oulton, V. J. Sorger, D. A. Genov, D. F. P. Pile, and X. Zhang, *Nature Phot.* **2**, 495-500 (2008).

[12] R. F. Oulton, G. Bartal, D. F. P. Pile and X. Zhang, *J. New Phys.* **10**, 105018 (2008).

[13] R. F. Oulton, V. J. Sorger, T. Zentgraf, R.-M. Ma, C. Gladden, L. Dai, G. Bartal, and X. Zhang, *Nature* **461**, 629-632 (2009).

[14] M. T. Hill, Y.-S. Oei, B. Smalbrugge, Y. Zhu, T. De Vries, P. J. van Veldhoven, F. W. M. van Otten, T. J. Eijkemans, J. P. Turkiewicz, H. de Waardt, E. J. Geluk, S.-H. Kwon, Y.-H. Lee, R. Notzel and M. K. Smit, *Nature Phot.* **1,** 589-594 (2007).

[15] W. Cai, J. S. White and M. L. Brongersma *Nano Lett.* **9**, 4403 - 4411 (2009).

[16] J. A. Dionne, K. Diest, L. A. Sweatlock and H. A. Atwater, *Nano Lett.* **9**, 2, 897-902 (2009).

[17] D. Pacifici, H. J. Lezec and H. A. Atwater *Nature Phot.* **1**, 402 - 406 (2007).

[18] E. Togan, Y. Chu, A. S. Trifonov, L. Jiang, J. Maze, L. Childress, M. V. G. Dutt, A. S. Sørensen, P. R. Hemmer, A. S. Zibrov and M. D. Lukin *Nature* **466**, 5, $730 - 735$ (2010).

[19] D. A. B. Miller, *Opt. Lett.* **14**, 146-148, (1989).

[20] W. M. J. Green, M. J. Rooks, L. Sekaricand and Y. A. Vlasov *Opt. Express.* **15**, $17106 - 17113$ (2007).

[21] J. Shainline, G. Fernandes, Z. Liu and J. Xu, *Frontiers in Optics,* FWZ4 (2009).

[22] E. Verhagen, M. Spasenovic, A. Polman and L. Kuipers *Phys. Rev. Lett.* **102**, 203904 (2009).

[23] S. I. Bozhevolnyi, V. S. Volkov, E. Devaux, and T. W. Ebbesen *Phys. Rev. Lett.* **95**, 046802 (2005).

[24] J. A. Dionne, H. J. Lezec and H. A. Atwater, *Nano Lett.* **6**, 9, 1928-1932 (2006).

[25] D. F. P. Pile, T. Ogawa, D. K. Gramotev, T. Okamoto, M. Haraguchi, M. Fukui and S. Matsuo, *App. Phys. Lett.* **87**, 061106 (2005).

[26] H.-S. Chu, E.-P. Li and R. Hedge *Appl. Phys. Lett.* **96**, 221103 (2010).

[27] K. K. Lee, D. R. Lim, L. C. Kimmerling, J. Shin and F. Cerrina *Optics Lett.* **26**, 1888-1890 (2001).

[28] J. N. Anker, W. P. Hall, O. Lyandres,N. C. Shah, J. Zhao, and R. P. Van Duyne, Nature Materials **7**, 442 - 453 (2008).

[29] P. B. Johnson, and R. W. Christy, *Phys. Rev. B* **6**, 4370-4379 (1972).

[30] V. J. Sorger, R. F. Oulton, J. Yao, G. Bartal and X. Xiang, *Nano Lett.* **9**, 3489-3493 (2009).

Chapter-4 (Part-1)

[1] Gordon, J. P., Zeiger, H. J. & Townes, C. H. The Maser – New type of microwave amplifier, Frequency Standard and Spectrometer. Phys. Rev. 99, 1264-1274 (1955).

[2] R. Boyd, R. Athale, L. Onural, W. Seka *Applied Optics* **49,** 25, LF1-LF1 (2010).

[3] F. Kärtner, M. Pollnau, K. Ueda and H. van Driel *JOSA B* **27,** 11,.LF1-LF1 (2010).

[4] D. F. Welch, F. A. Kish, R. Nagarajan, C. H. Joyner, R. P. Schneider, V. G. Dominic, M. L. Mitchell, S. G. Grubb, T.-K. Chiang, D. Perkins and A. C. Nilsson *IEEE Journal of Lightwave Tech.* **12** 4674 - 4683 (2006).

[5] G.Roelkens, L. Liu, D. Liang, R. Jones, A. Fang, B. Koch and J. Bowers *Laser Photonics Rev.* **4**, No. 6, 751–779 (2010).

[6] J. L. Pleumeekers, P. W. Evans, W. Chen, R. P. Schneider and R. Nagarajan *Optics and Photonics News* **20**, 3, 20-25 (2009).

[7] Intel Corporation, http://www.intel.com/technology/mooreslaw/ (2011).

[8] *M. C. Y. Huang, Y. Zhou, C. J. Chang-Hasnain Nature Photonics* **2**, 180-184 (2008).

[9] *R.-M. Ma, R. F. Oulton, V. J. Sorger, G. Bartal and X. Zhang Nature Materials* **10**, 110-113 (2010).

[10] G. Bjoerk and Y. Yamamoto , *IEEE* J. Quant Electronics **27** ,11, 2386-2396 (1991)

[11] R. F. Oulton, V. J. Sorger, T. Zentgraf, R.-M. Ma, C. Gladden, L. Dai, G. Bartal, and X. Zhang, *Nature* **461**, 629-632 (2009).

[12] Bergman, D. J. & Stockman, M. I. *Phys. Rev. Lett.* **90,** 027402 (2003).

[13] R. F. Oulton, V. J. Sorger, D. A. Genov, D. F. P. Pile, and X. Zhang, *Nature Phot.* **2**, 495-500 (2008).

[14] E. M. Purcell *Phys. Rev.* **69,** 681-681 (1946).

[15] V. J. Sorger et al. *Unpublished work* (2011).

[16] M. P. Nezhad et al. *Nature Photonics* **4**, 395-399 (2010).

[17] M. A. Noginov et al. *Nature* **460**, 1110-1113 (2009).

[18] M. Hill. et al. *Optics Express* **17**, 11107-11112 (2009).

[19] K. Yu, A. Lakhani and M. Wu *Optics Express* **18**, 8790–8799 (2010).

[20] S.-H. Kwon, J.-H. Kang, C. Seassal, S.-K. Kim, P. Regreny, Y.-H. Lee, Ch. M. Lieber and H.-G. Park *Nano Letters* **10**, 9, 3679–3683 (2010).

[21] S. A. Maier 'Plasmonics, Fundamentals and Applications' (Springer, New York, 2007).

[22] J. A. Dionne, H. J. Lezec and H. A. Atwater, *Nano Lett.* **6**, 9, 1928-1932 (2006).

Chapter-4 (Part-2)

[1] Gordon, J. P., Zeiger, H. J. & Townes, C. H. The Maser – New type of microwave amplifier, Frequency Standard and Spectrometer. *Phys. Rev.* **99,** 1264-1274 (1955).

[2] Drescher, M., Hentschel, M., Kienberger, R., Tempea, G., Spielmann, Ch., Reider, G. A., Corkum, P. B. & Krausz, F. X-ray Pulses Approaching the Attosecond Frontier. *Science* **291,** 1923-1927 (2001).

[3] Altug, H., Englund, D. & Vučković, J. Ultrafast photonic crystal nanocavity laser. *Nature Physics* **2,** 484-488 (2006).

[4] Hill, M. T., Oei, Y.-S., Smalbrugge, B., Zhu, Y., De Vries, T., van Veldhoven, P. J., van Otten, F. W. M., Eijkemans, T. J., Turkiewicz, J. P., de Waardt, H., Geluk, E. J., Kwon, S.-H., Lee, Y.-H., Notzel, R. & Smit, M. K. Lasing in metallic-coated nanocavities. *Nature Photonics* **1,** 589-594 (2007).

[5] Johnson, J. C., Choi, H.-J., Knutsen, K. P., Schaller, R. D., Yang P. & Saykally, R. J. Single Gallium Nitride nanowire lasers. *Nature Materials* **1,** 106-110 (2002).

[6] Duan, X., Huang, Y., Agarwal, R. & Lieber, C. M. Single-nanowire electrically driven lasers. *Nature* **421**, 241 - 245 (2003).

[7] Zimmler, M. A., Bao, J., Capasso, F., Müller, S. & Ronning, C. Laser action in nanowires: Observation of the transition from amplified spontaneous emission to laser oscillation. *Appl. Phys. Lett.* **93,** 051101 (2008).

[8] Astafiev, O., Inomata, K., Niskanen, A. O., Yamamoto, T., Pashkin, Y. A., Nakamura, Y. & Tsai, J. S., Single artificial atom lasing. *Nature* **449** 588-590 (2007*).*

[9] Scalari, G., Walther, C., Fischer, M. Terazzi, R., Beere, H., Ritchie, D., and Faist, J., THz and sub-THz quantum cascade lasers. Laser & Photon. Rev. **3**, 45-66 (2009).

[10] Bergman, D. J. & Stockman, M. I. Surface Plasmon Amplification by Stimulated Emission of Radiation: Quantum Generation of Coherent Surface Plasmons in Nanosystems. *Phys. Rev. Lett.* **90,** 027402 (2003).

[10] Zheludev, N. I., Prosvirnin, S. L., Papasimakis, N. & Fedotov, V. A. Lasing spaser. *Nature Photonics* **2**, 351 - 354 (2008).

[11] Maier, S. A., Kik, P. G., Atwater, H. A., Meltzer, S., Harel, E., Koel, B. E. & Requicha, A. A. G. Local detection of electromagnetic energy transport below the diffraction limit in metal nanoparticle plasmon waveguides. *Nature Materials* **2,** 229-232 (2003).

[12] Pile, D. F. P., Ogawa, T., Gramotnev, D. K., Okamoto, T., Haraguchi, M., Fukui, M. & Matsuo, S. Theoretical and experimental investigation of strongly localized plasmons on triangular metal wedges for subwavelength waveguiding. *Appl. Phys. Lett.* **87,** 061106 (2005).

[13] Ambati, M., Nam, S. H., Ulin-Avila, E., Genov, D. A., Bartal, G. & Zhang, X. Observation of Stimulated Emission of Surface Plasmon Polaritons. *Nano Lett.* **8,** 3998–4001 (2008).

[14] Noginov, M. A., Zhu, G., Mayy, M., Ritzo, B. A., Noginova, N. & Podolskiy, V. A. Stimulated Emission of Surface Plasmon Polaritons. *Phys. Rev. Lett.* **101,** 226806 (2008).

[15] Oulton, R. F., Sorger, V. J., Genov, D. A., Pile, D. F. P. & Zhang, X. A hybrid plasmonic waveguide for sub-wavelength confinement and long-range propagation. *Nature Photonics* **2,** 495-500 (2008).

[16] Purcell, E. M. Spontaneous emission probabilities at radio frequencies. *Phys. Rev.* **69,** 681-681 (1946).

[17] Volkov, V. S., Devaux, E., Laluet, J.-Y., Ebbesen, T. W. & Bozhevolnyi, S. I. Channel plasmon subwavelength waveguide components including interferometers and ring resonators. *Nature* **440**, 508-511 (2006).

[18] Anker, J. N., Hall, W. P., Lyandres, O., Shah, N. C., Zhao, J. & Van Duyne, R. P. Biosensing with plasmonic nanosensors. Nature Materials **7,** 442 - 453 (2008).

[19] Akimov, V., Mukherjee, A., Yu, C. L., Chang, D. E., Zibrov, A. S., Hemmer, P. R., Park, H. & Lukin, M. D. Generation of single optical plasmons in metallic nanowires coupled to quantum dots. *Nature* **450,** 402-406 (2007).

[20] Liu, Y., Bartal, G., Genov, D. A. & Zhang, X. Subwavelength Discrete Solitons in Nonlinear Metamaterials. *Phys. Rev. Lett.* **99**, 153901 (2007).

[21] Stockman, M. I. Nanofocusing of Optical Energy in Tapered Plasmonic Waveguides. *Phys. Rev. Lett.* **93,** 137404 (2004).

[22] Oulton, R. F., Bartal, G., Pile, D. F. P. & Zhang, X. Confinement and propagation characteristics of subwavelength plasmonic modes. *New J. Phys.* **10,** 105018 (2008).

[23] Ma, R. M., Dai, L. & Qin, G. G. Enhancement-mode metal-semiconductor field-effect transistors based on single n-CdS nanowires. *Appl. Phys. Lett.* **90,** 093109 (2007).

[24] Thomas, G. D. & Hopfield, J. J. Optical properties of bound exciton complexes in Cadmium Sulfide. *Phys. Rev.* **128,** 2135-2148 (1962).

[25] Siegman, A. E., Lasers. University Science Book, Mill Valley, California (1986).

[26] Weber, C., Becker, U., Renner, R. & Klingshirn, C. Measurement of the diffusion-length of carriers and excitons in CdS using laser-induced transient gratings. *Z. Phys. B - Condensed Matter* **72,** 379-384 (1988).

[27] Björk, G. & Yamamoto, Y. Analysis of semiconductor microcavity lasers using rate equations. *IEEE J. of Quantum Electronics* **27**, 2386-2396 (1991).

[29] Ford, G.W. & Weber, W.H. Electromagnetic Interactions of Molecules with Metal Surfaces. *Phys. Rep.* **113,** 195-287 (1984).

[30] Casperson, L. W. Threshold characteristics of multimode laser oscillators. *J. Appl. Phys.* **12,** 5194-5201 (1975).

Chapter-4 (Part-3)

[1] Bergman, D. J. & Stockman, M. I. Surface Plasmon Amplification by Stimulated Emission of Radiation: Quantum Generation of Coherent Surface Plasmons in Nanosystems. *Physical Review Letters* **90**, 027402 (2003)

[2] Hill, M. T. et al. Lasing in metal-insulator-metal sub-wavelength plasmonic waveguides. *Optics Express* **17**, 11107-11112 (2009).

[3] Noginov, M. A. et al. Demonstration of a spaser-based nanolaser. *Nature* **460**, 1110-1113 (2009).

[4] Oulton, R. F. et al. Plasmon lasers at deep subwavelength scale. *Nature* **461**, 629-632 (2009).

[5] Schuller, J. A. Barnard, E. S., Cai, W., Jun, Y. C., White, J. S. & Brongersma, M. L. Plasmonics for extreme light concentration and manipulation. *Nature Materials* **9**, 193-204 (2010)

[6] Gramotnev, D. K., & Bozhevolnyi, S. I. Plasmonics beyond the diffraction limit. *Nature Photonics* **4**, 83-91 (2010)

[7] Anker, J. N., Hall, W. P., Lyandres, O., Shah, N. C., Zhao, J. & Van Duyne, R. P. Biosensing with plasmonic nanosensors. *Nature Materials* **7**, 442-453 (2008).

[8] Dionne, J. A., Diest, K., Sweatlock, L. A. & Atwater, H. A. PlasMOStor: A Metal-Oxide-Si Field Effect Plasmonic Modulator. *Nano Letters* **9**, 897-902 (2009)

[9] Zijlstra, P., Chon, J. W. M. & Gu, M. Five-dimensional optical recording mediated by surface plasmons in gold nanorods. *Nature* **459**, 410–413 (2009).

[10] Challener, W. A. et al. Heat-assisted magnetic recording by a near-field transducer with efficient optical energy transfer. *Nature Photonics* **3**, 220-224 (2009).

[11] Stipe, B. C. et al. Magnetic recording at 1.5 Pb m-2 using an integrated plasmonic antenna. *Nature Photonics* **4**, 484-488 (2010) .

[12] Altug, H., Englund, Dirk. & Vuckovic, Jelena. Ultrafast photonic crystal nanocavity laser. *Nature Physics* **2**, 484-488 (2006).

[13] Song, Q., Cao, H., Ho, S. T. & Solomon, G. S. Near-IR subwavelength microdisk lasers. *Appl. Phys. Lett.* **94**, 061109 (2009).

[14] Hill, M. T. et al. Lasing in metallic-coated nanocavities. *Nature Photonics* **1**, 589–594 (2007).

[15] Nezhad, M. P. et al. Room-temperature subwavelength metallo-dielectric lasers. *Nature Photonics* **4**, 395-399 (2010).

[16] Yu, K., Lakhani, A. & Wu, M. C. Subwavelength metal-optic semiconductor nanopatch lasers. *Opt. Express* **18**, 8790–8799 (2010).

[17] Maier, S. A. Plasmonics: fundamentals and applications (Springer, 2007)

[18] Akimov, A. V. et al. Generation of single optical plasmons in metallic nanowires coupled to quantum dots. *Nature* **450**, 402–406 (2007).

[19] Kolesov, R. et al. Wave–particle duality of single surface plasmon polaritons. *Nature Physics* **5**, 470-474 (2009).

[20] Oulton, R. F., Sorger, V. J., Genov, D. A., Pile, D. F. P. & Zhang, X. A hybrid plasmonic waveguide for subwavelength confinement and long-range propagation. *Nature Photonics* **2**, 496-500 (2008).

[21] Notice, the convention used here defers from the TM wave definition with respect to the dielectric-air interface where the total internal reflection takes place

[22] Poon, A. W., Courvoisier, F. & Chang, R. K. Multimode resonances in square-shaped optical microcavities. *Optics Letters* **26**, 632-634 (2001)

[23] Huang, Y.-Z. Chen, Q. Guo, W.-H. & Yu, L.-J. Experimental observation of resonant modes in GaInAsP microsquare resonators. *IEEE Photonics Technology Letters* **17**, 2589–2591 (2005).

[24] Wiersig, J. Formation of long-lived, scarlike modes near avoided resonance crossings in optical microcavities. *Physical Review Letters* **97**, 253901 (2006).

[25] Purcell, E. M. Spontaneous emission probabilities at radio frequencies. *Physical Review* **69**, 681 (1946).

[26] Ninomiya, S. & Adachi, S. Optical properties of wurtzite CdS. *J. Appl. Phys*. **78**, 1193-1190 (1995).

[27] Ma, R.-M. Dai, L. & G.-G. Qin, High-Performance Nano-Schottky Diodes and Nano-MESFETs Made on Single CdS Nanobelts. *Nano Letters* **7**, 868-873 (2007).

Chapter-4 (Part-4)

[1] Bergman, D. J. & Stockman, M. I. *Phys. Rev. Lett.* **90,** 027402 (2003).

[2] M. A. Noginov et al. *Nature* **460**, 1110-1113 (2009).

[3] R. F. Oulton, V. J. Sorger, T. Zentgraf, R.-M. Ma, C. Gladden, L. Dai, G. Bartal, and X. Zhang, *Nature* **461**, 629-632 (2009).

[4] M. T. Hill Y.-S. Oei, B. Smalbrugge, Y. Zhu, T. de Vries, P. J. van Veldhoven, F. W. M. van Otten, T. J. Eijkemans, J. P. Turkiewicz, Huug de Waardt, E. J. Geluk, S.-H. Kwon, Y.-H. Lee, R. Notzel and M. K. Smit *Nature Photonics* **1,** 589 (2007)

[5] M. Hill. et al. *Optics Express* **17**, 11107-11112 (2009).

[6] R.-M. Ma, R. F. Oulton, V. J. Sorger, G. Bartal and X. Zhang *Nature Materials* **10**, 110-113 (2010).

[7] M. P. Nezhad et al. *Nature Photonics* **4**, 395-399 (2010).

[8] K. Yu, A. Lakhani and M.Wu *Opt. Express* **18**, 8790–8799 (2010).

[9] S.-H. Kwon, J.-H. Kang, C. Seassal, S.-K. Kim, P. Regreny, Y.-H. Lee, Ch. M. Lieber and H.-G. Park *Nano Letters* **10**, 9, 3679–3683 (2010).

[10] H. Altug, D. Englund, J. Vuckovic *Nature Physics* **2**, 484-488 (2006).

[11] A. Neogi et al. *Physical Review B* **66**, 153305 (2002)

[12] V. J. Sorger etl al. In review at *Physical Review Letters* (2011).

[13] E. Yablonovitch Physical Review Letters **58**, 2059 (1987)

[14] E. M. Purcell *Phys. Rev.* **69,** 681-681 (1946).

[15] V. J. Sorger, R. F. Oulton, J. Yao, G. Bartal and X. Xiang, *Nano Lett.* **9**, 3489-3493 (2009).

[16] Akimov, A. V., Mukherjee, A., Yu, C. L., Chang, D. E., Zibrov, A. S., Hemmer, P. R., Park, H. & Lukin, M. D *Nature* **450**, 402-406 (2007).

[17] A. Faraon, D. Englund, D. Bulla, B. Luther-Davies, B. J. Eggleton, N. Stoltz, P. Petroff and J. Vučković *Appl. Phys. Lett.* **92**, 043123 (2008).

[18] P. Anger, P. Bharadwaj and L. Novotny *Phys. Rev. Lett.* **96**, 113002 (2006).

[19] A. Kinkhabwala, Z.Yu, S.Fan, Y. Avlasevich, K. Muelen and W. E. Moerner *Nature* **443**, 1062 (2008).

[20] R. F. Oulton, V. J. Sorger, D. A. Genov, D. F. P. Pile, and X. Zhang, *Nature Phot.* **2**, 495-500 (2008).

[21] G. Bjoerk and Y. Yamamoto , *IEEE* J. Quant Electronics **27** ,11, 2386-2396 (1991).

[22] G.Roelkens, L. Liu, D. Liang, R. Jones, A. Fang, B. Koch and J. Bowers *Laser Photonics Rev.* **4**, 6, 751–779 (2010).

[23] Zimmler, M. A., Bao, J., Capasso, F., Müller, S. & Ronning, C. Laser action in nanowires: Observation of the transition from amplified spontaneous emission to laser oscillation. *Appl. Phys. Lett.* **93,** 051101 (2008).

[24] Casperson, L. W. Threshold characteristics of multimode laser oscillators. *J. Appl. Phys.* **12,** 5194-5201 (1975).

[25] Y. Shevy, J. Iandelli, J. Kitching and A. Yariv O*ptics Letters* **17**, 9, 661-663 (1992).

[26] Duan, X., Huang, Y., Agarwal, R. & Lieber, C. M. *Nature* **421**, 241 - 245 (2003).

[27] Siegman, A. E. *Lasers*. University Science Book, Mill Valley, California (1986).

[28] Johnson, P. B. & Christy, R. W. *Phys. Rev. B* **6** 4370-4379 (1972).

[29] Palik, E. D. Handbook of optical constants of solids. Academic, New York, 1985.

[30] V. J. Sorger, Z. Ye, R. F. Oulton, Y. Wang, G. Bartal, X. Yin and X. Zhang *accepted at Nature Communications* (2011).

[31] Thomas, G. D. & Hopfield, J. J. Optical properties of bound exciton complexes in Cadmium Sulfide. *Phys. Rev.* **128,** 2135-2148 (1962).

Chapter-4 (Part-5)

[1] R. Boyd, R. Athale, L. Onural, W. Seka *Applied Optics* **49,** 25, LF1-LF1 (2010).

[2] R. F. Oulton, V. J. Sorger, D. A. Genov, D. F. P. Pile, and X. Zhang, *Nature Phot.* **2**, 495-500 (2008).

[3] V. J. Sorger, Z. Ye, R. F. Oulton, Y. Wang, G. Bartal, X. Yin and X. Zhang *accepted at Nature Communications* (2011).

[4] S. E. Miller *Bell Sys. Tech. Journal* **48**, 7, 2059 (1969).

[5] Infinera Inc. www.infinera.com (2011).

[6] The International Technology Roadmap for Semiconductors www.itrs.net (2011).

[7] R. Kirchain and L. Kimerling *Nature Phot.* **1**, 303 (2007).

[8] J. M. Shainline and J. Xu *Laser & Photon. Rev.* **1**, 4, 334–348 (2007).

[9] D. F. Welch, F. A. Kish, R. Nagarajan, C. H. Joyner, R. P. Schneider, V. G. Dominic, M. L. Mitchell, S. G. Grubb, T.-K. Chiang, D. Perkins and A. C. Nilsson *IEEE Journal of Lightwave Tech.* **12** 4674 - 4683 (2006).

[10] L. Liao, D. Samara-Rubio, M. Morse, A. Liu, D. Hodge, D. Rubin, U. D. Keil and T. Franck, *Optics Express* **13**, 8, 3129-3135 (2005).

[11] B. Guha, B.B.C. Kyotoku and M. Lipson *Optics Express.* **18**, 15 (2010).

[12 Hill OE] M. Hill. et al. *Optics Express* **17**, 11107-11112 (2009).

[13] R.-M. Ma, R. F. Oulton, V. J. Sorger, G. Bartal and X. Zhang *Nature Materials* **10**, 110-113 (2010).

[14] M. T. Hill Y.-S. Oei, B. Smalbrugge, Y. Zhu, T. de Vries, P. J. van Veldhoven, F. W. M. van Otten, T. J. Eijkemans, J. P. Turkiewicz, Huug de Waardt, E. J. Geluk, S.-H. Kwon, Y.-H. Lee, R. Notzel and M. K. Smit *Nature Photonics* **1,** 589 (2007).

[15] R.M. Ma, V.J. Sorger, R.F. Oulton, X. Yin and X. Xiang *unpublished work* (2011).

[16] J. Chan, G. Hendry, A. Biberman, and K. Bergman *Journal of Lightwave Technology* **28** (9) 1305-1315 (2010).

[17] D. A. B. Miller, *Opt. Lett.* **14**, 146-148, (1989).

[18] B. G. Lee, B. A. Small, Q. Xu, M. Lipson, K. Bergman *IEEE Photonics Technology Letters* **19** (7) 456-458 (2007).

[19] Q. Yang, M. F. Arend, G. D. Hughes, F. G. Johnson and K. Bergman *Proceedings of the SPIE* **555** 4089 (2000).

[20] E. Lau A. Lakhani, R. Tucker and M. Wu *Optics Express* **17**, 10, 7790-7799 (2009).

[21] B. C. Johnson and A. Mooradian *Applied Physics Letters* **49**, 18, 1135-1147 (1986).

[22] Garcia-Vidal, F. J. & Moreno, E. Lasers go nano. *Nature* 461 604-605 (2009).

[23] Editorial. Birth of the nanolaser. *Nature Photonics* **3**, 545 (2009).

[24] Service, R. F. Ever-smaller lasers pave the way for data highways made of light. *Science* 328 810-811 (2010).

[25] M. P. Nezhad et al. *Nature Photonics* **4**, 395-399 (2010).

[26] D. A. B. Miller *Proceedings Integrated Photonics Research* **PMB3** (2010).

[27] E. Yablonovitch http://www.e3s-center.org/pubs/16/Eli%20Yablonovitch%20presentations.pdf (2010)

[28] Nature Insight, *Lab on a Chip* **442**, 7101, 367 (2010)

[29] J.*Witzens, T. Baehr-Jones, M. Hochberg Nature Photonics* **4**, 10-12 (2010).

[30] DARPA Grant „ExaScale Software Study: Software Challenges in Extreme Scale System" (2009).

[31] AFOSR fy-2011 Muri Topic # 17 "Large Scale Integrated Hybrid Nanophotonics" (2010).

Chapter-5 (Part-1)

[1] Intel Corporation, http://www.intel.com/technology/mooreslaw/ (2011).

[2] The International Technology Roadmap for Semiconductors www.itrs.net (2011).

[3] E. Yablonovitch http://www.e3s-center.org/pubs/16/Eli%20Yablonovitch%20presentations.pdf (2010).

[4] D. A. B. Miller *Nature Photonics* **4**, 3-5 (2010).

[5] A. K. Okyay, A. J. Pethe, D. Kuzum, S. Latif, D. A. B. Miller and K. C. Saraswat *Optics Letters* **32**, 14, 2022-2025 (2007).

[6] A. Liu, R. Jones, L. Liao, D. Samara-Rubio, D. Rubin, O. Cohen, R. Nicolaescu and M. Paniccia *Nature* **427**, 615-619 (2004).

[7] S. Manipatruni, K. Preston, L. Chen and M. Lipson *Optics Express* **18**, 17, 18235 (2011).

[8] E. L. Wooten et al. *IEEE J. Select. Topics Quant. Electron.* **6**, 69–82 (2000).

[9] A. Jen et al. *Macromolecules* **40**, 97-104 (2007).

[10] M. Liu et al. *Nature* (2011).

[11] V. J. Sorger, D. L. Kimuar, R.-M. Ma, T. Zentgraf and X. Xiang *status in preparation* (2011).

[12] F. J. Fortier et al. *Journal of Lightwave Technology* **27**, 11, 1707-1715 (2009).

[13] M. Hochberg et al. *Nature Materials* **5**, 703-710 (2006).

[14] V. J. Sorger, D. L. Kimuar, T. Zentgraf and X. Xiang *status in preparation* (2011).

Chapter-5 (Part-2)

[1] G. T. Reed, C. E. Png *Materials Today* 40–50 (2005).

[2] E. Feigenbaum, K. Diest and H. A. Atwater *Nano Letters* **10**, 2110-2116 (2010).

[3] A. Liu, R. Jones, L. Liao, D. Samara-Rubio, D. Rubin, O. Cohen, R. Nicolaescu and M. Paniccia *Nature* **427**, 615-619 (2004).

[4] D. A. B. Miller *Proceedings IPR* **PMB3** (2010).

Chapter-5 (Part-3)

[1] M. Hochberg et al. *Nature Materials* **5**, 703-710 (2006).

[2] The International Technology Roadmap for Semiconductors www.itrs.net (2011).

[3] R. F. Oulton, V. J. Sorger, D. A. Genov, D. F. P. Pile, and X. Zhang, *Nature Phot.* **2**, 495-500 (2008).

 [4] V. J. Sorger, D. L. Kimuar, T. Zentgraf and X. Xiang *status in preparation* (2011).

[5] B. J. Eggleton *Optics Express* **18**, 25, 26632-26634 (2010).

[6] V. G. Ta'eed et al. *Optics Express* **15**, 15, 9205-9222 (2007).

Chapter-6 (Part-1)

[1] The International Technology Roadmap for Semiconductors, www.itrs.net (2011).

[2] C. Drew, "Military is awash in data from drones." *New York Times* 10 January (2010).

[3] D. A. B. Miller, "Physical Reasons for Optical Interconnection" *International Journal of Optoelectronics* **11**, 155-168 (1997).

[4] R.J. Essiambre, G.J. Foschini, G. Kramer and P.J. Winzer "Capacity Limits on Information Transport in Fiber-Optic Networks" *Physical Review Letters* **101**, 163901 (2008).

[5] D. A. B. Miller "Optics for low-energy communication inside digital processors: quantum detectors, sources, and modulators as efficient impedance converters" *Optics Letters* **14**, 146-148 (1989)

[6] Z. Gaburro, "Optical Interconnect" in Silicon Photonics *Topics Appl. Phys.* **94**, 121-171 (2004).

[7] J. Lambe and S.L. McCarthy "Light Emission from Inelastic Electron Tunneling" *Physical Review Letters*, **37**, 923-925 (1976).

[8] L.C. Davis "Theory of surface-plasmon excitation in metal-insulator-metal tunnel junctions" *Physical Review B* **16**, 2482-2490 (1977).

[9] R. F. Oulton, V. J. Sorger, T. Zentgraf, R.-M. Ma, C. Gladden, L. Dai, G. Bartal, and X. Zhang, *Nature* **461**, 629-632 (2009).

[10] R.-M. Ma, R. F. Oulton, V. J. Sorger, G. Bartal and X. Zhang *Nature Materials* **10**, 110-113 (2010).

[11] V. J. Sorger et al. In review at *Physical Review Letters* (2011).

[12] D.P. Siu, R.K. Jain, and T.K. Gustafson "Stimulated Electron Tunneling in Metal-Barrier-Metal Structures due to Surface Plasmons" *Applied Physics Letters* **28**, 407-410 (1976).

[13] D.M. Drury "A stimulated inelastic tunneling theory of negative differential resistance in metial-insulator-metal diodes" *IEEE Journal of Quantum Electronics* **QE-16**, 58-69 (1980).

[14] L.Z. Xie "Stimulated Emission of Surface Plasmons in Metal-Insulator-Metal (Transition Metal Type Like) Structures" *Infrared Physics* **25**, 661-664 (1985).

Chapter-6 (Part-2)

[1] S. E. Miller *Bell Sys. Tech. Journal* **48**, 7, 2059 (1969).

[2] S. A. Maier *Plasmonics, Fundamentals and Applications*; Springer: New York, 2007.

[3] Gramotnev, D. K., Bozhevolnyi, S. I. Plasmonics beyond the diffraction limit. *Nature Photonics* **4,** 83-91 (2010).

[4] R. F. Oulton, V. J. Sorger, T. Zentgraf, R.-M. Ma, C. Gladden, L. Dai, G. Bartal, and X. Zhang, *Nature* **461**, 629-632 (2009).

[5] R.-M. Ma, R. F. Oulton, V. J. Sorger, G. Bartal and X. Zhang *Nature Materials* **10**, 110-113 (2010).

[6] J. Lambe and S.L. McCarthy Light Emission from Inelastic Electron Tunneling *Physical Review Letters*, **37**, 923-925 (1976).

[7] M.X. Wang, J.H. Yu and X.X. Sun "Light emission characteristics and negative resistance phenomemon of Si-based metal/insulator/semiconductor tunnel junction" *Applied Surface Science* **161**, 9-13 (2000).

[8] J. Seidel, T. Göhler, S. Grafström, and L. M. Eng *Applied Physics Letters* **92**, 103123 (2008).

[9] R. F. Oulton, V. J. Sorger, D. A. Genov, D. F. P. Pile, and X. Zhang, *Nature Phot.* **2**, 495-500 (2008).

[10] V. J. Sorger, Z. Ye, R. F. Oulton, Y. Wang, G. Bartal, X. Yin and X. Zhang *accepted at Nature Communications* (2011).

[11] S. M. Sze, *Physics of Semiconductor Devices* John Wiley & Sons, Inc. (1981).

[12] S. Szentirmay *Physical Review B* 36, 5, 2607-2614 (1986).

Chapter-6 (Part-3)

[1] S. Wang et al. "An integrated metal-oxide-metal device: A new integrated device with the widest band known" *IEEE Journal of Quantum Electronics* **13**,860 (1977).

[2] M. Uiberacker *et al*. "Attosecond real-time observation of electron tunneling in atoms" *Nature* **446**, 627-632 (2007).

[3] M.X. Wang, J.H. Yu and X.X. Sun "Light emission characteristics and negative resistance phenomemon of Si-based metal/insulator/semiconductor tunnel junction" *Applied Surface Science* **161**, 9-13 (2000).

[4] R. F. Oulton, V. J. Sorger, T. Zentgraf, R.-M. Ma, C. Gladden, L. Dai, G. Bartal, and X. Zhang, *Nature* **461**, 629-632 (2009).

[5] R.-M. Ma, R. F. Oulton, V. J. Sorger, G. Bartal and X. Zhang *Nature Materials* **10**, 110-113 (2010).

[6] J.A. Conway "Efficient Optical Coupling to the Nanoscale" *PhD Dissertation* (2006).

Chapter-7 (Part-1)

[1] http://www.itrs.net/

[2] Y.-H. Kuo, Y.-K. Lee, Y. Ge, S. Ren, J. E. Roth, T. I. Kamins, D. A. B. Miller & J. S. Harris, "Strong quantum-confined Stark effect in germanium quantum-well structures on silicon," *Nature* **437,** 1334-1336 (2005).

[3] J. E. Roth, O. Fidaner, E. H. Edwards, R. K. Schaevitz, Y.-H. Kuo, N. C. Helman, T. I. Kamins, J. S. Harris, and D. A. B. Miller, "C-band side-entry Ge quantum-well electroabsorption modulator on SOI operating at 1 V swing," Electronics Lett. **44**, 49 – 50 (2008).

[4] D. A. B. Miller, "Are optical transistors the next logical step?" *Nature Photonics* **4**, 3 - 5 (2010).

[5] D. A. B. Miller, "Device Requirements for Optical Interconnects to Silicon Chips," *Proc. IEEE* **97**, 1166 - 1185 (2009).

[6] R. H. Walden, "Analog-to-digital converter survey and analysis," *IEEE J. Selected Areas in Communications* **17** 539 -550 (1999).

[7] R. Urata, L. Y. Nathawad, R. Takahashi, K. Ma, D. A. B. Miller, B. A. Wooley, and J. S. Harris, "Photonic A/D conversion using low-temperature-grown GaAs MSM switches integrated with Si-CMOS," *J. Lightwave Technol*. **21**, 3104-3115 (2003).

[8] L. Tang, S. E. Kocabas, S. Latif, A. K. Okyay, D.-S. Ly-Gagnon, K. C. Saraswat and D. A. B. Miller, "Nanometre-Scale Germanium Photodetector Enhanced by a Near-Infrared Dipole Antenna," *Nature Photonics* **2**, 226 – 229 (2008)

[9] L. Tang, S. Latif, and D. A. B. Miller, "Plasmonic device in silicon CMOS," *Electronics Lett*. **45**, 706 – 708 (2009)

[10] R. F. Oulton, V. J. Sorger, D. A. Genov, D. F. P. Pile, and X. Zhang, *Nature Phot.* **2**, 495-500 (2008).

[11] V. J. Sorger, Z. Ye, R. F. Oulton, Y. Wang, G. Bartal, X. Yin and X. Zhang *accepted at Nature Communications* (2011).

[12] R.-M. Ma, R. F. Oulton, V. J. Sorger, G. Bartal and X. Zhang *Nature Materials* **10**, 110-113 (2010).

[13] R. F. Oulton, V. J. Sorger, T. Zentgraf, R.-M. Ma, C. Gladden, L. Dai, G. Bartal, and X. Zhang, *Nature* **461**, 629-632 (2009).

[14] W. Cai, J. S. White and M. L. Brongersma *Nano Lett.* **9**, 4403 - 4411 (2009).

[15] J. A. Dionne, K. Diest, L. A. Sweatlock and H. A. Atwater, *Nano Lett.* **9**, 2, 897-902 (2009).

[16] D. Pacifici, H. J. Lezec and H. A. Atwater *Nature Phot.* **1**, 402 - 406 (2007).

[17] M. L. Brongersma and V. M. Shalaev, *Science* **328**, 440-441 (2010).

[18] S. E. Miller *Bell Sys. Tech. Journal* **48**, 7, 2059 (1969).

[19] R.M. Ma, V.J. Sorger, R.F. Oulton, X. Yin and X. Xiang *unpublished work* (2011).

[20] V. J. Sorger et al. In review at *Physical Review Letters* (2011).

[21] S. A. Maier *Plasmonics, Fundamentals and Applications*; Springer: New York, 2007.

[22] K. M. Johnson Under the Secretary of Energy, Department of Energy
http://www1.eere.energy.gov/femp/regulations/requirements_by_subject.html#re (2011).

Chapter-7 (Part-2)

1] S.E. Miller, Bell *Sys. Tech. J.* **48**, 7, 2059 (1969).

[2] I. Hayashi, et al., *Appl. Phys. Lett,* **17**(3), 109 (1970).

[3] J. Shibata, et al., *Appl. Phys. Lett*., **45**(3), 191 (1984).

[4] O. Wada, et al., J. *Quantum Electron*., **22** (6), 805 (1986).

[5] T. L. Koch, et al., *J. Quantum Electron*., **27** (3), 641 (1991).

[6] M. Zirngibl, et al., *Electron Lett.,* **31** (7), 581 (1995).

[7] C.A.M. Steenbergen, et al., *ECOC (MoC4.1),* **129** (1996).

[8] C.G.P. Herben, et al, *Photon.Technol. Lett.,* **11** (12), 1599 (1999).

[9] L.A. Coldren, *J. Sel. Top. Quantum Electron*., **6** (6), 988 (2000).

[10] Y. Yoshikuni, *J. Sel. Top. Quantum Electron*., **8** (6), 1102 (2002).

[11] Y. Suzaki, et al., *IPRM (Sweden),* **681** (2002).

[12] M. L. Maˇsanoviˊc, et al., *Photon. Technol. Lett*., **15**(8), 1117 (2003).

[13] ASIP/Three-Five Photonics, www.rle.mit.edu/cips/conference04/Pennings_ASIP.pdf.

[14] R. Nagarajan, et al., *J. Sel. Top. Quantum Electron*., **11** (1), 50 (2005).

[15] R. Nagarajan, et al., *Electron. Lett.*, **42** (12), 771 (2006).

[16] M. Kato, et al., *Electron. Lett.,* **43** (8), 468 (2007).

[17] R. Nagarajan, et al., *OFC/NFOEC*, PDP**32** (2007).

[18] R. Nagarajan and M. Smit *IEEE Leos Newsletter* (2007).

Chapter-7 (Part-3)

1. Bergman, D. J. & Stockman, M. I. Surface Plasmon Amplification by Stimulated Emission of Radiation: Quantum Generation of Coherent Surface Plasmons in Nanosystems. *Physical Review Letters* **90,** 027402 (2003).

2. Ozbay, E. Plasmonics: merging photonics and electronics at nanoscale dimensions. *Science* **311**, 189-193 (2006).

3. MacDonald, K. F., Samson, Z. L., Stockman, M. I. & Zheludev, N. I. Ultrafast active plasmonics. *Nature Photonics* **3,** 55-58 (2009).

4. Brongersma, M. L., Shalaev, V. M. The case for plasmonics. *Science* **328**, 440-441 (2010).

5. Gramotnev, D. K., Bozhevolnyi, S. I. Plasmonics beyond the diffraction limit. *Nature Photonics* **4,** 83-91 (2010).

6. Miller, D. A. B. Device requirements for optical interconnects to silicon chips. *Proceedings of the IEEE* **97** 1166-1185 (2009).

7. Song, Q., Cao, H., Ho, S. T. & Solomon, G. S. Near-IR subwavelength microdisk lasers. *Appl. Phys. Lett.* **94**, 061109 (2009).

8. Gargas, D. J., *et al.* Whispering Gallery Mode Lasing from Zinc Oxide Hexagonal Nanodisks. *ACS Nano* **4**, 3270-3276 (2010).
9. Chen, R. *et al.* Nanolasers grown on silicon. *Nature Photonics* **5,** 170-175 (2011).

10. Hill, M. T. *et al.* Lasing in metal-insulator-metal sub-wavelength plasmonic waveguides. *Optics Express* **17**, 11107-11112 (2009).

11. Nezhad, M. P. *et al.* Room-temperature subwavelength metallo-dielectric lasers. *Nature Photonics* **4**, 395-399 (2010).

12. Yu, K., Lakhani, A. & Wu, M. C. Subwavelength metal-optic semiconductor nanopatch lasers. *Opt. Express* **18,** 8790–8799 (2010).

13. Hill, M. T. *et al.* Lasing in metallic-coated nanocavities. *Nature Photonics* **1,** 589–594 (2007).

14. Noginov, M. A. *et al.* Demonstration of a spaser-based nanolaser. *Nature* **460,** 1110-1113 (2009).

15. Oulton, R. F. *et al.* Plasmon lasers at deep subwavelength scale. *Nature*, **461,** 629-632 (2009).

16. Kwon, S.-H. *et al.* Subwavelength Plasmonic Lasing from a Semiconductor Nanodisk with Silver Nanopan Cavity. *Nano Letters* **10**, 3679-3683 (2010).

17. Ma, R.-M., Oulton, R. F., Sorger, V. J., Bartal, Guy. & Zhang, X. Room-temperature sub-diffraction-limited plasmon laser by total internal reflection. *Nature Materials* **10,** 110-113 (2011).

18. Garcia-Vidal, F. J. & Moreno, E. Lasers go nano. *Nature* **461** 604-605 (2009).

19. Editorial. Birth of the nanolaser. *Nature Photonics* **3,** 545 (2009).

20. Service, R. F. Ever-smaller lasers pave the way for data highways made of light. *Science* **328** 810-811 (2010).

21. Oulton, R. F., Sorger, V. J., Genov, D. A., Pile, D. F. P. & Zhang, X. A hybrid plasmonic waveguide for subwavelength confinement and long-range propagation. *Nature Photonics* **2**, 496-500 (2008).

22. Note about the simulation value lower than expected value.

23. Soref, R. A. Electrooptical effects in silicon. *IEEE Journal of Quantum Electronics* **QE-23** 123-129 (1987).

24. Roxlo, C. B., Putnam, R. S. & Salour, M. M. Optically pumped semiconductor platelet lasers. *IEEE Journal of Quantum Electronics* **QE-18** 338-342 (1982).

Chapter-8 (Part-1)

[1] D. E. Chang, A.S. Sorensen, E. Demler, M.D. Lukin, *Nature Physics* **3**, 807 (2007).

Chapter-8 (Part-2)

[1] E. M. Purcell *Phys. Rev.* **69**, 681 (1946).

[2] P. W. H. Pinkse, T. Fischer, P. Maunz and G. Rempe *Nature* **404**, 365–368 (2000).

[3] E. Peter, P. Senellart, D. Martrou, A. Lemaıtre, J. Hours, J. M. Gerard and J. Bloch *Phys. Rev. Lett.* **95**, 067401 (2005).

[4] I. Gontijo, M. Boroditsky and E. Yablonovitch *Phys Rev. Lett.* **60**, 11564 (1999).

[5] D. E. Chang, A.S. Sorensen, E. Demler, M.D. Lukin, *Nature Physics* **3**, 807 (2007).

[6] A. Faraon, D. Englund, D. Bulla, B. Luther-Davies, B. J. Eggleton, N. Stoltz, P. Petroff and J. Vučković *Appl. Phys. Lett.* **92**, 043123 (2008).

[7] P. Anger, P. Bharadwaj and L. Novotny *Phys. Rev. Lett.* **96**, 113002 (2006).

[8] A. Kinkhabwala, Z.Yu, S.Fan, Y. Avlasevich, K. Muelen and W. E. Moerner *Nature* **443**, 1062 (2008).

[9] T. Utikal, M. I. Stockman, A. P. Heberle, M. Lippitz, and H. Giessen *Phys. Rev. Lett.* **104**, 113903-1-4 (2010).

[10] M. I. Stockman *Physics Today* 39-44 (2011).

[11] D. E. Chang, A. S. Sørensen, P. R. Hemmer and M. D. Lukin Phys. Rev. Lett. 97, 053002 (2006).

[12] R. F. Oulton, V. J. Sorger, T. Zentgraf, C. Gladden, R.-M. Ma, G. Bartal, L. Dai and X. Zhang *Nature* **461**, 629 (2009).

[13] R.-M. Ma, R. F. Oulton, V. J. Sorger G. Bartal and X. Zhang *Nature Mat.* **10**, 110-113 (2010).

[14] R. F. Oulton, V. J. Sorger, D. A. Genov, D. F. P. Pile, and X. Zhang, *Nature Phot.* **2**, 495-500 (2008).

[15] V. J. Sorger, Z. Ye, R. F Oulton, Y. Wang, G. Bartal, X. Yin and X. Zhang, accepted at *Nature Comm.* (2011).

[16] M. D. Lukin, M. Fleischhauer, R. Cote, L. M. Duan, D. Jaksch, J. I. Cirac and P. Zoller *Phys. Rev. Lett.* **87**, 037901 (2001).

[17] Y. Fedutik, V. V. Temnov, O. Schoeps, and U. Woggon *Phys. Rev. Lett.* **99**, 136802 (2007).

[18] T. Lund-Hansen, S. Stobbe, B. Julsgaard, H. Thyrrestrup, T. Suenner, M. Kamp, A. Forchel and P. Lodahl *Phys. Rev. Lett.* **101**, 113903 (2008).

[19] G. Lecamp, P. Lalanne and J.P. Hugonin *Phys Rev. Lett.* **99**, 193901 (2007).

[20] M. I. Stockman *New J. Phys* **10**, 025031-1-20 (2008).

[21] C. Borchers, S. Müller, D. Stichtenoth, D. Schwen and C. Ronning, *J. Phys. Chem. B* **110**, 1656 (2006).

[22] See "Experimental Details" section chapter 8.2

[23] G. Zoriniants et al. *New J. of Phys.* **10,** 105002 (2008).

[24] R. F. Oulton, G. Bartal, D. F. P. Pile and X. Zhang, *New J. Phys.* **10**, 105018 (2008).

Chapter-8 (Part-3)

[1] D. K. Gramotnev and S. I. Bozhevolnyi *Nature Phot.* **4**, 83 - 91 (2010).

[2] S. A. Maier, P. G. Kik, and H. A. Atwater *Appl. Phys. Lett.* **81**, 1714-1716 (2002).

[3] A. V. Krasavin and A.V. Zayats *Optics Express* **18**, 11791-11799 (2010).

[4] R. F. Oulton, V. J. Sorger, D. A. Genov, D. F. P. Pile, and X. Zhang, *Nature Phot.* **2**, 495-500 (2008).

[5] R. F. Oulton, G. Bartal, D. F. P. Pile and X. Zhang, *J. New Phys.* **10**, 105018 (2008).

[6] V. J. Sorger, Z. Ye, R. F. Oulton, Y. Wang, G. Bartal, X. Yin and X. Zhang *accepted at Nature Communications* (2011).

[7] E. Verhagen, M. Spasenovic, A. Polman and L. Kuipers *Phys. Rev. Lett.* **102**, 203904 (2009).

[8] S. I. Bozhevolnyi, V. S. Volkov, E. Devaux, and T. W. Ebbesen *Phys. Rev. Lett.* **95**, 046802 (2005).

[9] J. A. Dionne, H. J. Lezec and H. A. Atwater, *Nano Lett.* **6**, 9, 1928-1932 (2006).

[10] D. F. P. Pile, T. Ogawa, D. K. Gramotev, T. Okamoto, M. Haraguchi, M. Fukui and S. Matsuo, *App. Phys. Lett.* **87**, 061106 (2005).

[11] H.-S. Chu, E.-P. Li and R. Hedge *Appl. Phys. Lett.* **96**, 221103 (2010).

[12] AFOSR fy-2011 Muri Topic # 17 "Large Scale Integrated Hybrid Nanophotonics" (2010).

[13] V. J. Sorger, R. F. Oulton, J. Yao, G. Bartal and X. Xiang, *Nano Lett.* **9**, 3489-3493 (2009).

[14]. Song, Q., Cao, H., Ho, S. T. & Solomon, G. S. Near-IR subwavelength microdisk lasers. *Appl. Phys. Lett.* **94**, 061109 (2009).

[15] Gargas, D. J., *et al.* Whispering Gallery Mode Lasing from Zinc Oxide Hexagonal Nanodisks. *ACS Nano* **4**, 3270-3276 (2010).

[16] Chen, R. *et al.* Nanolasers grown on silicon. *Nature Photonics* **5,** 170-175 (2011).

[17] Hill, M. T. *et al.* Lasing in metal-insulator-metal sub-wavelength plasmonic waveguides. *Optics Express* **17**, 11107-11112 (2009).

[18] Nezhad, M. P. *et al.* Room-temperature subwavelength metallo-dielectric lasers. *Nature Photonics* **4**, 395-399 (2010).

[19] Yu, K., Lakhani, A. & Wu, M. C. Subwavelength metal-optic semiconductor nanopatch lasers. *Opt. Express* **18,** 8790–8799 (2010).

[20] Hill, M. T. *et al.* Lasing in metallic-coated nanocavities. *Nature Photonics* **1,** 589–594 (2007).

[21] Noginov, M. A. *et al.* Demonstration of a spaser-based nanolaser. *Nature* **460,** 1110-1113 (2009).

[22] Oulton, R. F. *et al.* Plasmon lasers at deep subwavelength scale. *Nature*, **461,** 629-632 (2009).

[23] Kwon, S.-H. *et al.* Subwavelength Plasmonic Lasing from a Semiconductor Nanodisk with Silver Nanopan Cavity. *Nano Letters* **10**, 3679-3683 (2010).

[24] Ma, R.-M., Oulton, R. F., Sorger, V. J., Bartal, Guy. & Zhang, X. Room-temperature sub-diffraction-limited plasmon laser by total internal reflection. *Nature Materials* **10,** 110-113 (2011).

[25] Kinkhabwala, Z.Yu, S.Fan, Y. Avlasevich, K. Muelen and W. E. Moerner *Nature* **443**, 1062 (2008).

[26] D. A. B. Miller *Nature Photonics* **4**, 3-5 (2010).

[27] L. Liao, D. Samara-Rubio, M. Morse, A. Liu, D. Hodge, D. Rubin, U. D. Keil and T. Franck, *Optics Express* **13**, 8, 3129-3135 (2005).

[28] W. Cai, J. S. White and M. L. Brongersma *Nano Lett.* **9**, 4403 - 4411 (2009).

[29] J. A. Dionne, K. Diest, L. A. Sweatlock and H. A. Atwater, *Nano Lett.* **9**, 2, 897-902 (2009).

[30] V. J. Sorger, D. L. Kimuar, T. Zentgraf and X. Xiang *status in preparation* (2011).

[31] Altug, H., Englund, D. & Vuckovic, J. Ultrafast photonic crystal nanocavity laser. *Nature* **2**, 484 (2006).

Appendix A

Calculation of modal Purcell factor

This section relates to the modeling of the molecular emission coupling into a plasmonic hybrid waveguide mode with deep-subwavelength optical confinement. In particular it was used to predict the emission rates of the hybrid plasmon mode with varying gap thickness. The solid trend lines in Figure 8.2.3 from chapter 8.2 are calculated via the method described here.

The spontaneous emission rate of a transition dipole is given by Fermi's golden rule:

$$\gamma(\overrightarrow{r_0}; \omega) = 2\pi |g(\overrightarrow{r_0}; \omega)|^2 D_{1d}(\omega) \qquad (1)$$

where $|g_k(\overrightarrow{r_0}; \omega)|^2$ is the coupling strength between the transition dipole $\vec{\mu}$ and the electromagnetic field mode (with propagation wavevector $k = k_z$) at the dipole position $\overrightarrow{r_0}$ which can be written as

$$|g_k(\boldsymbol{r_0}; \omega)|^2 = \left| \boldsymbol{\mu} . \frac{\alpha \, \boldsymbol{E}(\mathrm{x_0, y_0})}{\hbar} \right| = \frac{\omega \mu^2}{2\hbar \, \epsilon \, \epsilon_0 V_{eff}(x_0, y_0)}$$

The electromagnetic flux of the mode is normalized to vacuum field fluctuation by a normalizing factor α

$$|\alpha|^2 \int \frac{Re(\boldsymbol{E} \times \boldsymbol{H}^*)}{2c^2} dV = |\alpha|^2 \int \frac{S_z(x, y)}{c^2} dA \, \ell = \frac{\hbar \omega}{2c}$$

S_z/c^2 is Abraham's pure electromagnetic momentum density [R. Loudon, L. Allen and D.F. Nelson, Phys Rev E, 55, 1, 1071, (1997)] of the optical mode. $D_{1d} = \frac{\ell}{\pi c}$ is the one-dimensional density of state of pure photonic field and ℓ is arbitrary quantization length along the waveguide such that the effective mode area and effective mode volume may be defined as $V_{eff}(\vec{r}_0) = \ell \, A_{eff}(x_0, y_0)$. We finally arrive at the expression for the spontaneous emission rate and Purcell factor of the optical mode F_m

$$F_m(\boldsymbol{r_0}) = \frac{\gamma_m(\boldsymbol{r_0})}{\gamma_i} = \frac{3}{4\pi} \left(\frac{\lambda_0^2}{A_{eff}(\boldsymbol{r_0})} \right) \frac{1}{n} = \frac{3}{4\pi} \left(\frac{\lambda_0}{n} \right)^2 \frac{\frac{1}{2} c \epsilon \epsilon_0 |\boldsymbol{E}(\boldsymbol{r_0})|^2}{\int S_z dA} \frac{1}{n}$$

$$= \frac{3\lambda_0^2}{4\pi} \left(\frac{c/n}{v_E} \right) \left[\frac{\varepsilon_0 |\boldsymbol{E}(\boldsymbol{r_0})|^2}{2 \int w(x, y) dA} \right]$$

where coupling rate to the mode γ_m is normalized to the intrinsic emission rate γ_i in an unbound host medium of index n.

$$\gamma_i = \frac{\mu^2 \omega^3 n}{3\pi \epsilon_0 c^3 \hbar}$$

In the final equality (3) we have written the Purcell factor in terms of modal energy density $w(x,y)$ and energy velocity v_E using the relationship $\int S_z(x,y)dA = v_E \int w(x,y)dA$ where $w(x,y) = \epsilon_0 \frac{d(\omega\epsilon(x,y))}{d\omega}|E(x,y)|^2 + \mu_0\mu(x,y)|H(x,y)|^2$. In the expression (3) above, we also have defined the mode area as

$$A_{eff}(r_0,\omega) = \frac{P}{I_0} = \frac{\int S_z dA}{\frac{1}{2}c\epsilon_0|E(r_0)|^2}$$

Our expression for Purcell factor is in perfect agreement with the formula derived from the guided mode expansion method in classical electromagnetic theory [J. D. Jackson, Classical Electrodynamics, Wiley, (1998)].

It is noteworthy that our expression is different from that conventionally derived for purely dielectric waveguides in references [C. Jun, R. D. Kekatpure, J. S. White, and M. L. Brongersma *Phys. Rev. B* 78, 153111 (2008), I. Gontijo, M. Boroditsky and E. Yablonovitch *Phys Rev. Lett.* **60**, 11564 (1999)], where one defines the density of state of photon as $D_{1D} = \frac{1}{\pi v_g}$ (where v_g is group velocity) and the mode area normalized to the photon vacuum energy as $A_{eff}(x_0,y_0) = \frac{\int w(x,y)dA}{w(x_0,y_0)}$ such that $\frac{\gamma_m}{\gamma_i} = \frac{3}{4\pi}\frac{\frac{c}{n}}{v_g}\frac{\lambda_0^2}{A_{eff}}$.

However, in dielectric waveguide with complex material properties, it is difficult to interpret the photonic density of state simply by an argument about the waveguide dispersion without a proper definition of mode area. If we stick to the convention above, we would have arrived at an expression for modal Purcell factor with the group velocity. However, if we solve the problem of dipole coupling to a guided mode by classical mode expansion method [J. D. Jackson, Classical Electrodynamics, Wiley, (1998)], we will have to reinterpret group velocity in the dispersive waveguide as energy velocity instead. By quantum-classical correspondence principle, we conclude that we could also arrived at the same classical result using quantum theory via a Fermi golden with a slightly different interpretation of mode area and 1D photonic density of state, where we should use Abraham (pure electromagnetic field excluding that of the medium) momentum density (instead of energy density) for normalizing the vacuum photon and a dispersionless vacuum photonic density of state.

When adding modal Purcell factor calculated with this method to the Purcell effect due to metal quenching and coupling to 2D surface plasmon for planar structure which can be calculated analytically according to [R. R. *Chance*, A. *Prock*, and R. *Silbey*, *Adv. Chem. Phys.* 37, 1 (1978)], the total Purcell factor follow closely the result from FEM simulation. This suggests that the presence of waveguide does not significantly modify the emission coupling rate to 2D surface plasmon and to metal quenching.